

COMMISSIONING OF A TRIPLE-FOIL PLUNGER FOR EXOTIC NUCLEI (TPEN)

A thesis submitted to the University of Manchester for the degree
of Doctor of Philosophy in the Faculty of Science and Engineering

2019

MICHAEL GILES

School of Physics and Astronomy

University of Manchester

The remainder of this page was intentionally left blank.

Contents

List of Figures	7
List of Tables	11
Abstract	13
Declaration of Authorship	15
Copyright Statement	17
Acknowledgements	20
1 Introduction	21
2 Theory	25
2.1 Measuring lifetimes with a plunger	26
2.1.1 Recoil distance Doppler shift method	27
2.1.2 Differential decay curve method	29
2.1.3 Triple foil plunger	32
2.1.4 Corrections required to detected γ -ray intensities	36
2.2 Nuclear models	41
2.2.1 Liquid drop model	41
2.2.2 Single-particle shell model	42
2.2.3 Two-state mixing	46
2.2.4 Nuclear deformations and rotations	46
2.2.5 The Coriolis interaction	53
2.3 Gamma-ray emission	54
2.3.1 Selection rules	54
2.3.2 Transition rates	55
2.4 Reactions	57
2.4.1 Heavy Ion fusion evaporation reactions	57
2.4.2 Coulomb excitation	58
2.5 Detecting gamma rays	61

2.6	Extracting component intensities from unresolved Gaussians . . .	62
3	Triple Foil Plunger Setup	65
3.1	Overview	65
3.2	Plunger foils	69
3.2.1	Aligning the foils	71
3.3	TPEN frame	74
3.4	Vacuum housing	75
3.5	LSP-45 Motors	77
3.6	E-871 control units	79
3.7	Micrometers	80
3.8	Data acquisition card	80
3.9	Software and feedback system	81
3.9.1	Motor virtual instrument	81
3.9.2	Micrometer virtual instrument	82
3.9.3	Voltage virtual instrument	83
3.9.4	Calibration virtual instrument	83
3.9.5	Feedback system	84
3.9.6	Modification to software	85
4	Commissioning TPEN	87
4.1	Introduction	87
4.2	K130 cyclotron	89
4.3	Phase 1 HPGe detectors	91
4.3.1	Energy calibration	91
4.3.2	Efficiency	92
4.3.3	Doppler broadening	93
4.4	Total Data Readout	94
4.5	GRAIN	94
5	Analysis and Results	97
5.1	TPEN performance	98
5.1.1	Testing the calibration of voltage and distance	98
5.1.2	Calibration during commissioning	99
5.1.3	Constant feedback system	101
5.2	Lifetime results	105
5.2.1	Reaction products	105
5.2.2	Differential lifetime measurements	107
5.2.3	TPEN with low statistics	112
5.2.4	TPEN working as a standard plunger	114
5.2.5	Beam-time improvement with TPEN	118
6	Discussion and future use	121
6.1	Beam-time reductions with TPEN	121
6.1.1	Using TPEN with a recoil separator	121

6.1.2	Mass analysing separators	122
6.1.3	Planning experiments with TPEN	124
6.2	Minimizing uncertainty with TPEN	127
6.2.1	Absolute foil distances	127
6.3	Future use of TPEN	128
6.3.1	Simultaneous lifetime measurements	128
6.3.2	Proton-rich nuclei	129
6.3.3	Coulex-Plunger measurements	134
7	Conclusions	139
A	Lifetime measurements in ^{112}I	141
B	Lifetime measurements in ^{50}Mn	151
C	Triple foil plunger for exotic nuclei (TPEN)	161
	Bibliography	171

Final word count: 25299

The remainder of this page was intentionally left blank.

List of Figures

2.1	Schematic diagram of typical two-foil plunger setup	26
2.2	Schematic level scheme	28
2.3	Schematic diagram of a triple foil plunger	32
2.4	The relative enhancement of γ emission for a travelling recoil at different angles	38
2.5	The first four even Legendre Polynomials	39
2.6	Woods-Saxon, harmonic oscillator and infinite well potentials . . .	43
2.7	Schematic diagram of the single-particle energy levels	45
2.8	Schematic diagram of two state mixing	46
2.9	Nuclear shape as described by the Lund convention	48
2.10	Vibrational modes of a spherical ground state	49
2.11	Schematic diagram of the separation of Nilsson single particle energy states	51
2.12	An example of a Nilsson diagram for neutrons	52
2.13	A schematic illustration a compound nucleus following a heavy-ion fusion evaporation reaction	58
2.14	A schematic diagram a compound nucleus following a heavy-ion fusion evaporation reaction	59
2.15	Schematic diagram of a Coulomb excitation reaction	60
2.16	Calculated differential Coulomb excitation cross sections	61
3.1	Schematic diagram of the triple foil plunger device used	68
3.2	Drawing of the foil frames used in TPEN	69
3.3	Schematic diagram of the plunger stretching cones.	70
3.4	Side view of a plunger degrader stretching cone	70
3.5	Drawing of the foil stretcher and cone	70
3.6	Schematic diagram of a plunger foil mount.	71
3.7	Photograph of the foil frame and stretching cone.	72
3.8	Photograph of all three foils aligned	74
3.9	Drawing of the frame for TPEN.	75
3.10	CAD drawing of the TPEN vacuum housing	76
3.11	CAD drawing of a cross section of TPEN	77
3.12	CAD drawing of the vacuum feedthroughs used on TPEN	77
3.13	Photograph of the LPS-45 motor	78
3.14	Photograph of the E-871 control unit	79
3.15	Photograph of the TESA TT20 and GT43 probes	81

3.16	Photograph of the NI USB-6251 DAQ card	82
3.17	Screen-shot of the motor virtual instruments	83
3.18	A diagram showing TPEN and the electronic modules used with TPEN	85
4.1	Partial level scheme of ^{156}Dy	88
4.2	An illustration of the TPEN vacuum housing surrounded by the 4 backward facing germanium detectors connected to RITU	89
4.3	A photograph of the TPEN vacuum housing surrounded by the 4 backward facing germanium detectors	90
4.4	Efficiency calibration for all four HPGe detectors	93
5.1	The induced voltage on the target foil with varying stopper distance	99
5.2	Target-to-degrader calibration curve	100
5.3	Reciprocal of the target-to-degrader calibration curve	100
5.4	Degrader-to-stopper calibration curve	101
5.5	Reciprocal of the degrader-to-stopper calibration curve	101
5.6	Induced target voltage for the $x = 700 \mu\text{m}$ $\Delta x = 31 \mu\text{m}$ plunger distance over time	103
5.7	Induced stopper voltage for the $x = 700 \mu\text{m}$ $\Delta x = 31 \mu\text{m}$ plunger distance over time	104
5.8	Induced stopper voltage over 30 minutes for the $x = 700 \mu\text{m}$ $\Delta x = 31 \mu\text{m}$ plunger distance	105
5.9	Induced stopper voltage for the $x = 700 \mu\text{m}$ $\Delta x = 51 \mu\text{m}$ plunger distance	106
5.10	Gated spectrum of γ rays in coincidence with the fully shifted and degraded components of the $6^+ \rightarrow 4^+$ in ^{156}Dy	107
5.11	γ ray coincidence energies for any detector versus any other detector at the $x = 700 \mu\text{m}$ $\Delta x = 31 \mu\text{m}$ plunger distance.	108
5.12	The three intensity components of the 266-keV transition in ^{156}Dy	110
5.13	The three intensity components of the 266-keV transition in ^{156}Dy with a logarithmic scale	111
5.14	Multiplicity three events at a plunger distance of $x = 700 \mu\text{m}$, $\Delta x = 51 \mu\text{m}$	113
5.15	The three intensity components of the 266-keV transition in ^{156}Dy from multiplicity three events	114
5.16	The three intensity components of the 266-keV transition in ^{156}Dy for standard plunger analysis	116
5.17	The intensity of the 266-keV transition in ^{156}Dy before and after a degrader foil for standard plunger analysis	117
5.18	The ^{156}Dy gated spectra obtained in the work by Möller <i>et. al.</i>	120
6.1	A schematic illustration of MARA	123
6.2	The energy distribution of recoils after passing through two $3\text{mg}/\text{cm}^2$ foils.	124

6.3	The angular distribution of recoils after passing through two 2.9 mg/cm ² Au foils.	125
6.4	The transmission probability of recoils through MARA	126
6.5	The level scheme of ¹⁶¹ Re	130
6.6	γ spectra obtained from gating on the α or proton decay in ¹⁶¹ Re	131
6.7	Simulated spectra of the three components in ¹⁶¹ Re	133
6.8	Schematic representation of kinematic corrections to Doppler shifted components in a Coulex-Plunger experiment	135
6.9	Drawing of TPEN fitted with a DSSD	136
6.10	Sliced drawing of TPEN fitted with a DSSD	137
6.11	Drawing of TPEN installed at the HIE-ISOLDE beamline.	138

The remainder of this page was intentionally left blank.

List of Tables

2.1	Table of the Weisskopf estimates	56
3.1	Micrometer adaptor pin layout	80
3.2	Table of changes made to the motor commands	86
4.1	Measured calibration coefficients between channel number and energy.	92
5.1	Measured target-to-degrader distance and degrader-to-stopper distance for each plunger run.	105
5.2	The main reaction channels from the $^{\text{nat}}\text{Mg}+^{136}\text{Xe}$ reaction at 590 MeV	106
5.3	Measured fully shifted, degraded and stopped intensities of the 266-keV γ ray.	109
5.4	Measured widths and centroids of the fully shifted, degraded and stopped components the 266-keV γ ray.	112
5.5	Measured intensities of the 266-keV γ ray before and after the degrader foil.	118

The remainder of this page was intentionally left blank.

Abstract

A Triple-foil differential Plunger for Exotic Nuclei (TPEN) has been developed to measure the lifetimes of excited states in nuclei with small production cross sections. TPEN utilises one target foil and two degrader foils to make differential lifetime measurements by directly determining the decay function and its derivative at a single plunger distance setting. The direct measurement of the decay function and its derivative removes the requirement to measure γ -ray intensities at several target-to-degrader distances, thereby reducing the beam-time required relative to a conventional plunger with a single-degrader foil. This thesis describes the construction and subsequent commissioning of TPEN with the lifetime measurement of the first excited 4^+ state in ^{156}Dy using this differential lifetime technique. The $46(2)$ ps measured lifetime of the 4^+ was found to be in good agreement with the $45.6(5)$ ps deduced from a previous high-statistics experiment using a conventional two-foil plunger. A comparison between the present work with TPEN and using conventional two-foil plungers reveals that TPEN achieves the same statistical accuracy with a ~ 4 -fold reduction in beam-time with this particular $^{24}\text{Mg}(^{136}\text{Xe},4n)$ reaction. TPEN therefore opens up new opportunities to study exotic nuclei with lower production cross sections that were previously inaccessible.

The remainder of this page was intentionally left blank.

Declaration of Authorship

I, MICHAEL GILES, confirm that no portion of the work referred to in the thesis has been submitted in support of an application for another degree or qualification of this or any other university or other institute of learning.

The remainder of this page was intentionally left blank.

Copyright Statement

- i. The author of this thesis (including any appendices and/or schedules to this thesis) owns certain copyright or related rights in it (the “Copyright”) and s/he has given The University of Manchester certain rights to use such Copyright, including for administrative purposes.
- ii. Copies of this thesis, either in full or in extracts and whether in hard or electronic copy, may be made **only** in accordance with the Copyright, Designs and Patents Act 1988 (as amended) and regulations issued under it or, where appropriate, in accordance with licensing agreements which the University has from time to time. This page must form part of any such copies made.
- iii. The ownership of certain Copyright, patents, designs, trade marks and other intellectual property (the “Intellectual Property”) and any reproductions of copyright works in the thesis, for example graphs and tables (“Reproductions”), which may be described in this thesis, may not be owned by the author and may be owned by third parties. Such Intellectual Property and Reproductions cannot and must not be made available for use without the prior written permission of the owner(s) of the relevant Intellectual Property and/or Reproductions.
- iv. Further information on the conditions under which disclosure, publication and commercialisation of this thesis, the Copyright and any Intellectual Property and/or Reproductions described in it may take place is available in the University IP Policy (see <http://documents.manchester.ac.uk/DocuInfo.aspx?DocID=24420>), in any relevant Thesis restriction declarations deposited in the University Library, The University Library’s regulations (see <http://www.library.manchester.ac.uk/about/regulations/>) and in The University’s policy on Presentation of Theses

The remainder of this page was intentionally left blank.

After climbing a great hill, one only finds that there are many more hills to climb.

Nelson Mandela.

Acknowledgements

Firstly, I would like to acknowledge my supervisor Dr David Cullen for the continuous support throughout my time as a Ph.D student. Dave, I would like to thank you for the countless hours you have spent helping me during my time at Manchester, without your help this document would not be possible.

Thanks to everyone working at Jyväskylä for your help during the commissioning of TPEN, with a special thanks to Liam, Jacob, Mike, Eddie and Phillipos. Liam and Jacob, thank you for the long days you spent helping to set up TPEN and more importantly, for the drinks shared in ‘The Green Fairy’.

To the nuclear physics department at The University of Manchester, this Ph.D wouldn’t have been the same without you. From day one I was made to feel welcome and the lunchtime conversation will be solely missed.

To Meg, Puneet, Jacob, Ben, Dan and Ed, thank you for keeping me sane with our weeknight lifting sessions.

Lastly, I’d like to thank my family, especially my Mum, for the continued encouragement and support shown throughout my life. I couldn’t have done it without you!

Chapter 1

Introduction

Experimental studies of nuclei at the limits of existence forms a major part of international research programs at radioactive ion beam facilities. Determining the lifetimes of excited states in these exotic nuclei can reveal subtle properties of the nuclear force that are masked in the more strongly bound nuclei near to the valley of stability. As the electromagnetic (EM) operator is well understood, transition rates between excited nuclear levels provide useful knowledge of the corresponding wavefunctions of the levels involved. Knowledge of the nuclear wavefunctions can then be used to determine information on the nuclear force. For example, the lifetimes of nuclear states are particularly sensitive to a variety of nuclear structure features including changes in conventional shell gaps, shape co-existence, isospin symmetry, proton-neutron coupling and the coupling between discrete levels and the continuum [1–5].

Dedicated plunger devices are capable of measuring lifetimes in the range of picosecond to nanosecond using techniques developed between 1949 and 1965 [6, 7]. The Recoil Distance Doppler Shift method (RDDS) [8] and, more recently, the differential decay curve method (DDCM) [9] have been used with two foil plunger devices since the advent of high-resolution γ -ray detectors in 1965 [7, 10]. Plunger devices typically consist of two foils close together with a well known separation. The target foil is used to produce recoiling nuclei of interest in an excited state. The second foil is used to stop the recoil. Hence, excited states in

recoils can decay in two velocity regimes. The two velocity regimes splits each γ -ray transition into two components, as γ rays emitted by moving nuclei will be measured with a Doppler shifted energy. γ rays emitted from stopped nuclei will not be Doppler shifted. By measuring the intensity of the two components at several foil separations, with known flight times, the lifetime of excited states can be measured.

The main obstacle in performing lifetime measurements on exotic nuclei far from stability is their small production cross sections. Conventional plunger devices such as the Differential Plunger for Unbound Nuclear States, (DPUNS) [11] are limited to measuring lifetimes in nuclei with production cross section greater than $10 - 20 \mu\text{b}$ with 14 days of beam time at the Accelerator Laboratory at the University of Jyväskylä (JYFL), Finland [12–16].

In order to study nuclei with smaller production cross sections, the Triple-foil differential Plunger for Exotic Nuclei (TPEN) has been developed at The University of Manchester. This thesis presents work conducted on the development of TPEN [17]. TPEN plans to improve on current plunger devices in a number of ways, primarily removing the requirement for measuring component intensities at several target-to-stopper distances. Hence reducing beam time requirements and allowing access to much smaller cross section reactions.

TPEN has been designed and built to utilise the differential mode of the DDC method, which was first presented in Ref [9]. TPEN consists of one target foil and two degrader foils which produce three velocity regimes. This produces three detected energies for a γ ray due to the three Doppler shifts, which allows for a measurement of a fully shifted, degraded and unshifted γ -ray intensities. These intensities provide a direct measurement of both the decay function, and the derivative of the decay function [9]. The direct measurement of the derivative of the decay function makes it possible to measure the lifetimes of excited nuclear states using only one plunger distance [6].

TPEN was commissioned at JYFL. This thesis presents the results of this commissioning experiment in which the known lifetime of the first excited 4^+ state in ^{156}Dy was measured. The experiment employed the inverse reaction $^{24}\text{Mg}(^{136}\text{Xe}, 4n)^{156}\text{Dy}$ at a beam energy of 590 MeV. The 1 pnA $^{136}\text{Xe}^{25+}$ beam was used to bombard a 1 mg/cm^2

target for six days. γ -ray intensities were recorded using four Compton-suppressed Jurogam Phase-1 [18, 19] germanium detectors placed at 157.5° from the beam axis, on a specially constructed table. The lifetime measured with TPEN was found to be in agreement with that determined from a conventional plunger experiment [20]. A comparison between these lifetime experiments reveals that TPEN achieves the same statistical accuracy with a ~ 4 -fold reduction in beam-time with this $^{24}\text{Mg}(^{136}\text{Xe}, 4n)$ reaction. Such improvements in beam-time efficiency will allow lifetime measurements in more exotic nuclei. Initially, heavy-ion fusion evaporation reactions will be used at JYFL. New proposals have been accepted at JYFL to measure lifetimes of excited nuclear states in the proton-rich nuclei ^{161}Re and ^{147}Tm using TPEN. ^{161}Re is the lightest known Re isotope with 24 neutrons less than its nearest stable isotope. It is also one of only ~ 50 nuclei across the entire nuclear chart to undergo proton emission. By measuring lifetimes in this nucleus, we plan to expand our work on developing a simultaneous understanding of proton- and γ -emission using lifetime measurements in proton-emitting nuclei [12, 21, 22]. ^{161}Re presents an exciting and rare opportunity to study the deformation of a nucleus which undergoes α and proton emission from the same state. Previous plunger devices such as DPUNS would require ~ 25 days beam time to perform lifetime measurements in this nucleus. TPEN makes it possible to perform this measurement with the same statistical uncertainty in only 9 days. TPEN will also be used for lifetime measurements in neutron-rich exotic with Coulex-Plunger experiments or multi-nucleon transfer reactions at the MINIBALL setup at HIE-ISOLDE, CERN [23, 24].

Software to control the plunger has also been written and modified using Labview [25], with the majority being adapted from current software from the University of Köln. The software is capable of remotely controlling multiple motors to vary foil distances, and has a capacitive feedback system between foils which keeps foil separations constant during experiment. This is required as heating of the foils from the beam generates deformations in the foil, changing the target-to-degrader and degrader-to-stopper distances. Beam fluctuations mean the heating is not uniform and is unpredictable, so constant feedback is required. The complete, adapted software suite has been successfully tested at the University of Jyväskylä during three separate experiments [26] for the ordinary two foil plunger, and for the triple plunger during the commissioning experiment.

In addition to work carried out on TPEN in this thesis, conventional two-foil plungers were also used to study the lifetimes of excited states in nuclei. The lifetimes of excited states in the rotational band of ^{112}I were measured with the DPUNS plunger at JYFL. The results were published in *Physical Review C*, and are presented in Appendix A. The lifetime of the first 2^+ state excited state in ^{50}Mn was measured using the Köln plunger to compare the transition probabilities of the $A = 50$ isobaric analogue nuclei. These results have been submitted to *Physical Review C* and are presented in Appendix B. The development and commissioning of TPEN has also been published in *Nuclear Instruments and Methods A*, and is presented in Appendix C.

Chapter 2

Theory

In this work, a new triple-foil plunger device is presented, which is designed to improve the efficiency of the current technique for measuring nuclear state lifetimes in the $10^{-12} - 10^{-8}$ s time range. This chapter describes the way in which a conventional two-foil plunger works and then expands the method to a three-foil plunger. The idea of a three-foil plunger was first discussed in Ref. [9]. The principles of the RDDS and the DDC methods are presented here and the equations used to measure lifetimes are given. The differential mode of the DDCM is explained along with how the three-foil plunger exploits the method.

Relations between measured γ -ray intensities and nuclear state lifetimes are derived for both the two-foil plunger and the three-foil plunger [9]. Relevant corrections to the measured γ -ray intensities, and when they become important is discussed [6].

Additionally, this chapter highlights some nuclear models, which are used to interpret the properties of γ -ray emission and measured nuclear state lifetimes. Single-particle models and collective models are discussed along with how the measurement of nuclear state lifetimes can provide stringent tests of these models. The main reactions used to produce exotic nuclei are also discussed.

2.1 Measuring lifetimes with a plunger

Figure 2.1 shows a typical setup for a plunger device. An incoming beam is incident on a target foil and produces nuclei in an excited state via fusion evaporation or Coulomb excitation (Coulex) reactions. These excited nuclei will then decay via γ -ray emission to their ground states. The excited nuclei are ejected from the target foil and travel towards the stopper foil with a velocity v , where they are subsequently stopped. If an excited state decays via γ -ray emission while the recoiling nucleus is moving, then the observed γ ray will be Doppler shifted. If the γ -ray decay occurs after the recoiling nucleus has stopped in the stopper foil, then the γ ray is observed with no Doppler shift. The γ energy observed if the γ ray is emitted before the stopper foil, i.e. when the recoiling nucleus is in flight is given by γ_s . The energy observed from the γ ray emitted by the nuclei in the stopper foil, i.e. when the recoiling nuclei has $v' = 0$ is given by γ_{us} . If a thinner degrader foil is used instead of a stopper foil, γ_d is the γ ray emitted by the nucleus after leaving the degrader foil, with velocity v' .

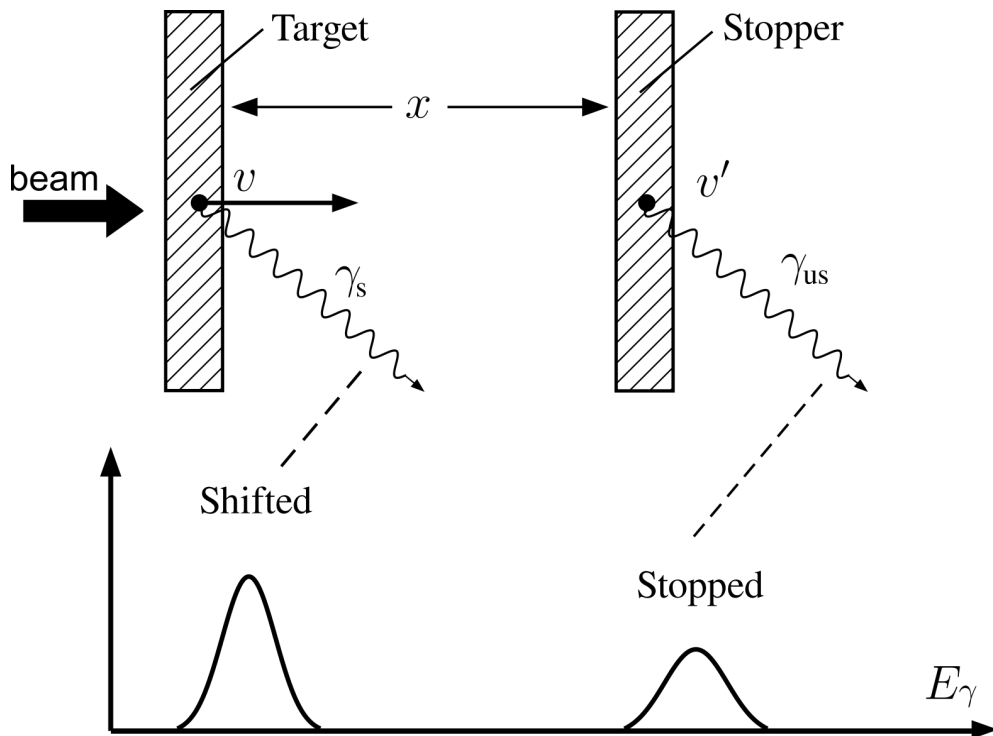


FIGURE 2.1: Schematic diagram of a typical two-foil plunger setup showing a target and stopper foil and an incoming beam. The stopper foil is interchangeable with a degrader foil. The shifted and stopped components shown are for backward angled detectors, which are typically used with recoil separators.

Figure adapted from Ref. [6].

γ rays emitted from a nucleus in flight will be observed in the lab frame with a Doppler shifted energy

$$E = E_0 \frac{1 - \beta \cos(\theta)}{|\sqrt{1 - \beta^2}|}, \quad (2.1)$$

where E is the energy of the γ ray in the lab frame, E_0 is the energy of the γ ray in the rest frame of the travelling nuclei, $\beta = v/c$ and θ is the angle between the beam axis and the direction the γ ray is traveling [6].

An observation of the energies of γ rays emitted from the decay of excited states of a recoiling nucleus provides information on whether the nucleus decayed before or after implanting into the stopper foil. If the lifetime of the excited state is short compared to the flight time from the target foil to the stopper foil, then the majority of the decays will occur in flight. This means that the intensity of the shifted peak, I_s , will be large compared to the intensity of the unshifted peak, as shown in Fig 2.1. Conversely, if the lifetime of the state is much longer than the flight time, then the majority of the recoiling nuclei will still be in an excited state when they reach the stopper foil. Hence, no Doppler shift will be experienced by the majority of emitted γ rays and the intensity of the unshifted peak, I_u , will be large compared to the intensity of the shifted peak. By varying the target-to-degrader distance, x , and measuring the intensities of the unshifted and shifted peaks, a lifetime of the excited nuclei can be calculated. Several techniques to calculate lifetimes using this principle are discussed in this chapter.

2.1.1 Recoil distance Doppler shift method

The Recoil Distance Doppler Shift (RDDS) method uses the principles described above to make lifetime measurements in the ps-ns range. The RDDS method uses the decay curve of a state to calculate the lifetime of that state. The decay curve is the normalised probability for a decay to occur after a recoiling nucleus has implanted into the stopper foil as a function of flight time, t [6].

In an ideal case of a single excited state with no feeding, the decay curve is related to the lifetime by

$$R(t) = n(0)e^{-t/\tau}, \quad (2.2)$$

where $n(0)$ is the initial population of the excited state and τ is the lifetime.

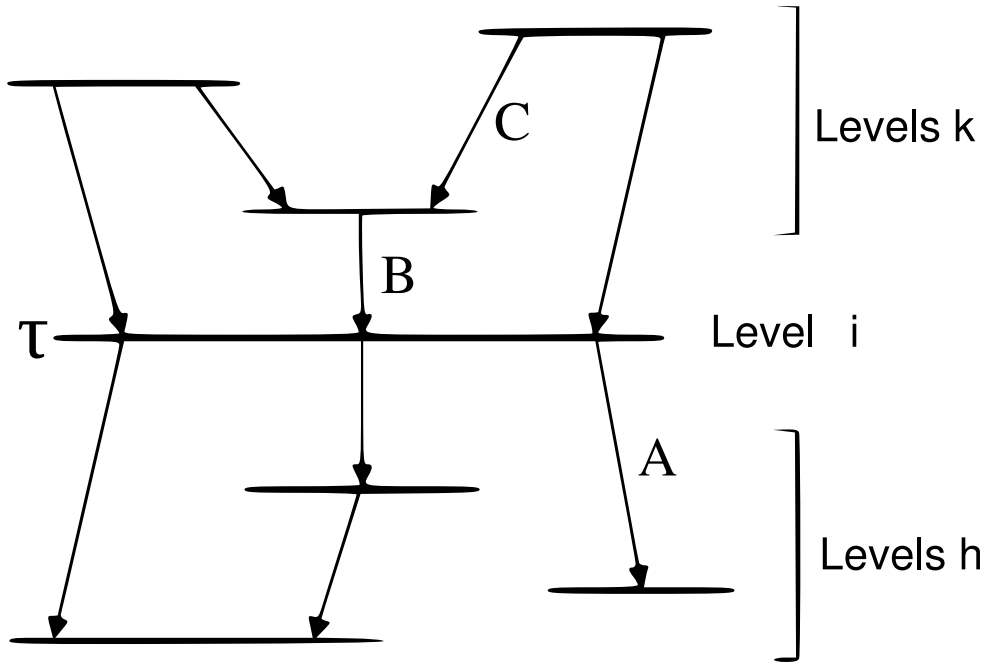


FIGURE 2.2: Schematic diagram of a nuclear level scheme showing levels k , i and h . γ -ray transitions C , B and A have been labeled as they are used to describe coincidence techniques in Section 2.1.2.1. Figure adapted from Ref. [6].

However, for a general excited state there are several states which feed into one another and a series of differential equations must be solved in order to extract τ . These equations are known as the Bateman equations [6, 27, 28]. In general, for a level scheme such as Fig. 2.2 [9] the change in population of state i as a function of time can be expressed as

$$\frac{d}{dt}n_i(t) = -\lambda_i n_i(t) + \sum_{k=i+1}^N \lambda_k n_k(t) b_{ki}, \quad (2.3)$$

where $n_i(t)$ is the population of state i at time t , λ_i, λ_k are the decay constant of states i and k , respectively, and b_{ki} are the branching ratios from levels k to i [6]. By integrating Eqn. 2.3

$$\int_t^\infty \frac{d}{dt}n_i(t) dt = - \int_t^\infty \lambda_i n_i(t) dt + \sum_{k=i+1}^N \int_t^\infty \lambda_k n_k(t) b_{ki} dt, \quad (2.4)$$

and using the definition of the decay curve, i.e. the normalised probability for a decay to occur after time t

$$R_i(t) = \lambda_i \int_t^\infty n_i(t) dt, \quad (2.5)$$

the decay curve for state i can be written as

$$R_i(t) = P_i(t)e^{-t\lambda_i} + \sum_{k=i+1}^N R_{ki}. \quad (2.6)$$

Here $P_i(t)$ is the direct feeding intensity of level i and $R_{ki}(t)$ is the decay curve of state k for transitions decaying to state i , i.e.

$$R_{ki}(t) = \lambda_k b_{ki} \int_t^{\infty} n_k(t) dt. \quad (2.7)$$

The decay curve can be found experimentally by measuring the intensities of shifted and unshifted γ rays according to Eqn. 2.8 [6]

$$R(t) = \frac{I_u(t)}{I_u(t) + I_s(t)}. \quad (2.8)$$

$R_i(t)$ can be fitted to the experimentally obtained intensities of the shifted and unshifted components using Eqn. 2.8 and the lifetime of state i can be deduced [6].

In practice, fits to RDDS data are often difficult as there are many free parameters such as branching ratios and initial populations. Unobserved side feeding must be estimated based on the time-behaviour of the state of interest. Additionally the absolute target-to-stopper distances are required to deduce the lifetime. These absolute distances are difficult to measure compared to relative distances. These problems often lead to large systematic uncertainties with the RDDS technique which can be eliminated using $\gamma-\gamma$ coincidence techniques and the Differential Decay Curve Method (DDCM), which is discussed in Section 2.1.2.

2.1.2 Differential decay curve method

DDCM is an alternative method to analyse RDDS data. The method still relies on measuring the intensities of γ rays before and after a stopper foil but several of the problems with the RDDS method are eliminated. Firstly, only relative flight times between different target-to-degrader distances are required for the DDCM, which can be measured more precisely than absolute times. Additionally, the systematic uncertainties associated with side-feeding can be removed using coincidence analysis. The

decay curve is fitted directly to the intensities of the unshifted components of a γ -ray transition eliminating any assumptions about the shape of the decay curve [6]. This section gives details of the DDCM framework and derives the equations used.

2.1.2.1 Coincidence analysis

Coincidence techniques with γ rays are a powerful tool in the DDCM. Only experimentally observed side feeding needs to be taken into account when coincidences with a feeding transition above the level of interest are demanded [29]. Often it is possible to remove side-feeding completely with this method. This is achieved by gating on the shifted component of the level directly above the level of interest, ensuring the observed intensity is fed only by the main feeding transition.

This section will derive the main equations used in the DDCM for both a gate on the direct feeder, B , and a gate on an indirect feeder, C , above the level of interest, see Fig. 2.2. Starting with the general expression for the decay curve from state i to state h , $R_i b_{ih} \equiv R_{ih}$, and taking the differential of Eqn. 2.6 one obtains

$$\frac{d}{dt} R_{ih}(t) = -\lambda_i R_{ih}(t) + \lambda_i b_{ih} \sum_k R_{ki}(t). \quad (2.9)$$

Rearranging Eqn. 2.9 gives

$$\tau_i = \frac{1}{\lambda_i} = \frac{-R_{ih}(t) + b_{ih} \sum_k R_{ki}(t)}{\frac{d}{dt} R_{ih}(t)}. \quad (2.10)$$

For a gate placed on an the fully shifted component of an indirect feeding transition above the level of interest, shown in Fig. 2.2 and denoted C , and using Eqn. 2.10, the lifetime of the state of decaying via the transition A , is given by [9]

$$\tau_i = \frac{-\{C, A_u\}(t) + \{C, B_u\}(t)}{\frac{d}{dt} \{C, A_u\}(t)}, \quad (2.11)$$

where the notation $\{C, A\}(t)$ denotes the intensity of transition A in coincidence with the transition C , and A_u, B_u denote the unshifted components of the transitions A and B , respectively, i.e. $A_u = \int_t^\infty A(t) dt = A_t^\infty$ and $B_u = B_t^\infty$. Note that $\{C, A_u\} = \{C_0^\infty, A_t^\infty\}$ are the transitions occurring through channel A from time t to time ∞ in

coincidence with channel C from time 0 to time ∞ . In general, the intensity of the transition A in coincidence with transition C is given by

$$\{C, A\} = \{C_0^\infty, A_0^\infty\} = \{C_0^t, A_0^t\}(t) + \{C_0^t, A_t^\infty\}(t) + \{C_t^\infty, A_0^t\}(t) + \{C_t^\infty, A_t^\infty\}(t). \quad (2.12)$$

Here, $\{C_t^\infty, A_0^t\} = \{C_u, A_s\} = 0$ as transition A occurs after transition C in time. This means that transition C occurs in the stopper foil, then transition A cannot occur in flight. Using this and the fact that Eqn. 2.12 is a constant in time, one obtains

$$\frac{d}{dt} \{C_0^t, A_0^t\}(t) = -\frac{d}{dt} \{C_0^\infty, A_t^\infty\}(t), \quad (2.13)$$

or in terms of shifted and unshifted components

$$\frac{d}{dt} \{C_s, A_s\}(t) = -\frac{d}{dt} \{C, A_u\}(t). \quad (2.14)$$

In a typical experiment, the quantities $\{C, A\}(t)$ are not measured. Rather the observed transitions (*ob*) $\{C, A\}_{ob} = \{C, A\}(t)\epsilon_{CA}$ are measured, where ϵ_{CA} depends on the detector efficiencies for transitions C and A . Writing Eqn. 2.11 in terms of experimental observables gives

$$\begin{aligned} \tau_i &= \frac{-\{C, A_u\}_{ob} \frac{1}{\epsilon_{CA}} + \{C, B_u\}_{ob} \frac{1}{\epsilon_{CB}}}{\frac{1}{\epsilon_{CA}} \frac{d}{dt} \{C, A_u\}_{ob}} \\ &= \frac{-\{C, A_u\}_{ob} + \{C, B_u\}_{ob} \frac{\{C, A\}_{ob}}{\{C, B\}_{ob}}}{\frac{d}{dt} \{C, A_u\}_{ob}}. \end{aligned} \quad (2.15)$$

Using Eqn. 2.14 and the identity $\{C_u, A_u\}(t) = \{C_u, B_u\}(t)$ the lifetime of state i can be given as

$$\tau_i = \frac{\{C_s, A_u\}_{ob} - \{C_s, B_u\}_{ob} \frac{\{C, A\}_{ob}}{\{C, B\}_{ob}}}{\frac{d}{dt} \{C_s, A_s\}_{ob}}. \quad (2.16)$$

For a gate placed on a direct feeding transition such as B , Eqn. 2.16 reduces to [6]

$$\tau_i = \frac{\{B_s, A_u\}_{ob}}{\frac{d}{dt} \{B_s, A_s\}_{ob}}, \quad (2.17)$$

as transition B cannot be in coincidence with itself, i.e. $\{B_s, B_u\}_{ob} = 0$. Equation 2.17 can be written more practically as [9]

$$\tau_i = \frac{\{B_s, A_u\}_{ob}(x)}{\frac{d}{dx} \{B_s, A_s\}_{ob}(x)} \frac{1}{v}. \quad (2.18)$$

Hence, the lifetime of state i can be measured using only a recoil velocity measurement and two intensity measurements as a function of distance. The measurement is also unaffected by side feeding completely in this coincidence approach [6]. In practice, several target-to-stopper distances are required to measure the lifetime of the state as the denominator of Eqn. 2.18 cannot be measured directly with a two-foil plunger and must be inferred from the shape of $\{B_s, A_s\}(x)$. Additionally large germanium detector arrays are typically required for the DDCM as the number of multiplicity two events is a factor of the detector array efficiency smaller than the number of multiplicity one events. These constraints limit the nuclei which can be studied with the standard two foil plunger and DDCM, as long runs are required at each distance to determine the component intensities, with low production cross sections.

2.1.3 Triple foil plunger

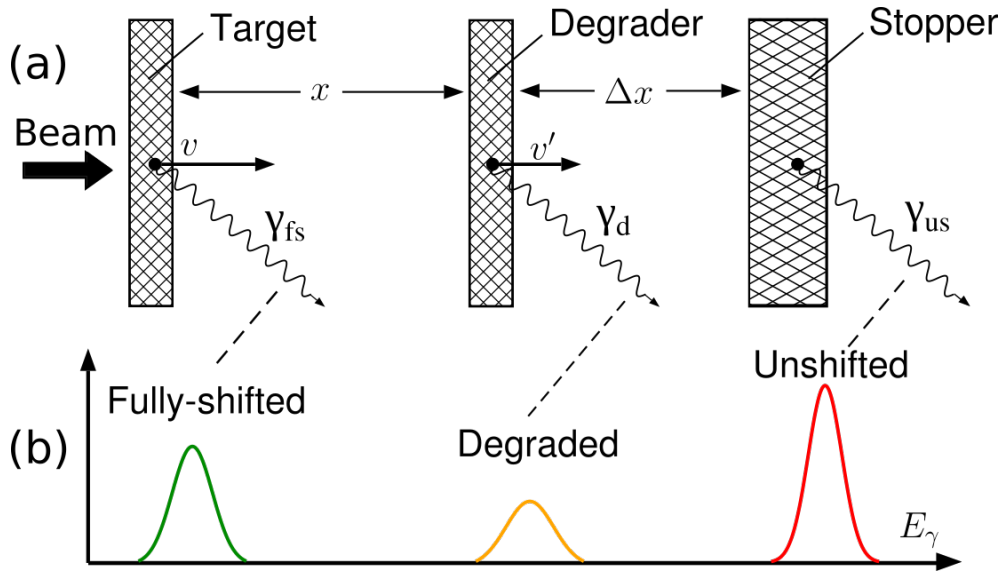


FIGURE 2.3: Schematic diagram of a triple foil plunger device, E_γ is for a forward angle detector. Figure adapted from [6].

A triple-foil plunger works in a similar way to a two-foil plunger, with a target foil and a stopper foil, but also has a third foil, see Fig. 2.3. The addition of a third,

central foil produces an additional degraded or ‘reduced-shifted’ γ -ray component. The reduced-shifted component provides a direct measure of the derivative of the decay curve, provided the flight time from the degrader foil to the stopper foil, Δt , is much less than the lifetime of the state of interest (see later, Eqn. 2.24). With a triple-foil plunger each γ -ray peak, A is therefore split into three components $A = A_{us} + A_{rs} + A_{fs}$. For two γ rays in coincidence with one another, each γ -ray transition, A , in coincidence with a γ ray C is therefore given by

$$\begin{aligned} I^{CA} = \{C, A\}(t) &= \{C_{us}, A_{us}\}(t) + \{C_{us}, A_{rs}\}(t) + \{C_{us}, A_{fs}\}(t) \\ &+ \{C_{rs}, A_{us}\}(t) + \{C_{rs}, A_{rs}\}(t) + \{C_{rs}, A_{fs}\}(t) \\ &+ \{C_{fs}, A_{us}\}(t) + \{C_{fs}, A_{rs}\}(t) + \{C_{fs}, A_{fs}\}(t), \quad (2.19) \end{aligned}$$

where the subscripts us, rs and fs denote the unshifted, reduced-shifted and fully shifted components of the transitions, respectively. With the three foil plunger, the decay curve $R_{ih}(t)$, i.e. the probability to decay after the recoil passes the first degrader foil, becomes

$$\begin{aligned} R_{ih}(t) &= \{C, A_{us}\}(t) + \{C, A_{rs}\}(t) \\ &= \{C_{us}, A_{us}\}(t) + \{C_{rs}, A_{us}\}(t) + \{C_{fs}, A_{us}\}(t) \\ &+ \{C_{us}, A_{rs}\}(t) + \{C_{rs}, A_{rs}\}(t) + \{C_{fs}, A_{rs}\}(t), \quad (2.20) \end{aligned}$$

and the decay curve, $R_{ih}(t')$, i.e. the probability to decay after the recoil passes the stopper foil is given by

$$\begin{aligned} R_{ih}(t') &= R_{ih}(t + \Delta t) = \{C, A_{us}\}(t') \\ &= \{C_{us}, A_{us}\}(t') + \{C_{rs}, A_{us}\}(t') + \{C_{fs}, A_{us}\}(t'), \quad (2.21) \end{aligned}$$

Here t' is the total flight time from the target foil to the stopper foil, i.e.

$$t' = t + \Delta t = t + \Delta x/v', \quad (2.22)$$

where t is the target-to-degrader flight time $t = x/v$, Δx is the degrader-to-stopper distance and v' is the reduced recoil velocity. Similarly, $R_{ki}(t')$ is given by

$$R_{ki}(t') = \{C, B_{us}\}(t') = \{C_{us}, B_{us}\}(t') + \{C_{rs}, B_{us}\}(t') + \{C_{fs}, B_{us}\}(t'). \quad (2.23)$$

In a traditional two-foil plunger the value of $dR(t)/dt$ is measured using $R_{ih}(t) - R_{ih}(t + \delta t)$, $R_{ih}(t)$ is measured at several distances in order to accurately interpret the shape of $R_{ih}(t)$, and hence infer $dR_{ih}(t)/dt$. Each of these distances must acquire sufficient statistics to accurately measure the component intensities, often resulting in large amounts of beam-time being required for a lifetime measurement. The addition of the third foil in TPEN allows for a direct measure of this quantity

$$\frac{dR_{ih}(t)}{dt} = \lim_{\Delta t \rightarrow 0} \frac{R_{ih}(t + \Delta t) - R_{ih}(t)}{\Delta t} = -\frac{\{C_{rs}, A_{rs}\}(t) + \{C_{fs}, A_{rs}\}(t)}{\Delta t} \quad (2.24)$$

Using Eqns 2.9, 2.21, 2.23, 2.24 and $\{C_{us}, B_{us}\} = \{C_{us}, A_{us}\}$ the lifetime of state i is given by

$$\tau_i = \frac{\{C_{fs+rs}, A_{us}\} - \{C_{fs+rs}, B_{us}\}}{\{C_{fs+rs}, A_{rs}\}} \Delta t. \quad (2.25)$$

Hence, if the γ coincidence gate is set on both the fully shifted and reduce-shifted components of transition B , directly above the level of interest then the lifetime of state i is given by

$$\tau = \frac{I_{us}^{BA}}{I_{rs}^{BA}} \Delta t = \frac{I_{us}^{BA}}{I_{rs}^{BA}} \frac{\Delta x}{v'}. \quad (2.26)$$

If coincidence techniques cannot be used due to limited statistics, then the triple-foil plunger can be used with γ ray singles events. Similarly to a two foil plunger in singles mode (Eqn. 2.10), with three foils the lifetime of a state i is given by

$$\tau_i = \frac{I_{ij}^{us} - b_{ij} \sum_h [\alpha_{hi}/\alpha_{ij}] I_{hi}^{us}}{I_{rs}^{ij}} \Delta t, \quad (2.27)$$

where $I_{ij}^{rs,us}$ is the reduce-shifted or unshifted component of the γ -ray transition from state i to state j , α_{ij} reflects any difference between the feeding and depopulating transitions and b_{ij} is the branching ratio from state i to state j . The quantity α_{ij} is

dependent on the experimental setup and is defined as [9]

$$\alpha_{ij} = \omega_{ij}(\theta)\epsilon_{ij}(E_{ij}), \quad (2.28)$$

where $\omega_{ij}(\theta)$ is the angular distribution of a the γ -ray transition and $\epsilon_{ij}(E_{ij})$ is the detector efficiency. It can be measured experimentally using the relation

$$\alpha_{ij} = \frac{I_{ij}}{I_{hi}}, \quad (2.29)$$

where I_{hi} is the intensity of all components of the transition feeding the level i from level h .

In this commissioning experiment a large amount of statistics were collected so a coincidence analysis was possible and a γ -singles analysis was not required. However, when TPEN's is used to measure an unknown lifetime in a nucleus with a low production cross section, it is likely that coincidence analysis may not be possible and a singles analysis will be performed.

With a measurement of the reduced-shifted component, it becomes possible to measure lifetimes using only one set of separations, rather than ~ 7 , reducing required beam time by a factor of ~ 7 [6]. A measurement of a state lifetime at a single distance also eliminates the need to normalise the component intensities across distances. This normalisation corrects for the different number of beam particles hitting the target across distances and contributes heavily towards the uncertainty in a typical RDDS lifetime measurement.

With TPEN the statistics are spread over three peaks close together in energy, rather than two peaks with a conventional two-foil plunger. This makes resolving the peaks difficult for low v/c values. The addition of the third foil also increases the background from secondary reactions and can reduce the efficiency of recoil transmission in recoil separators. Considering these effects, an improvement of a factor of ~ 4 is typically expected over a standard plunger. The actual reduction in beam-time is discussed in full detail in Chapters 5 and 6. Based on that analysis. the overall increased efficiency of TPEN will allow lifetime measurements in nuclei with production cross sections of a few microbarn.

2.1.4 Corrections required to detected γ -ray intensities

Several corrections to the measured γ -ray intensities must be made in order to accurately measure the lifetime of a state. This section briefly describes the origin of these corrections and shows when they become important.

2.1.4.1 Detector efficiencies

High-energy γ rays are more penetrating than low energy γ rays. Therefore, the efficiency of a germanium detector is a function of energy, and the efficiency typically decreases at higher energies [30]. When measuring the intensities of the shifted and degraded components of a transition, the two components lie at slightly different energies. The components are typically separated by ≈ 5 keV. In analysis where a γ ray coincidence gate is not used, the measured γ -ray intensities should be corrected for efficiency. Although this is a small correction of $\sim 0.1\%$, it is easy to correct for by performing an energy calibration using a source such as ^{152}Eu or ^{133}Ba . In coincidence analysis, this correction is not required as the efficiencies cancel out when the ratio is taken in Eqn. 2.18.

2.1.4.2 Lorentz correction

In RDDS experiments, the measured γ rays are emitted from recoiling nuclei. As the recoils are moving relative to the laboratory frame, relativistic corrections are required. These corrections, primarily the angular corrections, become important for $\beta > 0.04$ [9], where $\beta = v/c$. Firstly, for a nucleus moving with respect to the laboratory frame, time is dilated. This has the effect of increasing the intensity of the unshifted component, as more nuclei reach the stopper foil still in an excited state than they would have done without time dilation. Hence, the lifetime of the state is given by

$$\tau_o = \tau\sqrt{1 - \beta^2}, \quad (2.30)$$

where τ_o is the true lifetime, i.e. the lifetime in the rest frame of the recoil, τ is the lifetime measured in the laboratory and β is v_o/c . This effect is small for typical recoil velocities. For example, for a nucleus with $\beta = 0.07$, time dilation results in a

0.25% difference between the measured lifetime and the lifetime in the rest frame of the nucleus.

Additionally, and more importantly for TPEN, the direction of an emitted γ ray relative to the beam axis in the laboratory frame is altered by the relative motion of the recoil. The angle from the γ ray to the beam axis in the lab frame, θ is given by performing a Lorentz transformation on the γ ray in the rest frame of the recoil [31]. For a γ ray emitted at an angle θ_o to the beam axis in the recoils rest frame, the angle to the beam axis in the laboratory frame is given by [31]

$$\cos(\theta) = \frac{\cos(\theta_o) + \beta}{1 + \beta \cos(\theta_o)}, \quad (2.31)$$

where $\beta = v/c$. From Equation 2.31 and the definition of the solid angle, $d\Omega = \sin(\theta)d\theta d\phi$, the solid angle transforms as [31]

$$\frac{d\Omega}{d\Omega_o} = \frac{1 - \beta^2}{(1 + \beta \cos(\theta_o))^2}, \quad (2.32)$$

and the number of photons per unit solid angle, $dN/d\Omega$ transforms as

$$\frac{dN}{d\Omega} = \frac{dN}{d\Omega_o} \frac{d\Omega_o}{d\Omega} = \frac{dN}{d\Omega_o} \frac{(1 + \beta \cos(\theta))^2}{1 - \beta^2}, \quad (2.33)$$

where $dN/d\Omega_o$ is the number of photons per unit solid angle in the rest frame of the recoil. Therefore, $\frac{d\Omega_o}{d\Omega}$ gives the enhancement factor for emissions in the laboratory frame. This enhancement factor is shown in Figure 2.4 for different values of β . The transformation of solid angle between frames can be seen as a reduced collection efficiency for backward-angled detectors and an increased efficiency for forward angled detectors.

In a typical two-foil plunger experiment $\beta \approx 0.03$ and $\theta \approx 45^\circ$ or 135° . The forward focusing effect is small, increasing the number of photons in the forward detectors by about 4%. Only shifted components (fully shifted or degraded) of the γ ray will experience this enhancement as these are the peaks where the recoil is traveling. If a single detector angle is used for singles lifetime analysis, the number of photons detected in the shifted peaks needs to be corrected.

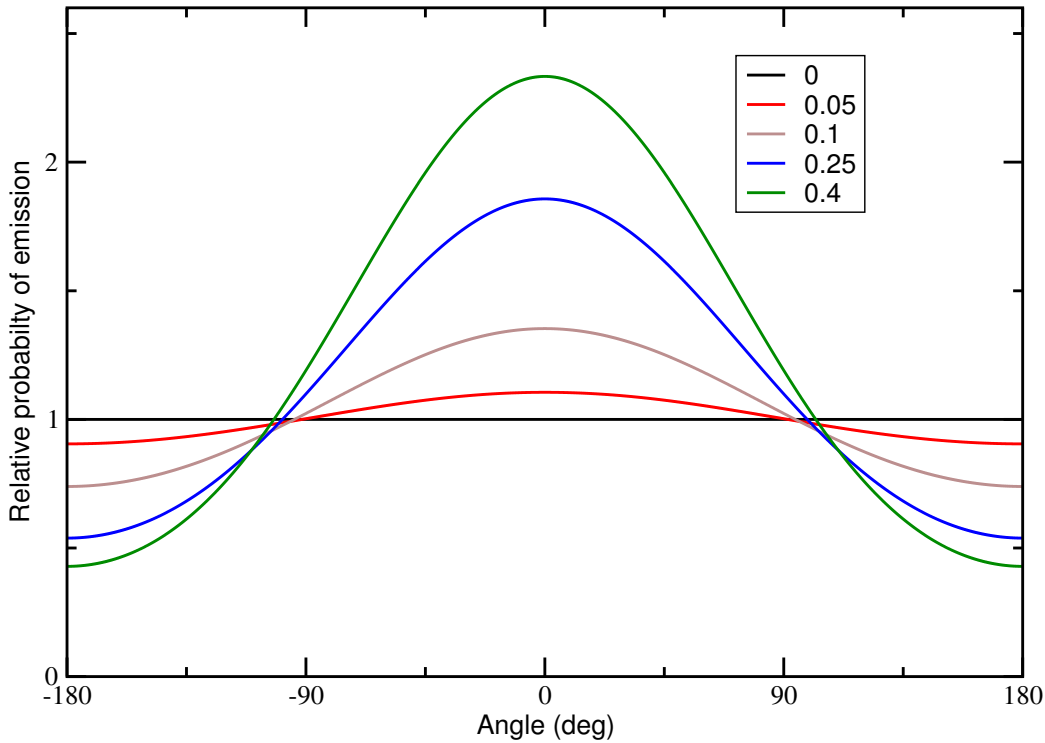


FIGURE 2.4: The relative enhancement of γ emission for a recoil at different angles for different values of β . θ is the angle from the detected γ ray to the beam axis in the laboratory frame, and β is shown in the legend.

In a triple-foil plunger experiment, $\beta \approx 0.1$ and the enhancement at 45° is $\sim 16\%$. Therefore this correction becomes important and the enhancement for the three different velocity regimes must be considered [8].

2.1.4.3 Deorientation

In general, the emission of γ rays is not isotropic and γ rays with different multiplicities have different angular distributions. The angular distribution of a γ -ray transition is given by

$$W(\theta) = \sum_n A_n P_n(\cos(\theta)), \quad (2.34)$$

where $W(\theta)$ is the intensity at angle θ to the beam axis, A_n are constants and $P_n(\cos(\theta))$ are the Legendre polynomials [32]. As γ decay is parity conserving only terms with $n = \text{even}$ and $n \leq 2l$ are non-zero. Here, l is the multipolarity of the transition. The values of A_n for different transitions are given in Ref. [33].

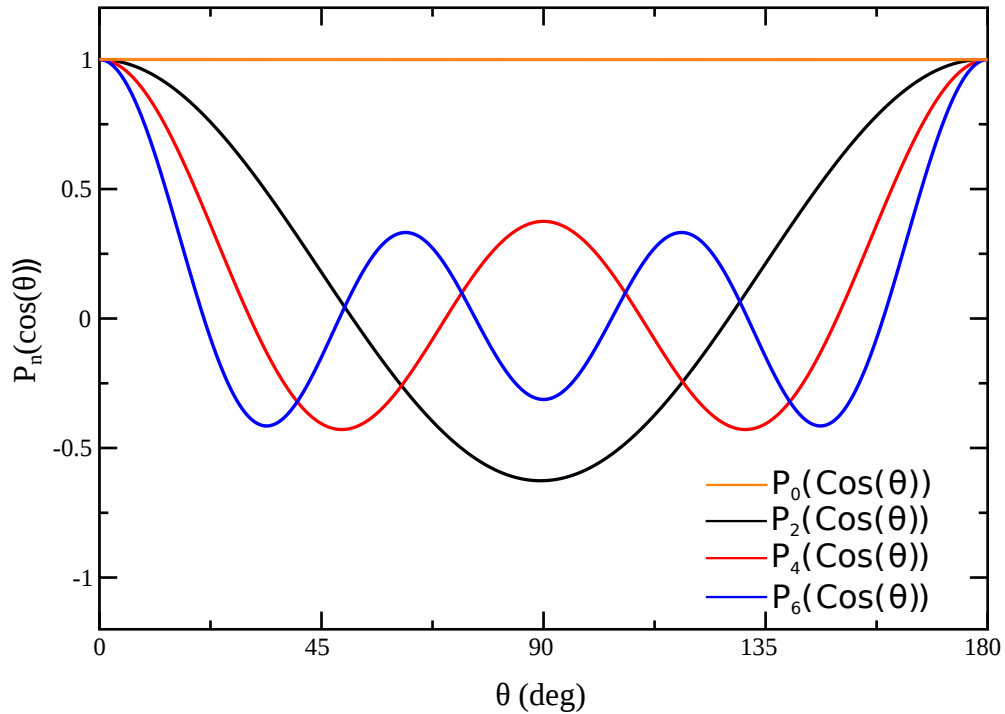


FIGURE 2.5: The first four even Legendre Polynomials.

For recoils produced in a fusion-evaporation reaction, the most common decays are E1, M1 and E2. For a pure E1 transition

$$W(\theta) = A_0[1 + A_2P_2(\cos(\theta))], \quad (2.35)$$

and for a pure E2 transition [34]

$$W(\theta) = A_0[1 + A_2P_2(\cos(\theta)) + A_4P_4(\cos(\theta))]. \quad (2.36)$$

This angular distribution of γ rays becomes important when measuring lifetimes. If the distribution was time independent, the effect would be irrelevant to lifetime measurements. However, this is not the case. Recoils are produced in a fusion evaporation reaction and are, on average, oriented perpendicular with the beam direction. The reaction distorts atomic electron configurations, which rearrange into the lowest energy configuration after leaving the target. The rearrangement of the atomic electrons produces time varying magnetic fields, which interact with the magnetic moment of the excited states in the nucleus. The length of this interaction is known as the ‘relaxation period’. After the relaxation period, the nuclei have a random orientation, and the

γ -ray distribution becomes isotropic [9]. Hence γ rays emitted from a nucleus shortly after leaving the target foil have a different angular distribution than those emitted at a later time in the stopper foil.

The relaxation period typically leads to a smaller lifetime measurement than the true value for an E2 transition. γ rays emitted in the stopper foil will have an isotropic distribution whereas those emitted in flight have enhancement at typical detector angles. The enhancement for γ rays emitted in flight increases the intensity of the shifted component, which leads to a smaller lifetime measurement. It is shown in Ref. [35] that coincidence techniques remove this effect. However, for singles analysis this must be corrected for by normalising the γ -ray intensities to a given detector angle for each flight time. Typically, 55° is chosen because the second order Legendre polynomial is close to zero at this angle, see Fig. 2.5.

2.1.4.4 Velocity distribution

To acquire sufficient statistics, target thicknesses of $\approx 1 \text{ mg/cm}^2$ are typically used in heavy-ion fusion evaporation (HIFE) reactions. This results in a distribution of velocities for the recoiling nuclei and a broadening of the shifted peak. If the target is too thick, this broadening can make it difficult to resolve the fully shifted and unshifted peaks.

The distribution in velocity of the recoils also affects the flight times and must be corrected for. Faster recoils reach the stopper foil in a shorter time than slower recoils. This means a decay is more likely to occur before the stopper foil if the recoil is slow. For a given distance, this results in the average velocity of a recoil decaying in-flight becoming dependent on the flight time. As the flight time increases the average velocity of a recoil decaying in-flight also increases, as the bias towards slower recoils is removed. If the velocity spread is large, the effective recoil velocity at every target-to-degrader distance must be considered and corrected for such as in Ref. [36]. This can be done by measuring the centroid of the fully shifted component at every target-to-degrader distance and using the shift in energy to calculate the velocity of the recoils decaying in-flight. This velocity can then be used to calculate the flight time of the recoil and the intensity of the fully shifted and degraded components can be plotted as a function of flight time.

Additionally, the finite slowing down time of recoils in the stopper foil can affect lifetime measurements of short-lived states. Recoils with velocities $\sim 1\% c$ typically take ~ 1 ps to fully stop in a stopper foil [6]. During this time there is a continuous velocity distribution of recoils, which leads to a tail on the measured γ -ray energies. As such, a Gaussian is not a suitable function to fit to the data for short lifetimes. Instead, the slowing down in the stopper foil must be simulated [37] and the effect of the slowing down must be taken into account. Simulated spectra for various lifetimes can be compared to measured spectra and the appropriate lifetime can be deduced. In this work all measured lifetimes were much greater than 1 ps so these techniques were not required.

2.2 Nuclear models

Lifetime measurement of excited states in nuclei provide a measurement of the matrix elements between initial and final states. These matrix elements contain information on the nuclear potential. This section describes several nuclear models, which are used to interpret lifetime measurements. The models are used to interpret the results of Appendix A and B and will be useful for future lifetime measurements with TPEN.

2.2.1 Liquid drop model

The liquid drop model was the first nuclear model which could explain the bulk properties of the nucleus. It was first proposed by G. Gamow [38] in 1930 after Rutherford scattering experiments showed that the nuclear density was constant and the nuclear volume increased with the number of nucleons [32]. Gamow described the nucleus as “built from α -particles in a way very similar to a water-drop held together by surface tension”.

The liquid drop model treats the nucleus of a single drop of incompressible fluid. This explains the well-defined nuclear surface. The model gained support in the 1930s for its ability to describe the process of fission [39]. Bohr and Wheeler reasoned that if sufficient energy is used to distort the drops surface, then a neck will form allowing the nucleus to break apart. The liquid drop model could not explain or predict how

the binding energy per nucleon changed as nucleon number increases, which led to the development on the single particle shell model.

2.2.2 Single-particle shell model

The nuclear shell model was developed by M. Goeppert-Mayer in order to explain the discontinuity of nuclear binding energies at certain values of N and Z [40, 41]. These non-continuities could not be explained using the liquid drop model. The nuclear shell model attempts to describe the nucleus in a similar way to the atomic shell model, whereby the nucleons fill shells in order of increasing energy and the properties of the nucleus can be described by where these nucleons lie. Experimentally, nuclear shell closures have been observed with $N, Z = 2, 8, 20, 28, 50, 82$ and $N = 126$. These are known as the magic numbers and a dramatic increase in the nuclear binding energy per nucleon is observed at these values of N or Z [34]. This increase is interpreted as a shell closure, stabilising the nucleus.

Nucleons fill shells in order of their energy. In the simplest case, the energy of the states can be described using their orbital angular momentum, l and index, n . Each state is $2(2l + 1)$ degenerate, as this is the number of nucleons that can fit into that state [34].

In the atomic shell model, the electrons are subject to a central Coulomb field generated by the nucleus, which allows the Schrödinger equation to be solved. This allows the energies of the shells closures to be calculated. However, for the nuclear shell model, the nucleons are subject to a potential that they themselves create. In theory, the nuclear mean field can be calculated and the interaction of an individual nucleon with the field can be used to describe the energy levels. This is, however, a many body problem, making it computationally difficult and can only be done for the lightest nuclei ($A < 12$) [34, 42–45].

If a potential is chosen to accurately describe the nucleus, it must reproduce shell closures. The infinite well, the harmonic oscillator and the Woods-Saxon potentials all reproduce the first three magic numbers. The Woods-Saxon potential is the most physical of the three and has the form

$$V(r) = \frac{-V_0}{1 + \exp[(r - R)/a]}, \quad (2.37)$$

where V_0 is the depth of the potential well, r is the nuclear radius, R is the mean nuclear radius and a is the skin thickness; the distance at which the potential changed from $0.1V_0$ to $0.9V_0$. All three potentials are plotted in Figure 2.6.

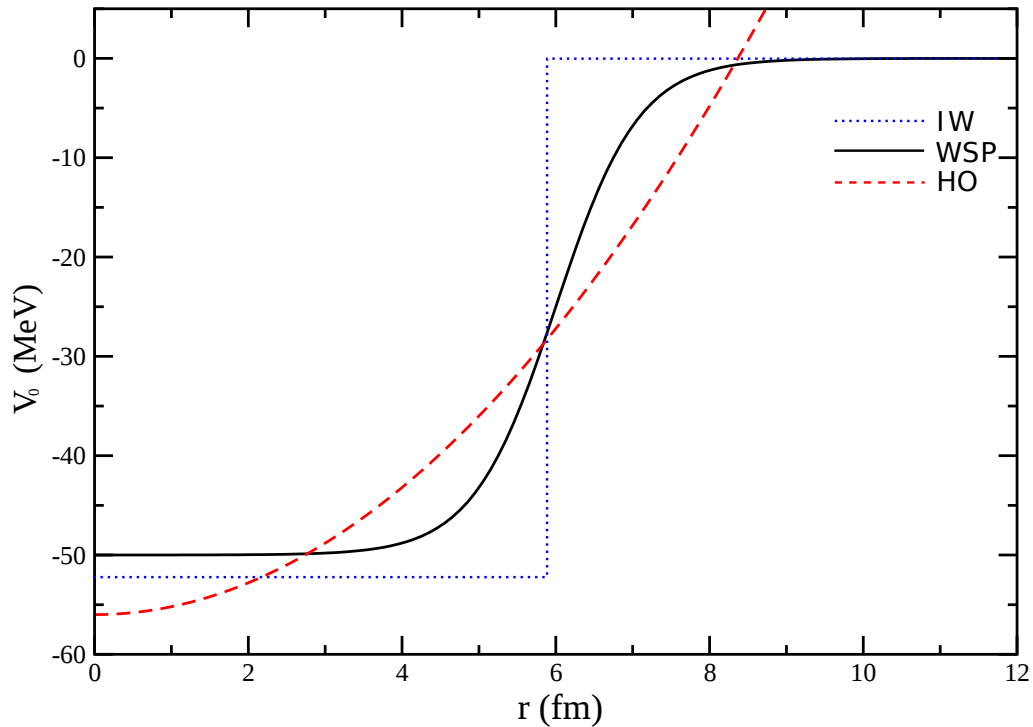


FIGURE 2.6: The infinite well (IW), Woods-Saxon (WSP), and harmonic oscillator (HO) potentials. Different values of V_0 have been chosen for clarity.

It was independently suggested by M. Goepfert-Mayer and O. Haxel *et al.* that the spin orbit interaction should effect the magic numbers [40, 41, 46, 47]. The interaction between the orbital angular momentum, l , and the nuclear spin, s , splits each l level into two levels, and alters the energies of the levels. As such, it is no longer appropriate to label the levels with l . Instead, the total angular momentum, $j = l + s$ is used. This interaction is known as the spin-orbit interaction and it breaks the l degeneracy. The degeneracy of a state is now dependent only on j and is given by $(2j + 1)$. The reordering of the levels changes the predicted magic numbers using the Woods-Saxon potential alone. With the spin-orbit interaction included, the predicted magic numbers match exactly with experimental results for stable nuclei. The effect of the spin orbit interaction is shown in Fig. 2.7.

Contrary to the spin-orbit effect in atomic electrons, the spin-orbit effect in nuclei lowers the energy of the state. The spin-orbit effect can lower the energy of the $j = l + 1/2$ orbit so much that it lies close to the levels of the next lowest shell. This results in many levels of a given parity close in energy to a level of the opposite parity. Since levels of opposite parity can only mix very weakly, this results in the configurations built on this opposite parity level being extremely pure. Such levels are known as unique parity or intruder levels [32]. The purity of these levels makes them ideal to experimentally test nuclear models.

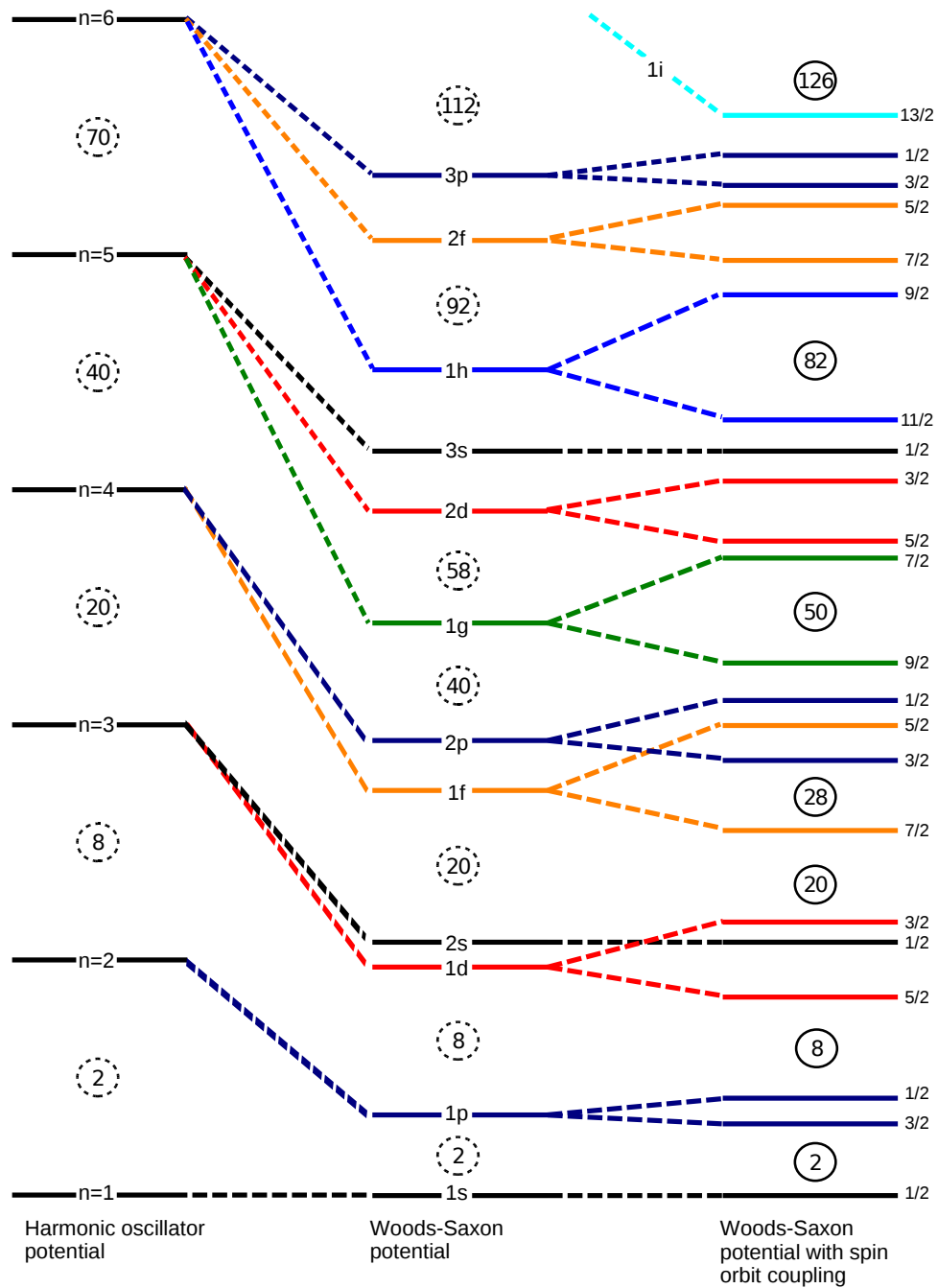


FIGURE 2.7: Schematic diagram of the single-particle energy levels. The figure shows how the energy levels change under different potentials and the splitting of levels when the spin-orbit interaction is included. The shell closures are shown in circles and the total angular momentum is shown on the right hand side. Figure adapted from Ref. [48].

2.2.3 Two-state mixing

Observed nuclear states are often the admixture of many configurations. If there are several nucleons outside of a closed shell, the possible configurations of these nucleons can ‘mix’. In the case of two-state mixing, if the two basis states have the same spin and parity, and lie close in energy, the observed nuclear states will be linear combinations of these basis states [49]. A schematic diagram of the basis states and the final states is shown in Figure 2.8.

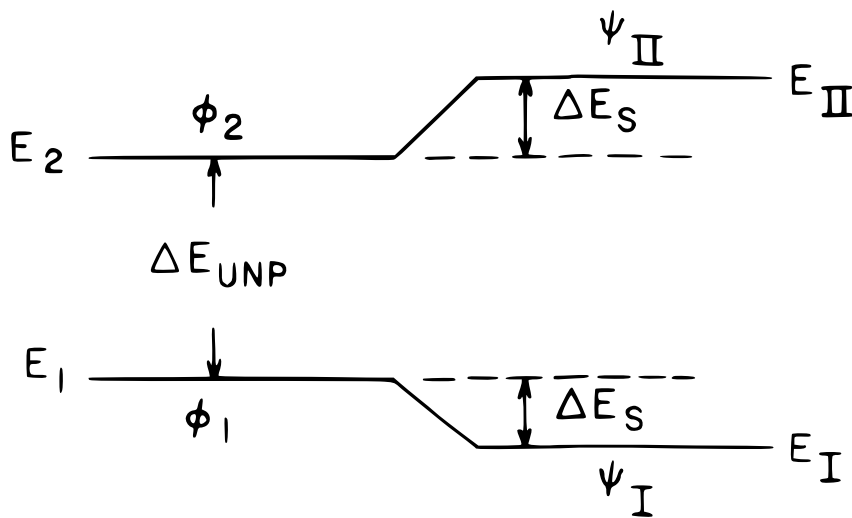


FIGURE 2.8: Schematic diagram of two state mixing, showing the initial basis states, $\phi_{1,2}$, the unperturbed energy difference between these states, ΔE_{UNP} and the mixed states, $\psi_{I,II}$. The difference in energy between the energy of the basis states, $E_{1,2}$ and the energy of the observed states, $E_{I,II}$, is ΔE_S . Taken from Ref. [32].

2.2.4 Nuclear deformations and rotations

The liquid drop model predicts the ground state of all nuclei to be spherical, as any deformation increases the surface-energy term [50]. In reality, nuclei can hold a variety of shapes and a multipole expansion can be used to describe this nuclear shape. The radial vector from the origin to the surface is given by

$$R = R_0 \sum_{\lambda=0}^{\infty} \sum_{m=-\lambda}^{\lambda} \alpha_{\lambda m}(t) Y_{\lambda}^m(\theta, \phi), \quad (2.38)$$

where R_0 is the radius of a sphere occupying the same volume, Y_λ^m are the spherical harmonics, θ is the polar angle, ϕ is the azimuthal angle and $\alpha_{\lambda m}(t)$ are the amplitudes of each harmonic, known as the deformation parameters.

Most nuclei are quadrupole deformed with small contributions from octupole deformation. Hence, the number of terms is reduced and typically only $\alpha_{2,m}$ terms are considered. As odd values of m do not conserve spatial symmetry, $\alpha_{2,1} = \alpha_{2,-1} = 0$. Additionally, if the nucleus is axially symmetric then $\alpha_{2,2} = \alpha_{2,-2}$. The relevant α parameters are then $\alpha_{2,0}$ and $\alpha_{2,2}$. These parameters can be expressed in terms of the quadrupole deformation, β , and the triaxiality parameter, γ , [51]

$$\alpha_{2,0} = \beta_2 \cos(\gamma) \quad (2.39)$$

and

$$\alpha_{2,2} = \frac{1}{\sqrt{2}} \beta_2 \sin(\gamma). \quad (2.40)$$

These parameters are commonly used to describe shapes in the Lund convention [32], which is represented in Fig. 2.9. The triaxiality parameter is equal to 0 for axially symmetric nuclei. For non-zero γ the nucleus is ‘triaxial’ and is shown in Fig. 2.9.

The shape of an axially symmetric nucleus is also often expressed by its deviation from a sphere using the parameter δ , where

$$\delta = \frac{\Delta R}{R_{rms}}. \quad (2.41)$$

Here, ΔR is the difference between the semi-minor and the semi-major axes of the nucleus and R_{rms} is the root mean squared radius. β_2 can be expressed in terms of δ by

$$\beta_2 = \sqrt{\frac{\pi}{5}} \left[\frac{4}{3} \delta + \frac{2}{3} \delta^2 + \frac{10}{27} \delta^3 + \mathcal{O}(\delta^4) \right], \quad (2.42)$$

where $\mathcal{O}(\delta^4)$ are terms of the order (δ^4) .

2.2.4.1 Vibrations

Figure 2.10 shows vibrational excitations of a spherical nuclei, with increasing λ from $\lambda = 0$ to $\lambda = 3$. For an incompressible nucleus, the monopole excitation is forbidden,

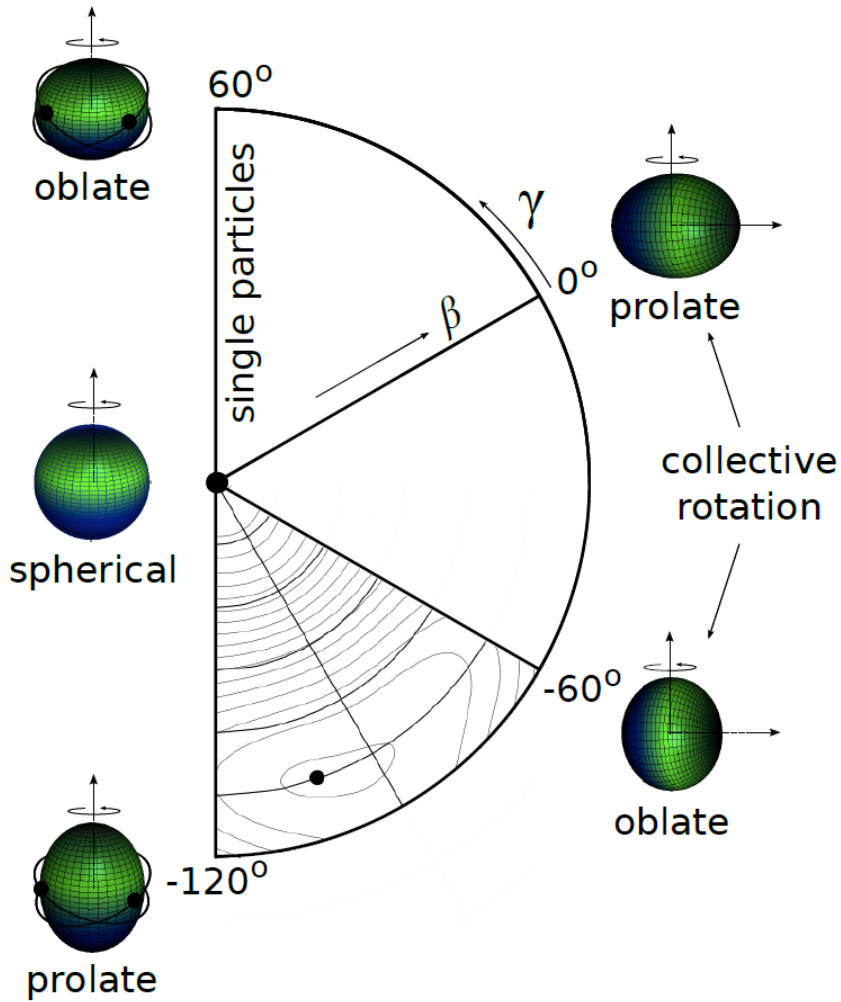


FIGURE 2.9: The nuclear shape as described by the Lund convention, taken from Ref. [52]. β is the quadrupole deformation parameter and γ is the angle from being axially symmetric.

as it is an expansion and contraction of R . However, nuclear matter is not completely incompressible, which leads to an excited 0^+ state at several hundred MeV above the ground state [50]. The $\lambda = 1$ vibration is seen as a translation of the centre of mass of the nucleus and is not an intrinsic excitation. Hence, the quadrupole deformation ($\lambda = 2$) is the lowest vibrational mode that requires no compression of nuclear matter or movement of the centre of mass of the nucleus, making it a common, low-energy excited state [50]. Vibrational excited states can be seen as quadrupole phonon excitation with energies given by,

$$E = \left(n + \frac{1}{2}\right) \hbar\omega, \quad (2.43)$$

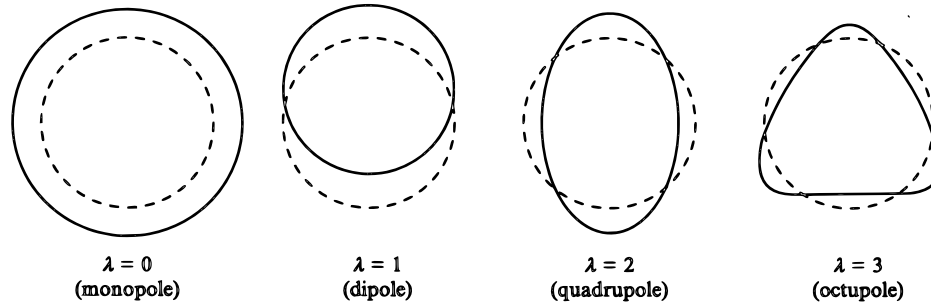


FIGURE 2.10: The first four axially symmetric vibrational modes for a spherical ground state. Taken from [50].

where n is the principal quantum number and ω is the frequency of vibration. This equation predicts the following relation between energy states [34]

$$\frac{E(4^+)}{E(2^+)} = 2.0 \quad (2.44)$$

Several nuclei, such as ^{112}Cd [53], exhibit vibrational level structures. The measurement of the lifetime of these quadrupole vibrational excited states provides information on β_2 parameters and hence an indication of the deformation of the state.

2.2.4.2 Rotations

A spherical body is rotationally invariant and as such, any rotations of a spherical body have degenerate energy levels. The observation of rotational energy states implies a breaking of this degeneracy in the form of a deformed state, contrary to the predictions of the liquid drop model [54, 55]. The deformation of the nuclear ground state can be explained using collective models. Coupling terms between nucleons reduce the overall energy in such a way that a non-spherical shape is favourable [55].

By considering the nucleus as a classically rotating body with quantised spin, the energy of the state can be expressed as

$$E = \frac{\hbar^2}{2\mathcal{I}} I(I + 1) - K^2, \quad (2.45)$$

where \mathfrak{S} is the moment of inertia of the nucleus and I is the spin [55]. In the adiabatic approximation of slowly changing \mathfrak{S} ,

$$\frac{E(4^+)}{E(2^+)} = 3.3. \quad (2.46)$$

Rotational excitations are common in nuclei with proton or neutron numbers far away from magic numbers [56]. The lifetimes of these rotationally excited states are typically in the picosecond range. This makes plunger techniques ideal to measure these lifetimes and hence extract the nuclear deformation parameters.

2.2.4.3 The Nilsson model

The Nilsson model is an extension of the single particle model. In the single particle model, the potential is assumed to be spherical. However, in general this is not true. For well-deformed nuclei ($150 \leq A \leq 190$ and $A > 230$), a potential that resembles the nuclear shape should be chosen, such as an ellipsoid. Since an ellipsoid is not invariant under rotations, l is no longer a good quantum number so can no longer be used to identify states [34, 57].

As the potential is no longer spherical, the orientation of the orbit of the single particle alters the energy of the level. The energy of the level is now dependent on the component of \mathbf{j} along the symmetry axis, Ω . A nucleon in a $d_{5/2}$ can take six values of \mathbf{j} , from $-\frac{5}{2}$ to $+\frac{5}{2}$. As the nucleus is symmetric under reflection, this splits the $d_{5/2}$ state into 3 states each with a degeneracy of 2. If there are multiple nucleons orbiting the nuclear core, then the projection of total angular momentum onto the symmetry axis is $K = \sum_i \Omega_i$. The angle, Θ , of different K -projections in the classical approximation is

$$\Theta = \arcsin(K/j). \quad (2.47)$$

Hence, as K increases, the change in Θ and so the separation in energy of states is greater for the same increment in K .

For prolate nuclei, the energy of a state is lower for lower values of Ω . This is because the component of \mathbf{j} along the symmetry axis is lower and therefore the interaction

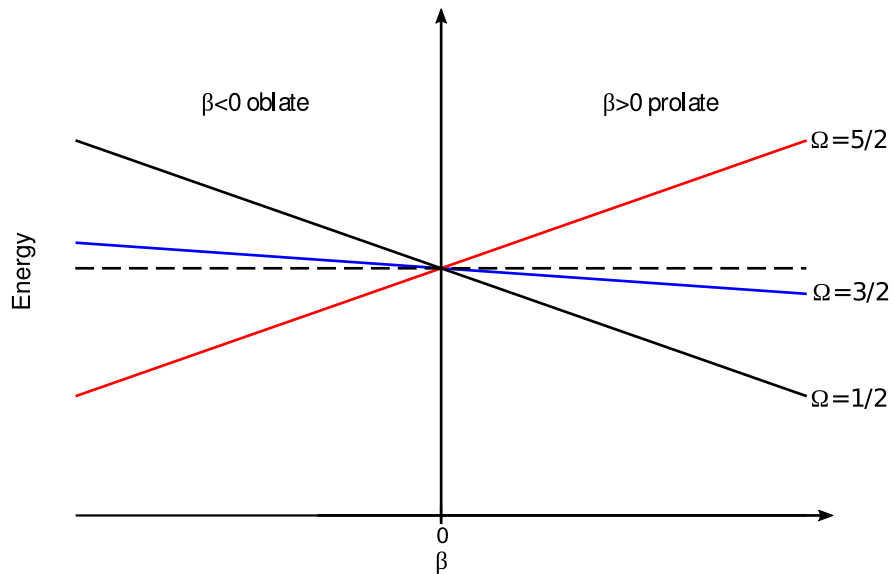


FIGURE 2.11: Schematic diagram of the separation of Nilsson single particle energy states for a $d_{5/2}$ orbit.

between the nucleon and the nuclear core is higher and therefore more tightly bound. The converse is true for oblate nuclei. This effect can be seen in Figure 2.11

By combining several j states, a full Nilsson diagram can be produced. An example of a Nilsson diagram for neutrons is shown in Figure 2.12. Since K is a good quantum number, no two lines with the same value of Ω can cross leading to large deflections in the states. This is observed in Figure 2.12. These deflections lead to orbits lying close together in energy for high deformations, enhancing configuration mixing. Additionally, states similar in K will mix more strongly [32].

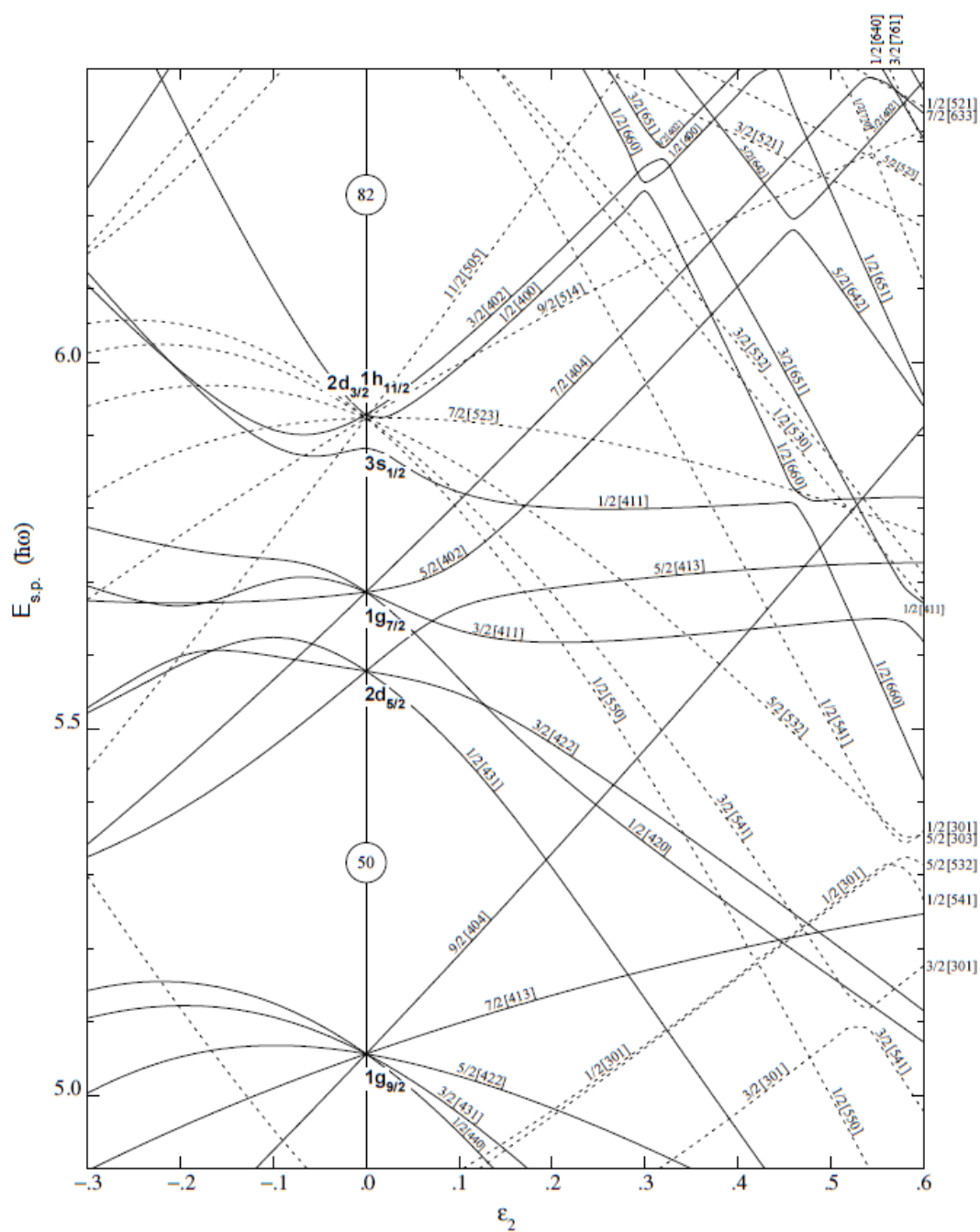


FIGURE 2.12: An example of a Nilsson diagram for neutrons for $N \geq 50 \leq 82$. The deformation is shown on the x -axis and the single particle energy state on the y -axis. The parameter ϵ_2 is proportional to β_2 . Taken from Ref. [58].

Nilsson orbitals are generally described using the notation

$$\Omega^\pi[N, n_z, \Lambda], \quad (2.48)$$

where N is the principal quantum number, n_z is the number of nodes in the z projection of the radial wavefunction and Λ is the projection of the orbital angular momentum onto the symmetry axis.

2.2.5 The Coriolis interaction

For a nucleus with a rotating core and an odd particle, the total angular momentum of the nucleus is the vector sum of the angular momentum of the core and angular momentum of the odd particle. The coupling of the intrinsic motion of the odd particle with the rotational motion gives rise to the Coriolis interaction.

The Coriolis interaction is similar to that of the classical Coriolis effect. When an object travels in a rotating frame, the object is subject to a fictitious force when viewed in the rotating frame. This results in the path of the object being deflected. It can be shown that the Coriolis potential is given by

$$V_{Coriolis} = \frac{\hbar^2}{2\mathfrak{I}}(I_+j_- + I_-j_+), \quad (2.49)$$

where \mathfrak{I} is the moment of inertia of the nucleus and I_\pm are the raising and lowering operators $I_\pm = I_1 \pm ij_2$ [32].

In the nucleus, the Coriolis interaction alters the projection of the single particle on the symmetry axis. This results in admixture between states differing by $K = 1$. This Coriolis effect can significantly affect the energy of levels in rotational nuclei. For example, in rare earth nuclei, this effect shifts the energies of some states by hundreds of keV [32].

2.3 Gamma-ray emission

Most nuclear reactions result in the final nucleus being produced in an excited state [34]. These excited states then decay to the ground state of the nucleus via one or more γ -ray emissions. Observations of these γ rays provide valuable information about the nucleus. As the decay occurs via the emission of a photon, certain selection rules apply that are a result of the conservation of angular momentum and parity.

2.3.1 Selection rules

Transitions from an initial state, with angular momentum I_i and parity π_i , to a final state, with angular momentum I_f and parity π_f , obey a set of selection rules. For a transition of multipole L , $L\hbar$ is the amount of momentum transferred per photon. The selection rule is given by

$$|I_i + I_f| \geq L \geq |I_i - I_f|, \quad (2.50)$$

and arises from the conservation of momentum. Here, $L \neq 0$, as the photon carries an intrinsic spin of $1\hbar$. If the multipolarity of a transition is $|I_i - I_f|$, the transition is said to be stretched.

A γ ray can be described as electric, (E), or magnetic, (M). Electric transitions change the electric moment of the nucleus, whereas magnetic transitions are said to change the magnetic moments. The parity of electric transitions is even and the parity of magnetic transitions is odd. The parity of the fields is given by

$$\pi(ML) = (-1)^{L+1}, \quad (2.51)$$

$$\pi(EL) = (-1)^L. \quad (2.52)$$

Hence for two states with $I_i = \frac{3}{2}$, $I_f = \frac{5}{2}$ and $\pi_i = \pi_f$, the possible radiation fields are $M1, E2, M3, E4$. In this case, the majority of the transition is a mixed $M1 - E2$ as the higher order terms are suppressed by the transition rate [34].

2.3.2 Transition rates

For a nucleus in an initial state ϕ_i decaying to a final state ϕ_f , the probability per unit time for photon emission is

$$\lambda(\sigma L) = \frac{2(L+1)}{\epsilon_0 \hbar L [(2L+1)!!]^2} \left(\frac{E_\gamma}{\hbar c} \right)^{2L+1} |\langle \phi_f || m(\sigma L) || \phi_i \rangle|^2, \quad (2.53)$$

where E_γ is the energy difference between the states, $m(\sigma L)$ is the operator acting between the initial and final states, and $\langle \phi_f || m(\sigma L) || \phi_i \rangle$ is the reduced matrix element. The reduced transition probability is

$$B(\sigma L; I_i \rightarrow I_f) = \frac{1}{2I_i + 1} |\langle \phi_f || m(\sigma L) || \phi_i \rangle|^2. \quad (2.54)$$

From Eqn 2.53 it is explained why radiation fields are dominated by lower order multipole transitions. Higher order fields are strongly suppressed by the $(2L+1)!!$ term.

2.3.2.1 Single-particle transition rates

For an excitation involving only a single nucleon, the theoretically calculated transition rates are known as the Weisskopf estimates. These calculations assume the transition is stretched and are used to benchmark measured transition rates. Weisskopf noted that the estimates should be applied with “the greatest reservations” as the estimates in deriving them are “extremely crude” [59]. For an electric transition, the reduced transition probability is

$$B(Wu : EL) = \frac{1.2^{2L}}{4\pi} \left(\frac{3}{L+3} \right)^2 A^{\frac{2L}{3}} e^2 \text{fm}^{2L}, \quad (2.55)$$

and for a magnetic transition:

$$B(Wu : ML) = \frac{10}{\pi} 1.2^{2L-2} \left(\frac{3}{L+2} \right)^2 A^{\frac{2L-2}{3}} \left(\frac{e\hbar}{2Mc} \right)^2 \text{fm}^{2L}, \quad (2.56)$$

where M is the proton mass. Table 2.1 shows the Weisskopf estimates for the transition probabilities for common transitions. Comparing observed transition rates to Weisskopf

TABLE 2.1: A Table showing the Weisskopf estimates for $E1-E4$ and $M1-M4$ transitions. E is the energy of the transition given in MeV.

Multipolarity	λ
E1	$1.0 \times 10^{14} A^{2/3} E^3$
E2	$7.3 \times 10^7 A^{4/3} E^5$
E3	$34 A^2 E^7$
E4	$1.1 \times 10^{-5} A^{8/3} E^9$
M1	$5.6 \times 10^{13} E^3$
M2	$3.5 \times 10^7 A^{2/3} E^5$
M3	$16 A^{4/3} E^7$
M4	$4.5 \times 10^{-6} A^2 E^9$

units gives information about the nucleus. If the observed rates are much lower than the estimates, then initial and final wavefunctions are likely to be very different. If the rates are much higher, then it is likely more than one nucleon is contributing to the transition suggesting collectivity in the nucleus [34].

2.3.2.2 Collective transition rates

A deformed nucleus has a non-zero electric quadrupole moment. The quadrupole moment, Q_o , is proportional to the reduced transition probability for $E2$ transitions, which are usually observed in rotational bands. Q_o is also related to the quadrupole deformation parameter, β_2 . Hence, by measuring the lifetime of an $E2$ transition, the deformation of the nucleus can be estimated. Equation 2.57 gives the relation between $B(E2)$ and Q_o .

$$B(E2) = \frac{5}{16\pi} e^2 Q_o^2 |\langle J_i K 20 | J_f K \rangle|^2, \quad (2.57)$$

where $|\langle J_i K 20 | J_f K \rangle|^2$ is the Clebsch-Gordan coefficient for an $E2$ transitions. Equation 2.58 shows the relation between β_2 and Q_o .

$$Q_o = \frac{3}{\sqrt{5}\pi} Z R^2 \beta_2 \left(1 + \frac{1}{8} \sqrt{\frac{5}{\pi}} \beta_2 \right). \quad (2.58)$$

2.4 Reactions

2.4.1 Heavy Ion fusion evaporation reactions

A common method for producing nuclei in excited states is to bombard a stable target with a stable beam. If the two nucleons are brought together with energy above the fusion barrier, they fuse into a compound nucleus, which is typically proton-rich. This is known as a heavy-ion fusion evaporation (HIFE) reaction [39]. The fusion barrier is commonly approximated to be the Coulomb barrier, although the fusion barrier is slightly higher [60]. For a spherical nucleus, the minimum energy required to overcome the Coulomb barrier is

$$V = \frac{e^2}{4\pi\epsilon_0} \left(\frac{Z_P Z_T}{R_P + R_T} \right), \quad (2.59)$$

where $Z_{P,T}$ are the proton numbers of the projectile and target respectively, and $R_{P,T}$ are the corresponding nuclear radii.

The compound nucleus is produced with excess energy, typically 30–40 MeV. The reaction also transfers large amounts of angular momentum to the compound nucleus [39], typically $\sim 40\hbar$ for heavy beam-target combinations [61, 62]. In the classical picture, this results in a nucleus with a rotational period of approximately 10^{-22} s. To remove excess energy, nucleon evaporation occurs. This is where nucleons are emitted from the nucleus with large amounts of kinetic energy. Typical beam-target combinations, and the Coulomb barrier, make neutron evaporation far more likely than proton evaporation [39], although proton evaporation can occur. After the nucleus has lost energy via nucleon evaporation and drops below the nucleon evaporation threshold at ~ 10 MeV, further excess energy is removed via statistical γ -ray emission. The γ rays are said to be statistical since the density of states is high enough that the energies of the states cannot be resolved. The nucleus will undergo statistical γ -ray emission until the nucleus reaches the yrast line. The nucleus will then undergo discrete γ -ray emission to carry away angular momentum, until the nucleus reaches its ground state.

Since HIFE reactions produce nuclei in high-spin yrast states, which cascade through the yrast band, they are often used to study the structure of nuclei and are typically the first type of reaction used to study newly observed nuclei. Figure 2.13 shows a

schematic illustration of a HIFE reaction. Figure 2.14 show a schematic illustration of the compound nucleus following a HIFE reaction.

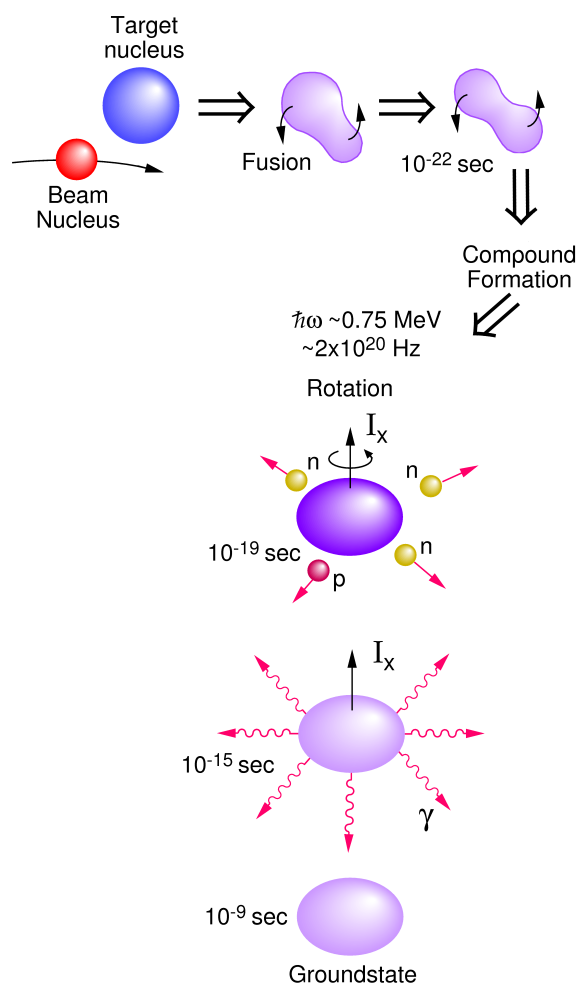


FIGURE 2.13: A schematic illustration a compound nucleus following a heavy-ion fusion evaporation reaction, taken from Ref. [52].

HIFE reactions typically use stable beam and stable targets. As the mass of nuclei increases, the proton to neutron ratio for stable nuclei decreases. Hence, these HIFE reactions typically produce proton-rich nuclei. In order to study neutron-rich nuclei, transfer reactions or radioactive beams are required.

2.4.2 Coulomb excitation

Figure 2.15 is a representation of a typical Coulomb excitation reaction (Coulux). A beam approaches the target with energies of ~ 5 MeV/u, and both the projectile and

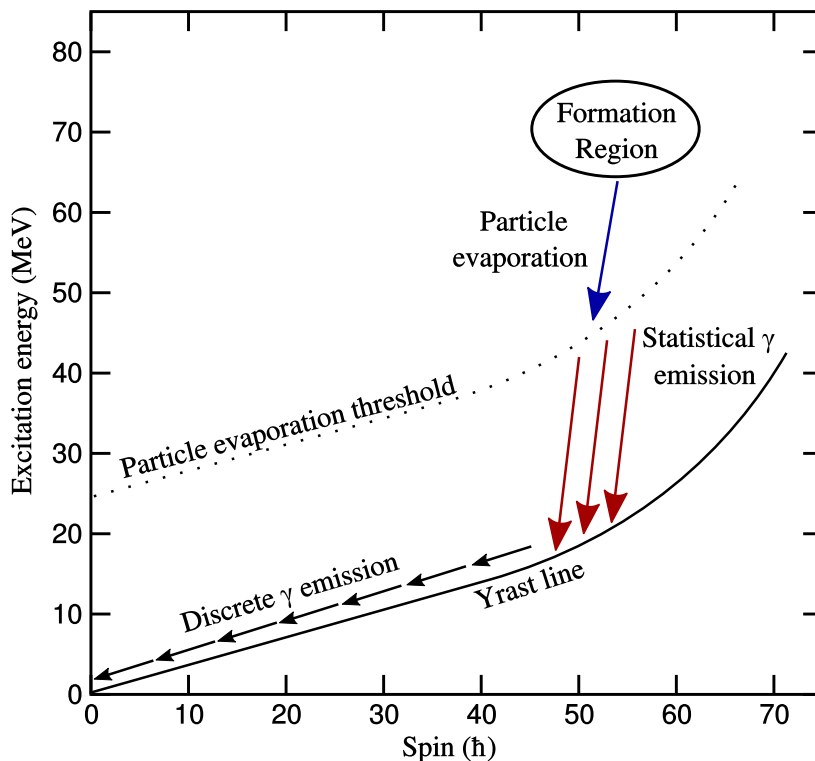


FIGURE 2.14: A schematic diagram a compound nucleus following a heavy-ion fusion evaporation reaction.

target are excited via the electromagnetic force [63]. The projectile recoils from its initial trajectory with an angle θ . The excited beam and target nuclei subsequently decay via γ emission to their ground states. The number of emitted γ rays is proportional to the number of nuclei in the beam and the transition probability of the state. Hence, by measuring the number of γ rays emitted in a Coulomb excitation reaction, and the number of recoils, the transition probabilities of the populated states can be measured. Coulomb excitation will often populate non-yrast states within nuclei and, as radioactive beams can be used as projectiles, Coulex provides a valuable tool to measure transition probabilities of non-yrast states in exotic nuclei. The condition that the number of emitted γ rays is proportional to the transition probabilities assumes that the excitation is purely electromagnetic, and therefore has no dependence on the nuclear force. To ensure the nuclear force does not contribute to the reaction, the ‘Cline safe criterion’ must be met [64]

$$b_{min} = [1.25(A_p^{1/3} + A_t^{1/3}) + 5] \text{ fm}, \quad (2.60)$$

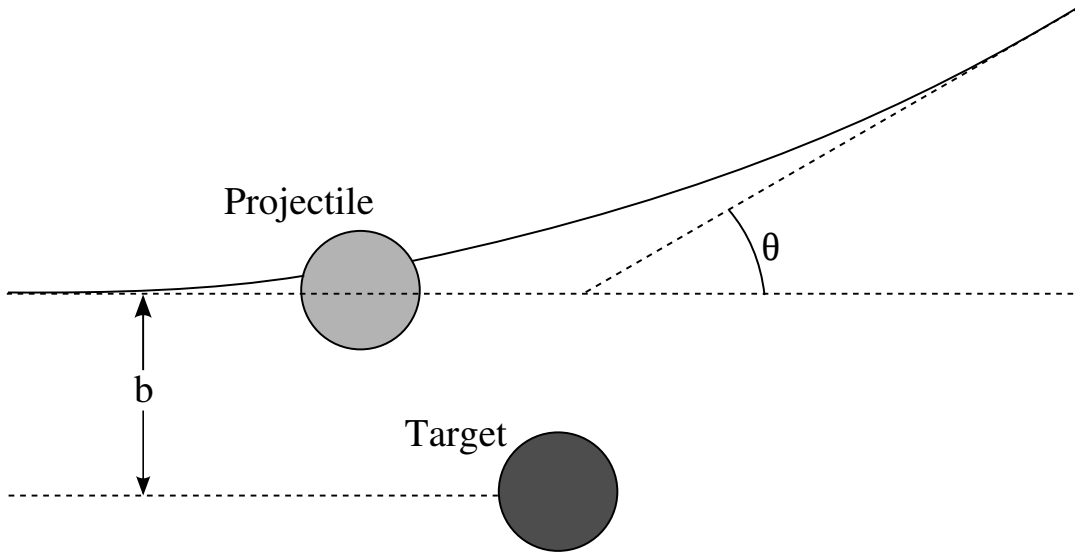


FIGURE 2.15: Schematic diagram of a Coulomb excitation reaction, showing the impact parameter, b , and the scattering angle θ .

where b_{min} is the minimum distance of closest approach and $A_{p,t}$ are the mass numbers of the projectile and target respectively. To ensure the distance of closest approach is larger than b_{min} , the centre of mass beam energy for projectiles scattered at an angle θ should be less than

$$E(\theta_{CM}) = 0.72 \frac{Z_p Z_t}{b_{min}} \frac{A_p + A_t}{A_t} \left(1 + \frac{1}{\sin \theta/2} \right) \quad (2.61)$$

The safest way to ensure this is to set $\theta = 0$ and use this as the maximum beam energy. For $A \sim 200$, this corresponds to a beam energy of ~ 4.5 MeV per nucleon. If larger beam energies are required, detectors can be placed at large values of θ for tagging, to ensure reactions with a small value of b are not seen.

For Coulex experiments with large excitation probabilities, second-order effects contribute to the overall probability and provide additional information on the electromagnetic matrix elements. These second-order effects are interpreted as virtual excitation of intermediate states close to the final state and are referred to as the reorientation effect [65]. This reorientation effect is dependent on the diagonal matrix element $\langle I || E2 || I \rangle$, and hence the shape of the nucleus. This results in the transition probability being dependent on the sign of the deformation parameter, which is illustrated in Fig. 2.16. The measurement of the sign of the deformation is extremely useful for measurements in nuclei which exhibit shape co-existence [66–69].

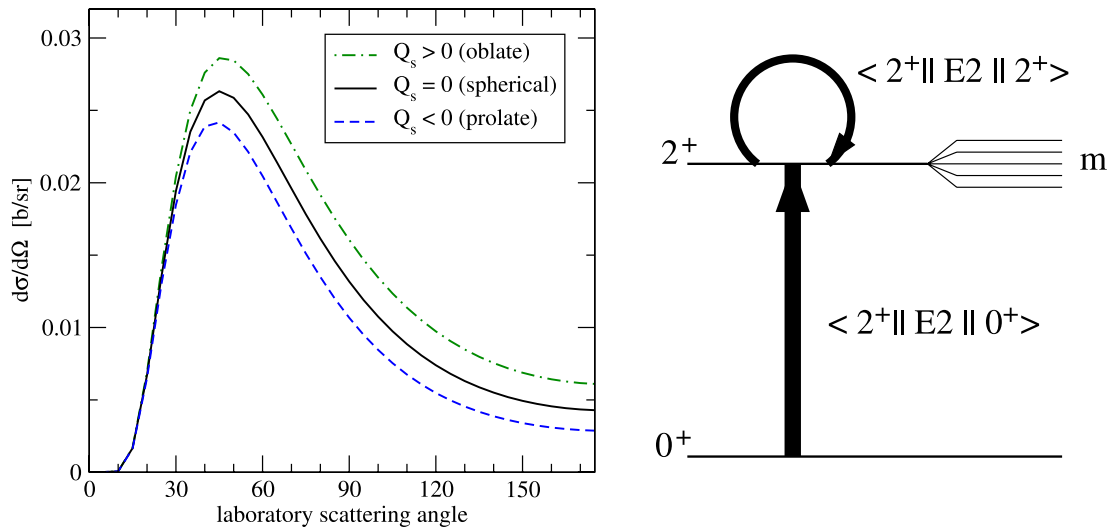


FIGURE 2.16: An example of a calculated differential Coulomb excitation cross sections for populating the 2^+ state, using the same $\langle 2^+ || E2 || 0^+ \rangle$ but different $\langle 2^+ || E2 || 2^+ \rangle$ matrix elements. The reorientation effect is illustrated on the right. Figure taken from Ref. [70]

2.5 Detecting gamma rays

When measuring nuclear state lifetimes with a plunger, the intensities of the different components of the γ rays, emitted from the state of interest, are measured. Hyper pure germanium detectors (HPGe) are commonly used for the measurement of γ rays due to their excellent energy resolution, typically around 2.5 keV at 1 MeV [71]. For a typical plunger experiment, the fully shifted and degraded components of a γ -ray transition are separated by ~ 4 keV. This makes sodium-iodide scintillators, and similar detectors, unsuitable for RDDS measurements as their intrinsic energy resolution is ~ 10 keV [72–75].

Germanium is a semiconductor with a band gap of 0.66 eV [30]. As a γ ray passes through a semiconductor, there is a chance that an electron will photoelectrically absorb the photon. This photoelectron will then pass through the semiconductor creating electron-hole pairs along its path until the electron has lost all of its kinetic energy. The amount of energy required to create these pairs is known as the ionisation energy, and is around 3 eV for germanium. The ionisation energy is independent of the energy and type of radiation, so the number of electron-hole pairs created is proportional to the energy of the incident radiation. A large bias voltage is applied across the crystal, which is used to drift the electron towards a cathode. A change in voltage on the

cathode is then measured, with the magnitude of the change being proportional to the energy of the incident photon [30].

The main advantage of germanium over other semiconductors, is the low ionisation energy. Most semiconductors have an ionisation energy of ~ 30 eV. Therefore, the number of charge carriers in germanium is ~ 10 times that of other semiconductors. This increases the number of charge carriers which, in turn, greatly increases the signal to noise ratio, resulting in a much better energy resolution.

The intrinsic photopeak detection efficiency of a HPGe crystal is typically $< 1\%$. Small production cross sections in exotic nuclei coupled with this low detection efficiency results in a large statistical uncertainty on RDDS lifetime measurements. To overcome the low efficiencies associated with measuring γ -ray yields, large arrays of HPGe detectors are often used. For example, the JUROGAM II array has been used previously with the DPUNS plunger and consists of 43 Compton-suppressed HPGe detectors with an overall photopeak detection efficiency of 4.3% at 1.3 MeV [18]. The plunger device described in this thesis, TPEN, is intended to be used at the MINIBALL array, located at the HIE-ISOLDE facility, CERN [23, 24, 76, 77]. The MINIBALL array has a total photopeak efficiency of $\sim 7\%$ making it well-suited for precision RDDS measurements [23].

2.6 Extracting component intensities from unresolved Gaussians

For high-mass nuclei ($A \approx 200$) the energy of excited states are often small (≈ 150 keV). A typical HIFE reaction with normal kinematics will produce recoils of $\approx 0.02c$. This gives a Doppler shift of ≈ 3 keV, the typical resolution of a HPGe detector. This often leads to the two components of the transition being unresolved, making it difficult to measure the intensities. In this case, the centroid of the superposition of these peaks can be used to determine the individual intensities, provided the widths and centroids of the two individual components are known. For two unresolved Gaussian functions with no background, the distribution is given by

$$h(x) = \frac{A}{\sqrt{2\pi\sigma^2}} e^{-\frac{(x-\mu)^2}{2\sigma^2}} + \frac{B}{\sqrt{2\pi\eta^2}} e^{-\frac{(x-\phi)^2}{2\eta^2}}, \quad (2.62)$$

where A and B are the areas of the first and second Gaussian functions, σ and η are the variances of the first and second Gaussian functions and μ and ϕ are the centroids of first and second Gaussian functions, respectively.

The centroid of a distribution is given by the integral

$$C = \langle h(x) \rangle = \frac{\int_{-\infty}^{\infty} xh(x)dx}{\int_{-\infty}^{\infty} h(x)dx}, \quad (2.63)$$

which for the distribution given by Eqn. 2.62 has the solution

$$\langle h(x) \rangle = \frac{A\sigma\mu + B\eta\phi}{A\sigma + B\phi}. \quad (2.64)$$

Rearranging Eqn. 2.64 to give the areas A and B gives

$$f = \frac{A}{B} = \left(\frac{\phi - \langle h(x) \rangle}{\langle h(x) \rangle - \mu} \right) \frac{\eta}{\sigma}. \quad (2.65)$$

Equation 2.65, and the knowledge that $A+B$ is equal to the total area of the superposition of the two components, allows for a measurement of A and B , provided ϕ, μ, η and σ are known. These parameters can be easily measured using very large and very small target-to-degrader distances. This, however, assumes that the widths and centroids of the two components of a transition are constant with respect to target-to-degrader distance. Additionally, the uncertainty on the areas of the two components is larger than for resolvable components and is given by

$$\frac{\sigma_f}{f} = \left[\left(\frac{\sigma_\phi}{\phi - \langle h(x) \rangle} \right)^2 + \left(\frac{(\mu - \phi)(\sigma_{\langle h(x) \rangle})}{(\langle h(x) \rangle - \mu)(\phi - \langle h(x) \rangle)} \right)^2 + \left(\frac{\sigma_\mu}{\langle h(x) \rangle - \mu} \right)^2 + \left(\frac{\sigma_\eta}{\eta} \right)^2 + \left(\frac{\sigma_\sigma}{\sigma} \right)^2 \right]^{0.5}. \quad (2.66)$$

From Eqn. 2.66, it is clear that the widths and centroids of the two components must be accurately known in order to accurately measure the areas. If this technique is to

be used, a large amount of data should be collected with very short and very long target-to-degrader distances to minimise the uncertainty on the lifetime.

Chapter 3

Triple Foil Plunger Setup

3.1 Overview

The triple plunger for exotic beams (TRIPLEX) was the first three-foil plunger to be developed [78]. TRIPLEX was built primarily for fragmentation reactions with high ($\sim 0.3c$) recoil velocities and relies on simulations of the three intensity components.

The majority of the work presented in this thesis has been to construct and commission a new triple foil plunger device seen in Fig. 3.1. The TPEN's three foils are mounted on stretching cones that sit inside a dedicated vacuum housing. A beam impinges on a target foil, producing nuclei of interest which move downstream towards a degrader foil. The recoils are slowed in the degrader foil and continue downstream towards a stopper foil, where the recoils are stopped. If tagging techniques on recoiling nuclei are required, a second degrader foil can replace the stopper foil. Boron Nitride (BN) insulating blocks were used to electrically isolate the foils from the foil-mounts but allow heat to dissipate into the mounts, preventing thermal build up when TPEN is used under vacuum conditions. The foil frames are connected to the foil mounts using three hard springs placed 120° apart which are compressed using screws. This allows the alignment of the foils. The target foil is at a fixed position, whereas the degrader and stopper foils are mounted on Physik Instrumente (PI) [79] Linear Piezo Positioning Stage-45 (LPS-45) piezoelectric motors which can change the target-to-degrader and

degrader-to-stopper distances independently. These motors utilise a constant negative-feedback system which keeps the target-to-degrader and degrader-to-stopper distances constant throughout the experiment. The LPS-45s have a total travel range of 26 mm and have a position resolution of 1 nm.

A BNC model PB-5 pulser is used to apply a voltage pulse to the degrader foil and the induced voltage on the target and stopper foils is monitored and used for to maintain a constant distance via negative feedback. Two TESA [80] GT43 axial miniature probes and a TESA TT20 electronic micrometer are used to calibrate the induced voltage against target-to-degrader and degrader-to-stopper distances. I modified the Köln plunger control software and adapted it for Windows 10, which was used to run the constant feedback system. The program can adjust the foil positions independently to ensure that the distances do not vary by more than $\sim 1 \mu\text{m}$. A 16 Bit National Instruments [81] USB-6251 data acquisition (DAQ) card was used to sample the induced voltage at a rate of 1.25 MS/s (1.25×10^6 Samples per second). The software was originally developed for the Köln plunger [6], and later used for the DPUNS plunger [11]. A more detailed explanation of this software is given in Section 3.9.5.

The entire internal workings of the plunger device is designed to be removable from its housing, allowing easy access for the alignment of foils. In addition to this, the foil mounts can easily be removed from the aluminium mount for changing foils if they become damaged.

During the project, the Köln plunger control software was extensively modified to accommodate the upgraded LSP-45 motors. The original software was used as a framework to control the new motors. New commands to move and control the foils have been written and implemented in the negative feedback system. The software has also been ported to Windows 10 from OpenSuse 10.3 for the first time, making the suite user friendly compatible with current operating systems.

TPEN can be used in two modes: the differential mode outlined in Section 2.1.3 and a mode to measure two very different lifetimes simultaneously, where TPEN works as two independent plungers simultaneously. As such, the orientation of the foils can be adjusted depending on the experiment. The change of orientation allows for an easier setup, but is not essential and either mode can be run with either orientation. In the differential mode, very small degrader-to-stopper distances are required, so the

degrader foil can be flipped so that the flat face of the degrader foil faces towards the flat face of the stopper foil. This allows a very good optical alignment between the degrader and stopper foils, which is typically much quicker than a capacitive alignment (see Section 3.2.1). Conversely, in the second mode, small target-to-degrader distances are typically required, so the flat faces of the target and degrader foils face each other. The following sections outline the main components of the plunger device and detail procedures required to setup the plunger for an experiment, starting with how to prepare the foils. In the following sections the orientation shown in Figs. 3.1 and 3.18 is used. Technical information on the components used in the TPEN is also given along with the modifications made to the control software.

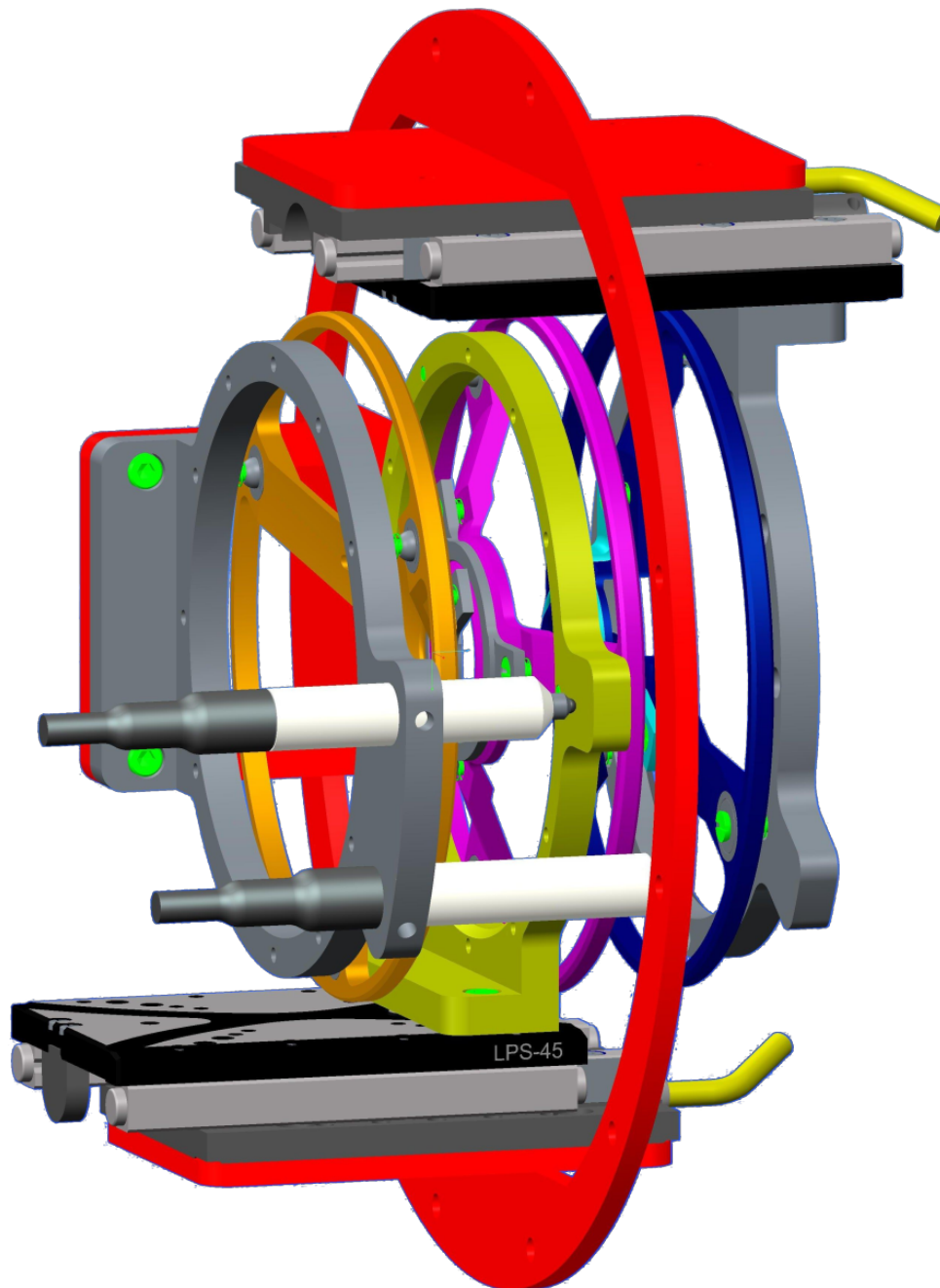


FIGURE 3.1: Engineering 3D drawing of the triple foil plunger device designed and built at the University of Manchester. Two LPS-45 National Instruments motors are at the top and bottom of the image in grey and black. The three mounts for the foils are in the centre of the image with the target (grey), degrader (yellow) and stopper (grey) foils from left to right. The target cone (orange), degrader cone (purple) and stopper cones (blue) can also be seen.

Two micrometers are seen in white mounted onto the target foil frame.

3.2 Plunger foils

Foils of the desired thickness are produced via vacuum evaporation [82] or rolling and are then glued to the foil stretchers shown in Fig. 3.2 using a small amount of aralditeTM. Any loose foil or raised edges must be carefully cut away using a scalpel. If any raised edges remain, then the edges can touch before the faces of the foils touch, limiting the achievable separation. The foil must be glued such that the surface is free from wrinkles, to allow it to be evenly stretched and to ensure a flat a surface as possible. Each of the three foil frames has its own specially shaped stretching cone, shown in Fig. 3.3, which are designed to nest inside each other.

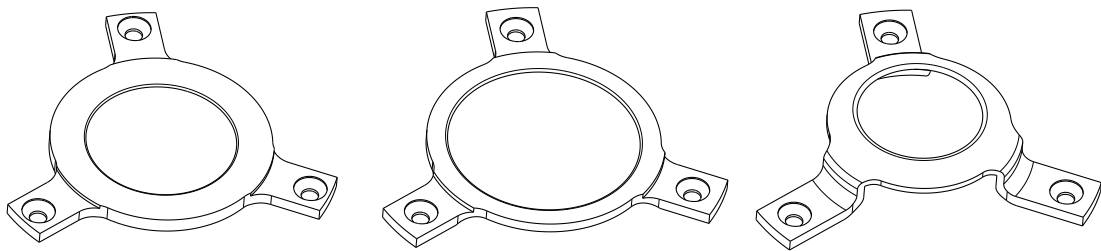


FIGURE 3.2: Drawing of the target, degrader and stopper foil stretcher frames used in TPEN, from left to right.

Once the foils have been glued to the frames and the glue has set (~ 2 hours for quick setting aralditeTM), they must be stretched using the cones. Springs slightly larger than M2 screws are placed into each of the countersunk screw holes in the top of the stretching cones shown in Fig. 3.3. These springs support the foil frame and should be stiff enough for the foil frame to rest on top of the springs. The springs are cut long enough so that at full extension the foil is not in contact with the stretching cone, but not so long that they limit the amount of stretching. Typically, the spring will be cut to 5 mm. Screws are placed through the three holes in the foil frame and are used to pull the frame and the stretching cone closer together. Each screw is turned slowly until a slight indentation from the stretching cone is seen all around the foil. Once an even indentation is seen on the foil, the screws are turned until the foil is flat. It is important to apply enough force such that the foil is flat and has no wrinkles. However, too much force will tear the foil, making it unusable. The dimensions of the degrader stretching cone is shown in Fig. 3.4 for reference. The stretcher-cone arrangement is shown in Fig. 3.5, with the foil frame shown in red.

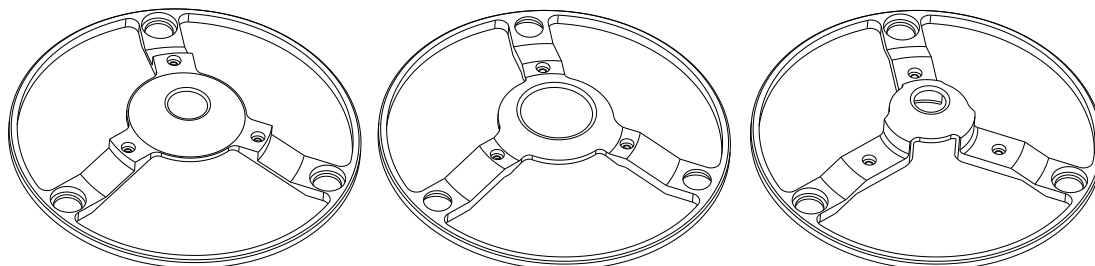


FIGURE 3.3: Isometric drawings of the stretching cones from TPEN showing the stretching cone for the target, degrader and stopper foils from left to right.

These cones fix to the foil mounts shown in Fig. 3.6.

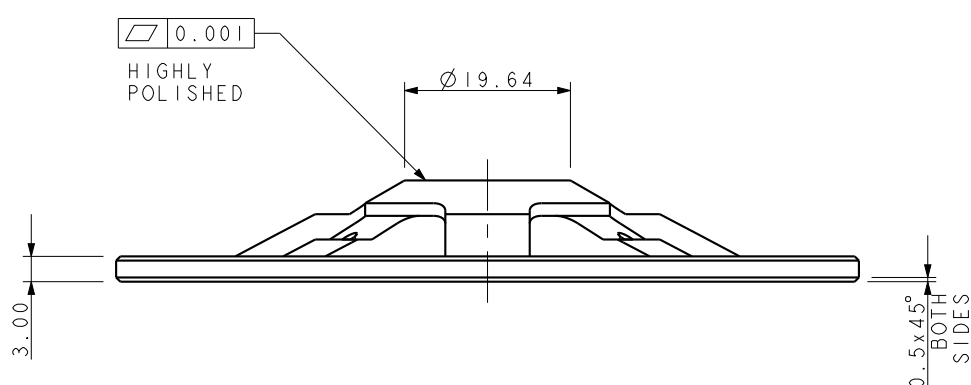


FIGURE 3.4: Drawing of the side view of a plunger degrader stretching cone.

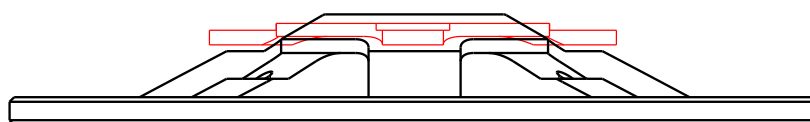


FIGURE 3.5: Drawing of the side view of the foil stretcher (red) placed over the stretching cone (black), to demonstrate the stretching technique.

The stretching cones are attached to the mounting frames via three M2 screws placed 120° apart. An example of the mounting frames is shown in Fig. 3.6. A hard spring is placed around the screw connecting the cone and the frame. This spring acts to push the stretching cone and mount apart. By varying the amount that the three screws are turned the angle of the stretched foil can be changed. A maximum angle of $\sim 5^\circ$ is achievable by varying the spring tensions. These screws are used for the alignment of the foils, which is described in Section 3.2.1. A photograph of a fully assembled stretched target foil, coupled with the target mount is shown in Fig. 3.7.

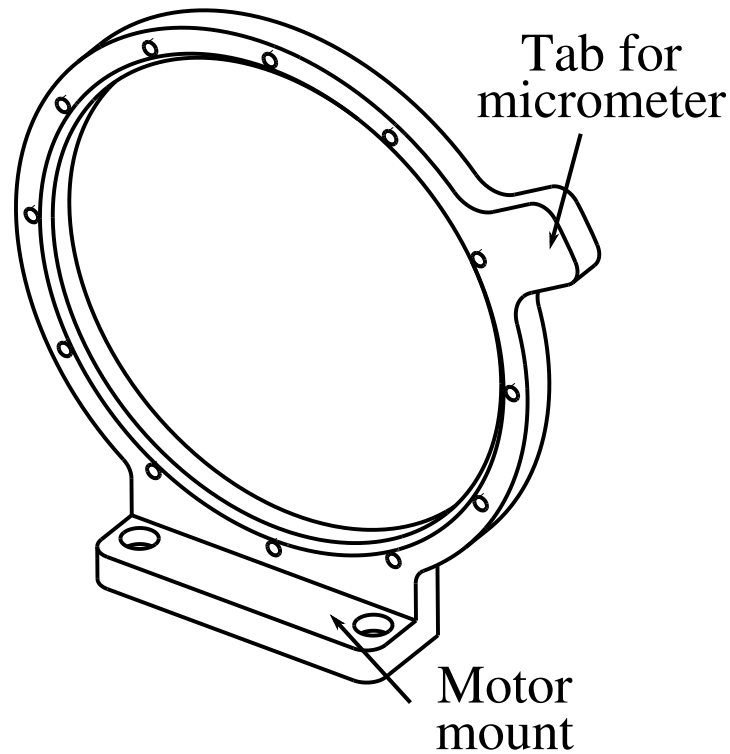


FIGURE 3.6: Schematic diagram of a the degrader foil mount.

Each of the target, degrader and stopper cones have their own unique mounts. The target mount has two circular holes to allow the micrometer probes to pass through, see Fig. 3.1. The degrader and stopper cones each have a metal tab which acts as a surface for the micrometer to press against during distance calibration. The mounting frame for the target foil is attached to a fixed position on the TPEN frame. The degrader mount and the stopper mounts are attached to an LPS-45 motor using two M3 screws. The motors allow the position between the foils to be varied, providing a maximum target-to-degrader separation of 26 mm and a maximum degrader-to-stopper separation of 20 mm.

3.2.1 Aligning the foils

Since the beam is not point-like and can move throughout the experiment, it is important the three foils are as close to parallel as possible. Any non-zero angle between the foils will increase the uncertainty on the true distance and limit the absolute separation between foils. For example, if the tops of the foils are in contact and the centres of the foils are separated by $10\ \mu\text{m}$, then the minimum absolute foil separation is $10\ \mu\text{m}$,



FIGURE 3.7: A photograph of a fully assembled foil frame and stretching cone ready to be screwed into the fixed target position. The cone is attached to the frame using the spring-screw mechanism described in Section 3.2.

assuming the beam passes through the centre of the foil. Assuming an average recoil velocity of $0.05c$, this $10\ \mu\text{m}$ offset would hinder measurements of lifetimes smaller than 5 ps. At 5 ps, the flight time between the degrader foil and the stopper foil becomes comparable to the lifetime of the state. The alignment of the foils is thus extremely important.

The first step in arranging the foils is to ensure the central foil is arranged such that the beam and foil are orthogonal. This is done by varying the turn on each of the three screws connecting the stretching cone to the foil mount. A class 2 laser pointer can be shone down the beam axis from the alignment telescope position. Minimizing the size of the laser spot on the foil will ensure the foil is orthogonal to the beam axis, as any angle would stretch the beam spot. The target and stopper foils are then aligned to the central foil individually using the following technique. The technique described assumes the differential mode of the plunger is used and hence the flat stretched face of the degrader foil will face the flat face of the stopper foil to achieve a very small degrader-to-stopper distance. Here, the ‘flat face’ is the face of the foil that can be seen in Fig. 3.7.

The screws attaching the cones to the frames are then loosened until the springs are almost fully extended. A 10 V signal is applied to the central foil using the PB-5 pulser and an induced voltage is measured on the outer foils. The degrader foil is arranged such that the flat face of the degrader foil faces the flat face of the target foil. Since the target foil is in a fixed position, the central foil is slowly moved closer to the target foil until electrical contact is established between the foils. The foils are then moved apart in 0.1 μm steps until they are no longer in electrical contact. A bright light is shone from behind the foils and the gap between the foils is observed. The foils are then optically aligned by adjusting the tension on the three foil mount springs until the faces of the foils appear parallel. The foils are then moved as close as possible together and the alignment is repeated until no angle can be observed between the foils. The foils should be observed from the top, and from both sides to ensure parallax error is minimised. Once the degrader foil appears to be parallel with the target foil, it is flipped through 180° so that the flat face of the degrader now points away from the flat face of the target foil.

Using the optical alignment as a starting point, the induced voltage in the target foil is recorded and the capacitance is used to make fine adjustments to the alignment. The degrader foil is moved closer to the target foil and the maximum induced voltage before electrical contact is recorded. After the foils have touched, they are moved apart by $\sim 50 \mu\text{m}$ and one of the three screws connecting the stretching cone to the foil mount is turned $1/4$ turn clockwise. This tightens the spring and moves the foils further apart. The foils are then brought together and the voltage is recorded until electrical contact is established. The measured voltage is compared to the previous measurement. Maximum voltage should occur when the foils are perfectly aligned, so if the voltage is higher than before then the alignment had improved. If the voltage had increased then the same screw is turned another $1/4$ turn clockwise. If the voltage had decreased, the screw is turned $1/4$ turn counter-clockwise and the process is repeated with smaller turns until the maximum voltage is achieved. This process is then repeated for the other two screws. Once all three screws have been turned to achieve maximum induced voltage, the entire process is repeated again starting with smaller turns to ensure that the true maximum in voltage was found. The target foil and the degrader foil are now aligned and a calibration can be performed to estimate the absolute distance between the foils.

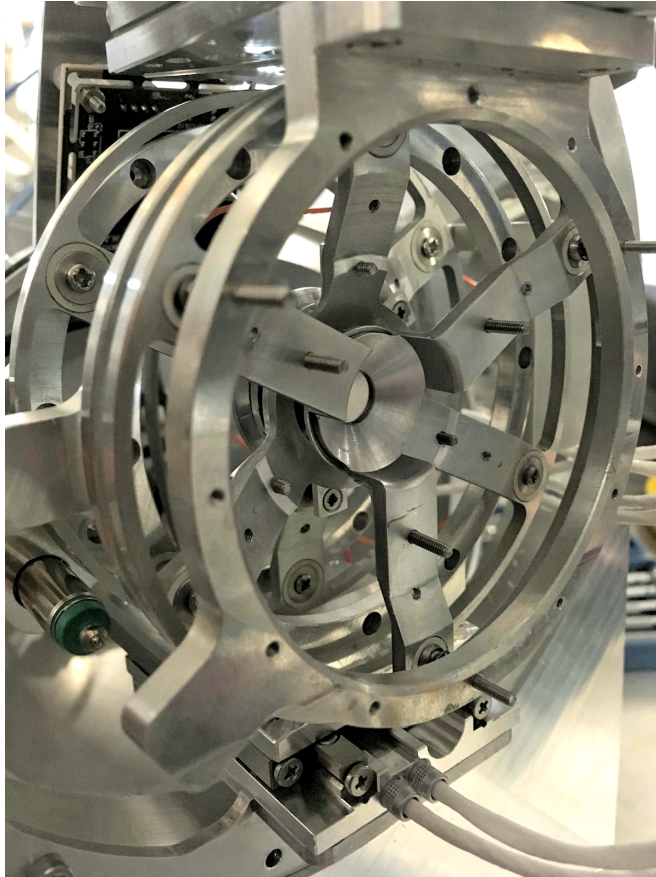


FIGURE 3.8: A photograph of all three foils aligned and ready for beam.

Once the target and degrader foils are aligned, the stopper foil is attached and moved close to the degrader foil. The stopper foil is aligned to the degrader foil using the optical alignment technique described previously. Only the screws between the stopper stretching cone and the stopper foil mount should be adjusted to ensure the target-degrader alignment is not changed. Once an optical alignment has been performed, the capacitance measurement described previously is used to fine-tune the alignment. Figure 3.8 shows a photograph of all three foils aligned.

3.3 TPEN frame

Figure 3.9 shows a drawing of the frame used to support the two LPS-45 PI motors and the target frame. The motors are mounted top and bottom of the drawing using four M2 screws and the target frame is mounted on the left hand side. The frame is completely removable from the vacuum housing to allow easy access to the foils.

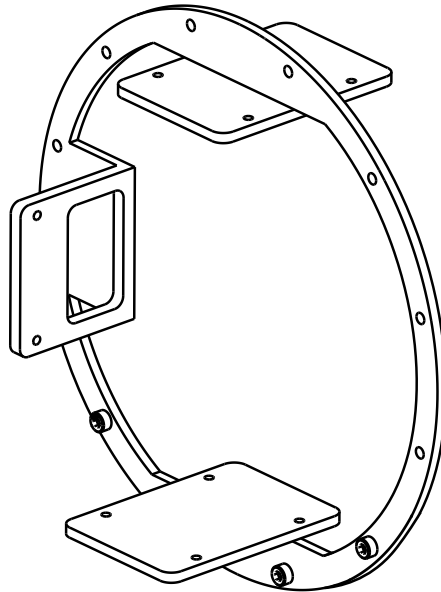


FIGURE 3.9: Drawing of the frame for TPEN, showing the two motor mounts (top and bottom).

The frame is made from a single piece of aluminium to minimise recoil scattering and out-gassing into the vacuum environment.

3.4 Vacuum housing

Figure 3.10 show a CAD drawing of the vacuum housing for TPEN, specifically the housing used at the University of Jyväskylä on the RITU beam line. The left-hand side of the housing connects upstream to the beam line. The right-hand side connects to RITU [83], where traveling recoils can be separated for tagging. The three foils of TPEN are enclosed in a spherical chamber. The chamber sits at the centre of the Jurogam II array [18,19,84] and splits at the centre to provide easy access to the three foils. The chamber is small enough that the JUROGAM II array can close fully around the chamber, maximizing geometric detection efficiency.

The central chamber of the vacuum housing is 176 mm in diameter and 2 mm thick. The foils are arranged inside TPEN such that γ rays detected at small angles, such as those used in this experiment, pass through only the 2 mm aluminium housing. This ensures γ attenuation is small.

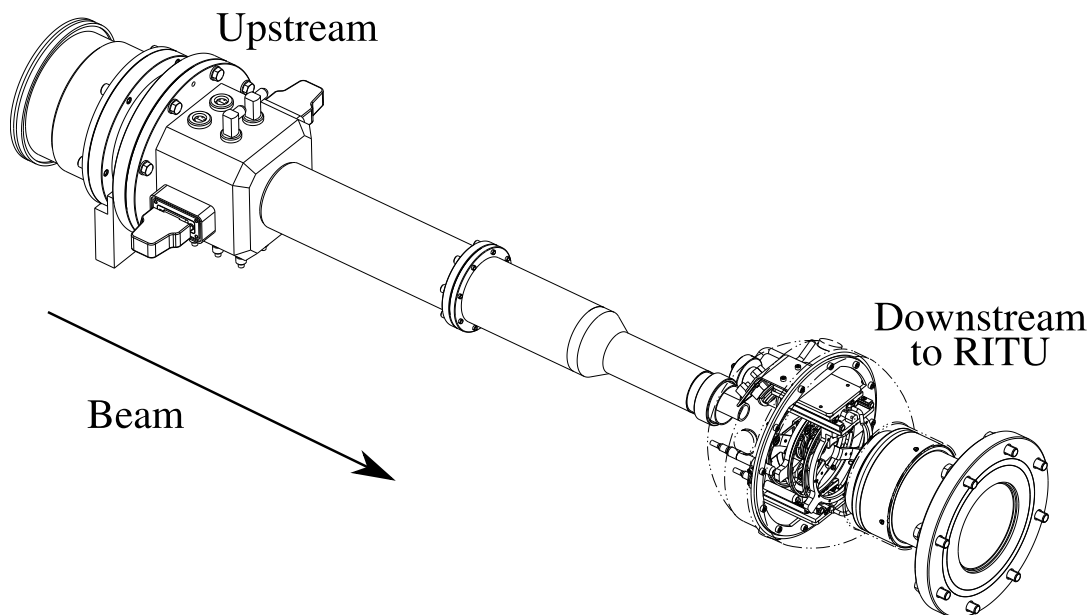


FIGURE 3.10: CAD drawing of the TPEN vacuum housing for RITU [85]

All electrical wires from TPEN are fed upstream and are protected from the beam by an aluminium cylinder, seen in Fig. 3.11. Electrical feed-throughs can be seen on the left hand side of Fig 3.10 which are used to send signals to and from TPEN. TPEN has 12 electrical feed-throughs: four four-pin LEMO connectors, six one-pin LEMO connectors and two fifteen-pin RS-232 connectors. The two fifteen-pin RS-232 connectors are used to send and receive signals to the two LSP-45 motors. Two of the four-pin connectors are used for the micrometer feed-throughs (one each) and one four-pin is used as a camera feed-through. The camera is used to view the target throughout the experiment to look for damage. Three one-pin feedthroughs are used for signal cables. One signal cable sends a 10 V signal to the central degrader foil and two signal cables are used to send the induced voltage signal. The remaining feed-throughs are not currently required and are used as spares. Internally, all connections are soldered to the LEMO connectors, ensuring a secure connection.

TPEN utilises a quartz viewer and camera system that is used to align the beam with the centre of the target foil. The viewer can be moved in and out of the beam axis without opening the vacuum chamber using a specially designed arm, removing the need to vent the chamber after the beam has been aligned. All components of the vacuum chamber were extensively leak tested in Manchester. The chamber reached

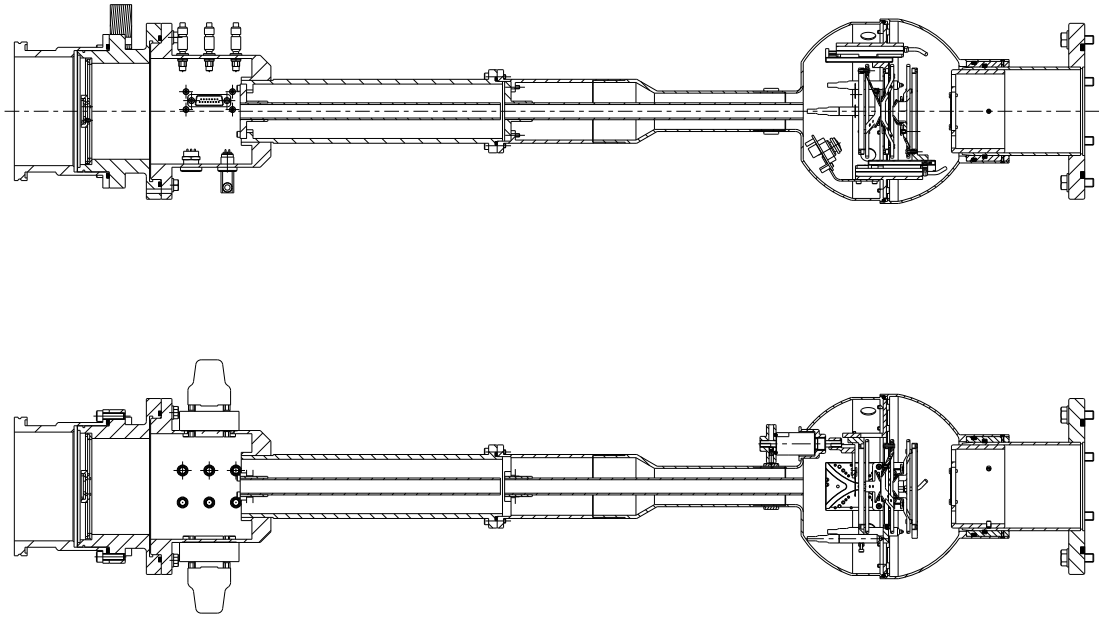


FIGURE 3.11: CAD drawing of a cross section of the TPEN vacuum housing for RITU. TPEN is shown from the top (top) and from the side (bottom).

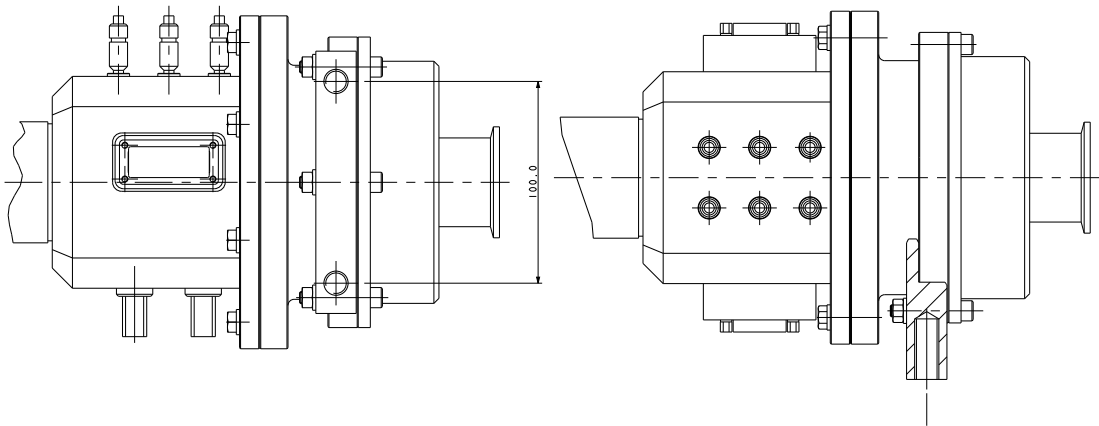


FIGURE 3.12: CAD drawing the vacuum feedthroughs used on TPEN from two different angles.

a pressure of 10^{-7} mbar using a single turbo pump. All components of TPEN also support gas environments, such as those used in the RITU gas environment [83].

3.5 LSP-45 Motors

TPEN utilises two LSP-45 linear piezo positioners to control the target-to-degrader distance and degrader-to-stopper distance independently. A photograph of one of the

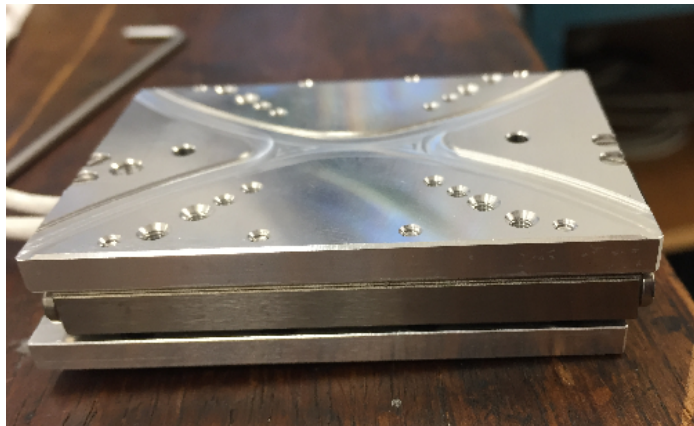


FIGURE 3.13: Photograph of the PI LPS-45 motor used to move the foils.

motors is shown in Fig. 3.13. The motors work via the piezoelectric effect, where electrical energy is converted to mechanical energy. Certain crystals produce an electric current when they experience mechanical stress [86]. Charge builds up on opposite faces of the crystal generating a current. This effect can be reversed, where an external electric potential alters the shape of the crystal. This effect is exploited in piezo motors, allowing nanometre-precision positioning.

The LPS-45 is controlled using a Physik Instrumente (PI) E-871 control unit. Each motor has dimensions of $64 \times 45 \times 15$ mm and is made mainly from aluminium. Speeds of up to 10 mm/s can be achieved and a maximum force of 8 N can be produced. A maximum travel distance of 26 mm is possible, with the motors moving 13 mm in each direction from a central position, allowing lifetime measurements of up to 2 ns. The LPS-45 is capable of working in vacuum environments and has been tested down to 10^{-9} mbar.

The motors can work in both open and closed loop modes of operation, with the closed loop mode preventing hysteresis. The motors have a typical resolution of 6 nm and a bidirectional repeatability of 18 nm. These properties make the LPS-45 ideal for controlling target-to-degrader and degrader-to-stopper distances.



FIGURE 3.14: Photograph of the E-871 control unit used to control the motors. USB, RS-232 and joystick connections can be seen on the front face. Baud rate control and address switches are seen on the right hand side of the front face.

3.6 E-871 control units

The LPS-45 is controlled using an E-871 control unit, such as the one in Fig. 3.14. The E-871 communicates with a computer via USB or 9-pin RS-232. TPEN makes use of the USB capabilities only. A joystick option is also available but is not used in the work presented in this thesis.

The E-871 has bi-directional communication with the computer. Inputs of four characters are used to communicate with the motor. For example, the input ‘IDN?’ requests the identification number of the motor and displays it on the computer. Similarly, the code ‘ERR?’ displays any errors the motor has encountered. Approximately 50 of these commands are used to provide all the functionality required for TPEN.

The E-871 works in two modes: normal operating mode and servo mode. In the normal operating mode, the output power to the motor, and hence the speed of the motor, is controlled using pulse width modulation (PWM). The output voltage is flipped from high to low producing an average power output dependent on the duty cycle. The duty cycle is the percentage of the ‘on’ time compared to the ‘off’ time.

In servo mode the duration of the ‘ON’ pulse provides a position to which the foil should be driven. The motor then draws power from its own supply to move to the

desired position. Typically, servo mode is used to move the foils quickly during setup. Once negative feedback is required, the normal operating mode of the E-871 is used.

3.7 Micrometers

To calibrate the target-degrader and degrader-stopper distances, a TESA TT20 electronic unit is used in conjunction with two GT43 probes, both shown in Fig. 3.15. The GT43 probe has a travel range of 2.1 mm and a maximum error in position of 0.2 μm . The probes have a repeatability of 0.1 μm and hysteresis of 0.15 μm . A bi-directional opto-electrical cable is used to transfer information between the TESA TT20 and the computer. It must be noted that the opto-electrical cable is RS-232, and when using an RS-232-to-USB adaptor, an additional adaptor is required with the pin layout shown in Table 3.1. This adapter was constructed in the present work for TPEN.

TABLE 3.1: Micrometer adaptor pin layout, here RxD, TxD, DTR, RTS and GND represent receive data, transmit data, data terminal ready, request to send and ground, respectively. All other pins remain unchanged.

9pin male	9pin female
2(RxD)	2(RxD)
3(TxD)	3(TxD)
4(DTR)	4(DTR)
7(RTS)	5(GND)

3.8 Data acquisition card

A National instruments (NI) USB-6251 16-bit data acquisition (DAQ) card is used to monitor induced voltage on the degrader foil. The card has 8 BNC analogue inputs, 2 analogue outputs and 24 digital input/outputs. It has a sample rate of 1.25 MS/s. One analogue input is used for each of the induced voltage signals, and one input is used as a trigger, from the PB-5 pulser. The remaining inputs are unused.

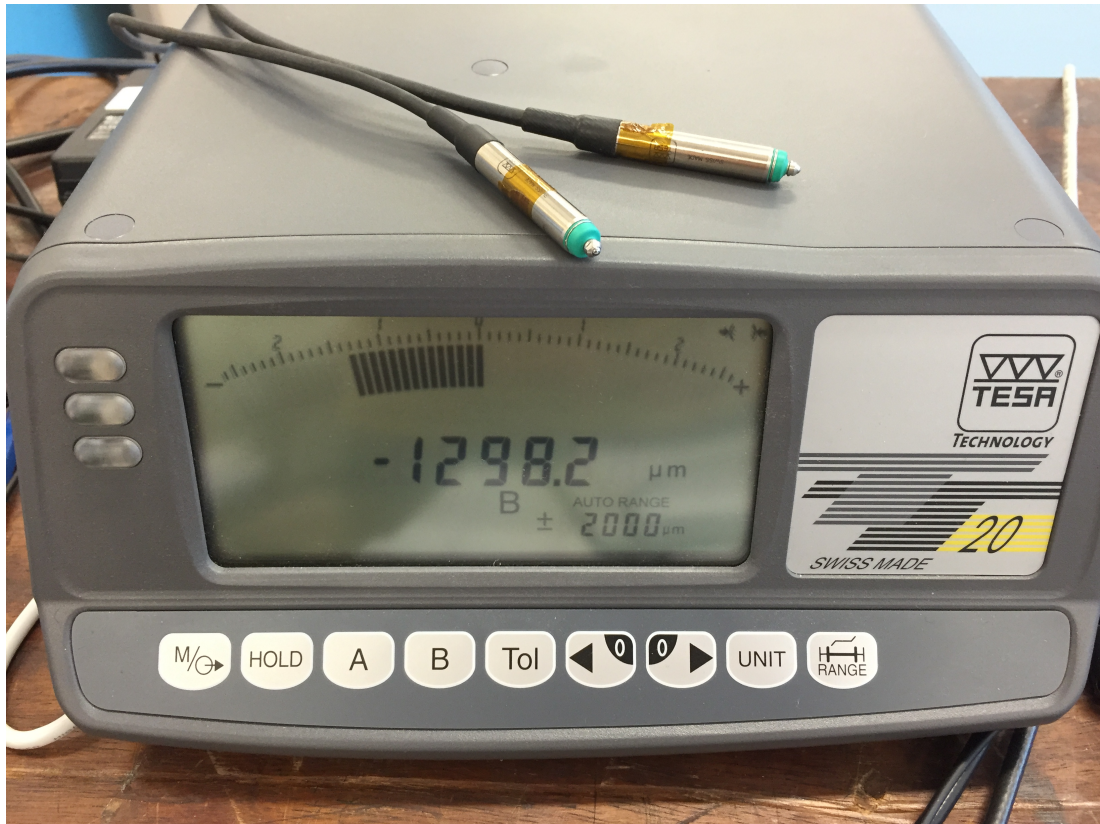


FIGURE 3.15: Photograph of the TESA TT20 and GT43 micrometer probes. The probes are seen on top of the TESA. The measured distance from probe B is displayed on the screen.

3.9 Software and feedback system

A LabVIEW software package, originally written at the University of Köln, has been extensively modified in order to work with the new LSP-45 motors and a Windows 10 operating system. The software is now a complete suite providing all of the functionality required for TPEN. The suite consists of 24 virtual instruments (VIs), which are all interlinked and provide either measurement, control or calibration of apparatus. An example of a VI is seen in Fig. 3.17. An overview of the most important VIs is given in the following sections.

3.9.1 Motor virtual instrument

The motor virtual instrument directly communicates with the LPS-45 motors in order to change the target-to-degrader and degrader-to-stopper distances independently. The

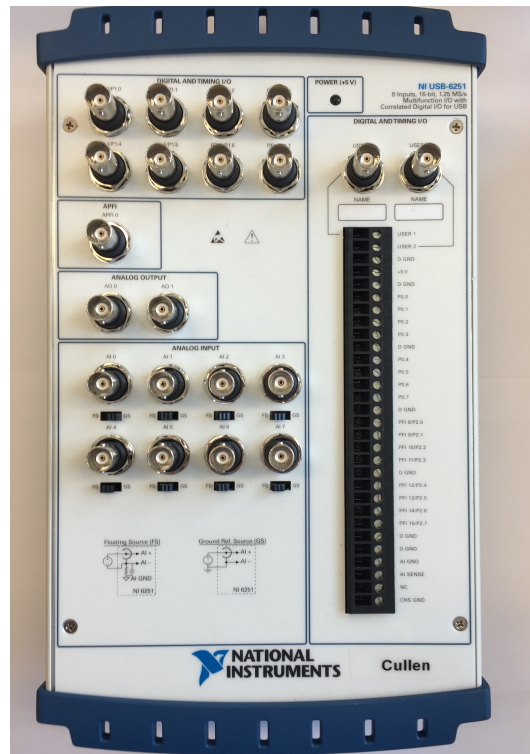


FIGURE 3.16: Photograph of the NI USB-6251 DAQ card used to acquire data. BNC connection for timing, digital input/outputs and analogue input/outputs are seen on the left. Screw terminals are seen on the right.

VI allows a variable motor speed controlled by the circular dials. The real time position of the motor is also given. The VI communicates with the motors using four character commands and uses the normal operating mode of the E-871 to allow for quick position changes. Many of the commands used by this VI have been re-written in this work. The functionality of the LSP-45 motor is different to that of the previous burleigh n-661k motor and as such the way the previous VI moved the motors was not compatible with the LSP-45. The new VI treats continuous movement as a series of discrete steps and the number of steps sent to the motor per second determines the stage velocity.

3.9.2 Micrometer virtual instrument

The micrometer VI is a simple VI that communicates with the TESA TT20 unit via an opto-electrical cable. The VI sends a request to the TESA TT20 for the micrometer value, and this value is sent back to the computer. The micrometer VI is unchanged compared to previous software versions with the exception of line break and carriage return characters being changed.

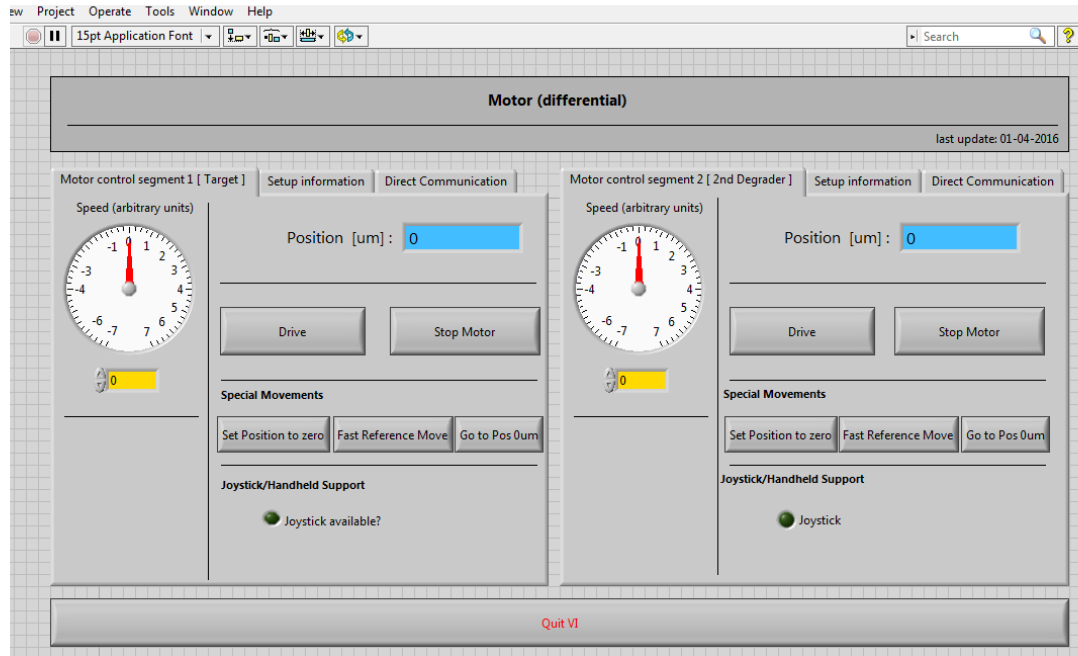


FIGURE 3.17: A screen-shot of the differential motor virtual instrument used to control the motors. The screen-shot shows the front face of the panel with the block diagram hidden. Speed is controlled with the circular dials.

3.9.3 Voltage virtual instrument

The voltage VI is a simple VI that communicates with the NI USB-6251 DAQ card to record the induced voltage on the target and stopper foils. The VI samples the induced voltage at up to 1.25 MS/s. In this experiment, the sampling rate was determined by the pulse frequency of 500 Hz. The VI records 10 voltages and averages them. The average voltage and the standard deviation is plotted as a function of time on a graph and is logged to a file. If finer sampling is required, then the averaging can be removed and the pulser frequency can be increased.

3.9.4 Calibration virtual instrument

In order to use the constant feedback system, a calibration of distance between foils and induced voltage on the foils is required. The distance between foils is measured using the two GT43 micrometer probes and the induced voltage on the target and degrader foil is measured and logged using the NI USB-6251 DAQ card.

The target-to-degrader and degrader-to-stopper distances are calibrated independently. The following section will describe the calibration of the target-to-degrader distance but the process is identical for the degrader-to-stopper distance. Firstly the motor VI, micrometer VI and the voltage VI are used to find the electrical contact point. The degrader foil is slowly moved towards the target foil and the voltage is monitored. When the voltage reaches 10 V, the foils are in contact and the micrometer is set to 0 μm . Several (~ 15) calibration distances are chosen and saved into a text file, which is used by the calibration VI.

The calibration VI allows an easy calibration of induced voltage versus distance. The VI moves the motor to the maximum decided calibration point and records the voltage. The motor is then moved in slowly, recording the voltage at every decided point until 0 μm is reached. These values are saved into a text file automatically which is called upon by the feedback system. The process is then repeated for the degrader-to-stopper distance and the calibration data is saved into a separate file. The calibration process is automated and has built in safety feature to avoid damaging the foils. A threshold voltage can be set such that if the induced voltage rises too high, the calibration will abort and move the foils apart. Additionally, the VI moves the foils at different speeds depending on the foil separations. If the foils are far apart, the foils are moved quickly. As the foils get closer, the velocity is automatically reduced.

3.9.5 Feedback system

Figure 3.18 shows a schematic drawing of TPEN and the electronic nuclear instrument modules (NIM) used to process the signals. A 10 V square pulse is applied to the central degrader foil at a rate of 500 Hz using the PB-5 pulser. A simultaneous pulse from the PB-5, delayed using a gate and delay generator, is used as a trigger for the DAQ card. The induced voltage on the target and stopper foils is amplified, stretched and measured using the NIMs shown. The measured voltages from the DAQ card are sent to the computer using USB 2.0.

The feedback system ensures the distance between foils is constant throughout the experiment. As the beam heats the foils, they are deformed and the distance can change. Fluctuations in the beam intensity result in this effect being unpredictable, so

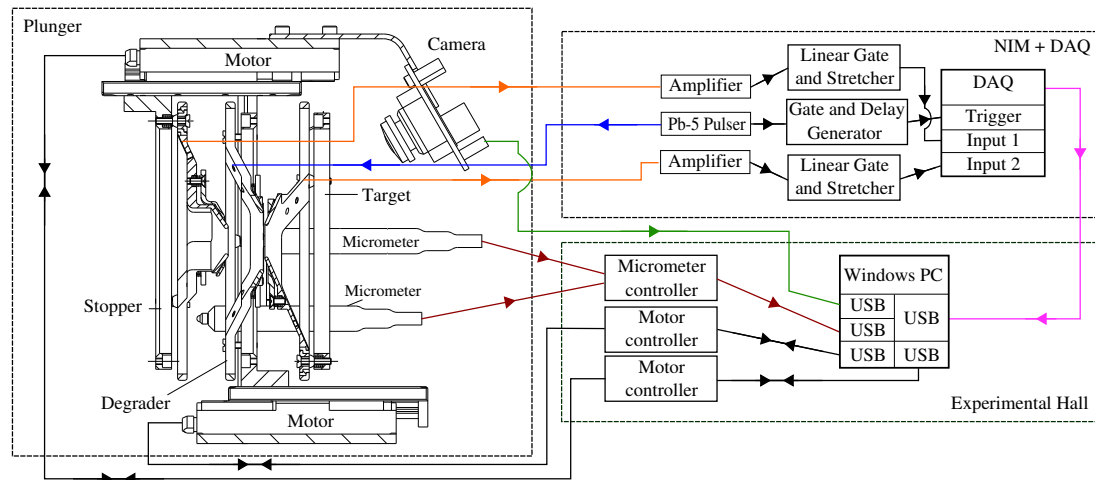


FIGURE 3.18: A diagram showing TPEN and the electronic modules used to control the constant feedback system. The arrows indicate the direction of signal flow. If required the target cone can be replaced with a stopper cone the degrader foil can be flipped to allow for very small degrader-to-stopper distances.

constant feedback is required. The feedback VI monitors the induced voltage on the foils in real time. If the voltage falls outside of a tolerance range, usually chosen to be $0.5 \mu\text{m}$, then the VI moves the motor accordingly. For example if the voltage on the target foil is too low, the VI will move the degrader foil closer to the target. The target-to-degrader and degrader-to-stopper distances are monitored independently and these distances can be adjusted independently.

The feedback VI writes the target voltage, stopper voltage, micrometer values, target-to-degrader distance and degrader-to-stopper distance to a text file once per second. These files can then be used to calculate the average distances and the standard deviation in the distance. In future plunger campaigns, the distances from this VI will also be implemented into the total data readout (TDR) [87] system so that γ -ray events can be sorted or filtered by distance using the GRAIN data analysis software [88].

3.9.6 Modification to software

Most of the modifications to the software was to port it to Windows. The majority of the modification only required simple syntax changes. However, the last plunger, DPUNS [11], used a PI n-661k motor with an E-870 control unit [89]. This motor and

control unit took different commands to the newer LSP-45. Many of the commands used by the control software did not exist in the E-871 control unit. As such, many of the programs had to be modified in order to restore functionality when using the new motors.

Rewiring of the block diagrams was required in order to produce desired functions; the rewiring is detailed in a separate document named ‘TPEN user manual’ [90]. Table 3.2 shows a list of commands used in the motor VI for both the E-870 and E-871 with the functions of each command.

TABLE 3.2: Table of changes made to the motor commands showing the commands for the E-870, the E-871 and the functions of these commands. The general format is ‘Command: axis: value’.

E-870	Function	E-871	Function
JON 1 0	Disable joy stick	No replacement	N/A
SVO 1 0	Turns servo mode off	SVO 1 1	Turns servo mode on
OVL 1 500	Set open loop velocity	SMO 1 500	Open loop control
SSA 1 10	Set step amplitude	SST 1 10	Set step size
RON 1 0	Set reference mode	RON 1 0	Set reference mode

Chapter 4

Commissioning TPEN

4.1 Introduction

TPEN was commissioned at the Accelerator Laboratory of the University of Jyväskylä, Finland, by measuring the known 45.6(5) ps lifetime of the first 4^+ excited state in ^{156}Dy [20]. Figure 6.5 shows the partial level scheme of ^{156}Dy taken from Ref. [91]. Our commissioning experiment tested the differential mode of TPEN and compared the lifetime obtained with that of the previous measurement [20]. Additionally, an analysis was performed by treating TPEN as a conventional plunger, to make a comparison between the standard mode and the differential mode.

Excited states in ^{156}Dy were populated in the $^{24}\text{Mg}(^{136}\text{Xe}, 4n)$ fusion-evaporation reaction with a cross section of ~ 100 mb using a beam energy of 590 MeV. A ~ 1 pA $^{136}\text{Xe}^{25+}$ beam, produced with the K130 cyclotron at JYFL, was used to bombard a 1 mg/cm² natural magnesium target foil placed inside TPEN for 6 days. The reaction employed inverse kinematics to produce recoils with high velocities. The average recoil velocity after leaving the target was measured to be 0.0699(9)c. Two 6.6 mg/cm² ^{56}Ni foils were placed downstream from the target position to degrade and stop the produced recoils. These degrader foils created the three velocity regimes required for the differential mode of TPEN.

Four Compton-suppressed JUROGAM Phase-1 [18, 19] HPGe detectors were placed at an angle of $157.5(5)^\circ$ with respect to the beam axis around TPEN in order to measure

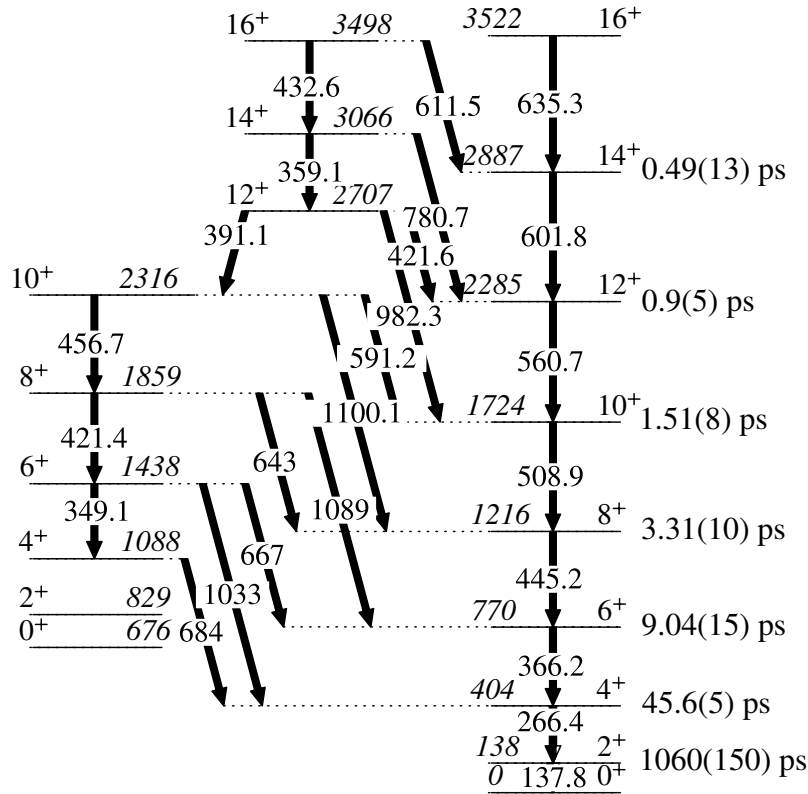


FIGURE 4.1: Partial level scheme of ^{156}Dy according to Ref. [91]. The lifetimes of the known states from Ref. [20] are given for the rotational band built upon the ground state.

the γ -ray intensities. The detectors were placed at a distance of 12.5(1) cm from the target position on a specially constructed table, where their combined absolute efficiency was measured to be 0.20(2)% at 1.3 MeV. The table was cut with grooves to allow a precise target to detector angle alignment. Figure 4.2 shows an illustration of the TPEN-RITU setup. Figure 4.3 shows TPEN installed inside the target vacuum chamber next to the four Compton-suppressed JUROGAM Phase I HPGe detectors used in the measurement.

The total data readout (TDR) [87] data acquisition system was employed to record the events from all four HPGe detectors. The GRAIN software package was used to perform offline analysis and construct 2D γ - γ coincidence matrices [88] where the two γ rays were detected within 100 ns of each other. A total of five sets of distances, $(x, \Delta x) = (700 \mu\text{m}, 31 \mu\text{m}), (700 \mu\text{m}, 51 \mu\text{m}), (400 \mu\text{m}, 31 \mu\text{m}), (400 \mu\text{m}, 51 \mu\text{m}), (400 \mu\text{m}, 71 \mu\text{m})$, were used for differential lifetime analysis. The three intensity components of the 266-keV γ ray were measured at each of these plunger distances and Eqn. 2.26 was used to extract the lifetime of the 4^+ state in ^{156}Dy . Although with the differential

mode it is possible to measure the lifetime of a state using a single set of distances, several sets were used to ensure the differential technique was valid across a range of distances. The lifetime of the 4^+ state was measured independently at each distance.

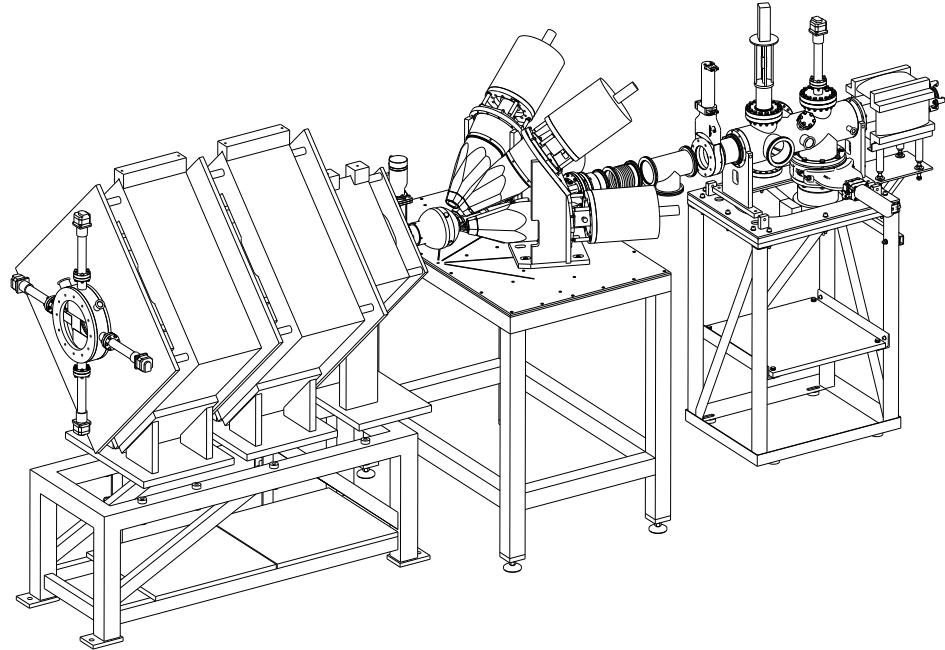


FIGURE 4.2: A drawing of the TPEN vacuum housing surrounded by the 4 backward facing germanium detectors connected to RITU. Various gauges and the ROOTS pump is shown on the right hand side of the image.

Data were collected at each of the five differential distances for approximately 16 hours.

In addition to testing the differential lifetime analysis technique, the updated plunger control software was successfully tested. The constant negative feedback system was tested at a range of beam-currents at a range of foil separations in order to understand the limits of TPEN. The following sections describe the specific experimental setup used for the commissioning experiment.

4.2 K130 cyclotron

The K-130 Cyclotron at the University of Jyväskylä was used in this commissioning experiment to produce the ^{136}Xe beam [92]. The cyclotron was installed in 1993 and produces heavy-ion beams for the JUROGAM-RITU-GREAT beamline. The cyclotron

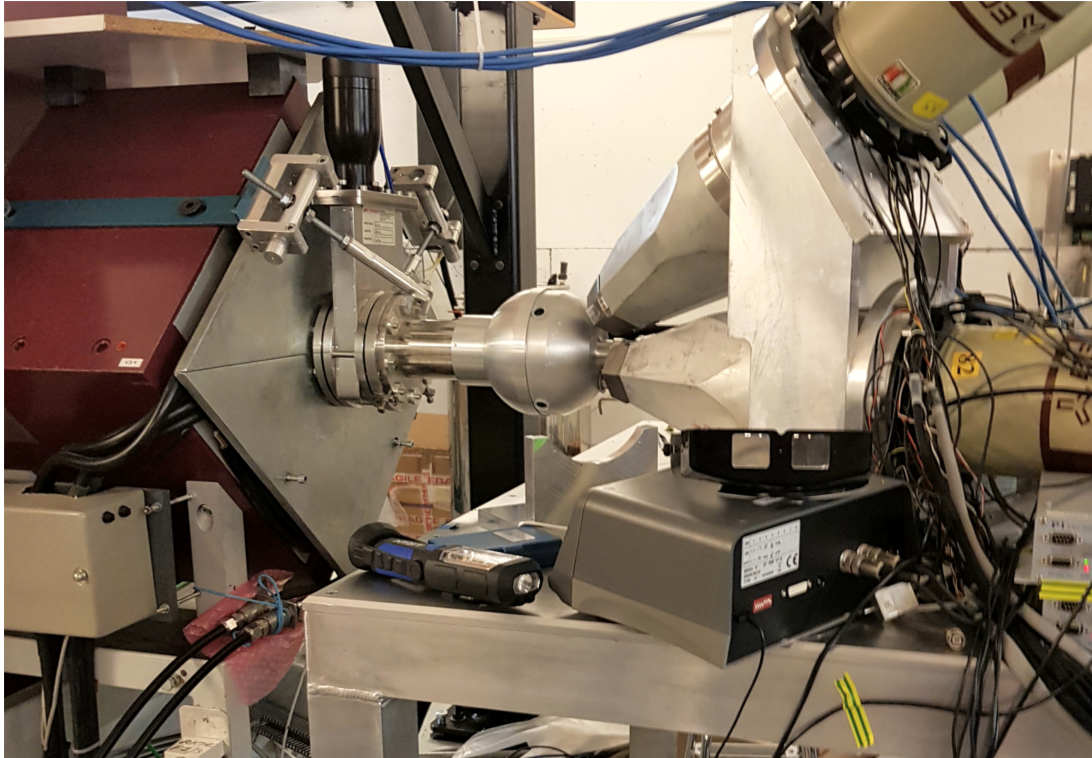


FIGURE 4.3: A photograph of the TPEN vacuum housing surrounded by the 4 backward facing germanium detectors. RITU [83] can also be seen downstream from the central chamber on the left-hand-side of the image.

exploits the constant angular velocity of charged particles in a uniform magnetic field. As charged particles are accelerated, their radius of orbit increases but their angular velocity is constant. Hence, an oscillating voltage with frequency equal to the orbital frequency can be applied to the particles within the cyclotron. Accelerated particles will spiral outwards as their radius increases with velocity. When the charged particles reach the edge of the cyclotron they are ejected as a beam and focused towards the target.

The cyclotron primarily uses Electron Cyclotron Resonance Ion Sources (ECRIS) [93] to produce charged ions. Electrons in a magnetic field will move in a spiral. If an external electromagnetic field is applied, electrons in phase with the field will be accelerated. A plasma of highly charged ions is produced by collisions with these electrons. The charge state of the ions is dependent on the confinement time of the plasma. These highly charged ions are then extracted from the trap and accelerated using a large voltage.

The energies of the ion beam is limited by the bending and focussing limits of the K130

cyclotron ($K_B = 130$ MeV and $K_F = 90$ MeV/A, respectively [94]). These limits impose limits on the maximum energy for the ion beam

$$\frac{T}{A} < K_B \left(\frac{Q}{A} \right)^2, \quad (4.1)$$

and

$$\frac{T}{A} < K_F \left(\frac{Q}{A} \right), \quad (4.2)$$

where T/A is the kinetic energy per nucleon and Q is the charge state of the ion. For heavy beams ($A > 10$), the bending limit is the limiting factor but beams of 5-10 MeV/A are still possible [94].

4.3 Phase 1 HPGe detectors

During the commissioning of TPEN, the JUROGAM II spectrometer [18] was not available for use. Instead, four Compton-suppressed JUROGAM phase-1 HPGe detectors [19] were used to measure prompt γ rays from the target position. These phase 1 detectors are tapered n-type coaxial germanium detectors which are surrounded by bismuth-germanate (BGO) Compton-suppression shields. These BGO shields act as a veto system to eliminate events that escape the HPGe detectors. This significantly reduces the Compton background.

The detectors were placed at a distance of 12.5 cm from the target position at an angle of 157.5° from the beam axis. As the phase-1 germanium detectors are not segmented, a large (~ 3 keV) Doppler broadening was observed for γ rays emitted from moving nuclei, see section 4.3.3 for more details.

4.3.1 Energy calibration

In this work, each of the four HPGe detectors were calibrated using a variety of radioactive sources. This calibration provides a well-defined relationship between the ADC channel number and the γ -ray energy. As events from multiple detectors are combined a good energy calibration is crucial in order to form well-defined peaks. Additionally, the average recoil velocity was measured using the Doppler shift of the

recoils at a given angle. This means any uncertainty in the energy of the components translates to increased uncertainty in the average recoil velocity.

The four HPGe detectors were calibrated using a mixed ^{152}Eu and ^{133}Ba source. Gaussian fits to the peaks were made to extract the centroids. The centroids were compared to the known energies from Ref. [95] and a calibration was made of the form

$$E = a + bX + cX^2 \quad (4.3)$$

for each detector. Here, E is the peak energy, X is the channel number and a, b and c are the calibration coefficients. The measured calibration coefficients are given in Table 4.1.

TABLE 4.1: The measured calibration coefficients between channel number, X and energy, E , for the four HPGe detectors.

HPGe number	a (keV)	b (keV/channel)	c (keV/channel ²)
1	0.1432(5)	0.27166(4)	$4.5(5) \cdot 10^{-8}$
2	1.1061(4)	0.32599(6)	$1.62(6) \cdot 10^{-8}$
3	0.8997(3)	0.44869(6)	$1.59(9) \cdot 10^{-8}$
4	0.2452(8)	0.41572(7)	$-3.8(2) \cdot 10^{-8}$

4.3.2 Efficiency

The relative efficiency of the four germanium array was calculated using standard ^{152}Eu and ^{133}Ba sources. ^{152}Eu and ^{133}Ba sources were placed at the target position and the photopeak intensities of γ rays from these sources were measured. The measured intensities were compared to the known intensities from Refs [95,96]. The ratio of the measured intensity to the known intensity was taken as the relative efficiency. The relative detection efficiency as a function of energy is shown in Fig. 4.4. The data were fitted with the function

$$\eta(E) = \exp[(A + Bx + Cx^2)^{-G} + (D + Ey + Fy^2)^{-G}]^{-\frac{1}{G}}, \quad (4.4)$$

where η is the relative efficiency, E is the energy in keV, $x = \log(E/100)$, $y = \log(E/1000)$ and the coefficients A, B, C, D, E, F and G are free parameters. The

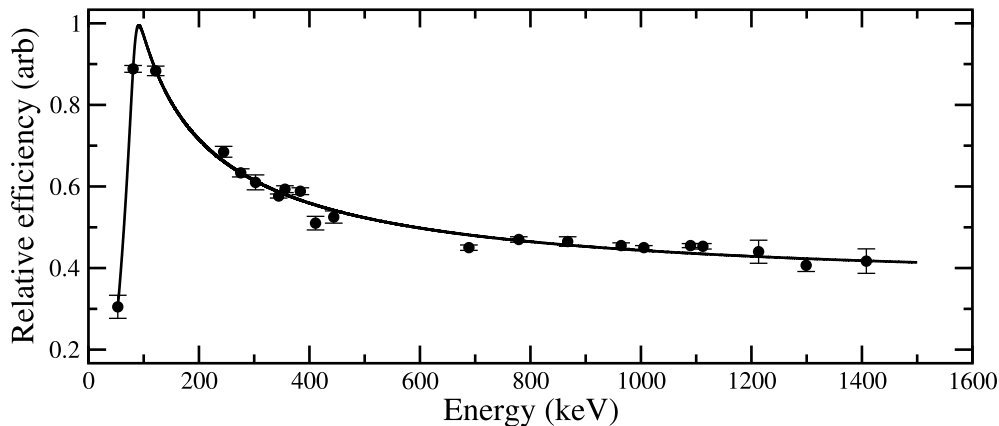


FIGURE 4.4: The relative efficiency of all four HPGe detectors as a function of energy.

coefficients A , B and C describe the efficiency at low energies and the coefficients D , E and F describe the efficiency at high energies. The parameter G describes the turning point between the two regions. The data were fitted using the EFFIT program of the RADWARE software suite [97]. The reduced χ^2 of the fit to the data is 2.8.

4.3.3 Doppler broadening

The total width of an observed γ -ray energy emitted from a recoiling nucleus is affected by both the intrinsic detector resolution and the Doppler broadening. The finite opening angle of a detector with respect to the beam axis means that γ rays are collected at a range of angles, rather than a single detector angle. From Eqn. 2.1 it can be seen that this range of angles allows for a range of Doppler-shifted energies to be measured for a single γ -ray energy emitted from a recoiling nucleus. This has the effect of increasing the width of the detected photopeak.

The amount of broadening introduced from the finite opening angle can be derived by differentiating Eqn. 2.1 with respect to the beam axis angle

$$\Delta E = \frac{E_0 \sqrt{\beta^2 - \beta^4} \sin(\theta) \Delta\theta}{(1 - \beta \cos(\theta))^2} \sim E_0 \beta \sin(\theta) \Delta\theta, \quad (4.5)$$

where all symbols are the same as Eqn. 2.1, $\Delta\theta$ is the opening angle of the detector and ΔE is the amount of Doppler broadening. The effect of Doppler broadening can hence be reduced by reducing the size of the opening angle, which comes at the cost of a smaller detection efficiency.

In this experiment standard detectors with no segmentation were used. The opening angle of the detector was $\sim 8^\circ$. For a recoil velocity of $0.07 c$ this resulted in a Doppler broadening of 2 keV for a 500 keV γ ray, which is comparable to the intrinsic detector resolution. For future experiments with large recoil velocities, it may be necessary to use segmented germanium detectors such as clover detectors. These clover detectors consist of four coaxial germanium diodes that share a cryostat. The segmentation reduces the opening angle of the detector and hence reduces the Doppler broadening.

4.4 Total Data Readout

The Total Data Readout (TDR) [87] is a trigger-less data acquisition system used at JYFL. TDR records every detector signal observed and time stamps it using a 100 MHz clock. These signals can then be correlated into events offline. The system ensures every event is recorded should it be needed. It also significantly reduces dead-time losses, as the only losses are due to the analogue shaping and conversion of each channel.

No tagging was used in this experiment, which simplified the data sorting. No events were recorded from the other JYFL detector systems such as the GREAT spectrometer [87, 98], DSSDs, planar detectors or MWPCs. Signals from the germanium detectors were shaped using shaping amplifiers before passing into Constant Fraction Discriminators (CFD). The output signals from the CFDs were then processed using Amplitude-to-Digital Converters (ADC) and the digital signal was passed to the event builder. In this experiment, no pre-filtering was required but is discussed in Ref. [99].

4.5 GRAIN

The data recorded with the TDR is sorted using the GRAIN software package [88]. GRAIN is a graphical-user-interface which allows for easy sorting of data collected at the University of Jyväskylä. GRAIN has pre-defined functions with all of the information of the JUROGAM array and the RITU separator known. In this experiment, different angles were used to that of the typical JUROGAM detectors so these functions could not be used. Instead, each detector was defined individually and called

upon when required. A sort code, written in Java, was used to decide which events should be included into the final output files. GRAIN takes the sort code and sorts the data into histograms which may be displayed in real time. Once the sort is complete, the histograms can be exported from GRAIN to be used with other software packages such as RADWARE [97].

The remainder of this page was intentionally left blank.

Chapter 5

Analysis and Results

In this work the lifetime of the first 4^+ excited state in ^{156}Dy has been measured to commission the TPEN plunger device. The measured lifetime was compared to the known lifetime from Ref. [20] and was found to be in good agreement. The differential mode of the well established DDCM technique [6] was tested at five independent target-to-degrader and degrader-to-stopper distances, where the lifetime of a state is measured using a single set of distances. The use of a third foil enables TPEN to directly determine both the decay function and the differential of the decay function, allowing a simultaneous collection of statistics at one distance.

This chapter describes the production of multiplicity two and three-fold $\gamma - \gamma$ coincidence matrices and details the conditions used to extract the lifetime of the 4^+ state in ^{156}Dy . The identification of other decay products created in the fusion evaporation reaction with the natural Mg target is also described. The performance of the TPEN plunger and the modified plunger control software is detailed. A comparison between the differential mode of TPEN, and TPEN working as a two-foil plunger is made. The improved efficiency of TPEN compared to a conventional two-foil plunger is estimated. The measured lifetime of 46(2) ps was found to be in good agreement with the literature value of 45.6(5) ps [20], successfully testing both the TPEN plunger and the differential mode of the DDCM framework.

5.1 TPEN performance

5.1.1 Testing the calibration of voltage and distance

Before the commissioning experiment took place, extensive testing of TPEN was conducted. As any uncertainty on the degrader-to-stopper foil directly effects lifetime measurements, the calibration of the voltage and distance was tested. When calibrating the induced voltage between foils, it is assumed that the central degrader foil shields the two outer foils from each other, when the applied voltage is on the central foil. Hence, the voltage induced on the outer foils is only dependent on the distance between itself and the central foil. For example, when calibrating the induced voltage on the target foil, it is assumed that any induced voltage on the degrader foil does not affect the target foil.

In order to confirm that the induced voltage on the target foil is independent of the position of the stopper foil, the target-to-degrader distance was held at a constant distance of 7 μm and the degrader-to-stopper distance was varied from 5 μm to 700 μm . The voltage on the target foil was measured as the stopper foil was placed 5, 10, 20, 40, 60, 80, 100, 150, 200, 300, 500 and 700 μm from the degrader foil. Figure 5.1 shows the voltages measured on the target foil at each of these degrader-to-stopper distances. If the target foil is not effected by the stopper foil then the voltage should be constant. Using a voltage to distance calibration, the distance corresponding to this voltage is also shown. The weighted mean of distance and voltage are shown in a solid black line, with the uncertainty shown in dotted-red line. The reduced χ^2 for the voltage and distance measurements relative to the average voltages are 1.4 and 0.75, respectively. This result is consistent with the outer foils being independent of each other. However, smaller reduced χ^2 values of 0.84 and 0.34 were achieved using a linear fit (dashed-blue line) for the voltage and distance, respectively. Although smaller χ^2 values are achieved using a linear fit, the range in voltage between minimum and maximum distances is comparable to the uncertainty on a typical distance measurement. Using the linear fit to the data in Fig 5.1, the range in distance measurements is $< 0.5 \mu\text{m}$ over a 700 μm range. Using this data, the assumption that the voltage on the two outer foils is independent of the position of the other outer foil holds.

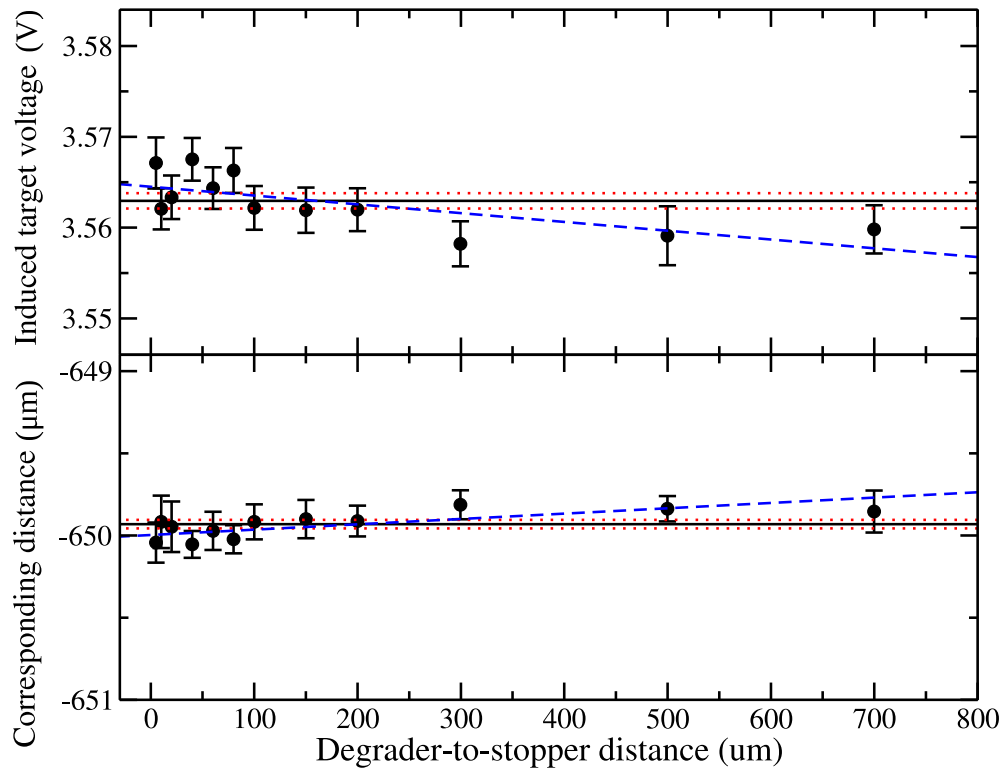


FIGURE 5.1: The induced voltage measured the target foil from the degrader foil, with varying stopper distance (upper panel). The target-to-degrader distance is 7 μm at every degrader-to-stopper distance. A linear fit to the data is shown in blue dashed, with a constant voltage in solid black. The target to degrader distance corresponding to this voltage is also shown, along with the fits (lower panel).

5.1.2 Calibration during commissioning

The distance between the target to degrader foil and degrader to stopper foil was calibrated to the voltage using the calibration VI described in Section 3.9.4. Figure 5.2 shows the induced voltage on the target foil versus micrometer reading from the TPEN commissioning experiment. Figure 5.3 shows the reciprocal of the induced target voltage versus micrometer distance. A semi-empirical fit of the form $ax^n + bx^2 + cx^{-1}$ to the voltage has been made [100]. The x^{-1} term represents the behaviour of the foils at small distances as they are expected to behave like parallel plate capacitors. The x^2 term represents edge effects and corrects for the distance between the foils being comparable to the separation. The x^n term is left as a free parameter when fitting and represents higher-order corrections such as the effect of nearby wires. The fit of the reciprocal of the voltage versus distance has been extrapolated to 0 μm in order to determine the absolute distance between the foils when they are in electrical

contact. The absolute target-to-degrader distance was extrapolated to be $90(20) \mu\text{m}$. The parameters a, n, b and c were found to be $0.044(5) \text{ V}/\mu\text{m}^n$, $0.34(4)$, $1.04(10) \times 10^{-8} \text{ V}/\mu\text{m}^2$ and $-0.385 \text{ V}\mu\text{m}$, respectively. The reduced χ^2 for the fit was 0.8.

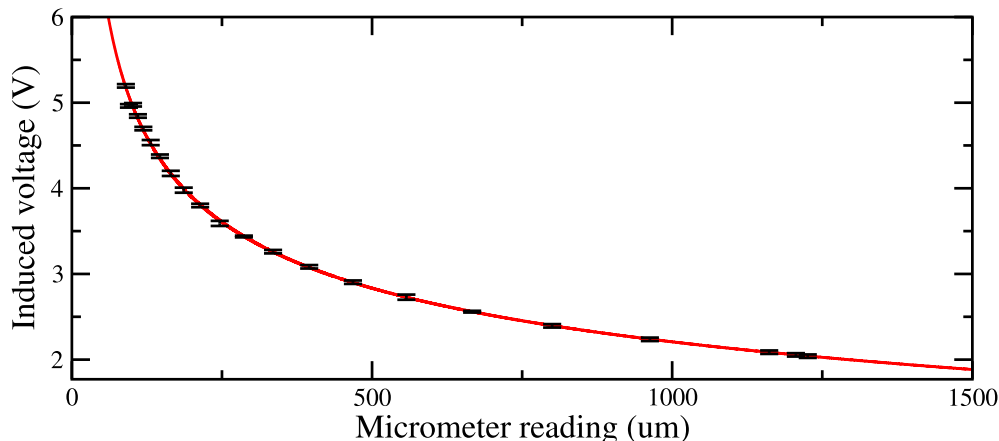


FIGURE 5.2: Calibration curve of voltage versus micrometer reading for the induced voltage on the target foil. A fit to the data is shown with a red black line. The micrometer reading has been offset such that the reading corresponds to the absolute distance between foils.

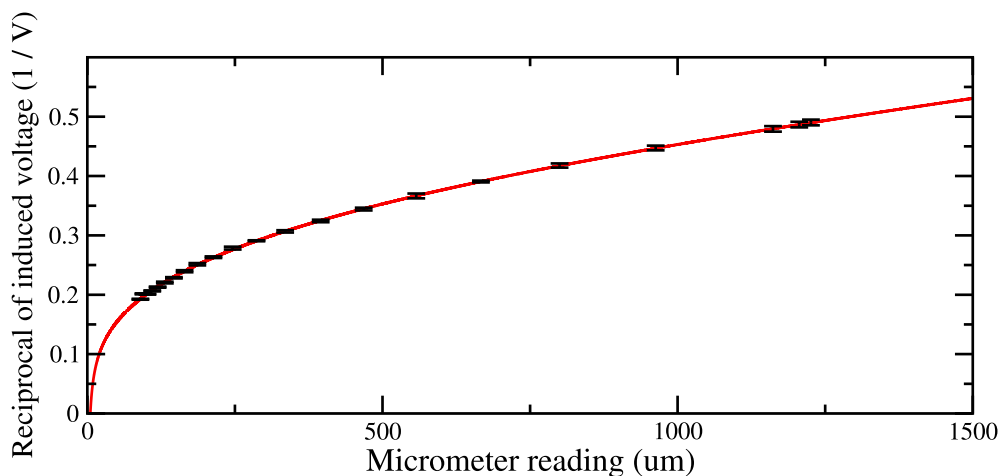


FIGURE 5.3: Calibration curve of the reciprocal of voltage versus micrometer reading for the induced voltage on the target foil. A fit to the data is shown with a solid red line. The micrometer reading has been offset such that the reading corresponds to the absolute distance between foils.

Figure 5.4 shows the induced voltage on the target foil versus micrometer reading from the TPEN commissioning experiment. Figure 5.5 shows the reciprocal of the induced target voltage versus micrometer distance. Using the same extrapolation technique as the target foil, the absolute degrader-to-stopper distance was extrapolated to be $8(1) \mu\text{m}$. The parameters a, n, b and c were found to be $0.0895(50) \text{ V}/\mu\text{m}^n$, $0.33(2)$,

$-7.84(50) \times 10^{-8} \text{ V}/\mu\text{m}^2$ and $-0.242(10) \text{ V}\mu\text{m}$, respectively. The reduced χ^2 for the fit was 1.62.

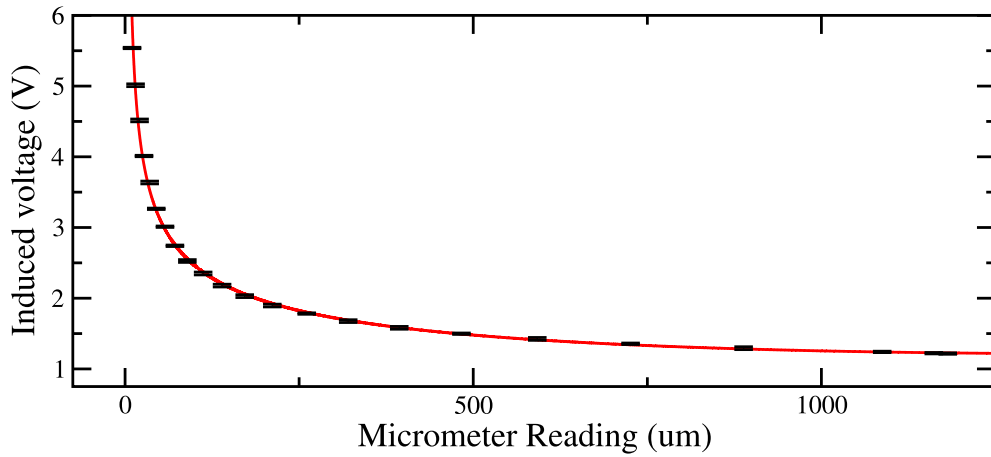


FIGURE 5.4: Calibration curve of voltage versus micrometer reading for the induced voltage on the stopper foil. A fit to the data is shown with a solid red line. The micrometer reading has been offset such that the reading corresponds to the absolute distance between foils.

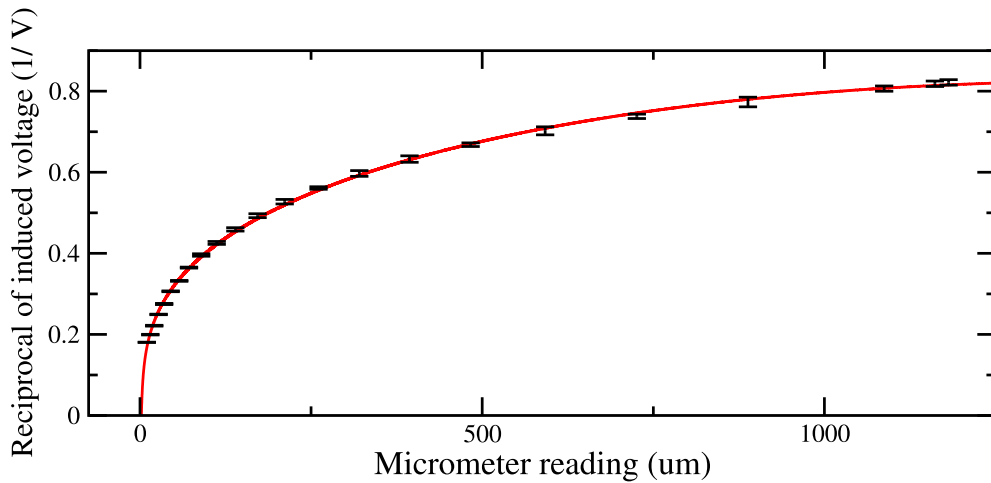


FIGURE 5.5: Calibration curve of the reciprocal of voltage versus micrometer reading for the induced voltage on the stopper foil. A fit to the data is shown with a solid red line. The micrometer reading has been offset such that the reading corresponds to the absolute distance between foils.

5.1.3 Constant feedback system

The constant negative feedback system is a vital part of TPEN's operation and is discussed in Section 3.9.5. Without an effective feedback system, foil distances drift as the foils expand from heating by the beam. This, in turn, changes the flight time between foils for recoiling nuclei and can lead to large uncertainties in measured lifetimes. The

feedback system is especially important for short nuclear lifetimes. For example, in the measurement of the 45.6 ps 4^+ state in ^{156}Dy in this work, a drift of only 15 μm in the degrader-to-stopper distance would lead to a lifetime uncertainty of up to 20 ps. Hence, prior to the commissioning experiment, the constant negative feedback system was thoroughly tested at The University of Manchester.

As it was not possible to test the feedback system at Manchester with beam on target until the commissioning run, the effects of the beam were simulated in the lab. For example, the output voltage from the PB-5 pulse generator was quickly increased to simulate the foils being too close. The feedback system acted accordingly to move the foils apart. A heat gun was also used to heat the target foil, resulting in a small expansion of the foil. This was seen in the induced voltage and the feedback system corrected for the decreased distance.

The commissioning experiment at JYFL was the first time the system could be tested with a beam. Hence, the constant negative feedback system was extensively tested throughout the commissioning experiment. A variety of target-to-degrader and degrader-to-stopper distances and a range of beam currents were used. Figure 5.6 shows the measured target voltage and the corresponding target-to-degrader distance throughout the $x = 700 \mu\text{m}$ $\Delta x = 31 \mu\text{m}$ run. A requested beam current of 1.25 pA was used throughout this run. The induced voltage is shown in intervals of 3 s. For the first 2 hours of the run the constant feedback system for the target foil was disabled to observe the effects of heating on the foil. During this time the target-to-degrader distance drifted from 700 μm to 725 μm , implying the foil deformed by approximately 25 μm . At 2 hours, the feedback system was turned on and the software quickly restored the distance to the desired 700 μm . Each time the distance moved outside of the 4 μm tolerance range, the system acted to bring the distance back to 700 μm , demonstrating the feedback system effective for the target-to-degrader distance. The average target-to-degrader distance for the entire run was measured to be 704(4) μm .

Figure 5.7 shows the measured induced stopper voltage and the corresponding degrader-to-stopper distance throughout the $x = 700 \mu\text{m}$ $\Delta x = 31 \mu\text{m}$ run at intervals of 3 s and Fig. 5.8 shows a zoomed in portion of Fig. 5.7, focussing on the 30 minutes to 90 minutes. The feedback system was turned on for the entire run. As the size of the deformations of the foil is of the same order as the size of the foil separation, the

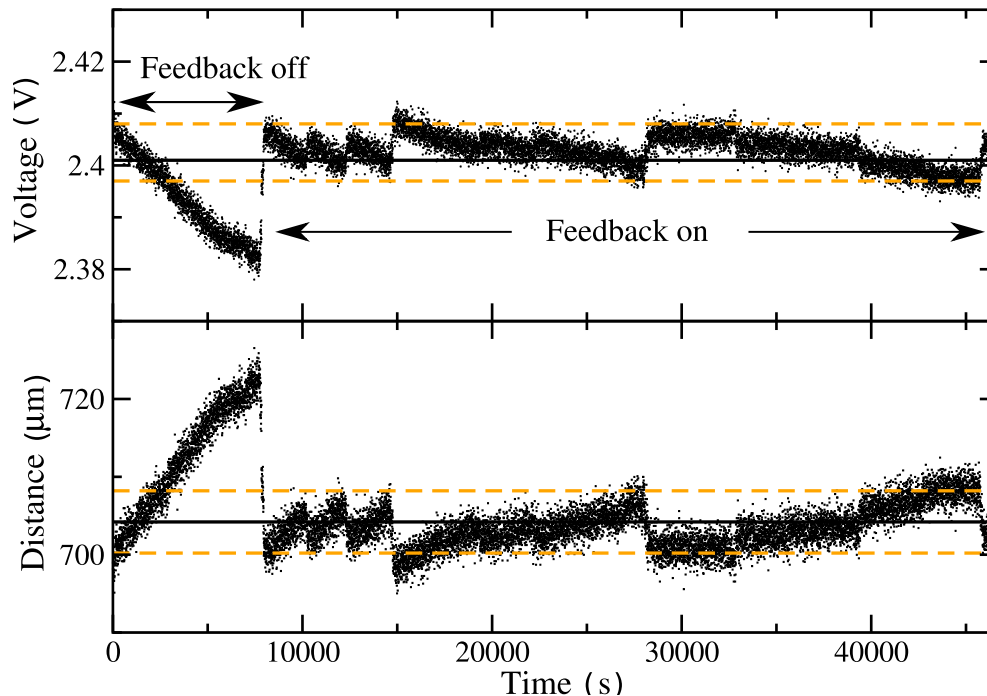


FIGURE 5.6: The measured induced target voltage and corresponding distance measured throughout the $x = 700 \mu\text{m}$ $\Delta x = 31 \mu\text{m}$ plunger distance. The average voltage and distance are shown with a black solid line, along with the tolerances in dashed-orange. Each data point for voltage has an uncertainty of $\sim 0.001\text{V}$ corresponding to $\sim 1 \mu\text{m}$ in distance. These uncertainties are omitted from the figure for clarity.

feedback system is essential for maintaining a constant distance. As seen in Fig. 5.7 the degrader-to-stopper distance often moves outside the tolerated range of $1.5 \mu\text{m}$ and is quickly brought back within the tolerance. The average measured degrader-to-stopper distance for the entire run was measured to be $31.2(2) \mu\text{m}$, demonstrating the feedback system works for small foil separations. The standard deviation of the distance was measured to be $3 \mu\text{m}$. This large relative standard deviation, and the large fluctuations in distance for this $30 \mu\text{m}$ degrader-to-stopper distance, implies that foil separations of less than $30 \mu\text{m}$ may lead to results with large uncertainties on distance. Additionally, contact between the foils occurred several times per hour when distances of less than $30 \mu\text{m}$ were used.

The constant negative feedback system employed with TPEN was successful for every plunger run. TPEN was least stable with foil separations of less than $40 \mu\text{m}$ with these foils, e.g. Fig. 5.8. At these distances, beam currents of less than 1.5pA were required. If the beam current increased above this, the system would become unstable and the foils would occasionally touch. This could be due to the heavy beam used in

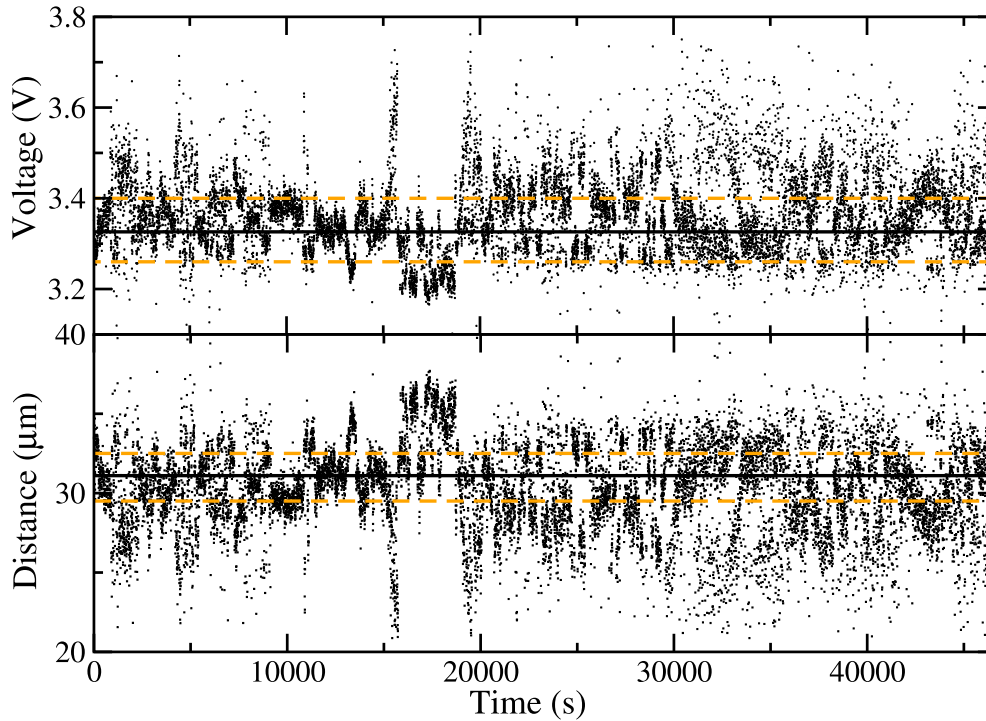


FIGURE 5.7: The measured induced stopper voltage and corresponding distance measured throughout the $x = 700 \mu\text{m}$ $\Delta x = 31 \mu\text{m}$ plunger distance. The average voltage and distance are shown with a black solid line, along with the tolerances in dashed-orange. Each data point for voltage has an uncertainty of $\sim 0.05 \text{ V}$ corresponding to $\sim 1 \mu\text{m}$ in distance. These uncertainties are omitted from the figure for clarity.

this experiment. If a lighter beam is used, less energy will be deposited in the stopper foil and less heating will occur. Additionally, if thinner, better stretched foils are used then less heating will occur.

TPEN performed well with larger separations. For comparison, Fig. 5.9 shows the measured induced stopper voltage and the corresponding degrader-to-stopper distance throughout the $x = 700 \mu\text{m}$ $\Delta x = 51 \mu\text{m}$ run. In this run the beam current was varied from 1.5 to 2 pA. The system was still stable at 2 pA. The target-to-degrader foil separation was more stable than the run with $\Delta x = 31 \mu\text{m}$. The average distance was measured to be $50.1(1) \mu\text{m}$ with a standard deviation of $3 \mu\text{m}$. The uncertainty on the average distance is the standard error. All target-to-degrader charts are comparable to Fig 5.6 and have been omitted for conciseness. The measured average target-to-degrader and degrader-to-stopper distances for all runs are given in Table. 5.1.

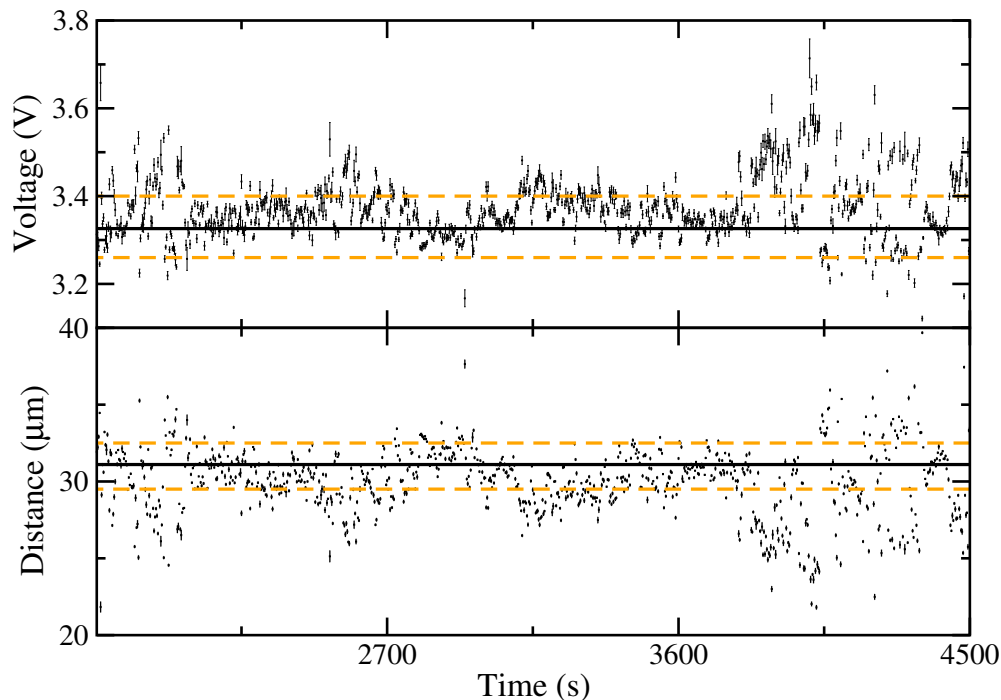


FIGURE 5.8: The measured induced stopper voltage and corresponding distance measured throughout 30 minutes of the $x = 700 \mu\text{m}$ $\Delta x = 31 \mu\text{m}$ plunger distance. The average voltage and distance are shown with a black solid line, along with the tolerances in dashed-orange.

TABLE 5.1: The requested target-to-degrader distance, x , and degrader-to-stopper distances, Δx and the actual measured distances. The distances given are relative to the electrical contact point between the foils. The quoted uncertainties on measured distance are the standard errors.

Requested $x(\mu\text{m})$	Requested $\Delta x(\mu\text{m})$	Measured $x(\mu\text{m})$	Standard dev in $x(\mu\text{m})$	Measured $\Delta x(\mu\text{m})$	Standard dev in $\Delta x(\mu\text{m})$
700	31	704(4)	15	31.2(2)	3
700	51	702(5)	4	50.1(1)	3
400	31	399(1)	21	30.9(1)	3
400	51	399(1)	1	49.9(1)	2
400	71	398(1)	1	73.8(1)	1

5.2 Lifetime results

5.2.1 Reaction products

The desired fusion-evaporation channel for this commissioning experiment was the $^{136}\text{Xe}(^{24}\text{Mg}, 4n)$ reaction. However, due to the prohibitive cost of a highly enriched ^{24}Mg , a natural magnesium foil was used. Natural Mg consists of 79% ^{24}Mg , 10% ^{25}Mg

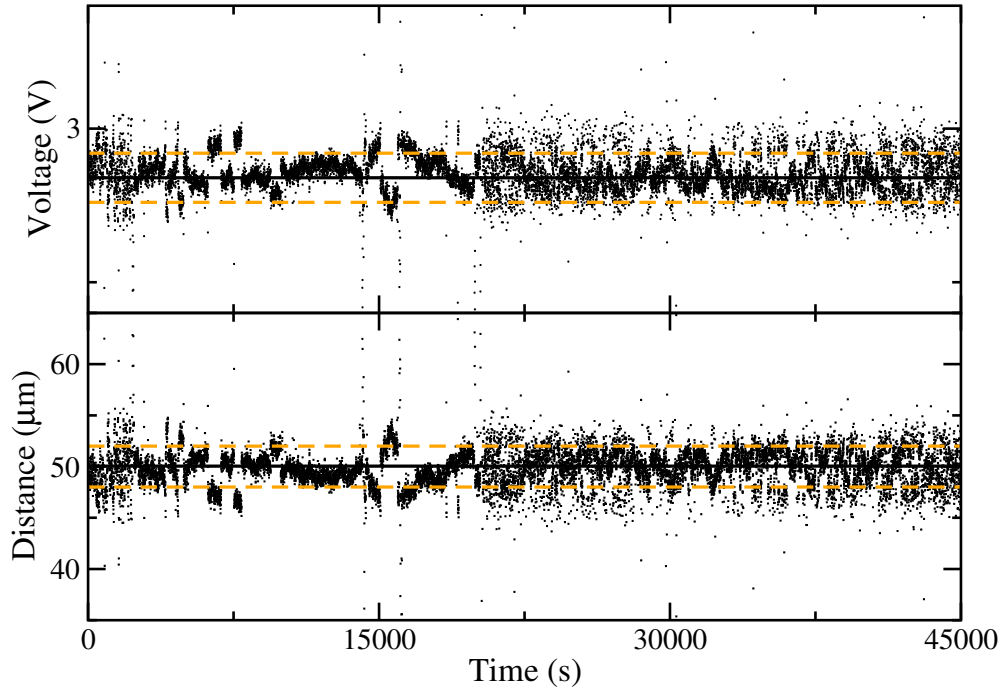


FIGURE 5.9: The measured induced stopper voltage and corresponding distance measured throughout the $x = 700 \mu\text{m}$ $\Delta x = 51 \mu\text{m}$ plunger distance. The average voltage and distance are shown with a black solid line, along with the tolerances in dashed-orange.

and 11% ^{26}Mg [101]. Hence, several different beam-target reactions were possible and contaminants were expected with a total cross section of $\sim 30 \text{ mb}$ [102, 103]. Table 5.2 gives the expected cross sections for different channels for the $^{\text{nat}}\text{Mg}-^{136}\text{Xe}$ target-beam combinations, along with the measured relative intensities from this experiment.

TABLE 5.2: The main reaction channels from the $^{\text{nat}}\text{Mg}+^{136}\text{Xe}$ reaction at 590 MeV. Estimated cross sections are from PACE4 [102, 103]. γ rays from ^{156}Tb , ^{157}Tb , ^{158}Tb , ^{153}Gd , ^{154}Gd or ^{155}Gd were not observed.

Exit Channel	Estimated cross section (mb)	Measured relative intensity
^{156}Dy	130	100(5)
^{157}Dy	40	25(3)
^{155}Dy	30	26(3)
^{158}Dy	30	22(3)
^{156}Tb	4	<2
^{157}Tb	1	<2
^{158}Tb	0.5	<2
^{153}Gd	3	<2
^{154}Gd	1	<2
^{155}Gd	0.75	<2

The main channels produced in the fusion evaporation reaction were identified using a prompt $\gamma - \gamma$ matrix for all 4 germanium detectors. The matrix was created in GRAIN [88] and included all events from all detectors whenever more than one γ ray was detected within a 10 ns window. A total of 7×10^7 $\gamma - \gamma$ events were collected in total. By applying gates on γ -ray energies and observing transitions in coincidence with specific γ -ray energies, it was possible to identify several reaction products. These reaction products are given in Table 5.2 and are highlighted in Fig. 5.10(a). Several of the expected exit channels, from PACE4, were not observed in the prompt $\gamma - \gamma$ matrix due to their small production cross sections relative to the main channels.

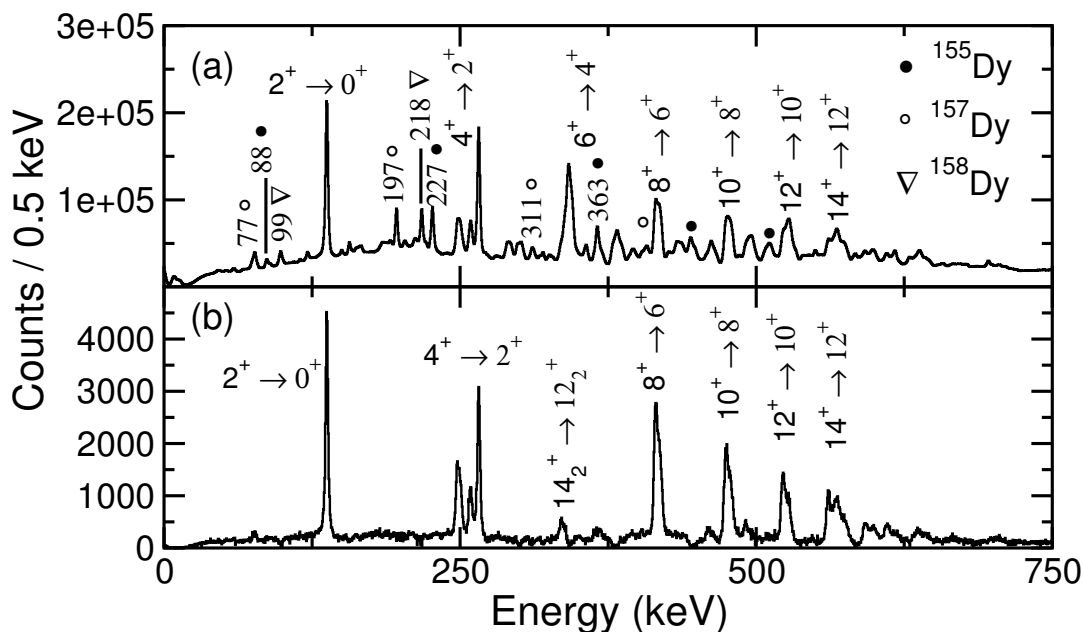


FIGURE 5.10: (a) Spectrum showing the total projection of a 2D $\gamma - \gamma$ coincidence matrix for any detector versus any detector, for all distances combined. The γ rays from transitions in ^{156}Dy are labelled with their initial and final states and the main contaminants are labelled with symbols. (b) Spectrum showing γ rays in coincidence with the fully shifted and degraded components of the $6^+ \rightarrow 4^+$ in ^{156}Dy , for all distances combined.

5.2.2 Differential lifetime measurements

The aim of the commissioning experiment was to test TPEN in the differential lifetime mode, where a direct measurement of the derivative of the decay curve is made. This makes a lifetime measurement using a single set of foil separations possible [9]. In the commissioning experiment, the differential lifetime mode was tested independently at

five sets of foil separations. The lifetime of the 4^+ state was calculated at each of these separations using only the information from that individual distance.

Two dimensional $\gamma-\gamma$ matrices were produced for each of the plunger distance settings collected in the experiment. Figure. 5.11 shows the matrix produced for the $x = 700, \Delta x = 31 \mu\text{m}$ distance. In order to analyse the lifetime of the 4^+ state in ^{156}Dy , a gate was placed on fully shifted and degraded components of the 366 keV 6^+ to 4^+ transition in each of these $\gamma-\gamma$ matrices. Figures 5.12 and 5.13 show the resultant gated spectra zoomed in on the 4^+ to 2^+ transition for each distance setting, on linear and logarithmic scales, respectively. Gaussian fits to the fully shifted (green), degraded

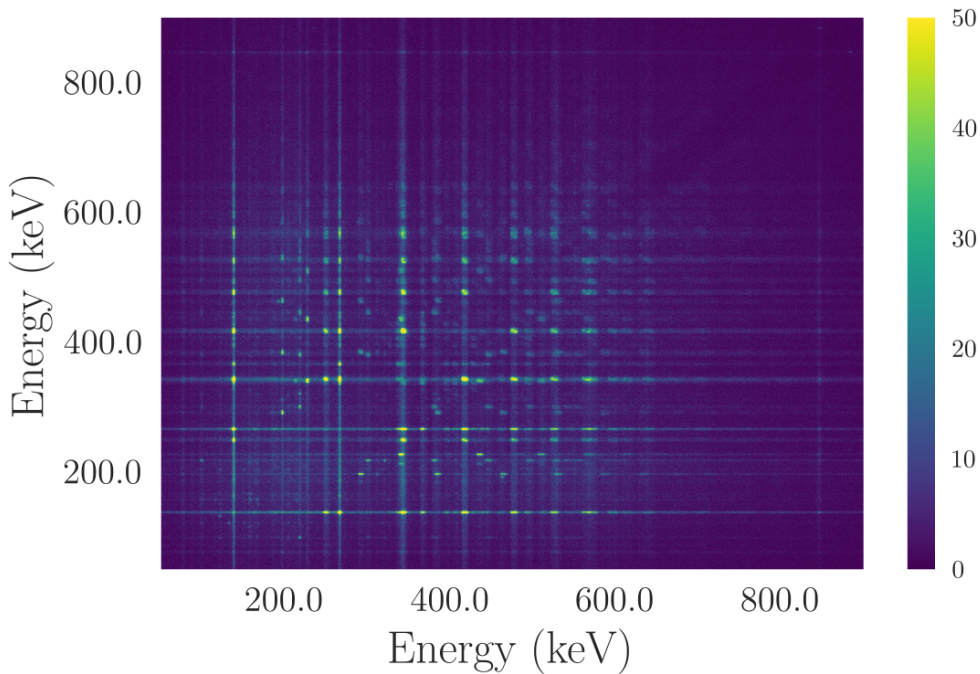


FIGURE 5.11: γ ray coincidence energies for any detector versus any other detector at the $x = 700 \mu\text{m}$ $\Delta x = 31 \mu\text{m}$ plunger distance. Histogram bin widths of 0.5 keV have been used. The number of counts are shown using the viridis colormap. Only energies up to 1000 keV are shown for clarity.

(orange) and stopped (red) intensity components of the 266-keV γ ray transition were made in order to extract the component intensities. These fits were made using the gf3 program from the RADWARE [97] software suite. The centroids, of the three intensity components were left as free parameters in the Gaussian fits. The widths of the peaks were also left free under the condition that the FWHM did not exceed 10 keV. The background under the peaks was fixed to be flat with the height as a free parameter.

The parameters were left free to represent an unknown lifetime measurement where it would not be possible to fix the widths and centroids of the components. Table 5.3 shows the measured intensities of each of the components at the five plunger distances. Table 5.4 gives the measured widths and centroids of the three components at each distance.

The measured centroids of the three intensity components, along with the known angle of the germanium detectors, were used to calculate the average full and degraded recoil velocities. The average full recoil velocity was measured to be $0.0699(9) c$ and the average degraded recoil velocity was measured to be $0.0286(6) c$. The measured centroids of the fully shifted and degraded components from all distances combined were used to calculate these velocities with Eqn. 2.1.

The measured intensities of the three components of the 266-keV transition were used to calculate the lifetime of the 4^+ state in ^{156}Dy using Eqn. 2.26, at each of the five plunger distances independently. The calculated lifetimes and the associated uncertainties are given in Table. 5.3. The lifetimes at each independent distance measurement are fully in agreement with the literature value of $45.6(5)$ ps [20]. A weighted average of $46(2)$ ps was calculated from the five independent distances, demonstrating that TPEN is capable of making direct measurements of the derivative of the decay curve, and therefore capable of measuring lifetimes using a single set of plunger distances.

TABLE 5.3: The target-to-degrader, x , and degrader-to-stopper distances, Δx used during the commissioning experiment. The distances given are relative to the electrical contact point between the foils. The intensities of the unshifted (I^{us}), degraded (I^d) and fully shifted (I^{fs}) components of the 266-keV transition are given for different x and Δx combinations, along with the lifetimes, τ .

$x(\mu\text{m})$	$\Delta x(\mu\text{m})$	I^{us}	I^d	I^{fs}	$\tau(\text{ps})$
700	31	1337(40)	140(20)	1149(40)	44(5)
700	51	1824(47)	275(27)	1827(49)	47(4)
400	31	786(30)	82(13)	395(23)	44(6)
400	51	1460(41)	222(22)	781(33)	47(4)
400	71	1048(34)	209(18)	520(26)	49(4)

As the lifetime is calculated independently at each plunger distance, no normalisation of the measured γ -ray intensities across distances was required. This removes a large

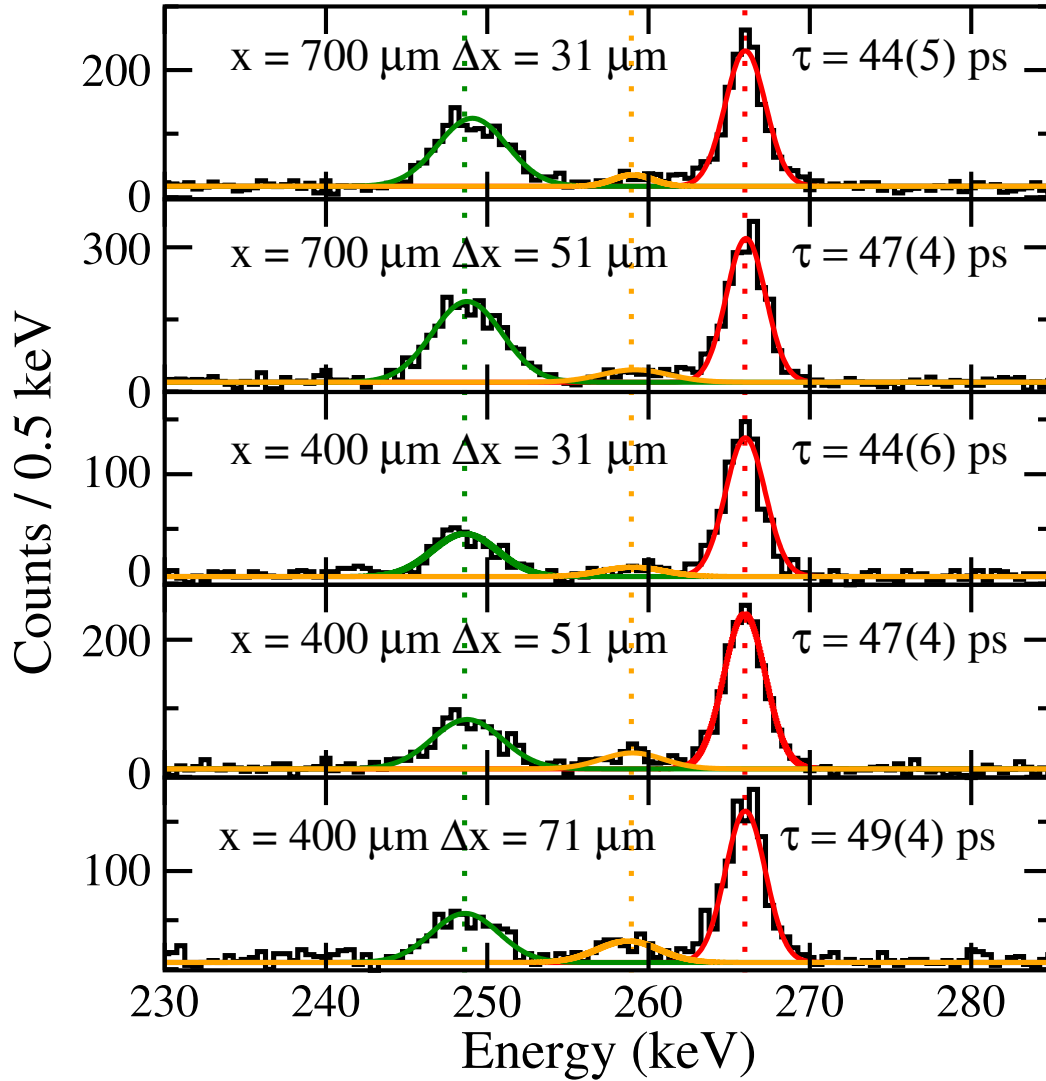


FIGURE 5.12: The background subtracted spectra showing the three intensity components of the 266-keV transition in ^{156}Dy , in coincidence with the moving components of the 366-keV transitions. Gaussian fits to the fully shifted (green-dashed), degraded (orange-solid) and stopped (red-dotted) components are also shown.

source of uncertainty associated with conventional two-foil plungers, where several distances (~ 10) are required to define the shape of the decay curve, a normalisation to the measured γ -ray intensities is required. The normalisation accounts for the different amount of beam-time and fluctuations in beam-current across different plunger distances.

When using TPEN, inverse kinematics are favorable to produce large recoil velocities. These large recoil velocities result in large Doppler shifts in the measured γ -ray energies which separate the three components of a transition. Since the velocity of the

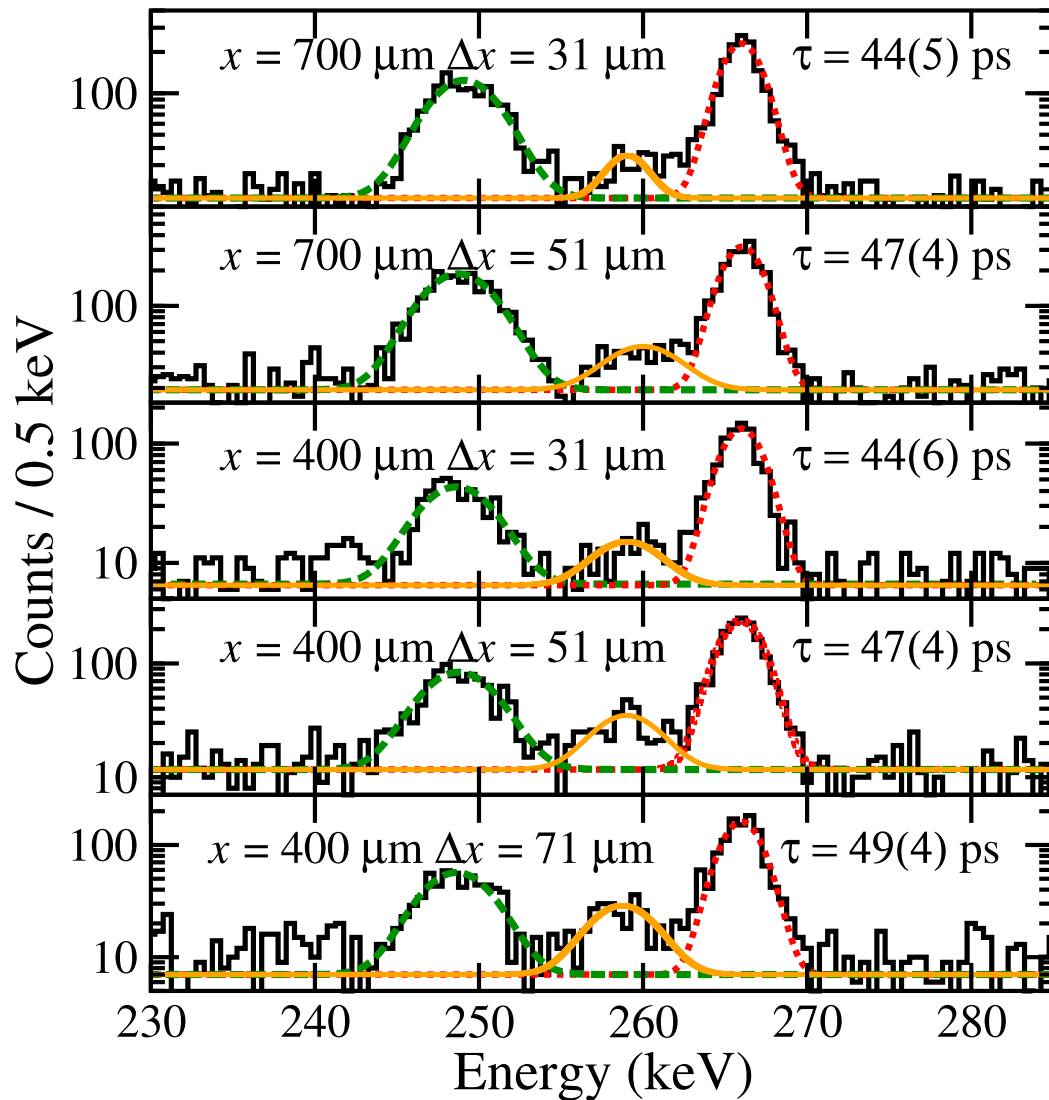


FIGURE 5.13: The background subtracted spectra showing the three intensity components of the 266-keV transition in ^{156}Dy , in coincidence with the moving components of the 366-keV transitions. The y-axes have been plotted on a logarithmic scale to emphasize the degraded component. Gaussian fits to the fully shifted (green-dashed), degraded (orange-solid) and stopped (red-dotted) components are also shown.

recoiling nucleus is large, relativistic corrections must be made to the measured γ -ray intensities. γ rays emitted in flight experience a forward focusing effect which is described in Section 2.1.4.2. In this experiment, the forward focusing effect accounted for a decreased detector efficiency for the degraded and fully shifted components. This decrease in efficiency was calculated to be 5 % and 12 %, for the degraded and fully shifted components, respectively. The measured average recoil velocities were used to calculate this decrease.

TABLE 5.4: Measured widths (FWHM) and centroids (C) of the fully shifted, degraded and stopped components the 266-keV γ ray at each distance. All widths and centroids are in keV.

x (μm)	Δx (μm)	$FWHM$ (us)	C (us)	$FWHM$ (d)	C (d)	$FWHM$ (fs)	C (fs)
700	31	2.95(5)	266.0(1)	4.2(1)	259.0(3)	5.05(15)	249.1(1)
700	51	2.9(1)	266.0(1)	5.0(2)	260.0(1)	5.05(2)	248.9(1)
400	31	2.9(1)	266.0(1)	4.6(1)	259.0(3)	4.75(1)	248.6(1)
400	51	3.05(5)	266.0(1)	4.5(2)	259.2(1)	5.1(2)	248.8(1)
400	71	3.2(1)	266.0(1)	4.5(2)	258.9(1)	4.9(2)	248.7(1)

Reference [9] gives the derivation of Eqn. 2.26 and shows that it only holds in the condition that Δt is small compared to τ . A correction factor $C(\tau, \Delta t)$, discussed in Ref. [78], is used to account for any difference between the measured quantity I^{us} and $\frac{d}{dt}R(t)$ and is given by

$$C(\tau, \Delta t) = \frac{\exp(\Delta t/\tau) - 1}{\Delta t/\tau}. \quad (5.1)$$

In this work, this correction factor has been applied iteratively to the lifetime calculated from Eqn. 2.18 and accounted for a $\sim 3\%$ change. If Δt becomes significant compared to the lifetime of the state, then this factor becomes large. It should be noted that the correction is only valid if the decay of the state follows a simple exponential decay.

5.2.3 TPEN with low statistics

In order to understand the performance of TPEN in the limit of low statistics, a subset of higher-fold, multiplicity 3 events were used to perform a lifetime analysis similar to the one described above. At a plunger distance of $x = 700 \mu\text{m}$, $\Delta x = 51 \mu\text{m}$, a 2D $\gamma - \gamma$ matrix was produced which only included events with multiplicity 3 or higher.

A coincidence gate was set on the fully shifted and degraded components of the 366-keV, 6^+ to 4^+ , transition in ^{156}Dy . Figure 5.14 shows the γ rays in coincidence with the 4^+ to 2^+ transition. Figure 5.15 shows a zoomed in spectrum with two histogram channel widths (a) 1 keV per channel and (b) 2 keV per channel. Both histogram channel widths are shown to highlight the degraded component.

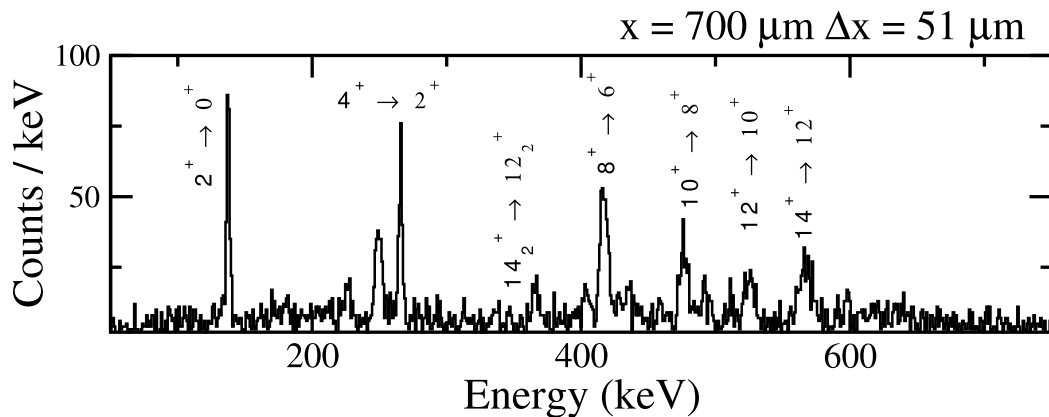


FIGURE 5.14: The background subtracted spectra showing multiplicity three or four events γ -ray events for a plunger distance of $x = 700 \mu\text{m}$, $\Delta x = 51 \mu\text{m}$.

Gaussian fits to the fully shifted (green-dashed), degraded (orange-solid) and stopped (red-dotted) intensity components of the 266-keV γ -ray transition are shown. These fits were used to extract the component intensities. The number of counts recorded in the fully shifted, degraded and stopped components of the 266-keV γ ray, were 210(20), 28(9) and 200(16), respectively. Using Eqn. 2.26 and the component intensities, the lifetime of the 4^+ state in ^{156}Dy was found to be 50(15) ps, which is in good agreement with the literature value [20]. This low-statistics analysis demonstrates that TPEN can be used in differential mode for lifetime measurements in nuclei with small production cross sections. Furthermore, this analysis shows that TPEN is capable of extracting nuclear state lifetimes using ~ 400 total γ -events.

This low statistics analysis also highlights the importance of using clean spectra. The three-fold matrix produced was significantly cleaner than the multiplicity 2 matrix, enabling much larger coincidence gates to be used. However, all runs other than the $x = 700 \mu\text{m}$, $\Delta x = 51 \mu\text{m}$ run had insufficient statistics to make a lifetime measurement with three-fold events.

If the statistics are collected in a region with a small overall background, then the uncertainty on the extracted intensities is dominated by the Poisson uncertainty. If the spectra are contaminated, then the overall uncertainty will increase. As tagging techniques are expected to be used with TPEN, Fig 5.15 is a good representation of the minimum quality of data expected in an experiment.

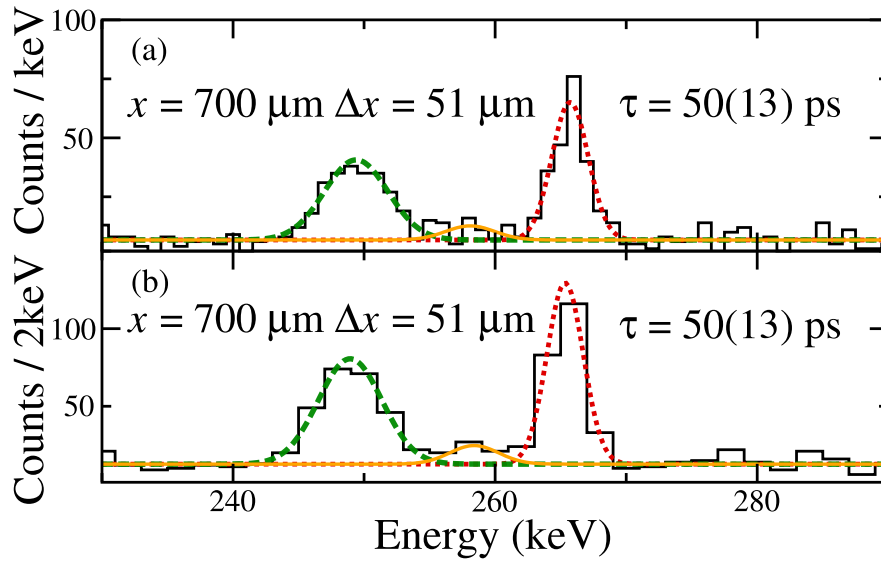


FIGURE 5.15: The background subtracted spectra showing the three intensity components of the 266-keV transition in ^{156}Dy , in coincidence with the moving components of the 366-keV transitions for multiplicity three or four events for a plunger distance of $x = 700 \mu\text{m}$, $\Delta x = 51 \mu\text{m}$. The data has been plotted using histogram bin widths of 1 keV and 2 keV. Gaussian fits to the fully shifted (green-dashed), degraded (orange-solid) and stopped (red-dotted) components are also shown.

5.2.4 TPEN working as a standard plunger

One of the aims of the commissioning experiment was to estimate the improvement in the required beam-time of the differential mode of TPEN compared to a conventional two-foil plunger. To make this comparison, the lifetime of the 4^+ state in ^{156}Dy was measured using TPEN acting as a standard plunger. To perform this standard DDCM analysis with TPEN, the intensities of the different components of the 266-keV γ rays were measured at 10 distances. Events were split into two regions: those decaying before the first degrader foil and those decaying after the first degrader foil. Hence, in this analysis the degraded and stopped components of the 266-keV transition were combined to form the decay curve and only the target-to-degrader distance was important. This allowed data from the differential measurements to be used, in addition to data collected specifically for this test.

The intensities of γ -ray decays before and after the first degrader foil were measured in coincidence with the fully shifted component of the 366-keV transition at target-to-degrader distances of 48 μm , 76 μm , 109 μm , 140 μm , 195 μm , 257 μm , 300 μm , 400 μm , 500 μm and 700 μm . These background subtracted spectra are shown in

Fig. 5.16. Gaussian fits to the data were made in order to extract the component intensities. Fits to the fully shifted components are shown with a red-dotted line. The width of the fully shifted component was fixed to be 5.3 keV, measured from summing the data from all distances. Similarly, the centroid of the fully shifted component was fixed to be 249.0(1) keV. Fits to the degraded and stopped components, which were combined to form the decay curve, are shown with a blue-solid line. The widths were fixed to be 5.0(1) keV and 2.9(1) keV for the degraded and stopped components, respectively. The centroids were fixed to be 259.0(1) keV and 266.1(1) keV, respectively. The measured intensities were normalised to the total number of counts in the gated projection at each distance. This normalisation corrects for the different number of beam-particles hitting the target foil between runs.

The degraded and stopped components of the 266-keV transition were combined to form the decay curve, i.e. the intensity of decays after the first degrader foil. Combining the stopped and degraded components effectively uses TPEN as a standard two-foil plunger; the decay curve is measured at various distances and the differential of the decay curve is inferred from the shape of the decay curve, see Section 2.1.2 for more details.

Figure 5.17(a) shows the lifetime of the 4^+ state in ^{156}Dy calculated using the standard DDCM analysis and the NAPATAU computer program. The normalised intensities of the fully shifted components of the 266-keV transition in coincidence with the fully shifted component of the 366-keV transition is shown as a function of distance in Fig. 5.17(b). The combined normalised intensities of the degraded and stopped components the 266-keV transition in coincidence with the fully shifted component of the 366-keV transition, as a function of distance are also shown in Fig. 5.17(c). A piecewise second order polynomial is fitted to the fully shifted component (red-dashed), the uncertainty on this fit is shown in red-shaded. The derivative of this second-order polynomial, multiplied by the lifetime of the state, is fitted to the intensity of decays after the degrader foil (blue-solid), with the uncertainty in blue-shaded, shown in 5.17(c). The normalised intensities of the decays before and after the degrader foil are given in Table. 5.5. The lifetime of the state is calculated at each of the 10 target-to-degrader distances using simultaneous fits defined by the data, see Section 2.1.2.1. These lifetimes are shown in Fig. 5.17(a) along with the uncertainty on the average lifetime, taking into account the uncertainty on the fit to the data.

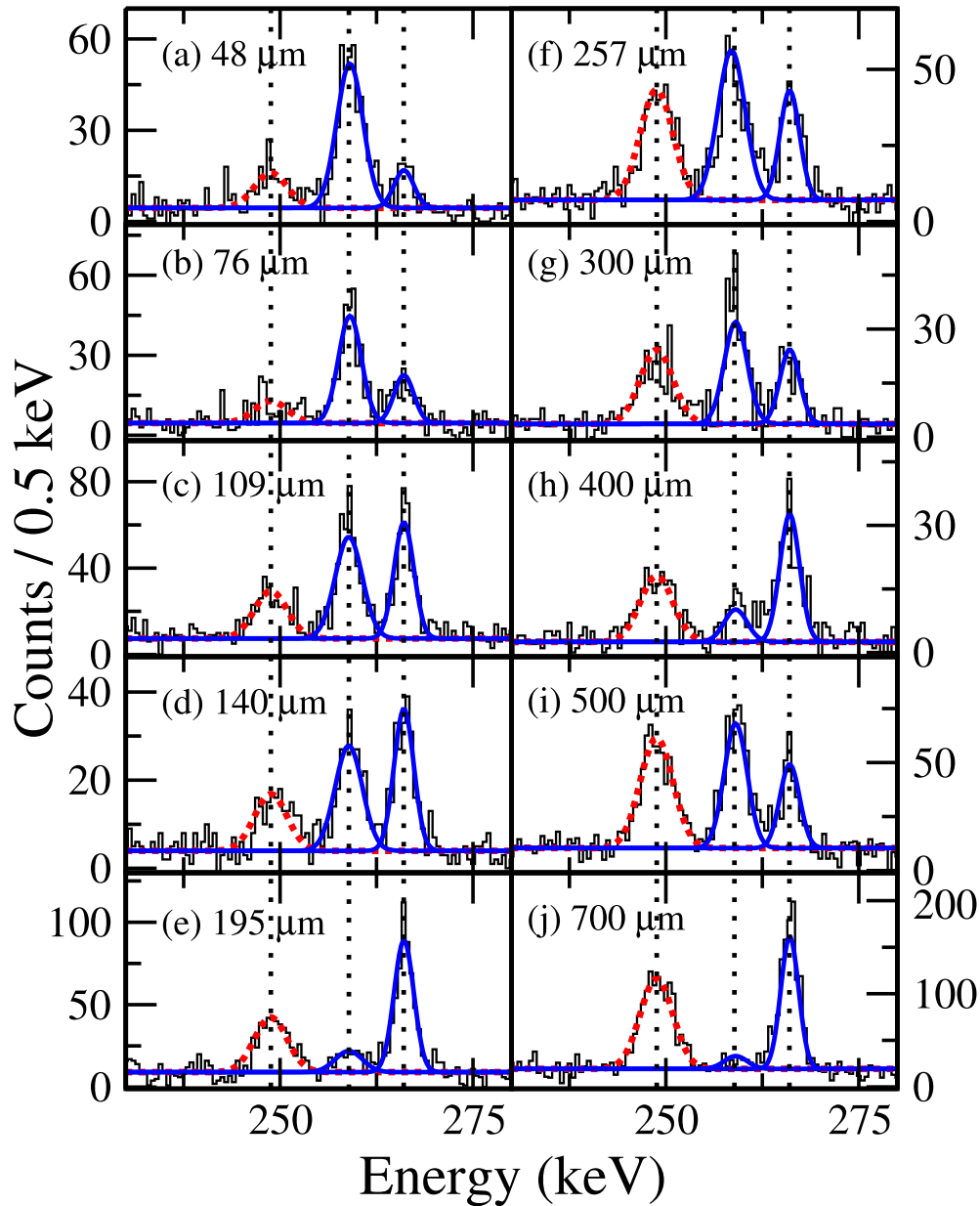


FIGURE 5.16: The background subtracted spectra showing the three intensity components of the 266-keV transition in ^{156}Dy , in coincidence with the fully shifted component of the 366-keV transition at 10 plunger distances. Gaussian fits to the decays occurring before the first degrader foil are shown in red-dashed and Gaussian fits to the decays occurring after the first-degrader foil are shown in blue-solid lines.

The lifetime of the 4^+ state in ^{156}Dy was measured to be $50(6)$ ps using TPEN as a standard two foil plunger. The NAPATAU computer program uses the measured intensities and a chi-squared minimisation procedure to find the best overall fit to extract the lifetime. The uncertainty on this result originates from the uncertainties in the measured intensities of the components of the 266-keV transition, the uncertainty on the total gated counts in each spectrum and the overall fits of the piece-wise polynomial

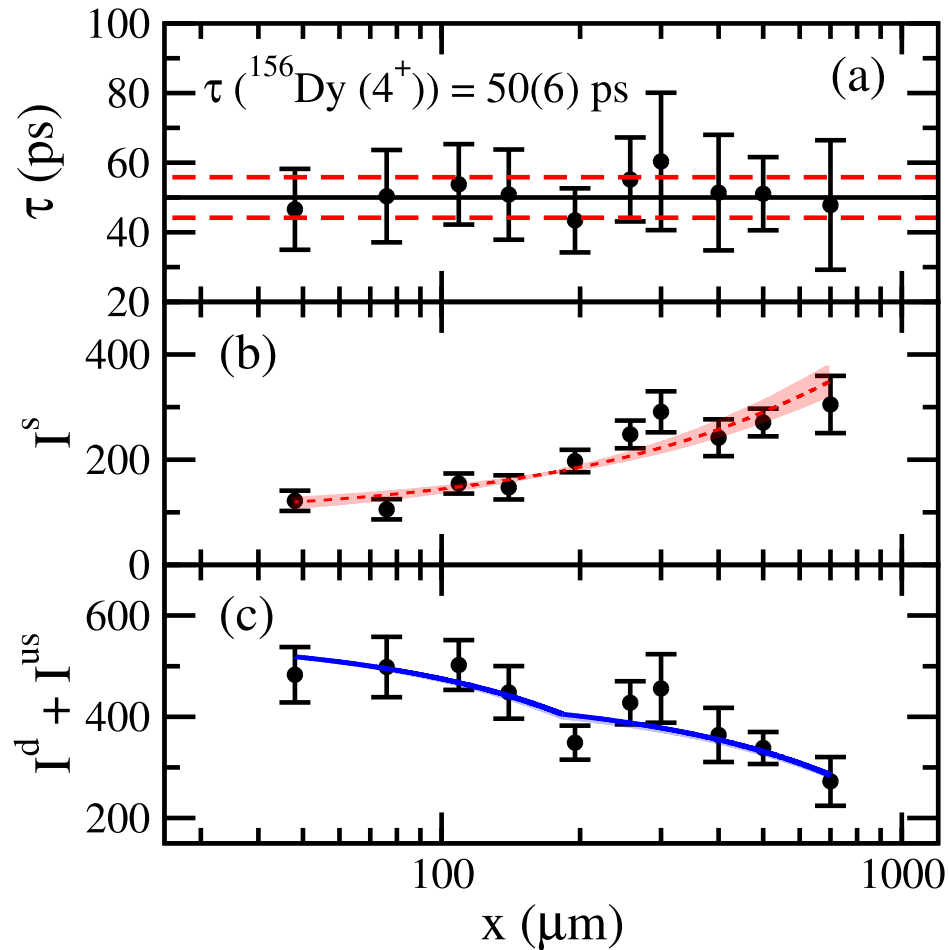


FIGURE 5.17: The intensity of the 266-keV transition in ^{156}Dy before and after a degrader foil, in coincidence with the fully shifted component of the 366-keV transition at 10 plunger distances. (a) the calculated lifetime at each of the plunger distances and the average lifetime, (b) the fully shifted component of the 266-keV transition and a piece-wise polynomial fit to the data (red-dashed) along with the uncertainty on the fit (red-shaded), (c) the derivative of the fit to (b) multiplied by τ (blue-solid) and the uncertainty on this (blue-shaded).

The blue shaded area is a comparable width to the line.

to the fully shifted component and its derivative to the stopped component. The uncertainty on the weighted average of the lifetimes calculated at each of the target-to-degrader distances was 3 ps. However, this does not account for any uncertainty on the fit within the NAPATAU program, or the covariance between the shifted and unshifted components. The dependence on the covariance arises from the fact that the derivative of the shifted component is fitted to the unshifted component. When using NAPATAU the fit of the unshifted component is dependent on the fit of the shifted component and the covariance must be calculated. The uncertainty on a calculated

TABLE 5.5: The target-to-degrader, x , and the unnormalised measured intensities of the 266-keV γ -ray transition before and after the degrader. The distances given are relative to the electrical contact point between the foils.

$x(\mu\text{m})$	I^{fs}	I^{us}	I^d	$I^d + I^{us}$
48	122(20)	80(10)	400(20)	480(25)
76	90(15)	115(15)	300(20)	415(25)
109	230(20)	345(20)	415(25)	760(31)
140	150(20)	290(20)	210(20)	500(25)
195	370(25)	730(30)	170(20)	900(35)
257	390(25)	230(20)	435(24)	665(40)
300	200(20)	130(15)	230(20)	360(25)
400	190(15)	260(30)	80(15)	340(35)
500	570(30)	330(20)	490(25)	820(35)
700	1240(40)	1340(40)	140(20)	1480(50)

lifetime at a distance i , $\Delta\tau_i$ is given in Ref. [104] by

$$\Delta\tau_i^2 = \frac{\Delta I_i^{us2}}{\dot{P}_{j(i)}^2} + \frac{I_i^{us2}}{\dot{P}_{j(i)}^4} \Delta \dot{P}_{j(i)}^2 + \frac{I_i^{us} \tau}{\dot{P}_{j(i)}^3} \Delta \dot{P}_{j(i)}^2, \quad (5.2)$$

where $\dot{P}_{j(i)}$ is the derivative of the decay curve evaluated at distance i .

The NAPATAU program can be used to estimate the uncertainty on the fits which is propagated to the uncertainty on the lifetimes. This is done by measuring the calculated lifetimes for a chi-squared of $\chi_{min}^2 + 1$, i.e. providing a lifetime value $+1\sigma$, and observing the effect of the fit on the lifetime. In this case, a chi-squared change of 1 (reduced chi-squared change of 0.07 with 14 degrees of freedom) changed the lifetime by ~ 5 ps. The change to the fit in doing this is shown in the shaded areas in Fig. 5.17(b). Additionally, the uncertainties on the measured average recoil velocities and the measured distances contribute to the overall uncertainty which is not taken into account directly by NAPATAU and must be propagated accordingly.

5.2.5 Beam-time improvement with TPEN

This commissioning experiment has demonstrated that the newly constructed TPEN is capable of performing differential lifetime measurements in the limit of low statistics.

The main advantage of a triple-foil differential plunger is the reduced beam-time required for a lifetime measurement compared to that of a conventional two-foil plunger. In order to quantify the beam-time improvement, a lifetime analysis of the 4^+ state in ^{156}Dy has been performed using TPEN as a conventional plunger, described above, and a direct comparison between the differential mode and the conventional mode has been made in this section.

In the present work, a total of 7×10^7 γ - γ events were collected using TPEN for the differential lifetime measurements performed at five sets of target-to-degrader and degrader-to-stopper distances. This resulted in a 13000(200) events in the three components of the 266-keV γ -ray transition for the differential lifetime analysis, yielding a lifetime value with a 4% uncertainty. When treating TPEN as a standard plunger, 10 000(100) counts were used to yield a lifetime value with a 12% uncertainty. From this, it is estimated that $\sim 50\,000$ (1000) counts would provide a measurement with a 4% uncertainty using TPEN as a two-foil plunger. This estimate is made by propagating uncertainties from Eqn. 5.2. Directly taking the ratio of the statistics required in the two modes of TPEN, with identical detector set-ups, it can be concluded that TPEN in differential mode requires a factor of 3.8(1) less in statistics or in beam time compared to a standard plunger.

A similar comparison between the lifetime measured in this work with TPEN and the lifetime measured by Möller *et. al.* can be made [20]. In the work by Möller *et. al.*, a conventional two-foil plunger using the collected 2.1×10^9 γ - γ events using the $^{124}\text{Sn}(^{36}\text{S},4n)$ reaction at 155 MeV. Figure 5.18 shows the spectra obtained in that work by gating on the 509 keV transition in ^{156}Dy . The spectra shows γ -ray events collected in one of the seven rings for 3 of the 23 plunger distances used in the experiment. In the measurement of the 4^+ state, only forward angles could be used for gating as two contaminating transitions hindered the use of backward rings for gating [20]. Four rings had sufficient Doppler shifts to use for lifetime analysis.

Using the spectra in Fig 5.18, and information given in Ref. [20], an estimated 12 000(1000) gated counts were collected for the 266-keV transition in each ring at each distance in their experiment. Hence, for all four rings and all 23 distances, $1.0(1) \times 10^6$ events were collected for the 266 keV transition. From the lifetime analysis figures in Ref. [20], it can be assumed that 14(2) distances were used for the lifetime analysis of the 4^+ state

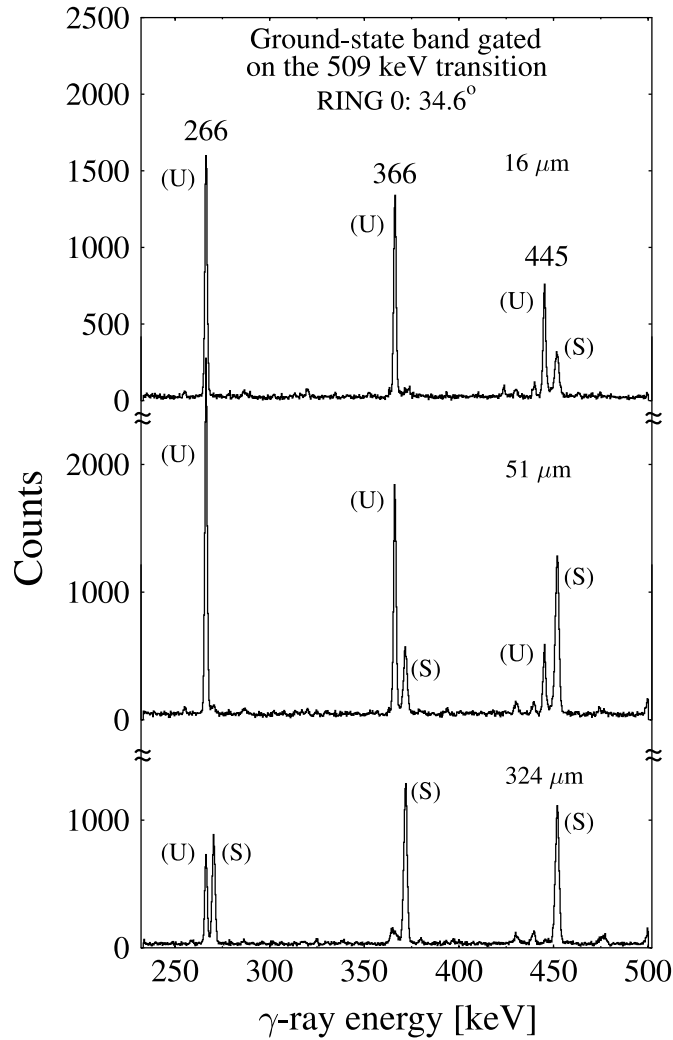


FIGURE 5.18: The spectra obtained in the work by Möller *et. al.* [20] by setting a gate on the 509 keV γ -ray transition in ^{156}Dy . The spectra are measured using ring 0 detectors in coincidence with ring 0, 1, 5 or 6.

in ^{156}Dy . From these estimates, 670 000(100000) events were used to achieve an uncertainty of 1%. Scaling these events down, a 4% uncertainty could have been achieved with only 42 000(7000) events. Directly taking the ratio of these 42 000 events required with the conventional two-foil plunger and the 13 000 required by TPEN shows a beam-time improvement by a factor of 3.2(5) using TPEN.

The improvement in beam-time is calculated for an experimental setup with no recoil separator. If a recoil separator is required then the reduced transmission of recoils from the introduction of the third foil will lessen this improvement and is discussed in Section 6.1.

Chapter 6

Discussion and future use

6.1 Beam-time reductions with TPEN

Section 5.2.5 estimated the beam-time improvement in lifetime experiments with TPEN compared to a conventional two-foil plunger. A factor of 3.8(1) less in required beam-time was estimated, which will allow the measurement of lifetimes in lower production cross section nuclei. The estimate was made using data from experiments where recoil tagging was not used. For lifetime measurements in nuclei produced with small production cross sections, it is often essential to use tagging techniques in order to select the nuclei of interest from the overwhelming background produced by the less exotic reaction products [26, 105–116]. These tagging techniques are often performed using recoil separators such as RITU [83] at JYFL. In such an experiment, the transmission efficiency of recoils through the separator with the extra degrader foil must be considered in order to estimate the total amount of beam-time required.

6.1.1 Using TPEN with a recoil separator

The overall transmission efficiency of recoil separators, such as RITU, is reduced by any material in the beam's path. As recoils pass through material, they interact randomly, broadening their energy and angular distributions. The energy broadening is known as straggling and the amount of straggling increases with the amount of material the

recoils pass through. Recoil separators are more efficient if the velocity spread of recoils is small. Hence, the three foils in TPEN will reduce the transmission efficiency of a separator, compared with the two foils in a conventional plunger.

The third foil in TPEN will therefore reduce the beam-time improvement estimated in Section 5.2.5. For example, with the RITU separator [83] the addition of a third 1 mg/cm^2 Mg degrader foil will reduce the overall transmission efficiency by $\sim 33\%$ [117, 118]. Therefore, if a recoil separator was used for tagging techniques with TPEN, then the overall beam-time improvement would be a factor of $\sim 3.8 \times 0.66 = 2.5$ relative to using a two-foil conventional plunger. As two-foil plungers have performed tagged lifetime measurements in nuclei with production cross sections of $10 - 20 \mu\text{b}$ [12, 21], TPEN is therefore capable of performing tagged lifetime measurements in nuclei with production cross sections down to $\sim 4 - 8 \mu\text{b}$, for experiments with 14 days beam-time at JYFL with RITU.

6.1.2 Mass analysing separators

Like with recoil separators, the overall transmission efficiency of mass separators is reduced by the third foil in TPEN. This section describes the effect of the third foil on the transmission efficiency of the Mass Analysing Recoil Apparatus (MARA) at JYFL. The effect is expected to be similar for other mass separators but specific simulations should be performed before experiments are scheduled.

Figure 6.1 shows a schematic illustration of the MARA separator. The separator consists of three quadrupole magnets, an electrostatic deflector and a magnetic dipole. The quadrupole magnets focus incoming recoils to increase the acceptance angle. The separator has a solid angle acceptance of 9.9 msr [119].

When using MARA, Mg foils are expected to cause a large elastic scattering background [120]. Hence Au foils would typically be used as degrader foils rather than Mg. As the stopping power of Au is less than Mg [37], more material is required for each degrader foil to achieve the same Doppler shifted energies. The large amount of material dramatically reduces the transmission efficiencies of recoils through MARA when a third foil is introduced. In cases where the energy of the γ -ray transition is

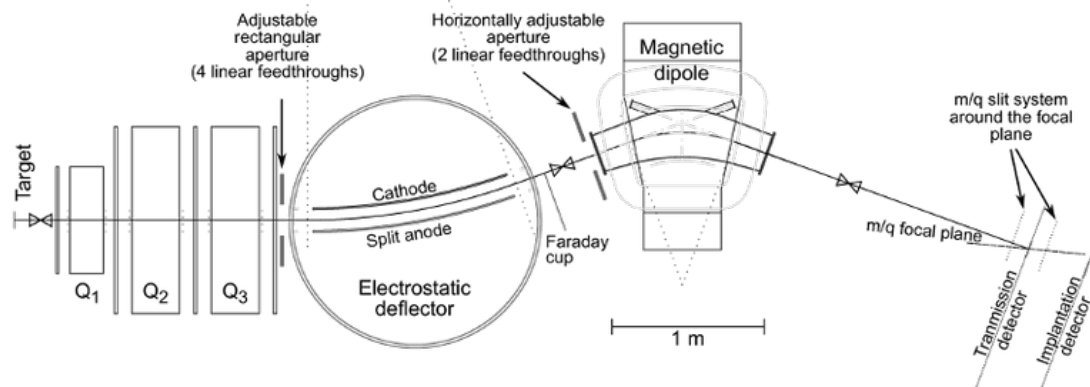


FIGURE 6.1: A schematic illustration of the MARA separator, taken from Ref [119]. On the left hand side are 3 quadrupole magnets, Q_1 , Q_2 and Q_3 .

small, thick degrader foils are required to separate components. In such cases, MARA may be incompatible with TPEN.

In order to estimate the effect of the third foil in TPEN on the transmission efficiency through MARA, simulations were performed for a specific reaction by J. Sarèn at JYFL [120]. The planned experiment on ^{161}Re , described in Section 6.3.2, was used for these simulations. The $^{106}\text{Cd} (^{58}\text{Ni}, p2n)$ reaction will be used to produce the ^{161}Re recoils. Figure 6.2 shows the energy distribution of ^{161}Re recoils before and after passing through two proposed 2.9 mg/cm^2 Au degrader foils. Significant straggling is predicted, producing a large range in recoil energies. This will reduce the transmission through MARA [120].

Figure 6.3 shows the angular distribution of ^{161}Re recoils after passing through two 2.9 mg/cm^2 Au degrader foils. The simulated angular cone of degraded recoils is large and therefore detrimental to the transmission through MARA. Using this distribution, the simulated transmission efficiency of ^{161}Re recoils is shown in Fig. 6.4. For a given energy to charge ratio, a range of energies and charge states will contribute to the total transmission. The total transmission efficiency for this reaction is $\sim 9\%$. Hence, the beam-time improvement for lifetime measurement with TPEN is negated by the loss in transmission from the third foil.

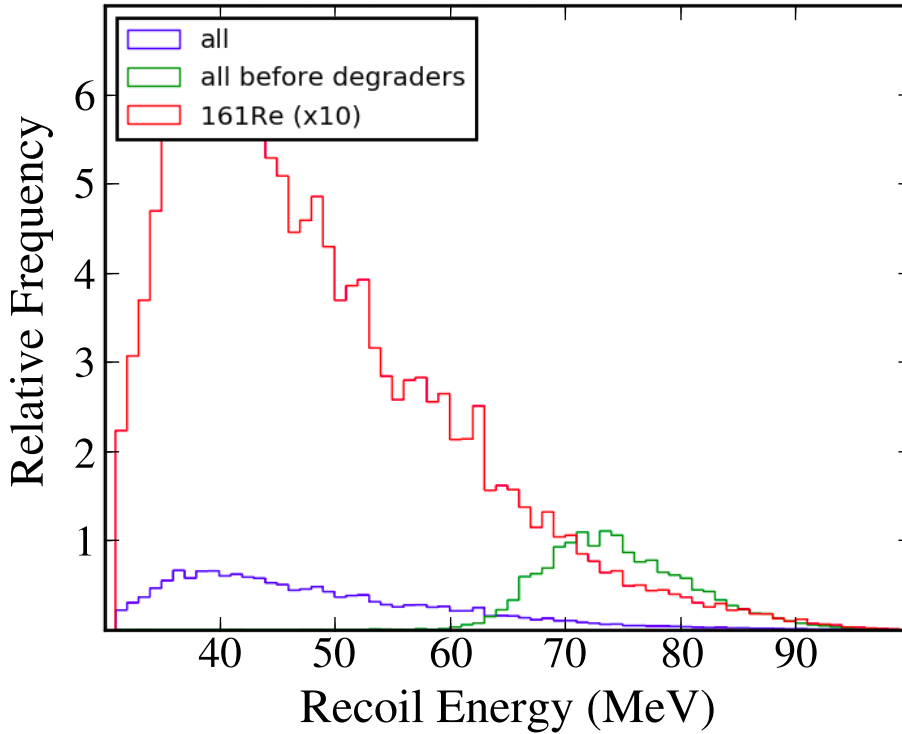


FIGURE 6.2: The energy distribution of ^{161}Re recoils after passing through two 2.9 mg/cm^2 foils from simulations ran by J. Sarèn [120]. The sum of all fusion-evaporation products from the $^{106}\text{Cd} (^{58}\text{Ni}, x)$ reaction, before the degrader foils is shown in blue, and after the degrader foils in green. 10 times the amount of ^{161}Re recoils after the degraders is shown in red.

It should be noted that the simulations shown here are specific to the reaction and detector combination. In this case TPEN was incompatible with a mass separator. However this is not the case in general and specific simulations should be performed when planning future experiments.

6.1.3 Planning experiments with TPEN

There are a few points to be considered when planning an experiment with TPEN. Firstly, the lifetime of the 4^+ state in ^{156}Dy was well known, therefore, x and Δx could be optimised prior to the commissioning experiment. In a two foil plunger experiment, the first target-to-degrader distance is typically based on the predicted lifetime and the collected γ -ray spectra are used to have a preliminary estimate of the actual lifetime of the nuclear state. This serves as the basis to choose next set of target-to-degrader distances for measurement.

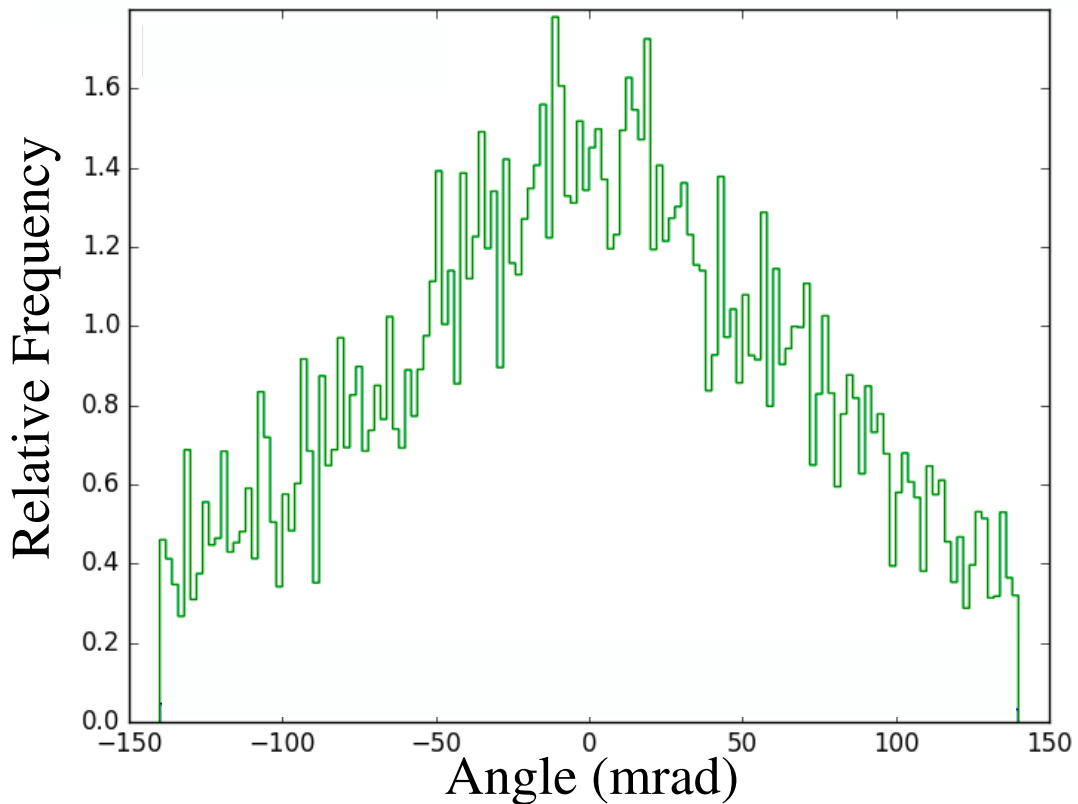


FIGURE 6.3: The angular distribution of ^{161}Re recoils after passing through two 3 mg/cm^2 Au foils from simulations ran by J. Sarèn [120].

In the case of TPEN, Δx must be small in order to meet the condition that $\Delta t \ll \tau$. However, if Δx is too small, then deformations in the degrader and stopper foils will result in electrical contact between the foils and loss of the feedback system. Section 5.1.3 shows that for the foils used in this experiment TPEN's constant feedback system started to become unstable at foil separations of $< 30\ \mu\text{m}$, with beam currents of $\sim 1\ \text{pA}$. With better stretched foils, smaller separations may be possible. If the foils are of a similar quality to the ones in this experiment, then Δx will typically be chosen to be $30 - 60\ \mu\text{m}$ in order to maintain the condition that $\Delta t \ll \tau$. In a manner similar to a two-foil plunger measurement, the intensities of the fully shifted and stopped components can be used to decide if the initial plunger conditions are optimal. In particular, if the conditions are optimised for the differential mode, then around one third of the total intensity for a transition should be in the fully shifted component. In this case, the majority of the statistics are in the degraded and stopped peak components, thus minimising the statistical uncertainty in the measured lifetime of a nuclear

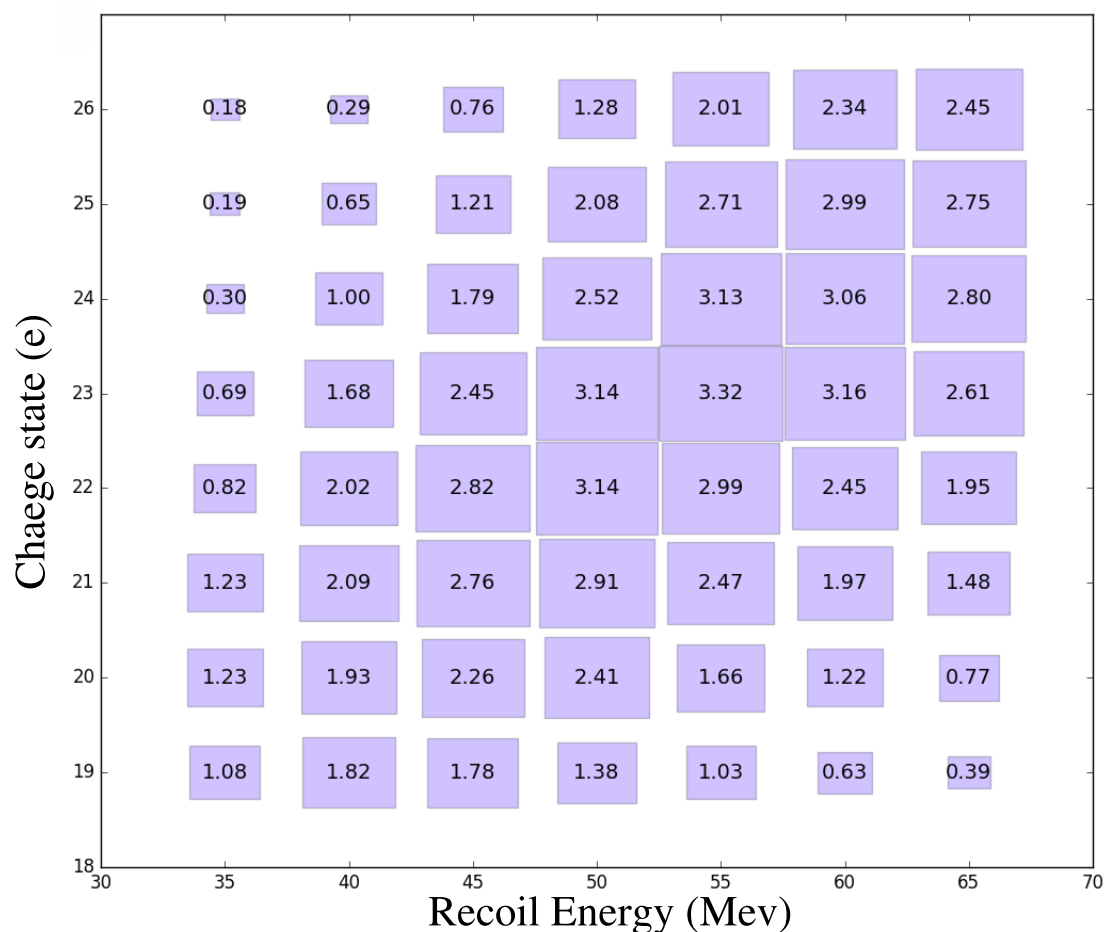


FIGURE 6.4: The percentage transmission probability of degraded ^{161}Re recoils through MARA, from simulations ran by J. Sarèn [120].

level. Additionally, for a typical rotational band, this ensures that the majority of the feeding transition decays before the degrader foil, maximizing the amount of events in the gate for coincidence analysis.

With TPEN, the three intensity components can be difficult to separate for low-energy transitions. In order to achieve a good separation, inverse kinematics can be used. Inverse reactions produce recoils with a greater velocity, producing larger Doppler shifts. These large Doppler shifts make the components easier to separate but often result in the overlapping of energy peaks with other observed γ -ray energies. Hence, possible contaminants, and their Doppler shifted components, need to be carefully considered when using inverse kinematics.

6.2 Minimizing uncertainty with TPEN

When measuring lifetimes in the differential mode with TPEN, the statistical uncertainty on the lifetime is dominated by the uncertainty on the area of the degraded component. The total relative uncertainty a lifetime calculated using Eqn. 2.26 is

$$\frac{\sigma_{\tau}^2}{\tau^2} = \frac{\sigma_{I_{us}}^2}{I_{us}^2} + \frac{\sigma_{I_d}^2}{I_d^2} + \frac{\sigma_{\Delta x}^2}{\Delta x^2} + \frac{\sigma_{v'}^2}{v'^2} - 2 \frac{\sigma_{I_{us}} \sigma_{I_d}}{I_d^2} \text{cov}(I_{us}, I_d), \quad (6.1)$$

where $\text{cov}(I_{us}, I_d)$ is the co-variance of I_{us} and I_d and is given by $\overline{I_{us} I_d} - \overline{I_{us}} \overline{I_d}$. In the standard DDCM approach, using Eqn. 2.17 with intensities measured at several distances, the covariance between the numerator and denominator is large yet is often neglected leading to an underestimate in the uncertainty on a measurement [26]. In the differential mode, the covariance between the two components is small since the numerator of Eqn. 2.26 does not depend on the denominator. However, the covariance should still be calculated to achieve an accurate uncertainty.

With TPEN in the differential mode, the degraded component will always have the fewest counts, and therefore the largest uncertainty. This is to ensure that the flight time between the degrader and stopper is small compared to the lifetime of the state. Hence, from Eqn. 6.1, it can be seen that the uncertainty on the degraded component is the largest contributor to the overall uncertainty of the lifetime. In this work, the $\frac{\sigma_{\Delta x}}{\Delta x}$ and the $\frac{\sigma_{v'}}{v'}$ terms were ~ 0.0001 , the $\frac{\sigma_{I_{us}}^2}{I_{us}^2}$ term ~ 0.0025 , the $\frac{\sigma_{I_{us}} \sigma_{I_d}}{I_d^2}$ term ~ 0.005 and the $\frac{\sigma_{I_d}}{I_d}$ term ~ 0.01 . Hence, in order to estimate the uncertainty on a lifetime measurement, the uncertainty on the number of counts in the degraded components can be used. This is useful when planning experiments as the accuracy of a planned measurement can be quickly estimated. It should be noted that Eqn. 6.1 assumes that the three Doppler shifted components are easily separated, which satisfies the condition $\text{cov}(I_{us}, v') = 0 = \text{cov}(I_d, v')$.

6.2.1 Absolute foil distances

The other major contributor to the overall uncertainty of a lifetime measurement is the systematic uncertainty from measuring the absolute degrader-to-stopper distance. If the foils are perfectly aligned then electrical contact will occur between the foils when

the centres touch. If the foils are not perfectly aligned, then the edges of the foils will touch before the centres of the foils touch. The touching of the edges causes electrical contact even though the distance between the centres of the foils is non-zero. The distance between the centres of the foils when they are in electrical contact is known as the distance offset. In standard DDCM with multiple distances, only the relative distances between foil separations are important and the distance offset is irrelevant. However, with a measurement at a single set of distances, the distance offset must be measured.

In this commissioning experiment the distance offset was measured by extrapolating the degrader-to-stopper calibration curve to zero distance, as shown in Section 5.1.2. Using this extrapolation, the distance offset was measured to be $8(1) \mu\text{m}$. The shortest degrader-to-stopper distance from electrical contact used in this work was $31.2(2) \mu\text{m}$ resulting in a total distance of $39.2(10) \mu\text{m}$. The systematic uncertainty on this distance is 2.6%, which has been included in the overall uncertainty of the measurement. For lifetime measurements with high-statistics, this systematic uncertainty will become comparable to the statistical uncertainty.

For a high statistics experiment with TPEN in the differential mode, a thin layer of ^{181}Ta could be added to the target foil. In a reaction, the states in ^{181}Ta will be Coulomb excited and recoil from the target. The ^{181}Ta recoils will subsequently γ decay. The precise lifetimes measured in Ref. [9] allow for the absolute foil separations to be measured by measuring the different intensity components. As the lifetimes of the states in ^{181}Ta vary from 1 ps to 24 ps, a large range of distances can be accurately measured.

6.3 Future use of TPEN

6.3.1 Simultaneous lifetime measurements

In an experiment with TPEN, there are three regions of constant velocity. This provides the possibility to use TPEN in an alternate mode that can probe two regions of sensitivity simultaneously. For example, a short target-to-degrader distance coupled

with a longer degrader-to-stopper distance may probe a short lived state and a long-lived state simultaneously. Therefore, simultaneous measurements of two very different lifetimes of excited states within one nucleus can be performed. In effect, TPEN can act as two two-foil plungers working simultaneously. This secondary mode of TPEN reduces the beam time requirement for experiments where the lifetime of several nuclear states in a single nucleus is required and is detailed in Ref. [121].

6.3.2 Proton-rich nuclei

HIFE reactions typically produce neutron-deficient recoils. As nuclei become increasingly proton-rich, proton emission from the nucleus becomes possible. Several studies have been performed to explain proton emission from nuclei [122, 123]. Many of these studies treat the nucleus as a spherical potential and calculate the probability for a proton to tunnel through this potential. As expected, these studies work well for spherical nuclei, but fail to reproduce proton emission rates for deformed nuclei. Hence, the measurement of lifetimes within proton-emitting nuclei, and the extraction of deformation parameters, provides valuable information to expand these studies.

Over the past few years at JYFL, there has been development of a simultaneous understanding of proton- and γ -emission using lifetime measurements in proton-emitting nuclei [12, 13, 21, 22]. A non-adiabatic particle-rotor model has been developed in order to understand proton emission from parent nuclei which have a non-rigid cores with finite moments of inertia [12]. In order to expand this study, we will measure lifetimes in the proton-rich nucleus ^{161}Re using the newly commissioned TPEN.

^{161}Re is the lightest known Re isotope with some 24 neutrons less than its nearest stable isotope. It is also one of only ~ 50 nuclei across the entire nuclear chart to undergo proton emission. ^{161}Re presents an exciting opportunity to study the deformation of a nucleus which undergoes both α and proton emission from the same state. Figure 6.5 shows the level scheme of ^{161}Re . ^{161}Re decays via proton emission from both the ground state and from an isomeric state [124, 125]. The isomeric state has a spin of $11/2^-$ and hence the proton decay to the 0^+ ground state in ^{160}W is hindered [125]. This allows α decay to compete from this $11/2^-$ state, and both decay modes are observed. The shape of ^{161}Re in this isomeric state is predicted to be similar to that

of ^{160}W : prolate with $\beta_2 \sim 0.1$ from Ref. [125]. The ground state is predicted to be prolate with $\beta_2 \sim 0.2$ from Moller and Nix [126].

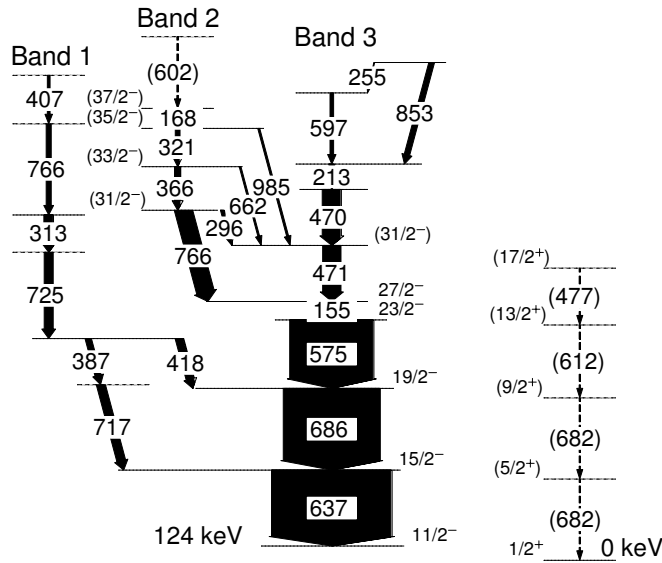


FIGURE 6.5: The level scheme of ^{161}Re taken from Ref. [125]. ^{161}Re proton- and α -decays from the $11/2^-$ state with energies of 1323(7)- and 6432(6)-keV, respectively.

With a measurement of the lifetimes of the states in this nucleus, it is possible to calculate wavefunctions for parent and daughter nuclear states at a particular deformation using the non-adiabatic particle-rotor model. Wavefunctions will be extracted from this model which represents the best description of the experimental level energies as a function of deformation. These wavefunctions are then fixed and used in the proton emission code [13], an α -emission code, and in a γ -transition code [13]) to predict the proton, α and γ -decay rates within a simultaneous theoretical approach. The calculated γ -, α - and proton-transition rates are then compared with the experimentally deduced rates, providing a stringent test of each of these nuclear models. We note that in particular the $11/2^-$ state in ^{161}Re is common in each of the γ -, α - and proton-emission processes. Our approach for γ and proton emission, has been used previously in lifetime measurements of the proton emitter ^{151}Lu [22]. Here, we have the exciting new possibility to take the approach one step further to include the α -emission process.

The $^{106}\text{Cd} (^{58}\text{Ni}, p2n) ^{161}\text{Re}$ reaction will be used at a beam energy of 272 MeV (264 MeV at the centre of a 1 mg/cm^2 ^{106}Cd foil) to produce ^{161}Re recoils at a velocity of 3.3 %c. The timing and energy information of γ rays emitted from ^{161}Re will be collected with the JUROGAM III array. Events will be constructed by correlating the

timestamps of the detected γ rays with the timestamps of proton or alpha emission in the focal plane of RITU, producing clean spectra. Figure 6.6 shows the particle tagged spectra obtained using the previous JUROGAM II array with the same reaction for 6 days with a 6 pnA beam. Figure 6.6(a) shows the γ rays correlated with the subsequent α -decay of ^{161}Re at the RITU focal plane. Figure 6.6(b) shows the γ rays correlated with the subsequent emission of a proton from the $11/2^-$ isomeric state in ^{161}Re . Figure 6.6(c) shows the γ rays correlated with the subsequent emission of a proton from the ground state in ^{161}Re . The production cross section for this ^{106}Cd ($^{58}\text{Ni}, p2n$) reac-

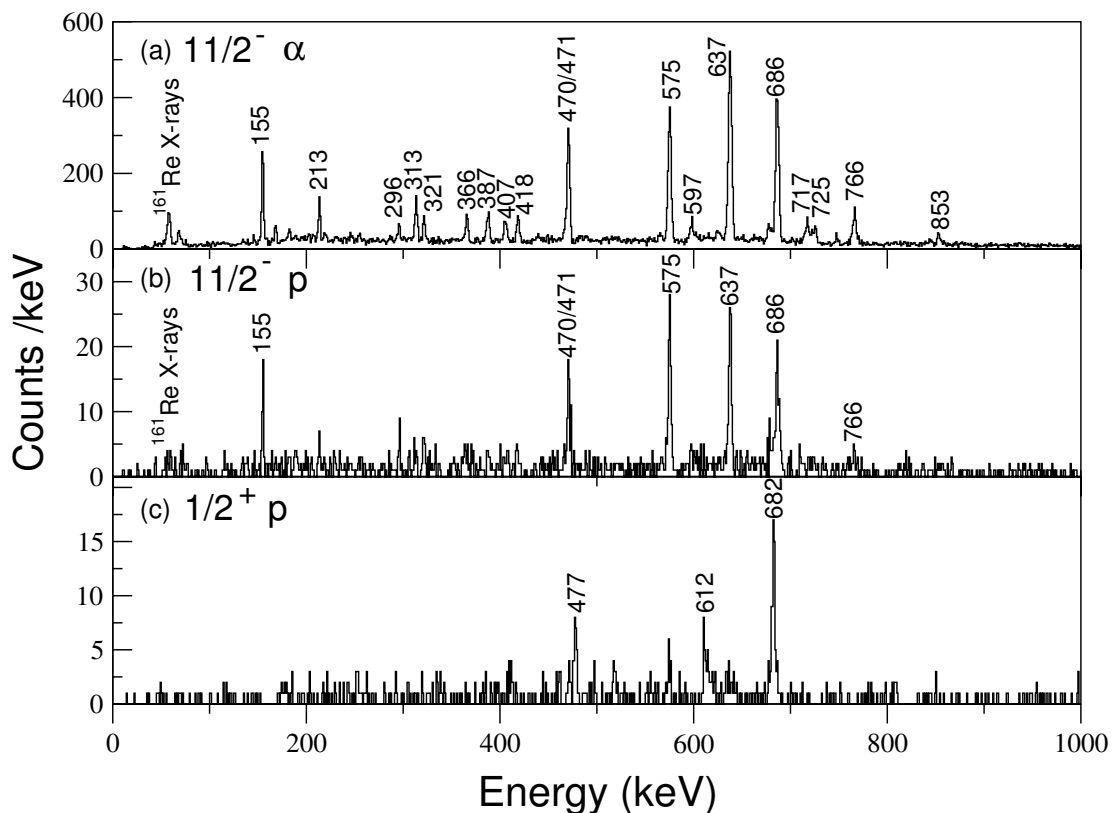


FIGURE 6.6: (a) γ spectra obtained from gating on the α -decay of ^{161}Re . (b) γ spectra obtained from gating on the proton decay from the isomeric state in ^{161}Re . (c) γ spectra obtained from gating on the proton decay from the ground state in ^{161}Re . Data was collected using 6 days of beam at 6 pnA, taken from Ref. [125]. γ rays have been labeled with their energies.

tion is $\sim 5 \mu\text{b}$ [124], making the measurement inaccessible using conventional two-foil plungers. With TPEN, we plan to measure the lifetimes of the states built upon the $11/2^-$ isomeric state using 9 days of beam-time. Proton-tagging at the focal plane of RITU will be employed to produce clean γ -singles spectra which will then be used to extract lifetime information.

Previous proton-tagged plunger experiments have shown that beam currents of ~ 3 pA can be used without deforming the degrader foils with light beams [11]. Hence, a 2.5 pA beam will be used for 9 days with TPEN. Reference [125] used the same beam-target combination for 6 days with a 6 pA beam. Noting the near identical setups and accounting for $\sim 50\%$ of the beam current for 50% longer in beam-time than Ref. [125], 75 % of the number of γ rays observed in Ref [125] will be collected. Assuming a 60% transmission efficiency through RITU compared to Ref. [125] results in 45 % of the correlated particle- γ -ray events. As only Ring 1 and Ring 2 detectors are at large angles to the beam axis, 10% of the statistics of that from Ref. [125] are expected to be used. With TPEN in the optimal setup this would allow for a measurement with ~ 25 % uncertainty using α, p tagging. Here, the optimum setup is where 10-15 % of the statistics are collected in the reduced-shifted component to allow the differential mode to be used. It should be noted that using this reaction with DPUNS, we would require 28 days to obtain a measurement with a 25 % uncertainty.

The recoils will exit the 1 mg/cm^2 ^{106}Cd target with a velocity of $\sim 3.3 \%c$ which will be slowed to $\sim 2.6 \%c$ and $\sim 1.8 \%c$ by two ^{24}Mg degrader foils with thicknesses of 0.7 mg/cm^2 each. This leaves the ^{161}Re recoils with a kinetic energy of 25 MeV entering RITU. Monte Carlo simulations performed with the stopping ranges in materials (SRIM) [37] program show that the recoils implant into the DSSD with around 14 MeV. The calculations assumed 2.1 μm of mylar and 4 m of 1 mbar He gas.

The three velocity regimes will produce fully shifted, reduced-shifted and degraded peaks with $\sim 5\text{-keV}$ separation. Figure 6.7 shows simulated spectra for the 637-keV transition based on these conditions. The three intensity components of the transition have been estimated with FWHMs of 3.8, 3.3 and 2.9 keV, for the fully shifted, reduced-shifted and degraded components, respectively. These widths were estimated from the TPEN commissioning experiment [17] and account for the intrinsic detector resolution and Doppler broadening. A random background of 5% of the total photopeak height, has been added to the spectra to represent the level of background that is expected from the previous experiment, see Fig 6.6 from Ref. [125].

The relative intensities of the three components have been calculated by assuming a lifetime of 30 ps, from Moller and Nix [126], and target-to-degrader and degrader-to-stopper distances of 100 μm and 30 μm , respectively. Using the simulated velocities

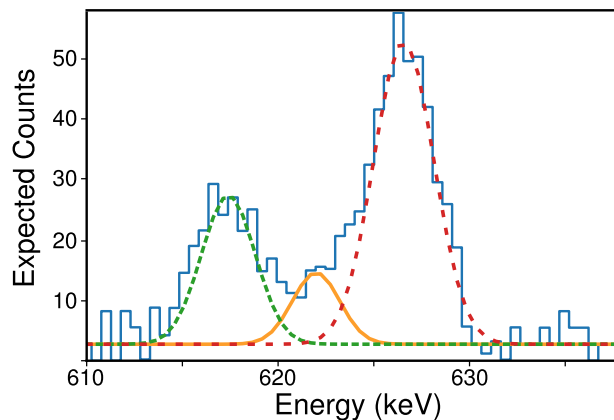


FIGURE 6.7: Simulated spectra showing the fully shifted (green-dash), reduced-shifted (orange solid) and degraded (red-dashed) components peaks of the 637 keV transitions for $(\alpha+p)$ tagging. A random background estimated from Fig 6.6 has been applied to the simulated data to indicate the level of noise expected.

from above, the flight time between the target foil and degrader foil will be 10 ps and the flight time between the degrader and final degrader will be 4 ps. Approximating the lifetime of the state to follow an exponential distribution then gives relative intensities of 30%, 10% and 60% for the fully shifted, reduced-shifted and degraded, respectively.

Using the spectra obtained in Ref. [125], and accounting for the reduced beam current and an additional factor of 2 loss in transmission through RITU (from the 1.4 mg/cm^2 ^{24}Mg), we estimate 350 α -tagged or p -tagged events in total, will be recorded in Ring 1 or Ring 2 detectors. These are split between the three components of the 637-keV transition, with ~ 35 of these in the degraded component, similar to the statistics in Fig 5.15. This will provide a lifetime measurement with an uncertainty of $\sim 25\%$.

Figure 6.6 has also been used to check for potential contaminant lines which might be shifted into the regions of interest of the three component peaks. The region of the spectrum occupied by the three components of the 637-keV transition will be free from contamination. The closest peak was found to be the fully shifted component of the 686-keV transition, which will lie at 665-keV. The cleanliness of the spectra in this experiment will minimise the uncertainties on the fits of the three intensity components of the 637-keV transition.

The proposed experiment was approved by the Jyväskylä Programme Advisory Committee (PAC) on 21st November 2018 (JR152). The experiment should take place

within the next year and will be the first new lifetime measurement with TPEN. The experiment will be run back to back with lifetime measurements of the proton emitter ^{147}Tm (JR153), which will also use TPEN with RITU.

6.3.3 Coulex-Plunger measurements

TPEN was constructed with the intention of performing Coulex-Plunger lifetime measurements at the HIE-ISOLDE facility at CERN. Coulex experiments use Coulomb excitation to excite nuclei, populating non-yrast states. Coulex is one of the few techniques available that allow non-yrast states to be studied [9]. In principle, the transition probabilities of these states can be measured by measuring the γ -ray yields as the states decay. Using the Coulomb excitation alone requires the fit of many matrix elements simultaneously, including the signs of these matrix elements for multi-step excitations. Additionally, the projectile energy is limited to ensure excitations do not have contributions from nuclear interactions. By combining Coulex measurements with lifetime measurements, these problems are eliminated and a more reliable measurement of the sign and the magnitude of quadrupole moments can be made. Additionally, the possibility to study nuclei using Coulomb-nuclear excitation becomes possible, without hindering the measurement of transition probabilities. Coulomb-nuclear excitations often have higher cross sections than pure Coulomb, increasing the number of measurable statistics in a given beam-time.

Measurements that yield reliable quadrupole moments are particularly important in the shape-coexistence regions around $Z = 50$ and $Z = 82$ where nuclei are close to spherical. In these regions, the sign of the deformation must be measured to ensure the shape of the nucleus is determined correctly. However, since many of these nuclei are far from stability, their production cross sections are extremely small. Hence traditional two-foil plunger experiments in this region are beam-time intensive. As TPEN has shown a significant improvement in the required beam-time for a result with the same accuracy compared to a two-foil plunger, it is well suited to perform these measurements. Combining lifetime measurements with Coulex measurements also removes the reliance on coincidence measurements, further enhancing the statistics. With Coulex, only low-lying states are populated and the level feeding can be calculated reliably, which removes many of the complications associated with side-feeding.

When combining Coulex-plunger experiments, the experimental setup requires modification compared to a standard plunger experiment. Only nuclei which leave the target with a high recoil velocity are of interest and should be selected. Additionally, for pure Coulex reactions, only recoils scattering through large angles should be selected as this ensures a small impact parameter, and hence a low interaction energy. The selection is performed using a particle detector placed close to the final degrader foil. The annular silicon particle detector allows a measurement of the polar and azimuthal angles with respect to the beam axis. These angles can provide a reconstruction of the kinematics of the reaction which greatly improves the accuracy of the measured velocity for a given recoil. This allows a more accurate Doppler correction to the γ -ray energies compared to measuring the average recoil velocity, see Fig 6.8. Demanding coincidences with the target recoils also ensures the reduced-shifted and degraded intensity components do not have contributions from secondary Coulex reactions on the degrader foils.

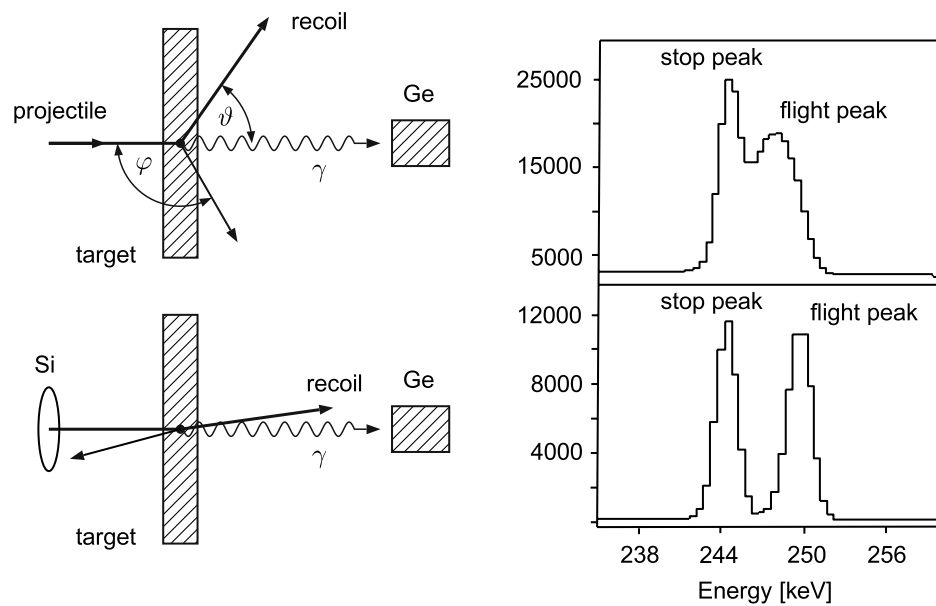


FIGURE 6.8: Schematic representation of kinematic corrections to Doppler shifted components in a Coulex-Plunger experiment. The kinematics are shown on the left-hand-side with the corresponding components of the $4^+ \rightarrow 2^+$ transition in ^{152}Sm shown on the right. The top panel shows the data with no kinematic correction and the bottom panel shows the data with the correction applied. Figure taken from Ref. [127].

Figure 6.9 shows a provisional illustration of the TPEN device adapted for Coulex-Plunger experiments at CERN. The device is similar to the one commissioned in this work, using identical foil cones, frames and mounts. Smaller motors are intended to be used to allow a smaller central chamber. The Q-552 Q-Motion Miniature Linear Stage

motors have the same spatial resolution as the LPS-45 motors while being smaller and thinner.

The main difference between TPEN at ISOLDE and TPEN at JYFL is the addition of a double-sided silicon-strip detector (DSSD), which has been added downstream to the second degrader foil. This DSSD will allow the tagging of recoils. The DSSD is sensitive to the position of implantation and is capable of measuring the energy of the implantation. This will allow the polar and azimuthal angles of the projectile to be measured and hence the kinematics can be reconstructed. Figure 6.10 shows a slice of the TPEN plunger with the DSSD installed.

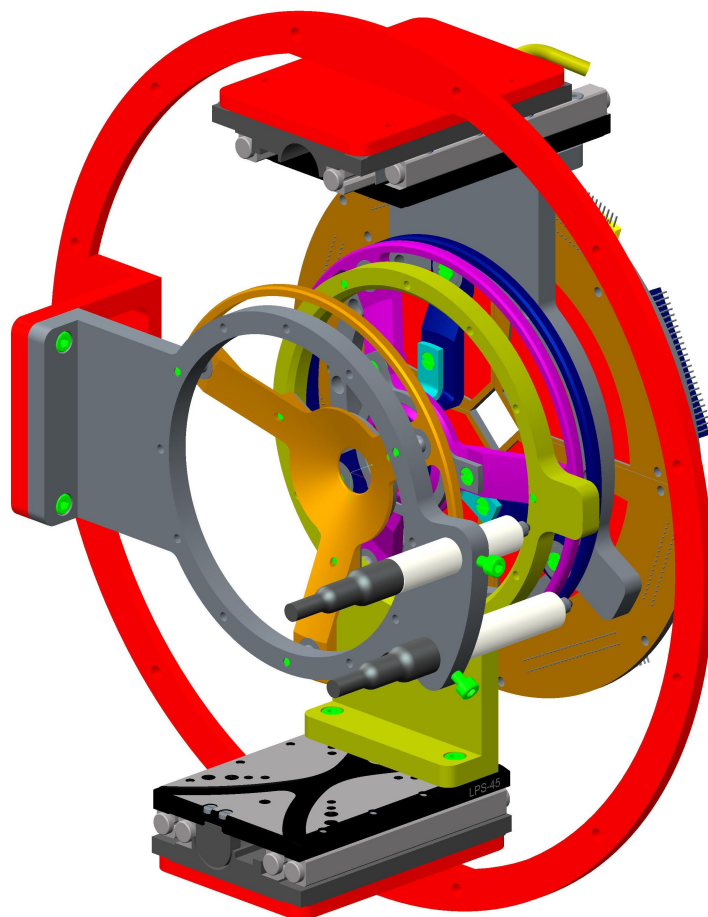


FIGURE 6.9: Drawing of TPEN fitted with a DSSD (orange) to be used at the HIE-ISOLDE facility at CERN.

Recoils passing through the degrader foil at small angles to the beam axis will pass through a hole in the centre of the DSSD and do not register as an event. This ensures that interactions with small impact parameters are not registered, and that the Coulex

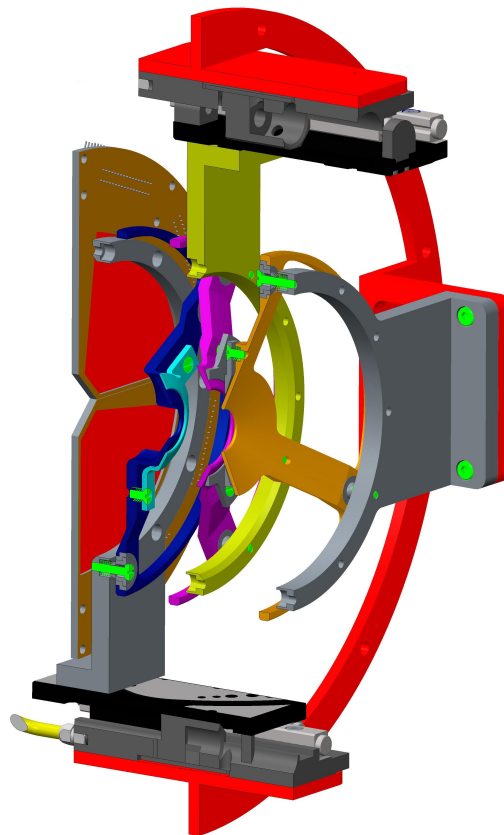


FIGURE 6.10: Sliced drawing of half of TPEN fitted with a DSSD (orange) to be used at the HIE-ISOLDE facility at CERN.

safe criterion is met. The small hole in the detector also has the advantage of reducing radiation damage to the DSSD.

The two degrader foils in TPEN are expected to reduce the effectiveness of the kinematic reconstruction using the DSSD, compared to standard Coulex experiments. As the recoils pass through the degraders, they can be deflected at a range of angles resulting in an angular cone of implantation for each original recoil trajectory. The uncertainty on the original position of the recoil leads to an uncertainty in the flight distance, and hence measured lifetime. To reduce this effect, the DSSD should be placed close to the second degrader foil, minimising the size of the angular cone.

The effects of the degrader foils may reduce the overall beam-time improvement quoted in Section 5.2.5. Experimental data are required to quantify these effects. However, as there is only a very small loss in transmission or detection of recoils due to the extra foils, the reduction is not expected to be severe. From initial SRIM calculations, a

conservative estimate of a factor of 3 should be placed on the improvement to beam-time. This factor will be fully quantified after the first Coulex-Plunger experiment. When planning Coulex-Plunger experiments, wider peaks should be estimated to ensure the peaks are well separated in the data.

The vacuum housing of TPEN at CERN will match the existing housing used for Coulex experiments. TPEN and all electrical feed-throughs will be fitted upstream, and the downstream section of beamline will be unchanged. This allows easy installation of TPEN with minimal effect on the electrical feed-throughs of other experiments. TPEN

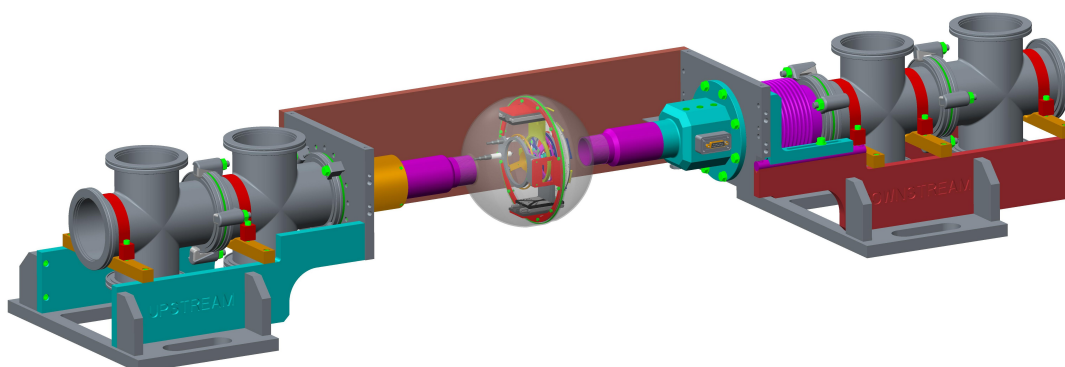


FIGURE 6.11: Drawing of TPEN installed at the HIE-ISOLDE beamline.

will be surrounded by the MINIBALL germanium array which will detect emitted γ rays. MINIBALL consists of 24 six-fold segmented tapered HPGe. The high granularity and efficiency of MINIBALL make it ideal for RDDS experiments with small production cross sections. γ rays detected in MINIBALL will be correlated with particles detected in the DSSD to provide tagged spectra for lifetime analysis.

Chapter 7

Conclusions

This thesis has presented the new triple-foil plunger device TPEN which has been designed and built at The University of Manchester. TPEN was built to improve the current method of measuring lifetimes by removing the requirement for several target-to-stopper distances. TPEN utilises the differential mode of DDCM to directly determine the decay function and its derivative at a single plunger distance setting. This, in turn, reduces the beam time required for a lifetime measurement, giving access to nuclei with much smaller production cross sections.

A constant negative feedback system, used to minimise the variation in the distances between foils has been successfully tested. When a heavy-ion beam impinges on a foil, it deforms and bulges. The feedback system employs a capacitive voltage measurement and two linear-stage motors to adjust the foil positions to keep the distance between foils constant. The feedback system coped extremely well with large foil separations with both low and high beam currents. For foil separations of less than 30 μm , a maximum of 1 pA could be used with the $^{136}\text{Xe}^{25+}$ beam.

TPEN was commissioned in the measurement of the lifetime of the first 4^+ state in ^{156}Dy . TPEN demonstrated the capability to measure lifetimes using a single set of plunger distances, both with moderate and with low statistics. The measured lifetime of 46(2) ps is in good agreement with the literature value of 45.6(5) ps.

A comparison of the lifetime analysis using the differential mode of TPEN compared to TPEN acting as a two-foil plunger has been made. This comparison revealed that

TPEN required a factor of ~ 3.5 less in beam time for a lifetime measurement compared to a conventional two-foil plunger, when tagging techniques were not used. If tagging techniques are required, the improvement is expected to be a factor of ~ 2.5 .

The vast improvement in the beam-time requirement shown by TPEN allows the measurement of lifetimes in nuclei with extremely small production cross sections. As the DPUNS plunger was able to measure lifetimes in nuclei with production cross sections of $10 - 20 \mu\text{b}$, TPEN is expected to be able to make measurements in nuclei with production cross sections of $4 - 8 \mu\text{b}$.

Several experiments have been accepted that would not be feasible with conventional two-foil plungers. The lifetimes of excited states in the proton emitting nuclei ^{161}Re will be measured using proton-decay tagged spectra with TPEN. TPEN will then be used to perform Coulex-Plunger experiments at the HIE-ISOLDE facility at CERN.

Appendix A

Lifetime measurements in ^{112}I

This appendix presents the lifetime measurements of excited states in ^{112}I . The lifetimes were measured using the DPUNS plunger and the JUROGAM II array at the University of Jyväskylä, Finland. ^{112}I was a side channel in the ^{58}Ni beam ^{58}Ni target reaction and hence the level of contamination was high. γ gated γ - γ matrices were produced to produce clean spectra and the results were published in the journal Physical Review C.

Lifetime measurements of lowest states in the $\pi g_{7/2} \otimes \nu h_{11/2}$ rotational band in ^{112}I


M. M. Giles, D. M. Cullen, B. S. Nara Singh, D. Hodge, M. J. Taylor,^{*} M. J. Mallaburn, N. V. Sosnin, and L. Barber
School of Physics and Astronomy, Schuster Building, The University of Manchester, Manchester M13 9PL, United Kingdom

J. F. Smith, L. Capponi, and M. Smolen
School of Engineering and Computing, University of the West of Scotland, Paisley, PA1 2BE, United Kingdom

C. Scholey, P. Rahkila, T. Grahn, H. Badran, A. Girka, P. T. Greenlees, R. Julin, J. Konki, O. Nefodov, P. Ruotsalainen,
 M. Sandzelius, J. Sarén, J. Sorri, S. Stolze, J. Uusitalo, J. Pakarinen, P. Papadakis, and J. Partanen
University of Jyväskylä, Department of Physics, P.O. Box 35, FI-40014, University of Jyväskylä, Finland

T. Braunroth
Institut für Kernphysik der Universität zu Köln, D-50937 Cologne, Germany

G. G. O'Neill
Department of Physics, Oliver Lodge Laboratory, University of Liverpool, Liverpool, L69 7ZE, United Kingdom

 (Received 18 April 2018; revised manuscript received 30 August 2018; published 17 October 2018)

A differential-plunger device was used to measure the lifetimes of the lowest states in the $\pi g_{7/2} \otimes \nu h_{11/2}$ rotational band in doubly odd ^{112}I with the $^{58}\text{Ni}(^{58}\text{Ni}, 3pn)$ reaction. A differential decay curve method was performed using the fully shifted and degraded γ -ray intensity measurements as a function of target-to-degrader distance. The lifetimes of the lowest three states in the $\pi g_{7/2} \otimes \nu h_{11/2}$ band in ^{112}I were measured to be 124(30), 130(25), and $\leq 6.5(5)$ ps, respectively. As the lifetimes of successive excited states in a rotational band are expected to decrease with increasing excitation energy, these measurements suggest that the order of the transitions in the established band in ^{112}I may need revising and that the state tentatively assigned to be (7^-) may not belong to the rotational band.

DOI: [10.1103/PhysRevC.98.044315](https://doi.org/10.1103/PhysRevC.98.044315)

I. INTRODUCTION

The heavy mass isotopes of iodine are known to exhibit features normally associated with collective behavior. For example, a series of strongly coupled rotational bands have been observed in the doubly odd I isotopes [1–4]. The strongly coupled nature of these bands is usually characterized by their signature splitting. Signature splitting can be quantified as the energy of the $M1$ transition linking the strongly coupled rotational bands minus the average energy of the $M1$ transitions directly above and below it [5]. In $^{116-122}\text{I}$ [1,6,7], the strongly coupled rotational bands built upon the $\pi g_{7/2}^{-1} \otimes \nu h_{11/2}$ configuration exhibit a small signature splitting, $S(I^\pi)$ [1,2,5]. For example, in ^{116}I $S(9^-) = 9$ keV and in ^{118}I $S(9^-) = 21$ keV for these $\pi g_{7/2}^{-1} \otimes \nu h_{11/2}$ bands. In contrast, in the lighter mass isotopes, the collective rotational bands are interpreted to be built upon a lower-K proton $g_{7/2}$ configuration coupled to the same neutron $h_{11/2}$ orbital. As a consequence, the strongly coupled nature of the bands in the heavier mass isotopes diminishes in the lighter mass isotopes and larger signature splittings are observed. For example, in ^{114}I the signature

splitting is $S(9^-) \approx 400$ keV [8] and becomes so large in ^{112}I that only one signature of the rotational band is experimentally observed [9].

^{112}I was previously studied by Paul *et al.* [9]. In that work, a series of single-particle states were established at low spins, which were fed by a rotational band at higher spins. The band was interpreted as the favored signature of $\pi g_{7/2} \otimes \nu h_{11/2}$ configuration [9]. The aligned angular momentum for this band showed somewhat irregular behavior at low rotational frequencies as the nucleus went through the simultaneous alignments of both proton and neutron $h_{11/2}$ orbitals [9]. In order to shed some light on the nature of the $\pi g_{7/2} \otimes \nu h_{11/2}$ collective rotational band in ^{112}I , lifetime measurements have been performed in the present work using the Differential Plunger for Unbound Nuclear States (DPUNS) [10].

II. EXPERIMENTAL DETAILS AND ANALYSIS

Excited states in ^{112}I were populated with the $^{58}\text{Ni}(^{58}\text{Ni}, 3pn)$ fusion-evaporation reaction. The experiment employed a 230-MeV 4-pnA ^{58}Ni beam, produced with the K130 cyclotron at the Accelerator Laboratory of the University of Jyväskylä, which was used to bombard a 1.1-mg/cm² ^{58}Ni target for 12 days. A 1.5-mg/cm² ^{24}Mg

^{*}Present address: Division of Cancer Sciences, University of Manchester, Manchester, M20 4BX, United Kingdom.

degrader foil was placed downstream from the target. Subsequently, the degraded recoils traveled through the recoil ion transport unit (RITU) [11], triggering a multiwire proportional counter (MWPC) before they were implanted into a double-sided silicon strip detector (DSSD) [12]. RITU was used to transport the recoiling evaporation products, or recoils, to the focal plane while suppressing any primary beam.

The target was mounted at the center of JUROGAM-II γ -ray spectrometer, inside the DPUNS [10], along with the ^{24}Mg degrader foil. The JUROGAM-II array was used to measure the γ -ray intensities [13]. JUROGAM-II consisted of 39 Compton-suppressed germanium detectors arranged into four rings, with angles $\theta = 76^\circ, 105^\circ, 134^\circ$, and 158° with respect to the beam axis. Rings 1 and 2 consisted of 5 and 10 EUROGAM phase I-type detectors at angles of 158° and 134° , respectively [14]. The remaining two rings each contained 12 Clover detectors at $\theta = 76^\circ$ and $\theta = 105^\circ$ [15]. A total data readout (TDR) system recorded all detector events with a time stamp [16], allowing the GRAIN package to be used for offline analysis [17].

The degrader foil inside DPUNS reduced the velocity of the recoils, which split the intensity of each detected γ -ray transition into two Doppler-shifted components, $I^s(x)$ and $I^d(x)$. Here $I^s(x)$ is the component peak intensity corresponding to decays before the degrader foil (fully shifted), and $I^d(x)$ is the component peak intensity corresponding to decays after the degrader foil (degraded). The differential decay curve method (DDCM) was used on these component peak intensities as a function of plunger distance, $x = 135, 210, 300, 590$, and $3000 \mu\text{m}$, to deduce the lifetimes of the states of interest [18,19].

To remove the effect of potential side-feeding from higher lying states, a gate on the fully-shifted (fs) component of the γ ray directly above the level of interest was placed using the *gf3* software package [20,21]. The lifetime was determined by using Eq. (1) [18],

$$\tau(x) = \frac{1}{v} \frac{\{I_{\text{feed}}^s, I_{\text{dec}}^d\}(x)}{v \frac{d}{dx} \{I_{\text{feed}}^s, I_{\text{dec}}^s\}(x)}. \quad (1)$$

Here, v is the average recoil velocity and $\{I_{\text{feed}}^s, I_{\text{dec}}^d\}$ denotes the intensity in the degraded component of the γ ray from the decay of the level of interest measured in coincidence with the fully shifted peak of the γ ray from the decay of the direct feeding level. When a coincidence gate was set on a transition C above the level of interest, but not directly above (see Sec. III A), Eq. (2) was used:

$$\tau(x) = \frac{1}{v} \frac{\{I_C^s, I_{\text{dec}}^d\}(x) - \{I_C^s, I_B^d\}(x) \frac{I_C, I_{\text{dec}}}{I_C, I_B}}{\frac{d}{dx} \{I_{\text{feed}}^s, I_{\text{dec}}^s\}(x)}, \quad (2)$$

where $\{I_C^s, I_B^d\}$ is the intensity of the degraded components of transition B between the gate and the the state of interest. The term $\frac{I_C, I_{\text{dec}}}{I_C, I_B}$, which is often called α [18], reflects any intensity difference between the feeding and depopulating transitions.

As ^{112}I was a weakly populated channel in the $^{58}\text{Ni}(^{58}\text{Ni}, 3pn)$ reaction, a γ -ray coincidence gate was first required to select the ^{112}I nuclei from other reaction products.

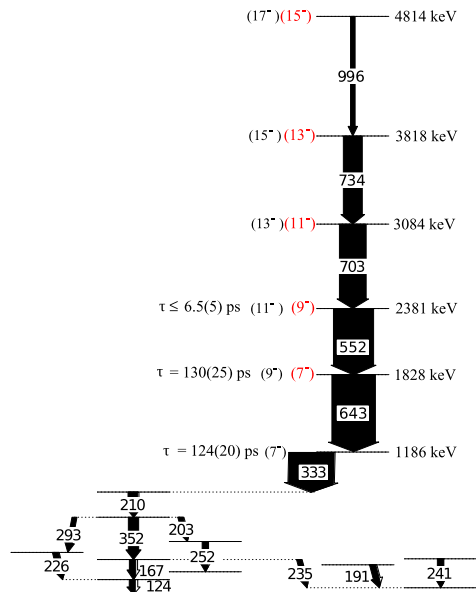


FIG. 1. The level scheme observed in this work for ^{112}I showing the low-spin single-particle levels and the higher lying single-signature rotational band. The level scheme is in agreement with Ref. [9] apart from the ordering of the 552- and 643-keV transitions which have been reversed in the present work (see Sec. IV). Proposed spin assignments from Ref. [9] are shown in black, and proposed assignments from this work are shown in red.

This selection gate set a requirement that only γ -ray events in coincidence with both components of either the 203- or 210-keV γ rays at the top of the lower spin single-particle structure in ^{112}I (see Fig. 1) were used in the subsequent γ - γ lifetime matrices. These gated two-dimensional (2D) γ - γ matrices were produced for ring 1 versus any detector in ring 1 or ring 2 (all) as a function of plunger distance. Likewise, 2D gated matrices were produced for ring 2 versus any detector in ring 1 or ring 2. These matrices are referred to as ring 1-all, and ring 2-all, respectively. In these matrices, a second gate on the fully-shifted component of the γ ray directly above the level of interest was then applied to remove potential side feeding. This gate was applied onto the all axis in order to produce the final double-gated spectra projected onto the ring 1 or ring 2 axis, which were used for to obtain the lifetime of interest. A single gate on the fully-shifted component on the all axis was used, as the Doppler shifts in rings 1 and 2 were very similar. In this work, the double gated spectra are denoted ($E_{\gamma}^{\text{below}}/E_{\gamma}^{\text{above}}$).

$I^s(x)$ and $I^d(x)$ were measured and normalized to the total number of counts in the x projection of the gated 2D matrix for a given x . A piecewise second-order polynomial was fitted to the fully-shifted component as a function of distance. The derivative of this was fitted to the degraded components and

TABLE I. The γ -ray energies and relative intensities of the lower transitions in the rotational band measured in this work from a double-gated spectrum, using the gates 203 or 210 keV with the 333-keV γ -ray transition.

E_γ (keV)	I_γ
551.5(3)	98(4)
642.7(2)	100(3)
702.5(2)	59(4)
733.7(3)	35(2)
996.7(4)	19(2)

Eq. (1) was used to calculate the lifetime at each of the target-to-degrader distances [19].

III. RESULTS

Figure 1 shows a partial level scheme of ^{112}I from this work, showing the single-particle states at low excitation energy and the collective band emerging at higher excitation energies. The observed sequence is in agreement with previous studies [9] apart from the order of the first two states in the rotational band (see Sec. IV). The widths of the arrows correspond to the efficiency corrected intensities measured in this experiment. The level scheme was constructed using data from clover versus clover gated γ - γ spectra, which combined the data from all distances. These detector rings are at 76° and 105° and hence the γ -ray Doppler shift is small. The measured γ -ray energies and intensities of the rotational structure from these gated γ - γ matrices are given in Table I.

Figure 2 shows typical spectra obtained for the band of interest, used to deduce the level scheme in Fig. 1. Figure 2(a) shows a projection of the JUROGAM-II clover versus clover γ - γ fully shifted matrix, for all distances combined for multiplicity 3 or higher events, where at least one of the events was detected in coincidence with the 203- or 210-keV transitions. The ^{112}I transitions are labeled with their γ -ray energies whereas γ rays originating from other reaction channels are labeled with symbols, defined in the legend. The main contaminants, with $A \approx 80$, were produced from ^{58}Ni reactions with the ^{24}Mg degrader foil. Figures 2(b) and 2(c) were created using the same gated γ - γ matrix and show decays in coincidence with the 552- and 703-keV transitions, respectively. The data were sorted using the measured recoil velocity of $v/c = 0.038(2)$ after leaving the target (fully shifted). The measured velocity after passing through the degrader (degraded) was $v/c = 0.018(2)$.

A. Lifetime analysis

In order to extract fully shifted and degraded component peak intensities as a function of target-to-degrader distance to perform a lifetime analysis, the fully shifted and degraded components of the γ -ray transitions depopulating the states of interest were measured using the gated background subtracted matrices of ring 1-all and ring 2-all. Gaussian fits were made to the fully shifted and degraded components. To reduce the

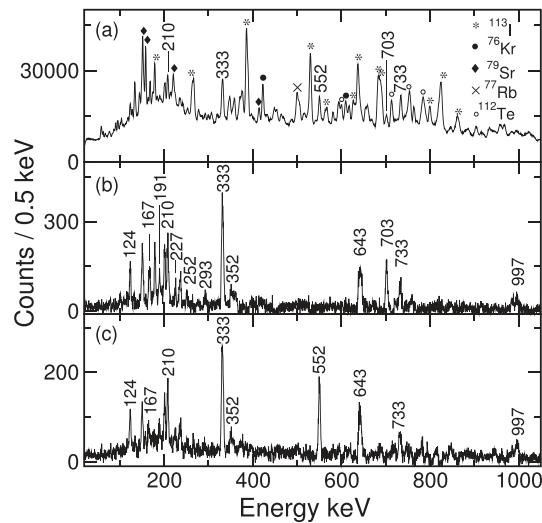


FIG. 2. ^{112}I spectra obtained from JUROGAM-II clover vs clover γ - γ matrices. (a) Single-gated projection using gates on both the 210- and the 203-keV transitions. ^{112}I transitions are labeled with their energies and contaminants are labeled with symbols given in the legend. Panel (b) shows a double-gated spectrum, using the same gate as panel (a) in coincidence with an additional 552-keV gate. Panel (c) is also a double-gated spectrum using the gate from (a) and an additional gate on the 703-keV transition.

fitting errors, the widths and centroids of the peaks were fixed. The fully shifted widths and centroids were fixed using the $3000\ \mu\text{m}$ distance and the degraded widths and centroids were fixed using the $135\ \mu\text{m}$ distance. At these respective distances, only one of the fully shifted or degraded components were present. Table II shows the fitted widths and centroids for 333- and 643-keV transitions.

1. Lifetime of the state which decays by the 333-keV transition

To examine the lifetime of the state at 1186 keV in ^{112}I , the 2D γ - γ ring 1-all and ring 2-all matrices were used to produce $((203, 210)/643_{f_s})$ gated spectra for each plunger distance.

TABLE II. The centroids (C) and widths (W) of the fully shifted and degraded components of the 333- and 643-keV transitions in ^{112}I from the ring 1-all and ring 2-all double-gated matrices. The double gates $((210, 203)/643_{f_s})$ and $((210, 203)/552_{f_s})$ are used, respectively.

γ -ray transition	Ring 1		Ring 2	
	C (keV)	W (keV)	C (keV)	W (keV)
333 keV (Shifted)	332.8	3.7	332.8	3.8
333 keV (Degraded)	337.8	3.6	336.8	3.3
643 keV (Shifted)	642.6	5.8	642.7	4.1
643 keV (Degraded)	653.2	4.1	650.5	3.6

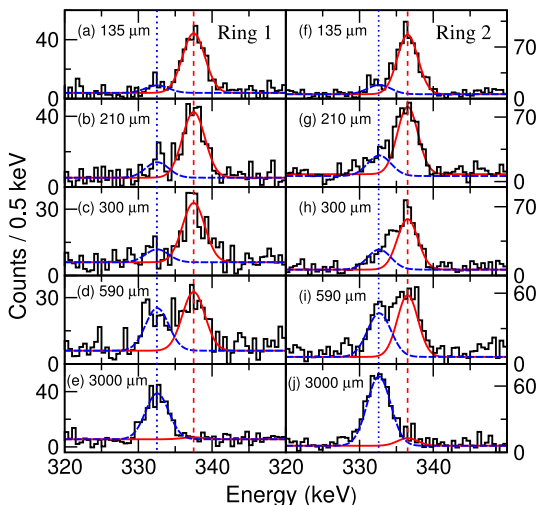


FIG. 3. ^{112}I double-gated spectra from the ring 1-all (left) and ring 2-all (right) matrices, using gates on both components of the 203- or 210-keV γ -ray transitions with the fully-shifted component of the 643-keV γ -ray transition. The fully shifted (blue-dashed) and degraded (red-solid) components of the 333-keV peak for ring 1 and ring 2 are shown for target-to-degrader distances 135 to 3000 μm , for panels (a) to (e) and (f) to (j). The presented spectra are Doppler corrected with respect to the recoil velocity after the target ($v/c = 0.038(2)\%$).

These spectra are shown in Fig. 3. The measured centroids of the fully shifted and degraded components are shown in dotted and dashed vertical lines, respectively. The normalized intensities of the two components of the 333- and 643-keV transitions are given at each distance in Table III.

The differential decay curve method was used to find the lifetime of the state decaying by the 333-keV γ -ray transition. Figures 4(a) and 4(d) show the lifetime of the state decaying via the 333-keV γ -ray transition for target-to-degrader distances in the region of sensitivity for ring 1 and ring 2, respectively. Figures 4(b) and 4(e) show the normalized component peak intensities of the fully-shifted component as a function of distance for rings 1 and 2, respectively, which were used to deduce the lifetimes of the states. Figures 4(c) and 4(f) show the normalized peak intensities of the degraded

TABLE III. The normalized intensities of the fully shifted and degraded γ -ray peak components of the 333- and 643-keV transitions in ^{112}I for both ring 1 and ring 2 detectors, using the double gates $((203, 210)/643_{fs})$ and $((203, 210)/552_{fs})$, respectively.

Distance (μm)	Ring 1 (134°)				Ring 2 (158°)			
	I_{333}^s	I_{333}^d	I_{643}^s	I_{643}^d	I_{333}^s	I_{333}^d	I_{643}^s	I_{643}^d
135	40(10)	310(20)	20(10)	150(30)	100(20)	570(60)	70(20)	260(40)
210	60(20)	260(30)	40(10)	120(20)	150(20)	440(40)	60(10)	230(30)
300	40(15)	190(20)	40(10)	140(20)	190(30)	420(50)	50(20)	210(30)
590	100(10)	140(15)	80(10)	120(20)	250(30)	320(40)	140(20)	150(20)
3000	230(30)	10(10)	170(20)	24(10)	550(60)	50(20)	230(30)	20(10)

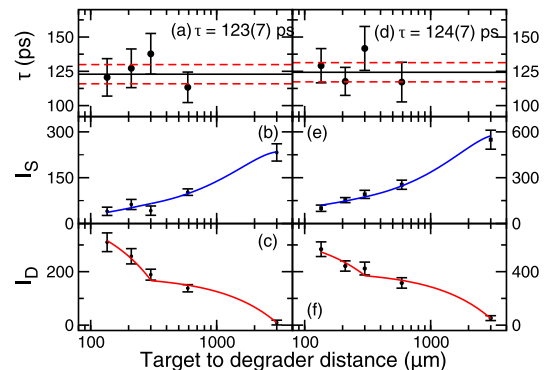


FIG. 4. (a) Lifetime analysis of the state in ^{112}I decaying via the 333-keV transition, based on DDCM using the ring 1 (left) and ring 2 (right) detectors. The intensities of the fully-shifted components of the 333-keV γ ray as a function of distance are shown in panels (b) and (e), with the degraded components in panels (c) and (f).

component as a function of distance. The weighted mean lifetimes calculated from ring 1 and ring 2 of $\tau = 123(7)$ ps and $\tau = 124(7)$ ps, respectively, are also shown.

The uncertainty shown on the lifetime fits is the weighted uncertainty of the lifetimes calculated at each distance. As the number of data points in the region of sensitivity was small, the fit to the data has relatively large uncertainties. This is partly due to not having an “anchor” point at small distances to constrain the fit. In this case, the weighted average of the lifetime from the four distance measurements results in an underestimate of the true lifetime uncertainty. A more accurate estimate of the uncertainty was made by varying the fit on the data to increase and decrease the χ^2 by 0.5, which gave an error of 20 ps. In view of this, the average lifetime of the state decaying via the 333-keV E1 γ -ray transition, using both ring 1 and ring 2, was deduced to be $\tau = 124(20)$ ps.

2. Lifetime of the state decaying by the 643-keV transition

Figure 5 shows the $((203, 210)/552_{fs})$ double-gated spectra used to obtain the intensities of the two components of the 643-keV transition. The intensities of each component at each distance are given in Table III, for ring 1 (left) and ring 2 (right).

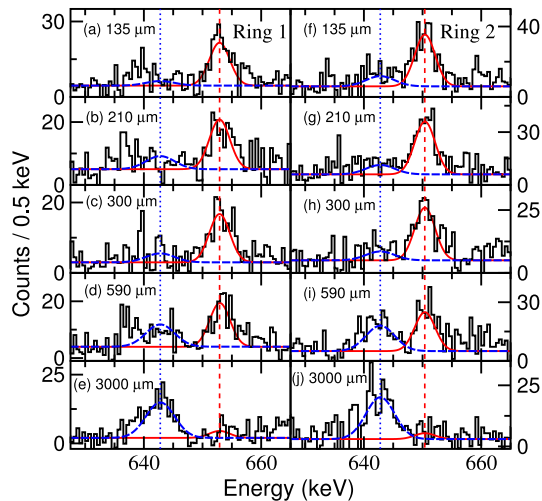


FIG. 5. ^{112}I double-gated spectra projected from the ring 1-all and ring 2-all matrices, using gates on both components of the 203- or 210-keV γ -ray transitions with the fully-shifted component of the 552-keV γ -ray transition. The fully shifted (blue-dashed) and degraded (red-solid) components of the 643-keV peak for ring 1 and ring 2 (left and right) are shown for target-to-degrader distances 135 to 3000 μm , for panels (a) to (e) and (f) to (j). The presented spectra are Doppler corrected with respect to the recoil velocity after the target ($v/c = 0.038(2)\%$).

Figures 6(a) and 6(d) show the lifetime of the state decaying by the 643-keV γ -ray transition for plunger distances in the region of sensitivity for ring 1 and ring 2, respectively. Figures 6(b) and 6(e) show the normalized intensities of the

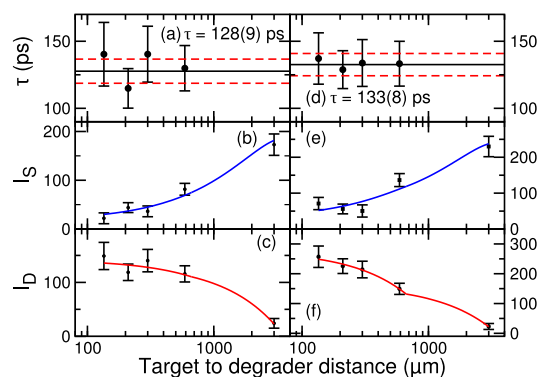


FIG. 6. (a) and (d) Lifetime analysis of the state in ^{112}I decaying by the 643-keV transition, based on DDCM using the ring 1 (left) and ring 2 (right) detectors. The intensities of the fully-shifted components of the 643-keV γ ray as function of distance are shown in panels (b) and (e), with the degraded components in panels (c) and (f).

fully-shifted component of the 643-keV γ -ray as a function of distance for rings 1 and 2, respectively. The solid lines show a least squares fit to the data. Figures 6(c) and 6(f) show the normalized intensities of the degraded component of the 643-keV γ ray as a function of distance with a least squares fit to the data (solid line). The weighted mean lifetimes for ring 1 and ring 2 of $\tau = 128(9)$ ps and $\tau = 133(8)$ ps are also shown.

As previously discussed, to better estimate the true error on the lifetime measurement for this state, the fit to the data was varied to increase and decrease the χ^2 by 0.5. The average lifetime of the state decaying by the 643-keV γ -ray was thereby deduced to be $\tau = 130(25)$ ps.

It should be noted that the γ -ray intensities of the 552- and 643-keV transitions from the lowest two states in the band are equal to each other within one standard deviation of their measured uncertainties in both the present and previous experiments [9]. This equality of transition intensities for the lowest two transitions in the band means that their order is somewhat ambiguous. This ambiguity could potentially affect the lifetime measurement, as in order to remove potential side feeding, the coincidence gate must be set above the transition of interest. For the lifetime analysis of the 1828-keV state shown in Fig. 1, both possible transition orderings for the 552- and 643-keV transitions were considered.

In the original level scheme proposed by Paul *et al.* [9], the 703-keV γ -ray directly feeds the state decaying by the 643-keV transition. For this level ordering, a lifetime analysis for the state decaying by the 643-keV transition was performed using a gate from above on the fully-shifted component of the 703-keV transition, which resulted in a lifetime of 135(20) ps.

In our revised level scheme, the 552-keV transition is the direct feeder of the 1828-keV state, and hence for the lifetime analysis of the 1828-keV state a gate was effectively placed on the fully-shifted component of the 552-keV transition and the lifetime was found to be 130(25) ps. In both approaches, Eq. (2) was used but the term $\langle I_{\vec{e}, l}^g(X) \rangle \approx 0$. Both measured lifetime values are consistent within one standard deviation.

The agreement in the lifetime values of the 1828-keV state from the two different gates distinguishes between the ordering presented in Fig. 1 and the ordering presented in Ref. [9]. If the original ordering from Ref. [9] remained unchanged, our gate on the fully-shifted component of the 552-keV transition would have yielded no events in the degraded component of the 643-keV transition because the gate would have been below the state of interest. The spectra produced using the gate on the fully-shifted component of the 552-keV transition is shown in Fig. 5 and events in both components of the 643-keV transition are observed. Using a similar logic, if the ordering in Fig. 1 is assumed, then a gate placed on the fully-shifted component of the 643-keV transition should produce no events in the degraded component of the 552-keV transition because the gate is set below the state of interest. In Fig. 7, it can be seen that no intensity in the degraded component of the 552-keV transition is observed at any target-to-degrader distance. These two points demonstrate that the 552-keV transition lies above the 643-keV transition. This is further discussed in Sec. IV A.

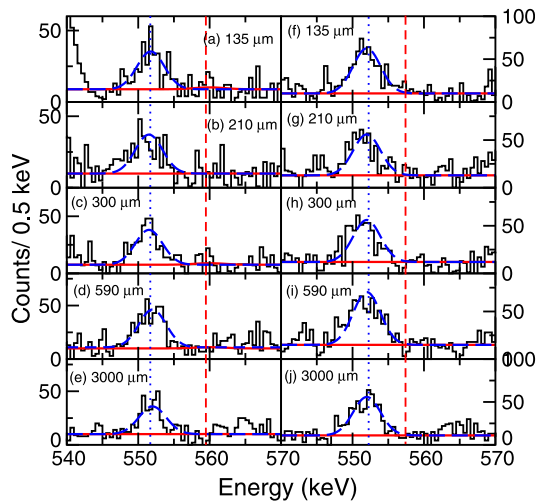


FIG. 7. ^{112}I double-gated spectra from the ring 1-all (left) and ring 2-all (right) matrices, using gates on both components of the 203- or 210-keV γ -ray transitions with the fully-shifted component of the 643-keV γ -ray transition. The fully shifted (blue-dashed) components of the 552-keV peak for ring 1 and ring 2 are shown. No intensity in the degraded component of the 552-keV peak is observed at any distance. The presented spectra are Doppler corrected with respect to the recoil velocity after the target ($v/c = 0.038(2)\%$).

3. Lifetime of the state decaying by the 552-keV transition

An attempt was made to deduce the lifetime of the state decaying via the 552-keV γ -ray transition. However, only a small component in the degraded peak of this transition was observed at the shortest 135 μm target-to-degrader distance; see Fig. 8. No intensity in the degraded peak was observed for larger distances.

Using the ratio of degraded to fully shifted intensities at 135 μm , an upper limit of $\tau \leq 6.5$ ps was de-

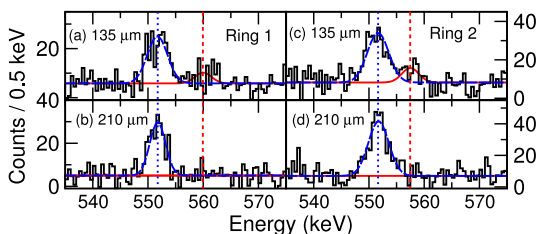


FIG. 8. ^{112}I double-gated spectra from the ring 1-all (left) and ring 2-all (right) matrices, using gates on both components of the 203- or 210-keV γ -ray transitions with the fully-shifted component of the 703-keV γ -ray transition. The fully shifted (blue-dashed) and degraded (red-solid) components of the 552-keV peak for ring 1 and ring 2 are shown for target-to-degrader distances of 135 and 210 μm . The presented spectra are Doppler corrected with respect to the recoil velocity after the target ($v/c = 0.038(2)\%$).

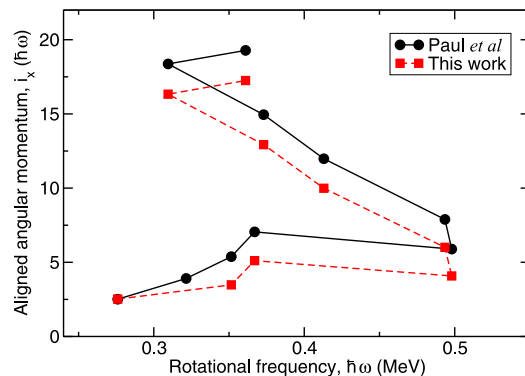


FIG. 9. Aligned angular momentum or alignment, i_x , for the band structure in ^{112}I from Ref. [9] in black solid line and from this work (red-dashed line) with the first two states in the band reordered (see text for details). Harris parameters [24] $\mathcal{J}_0 = 15\hbar^2 \text{MeV}^{-1}$ and $\mathcal{J}_1 = 25\hbar^4 \text{MeV}^{-3}$ have been subtracted from each band plotted in the figure.

duced for the lifetime of the state decaying via the 552-keV transition. Shorter target-to-degrader distances would be required to firmly establish the lifetime of this state.

IV. DISCUSSION

In the previous work [9], cranked shell model (CSM) and total Routhian surface calculations (TRS) [22,23] were performed in order to interpret the underlying configuration of the single rotational band in ^{112}I . These calculations predicted that the rotational structure in ^{112}I had a $\pi g_{7/2} \otimes \nu h_{11/2}$ configuration at low rotational frequencies. Additionally, in the previous work, directional correlation (DCO) ratios for several γ -ray transitions were measured. For example, the 643-keV transition was reasoned to be an $E2$ transition from the DCO ratio of 1.04(8) and the 333-keV transition was reasoned to be a dipole transition with some possible $E2$ mixing from the measured DCO ratio of 0.64(7) [9]. Based on these DCO ratios along with the TRS calculations, the state at 1186 keV was assigned to be the (7^-) bandhead of the $\pi g_{7/2} \otimes \nu h_{11/2}$ configuration [9]. From Ref. [9], the lower lying levels are due to single-particle structure.

A. Ordering of the states in the $\pi g_{7/2} \otimes \nu h_{11/2}$ band

The aligned angular momentum or alignment, i_x , for the $\pi g_{7/2} \otimes \nu h_{11/2}$ band is plotted (black solid line) in Fig. 9 from Ref. [9].

The large ($\approx 20\hbar$) gain in aligned angular momentum around rotational frequencies $\hbar\omega \approx 0.4$ MeV was interpreted to be due to simultaneous alignment of both proton and neutron in the $h_{11/2}$ orbitals [9]. Hence, the configuration of the structure at high rotational frequencies was deduced to be based upon a $\pi g_{7/2}[h_{11/2}]^2 \otimes \nu[h_{11/2}]^3$ configuration [9].

This configuration was the basis of the spin assignment for the band.

In the previous work [9], the γ -ray transitions in the rotational structure were ordered based on their intensities and coincidence relationships alone. In the present work, lifetimes of several of the states in this $\pi g_{7/2} \otimes \nu h_{11/2}$ rotational band have been measured for the first time. These lifetimes, and measured γ -ray coincidence relations between fully shifted and degraded components of consecutive transitions, suggested a reordering of two transitions in the band was required compared to Ref. [9]. Figure 5 shows the γ rays from the 643-keV transition in coincidence with the fully-shifted component of the 552-keV transition. Events in both the fully shifted and degraded components of the 643-keV transition are observed. The degraded component of the 643-keV transition can only be in coincidence with the fully-shifted component of the 552-keV transition if the 643-keV transition occurs after the 552-keV transition in time, supporting the ordering in Fig. 1. In a similar way, Fig. 7 shows the γ rays from the 552-keV transition in coincidence with the fully-shifted component of the 643-keV transition. No events in the degraded component of the 552-keV transition are observed at any distance. This suggests the 552-keV transition occurs before the 643-keV transition, again supporting the ordering presented in Fig. 1. This lifetime evidence supports a reordering of the 552- and the 643-keV transitions compared to the level scheme in Ref. [9]. However, it must be noted that the short lifetime of the state at 2381 keV would also produce spectra with no events in the degraded component of the 552-keV transition. Figure 1 shows the revised level scheme for the $\pi g_{7/2} \otimes \nu h_{11/2}$ rotational band based on the evidence presented in Sec. III A.

The long lifetime of the state at 1828-keV indicates that the state at 1186-keV has non-collective or hindered single-particle behavior (see Sec. IV B). This suggests that the 1186-keV state may not belong to the band. Thus, based on our lifetime measurements, we propose that the (7^-) bandhead may in fact be higher at 1828 keV. The rotational band is then built upon this (7^-) bandhead state at 1828-keV as suggested in Ref. [9]. Hence, Fig. 1 also shows revised tentative spin assignments for the rotational band.

Figure 9 shows the aligned angular momentum for the reordered structure in ^{112}I (red squares) where the first two states in the rotational band have been reversed in accordance with our lifetime measurements and the state at 1186 keV is no longer part of the band. The new tentative spin assignments from Fig. 1 are used. The revised alignment plot affects the alignment pattern of the lowest two states and does not change any of the proposed configurations and band crossings concluded in Ref. [9].

B. A comparison of predicted and experimentally deduced deformations

In the previous work [9], TRS calculations for the $\pi g_{7/2} \otimes \nu h_{11/2}$ configuration below the crossing predicted a quadrupole deformation and triaxiality, $(\beta_2, \gamma) \approx (0.175, 9^\circ)$. Above the crossing, these TRS calculations predict a more deformed and triaxial shape with $(\beta_2, \gamma) \approx (0.22, >15^\circ)$ for the $\pi g_{7/2}[h_{11/2}]^2 \otimes \nu[h_{11/2}]^3$ configuration [9]. The TRS calculations showed a trend of increasing triaxiality with increasing rotational frequency or seniority [9].

The deformation deduced from the lifetime measurement of the 643-keV transition in the present work was $\beta_2 = 0.021(8)$ [25]. This is 10 times smaller than the value predicted by the TRS calculations. Hence it was concluded that the state at 1186 keV does not form a part of the band. The deformation obtained from the limit on the lifetime of the 552-keV transition was $\beta_2 \geq 0.13$ [25]. This deformation is more comparable to that predicted from the TRS calculations for the $\pi g_{7/2} \otimes \nu h_{11/2}$ configuration, although the experimental value is only a lower limit. A more thorough lifetime experiment focused on ^{112}I would be required in order to make a full comparison with TRS.

V. CONCLUSIONS

In summary, the new lifetime measurements made in the present work reveal that the structure of the proposed rotational band in ^{112}I is more complicated than intensity and coincidence measurements alone reveal. Although the majority of the level scheme in this work is consistent with that established in Ref. [9], the lifetime measurements suggest a reordering of the lowest two transitions in the band. The relatively long lifetime of the state at 1828-keV suggest that it is the (7^-) bandhead. Hence, new tentative spin assignments have been given on the assumption that the state at 1828 keV is the true bandhead of the $\pi g_{7/2} \otimes \nu h_{11/2}$ band. Higher statistics data from γ -ray spectroscopy or an additional lifetime experiment, optimized for ^{112}I , would be required to help fully confirm the revised level ordering presented here.

ACKNOWLEDGMENTS

This work was supported by the EU 7th Framework Programme, Integrating Activities Transnational Access, Project No. 262010 ENSAR, and by the Academy of Finland under the Finnish Centre of Excellence Programme (Nuclear and Accelerator Based Physics Programme at JYFL). The authors acknowledge GAMMAPOOL support for the JUROGAM detectors and M.M.G., D.M.C., B.S.N.S., D.H., M.J.T., M.J.M., J.F.S., and M.S. acknowledge support of the Science and Technology Facilities Council, Grant No. ST/L005794/1.

- [1] C.-B. Moon, T. Komatsubara, and K. Furuno, Band structures in ^{116}I , *Nucl. Phys. A* **730**, 3 (2004).
 [2] E. S. Paul, D. B. Fossan, K. Hauschild, I. M. Hibbert, H. Schnare, J. M. Sears, I. Thorslund, R. Wadsworth, A. N. Wilson,

and J. N. Wilson, High-spin rotational bands in doubly odd ^{118}I , *J. Phys. G: Nucl. Part. Phys.* **22**, 653 (1996).

- [3] C.-B. Moon, G. Dracoulis, R. A. Bark, A. Byrne, P. Davidson, T. Kibedi, G. Lane, and A. Wilson, Various isomers

- in doubly odd I isotopes, *J. Korean Phys. Soc.* **59**, 1525 (2011).
- [4] P. Singh, S. Nag, K. Selvakumar, A. K. Singh, I. Ragnarsson, A. Bisoi, A. Goswami, S. Bhattacharya, S. Kumar, K. Singh *et al.*, High-spin spectroscopy of ^{122}I , *Phys. Rev. C* **85**, 054311 (2012).
- [5] R. Zheng, S. Zhu, N. Cheng, and J. Wen, Systematics of signature inversion in odd-odd nuclei in the mass regions $a = 80$ and $a = 160$, *Phys. Rev. C* **64**, 014313 (2001).
- [6] E. S. Paul, P. J. Woods, T. Davinson, R. D. Page, P. J. Sellin, C. W. Beausang, R. M. Clark, R. A. Cunningham, S. A. Forbes, D. B. Fossan *et al.*, In-beam γ -ray spectroscopy above ^{100}Sn using the new technique of recoil decay tagging, *Phys. Rev. C* **51**, 78 (1995).
- [7] M. A. Quader, W. F. Piel, S. Vajda, W. A. Watson, F. C. Yang, and D. B. Fossan, Proton-hole-induced bands in odd-odd $^{116,118,120,122}\text{I}$ nuclides, *Phys. Rev. C* **30**, 1772 (1984).
- [8] E. S. Paul, H. R. Andrews, T. E. Drake, J. DeGraaf, V. P. Janzen, S. Pilotte, D. C. Radford, and D. Ward, High-spin states in doubly odd ^{114}I , *Phys. Rev. C* **52**, 1691 (1995).
- [9] E. S. Paul, C. W. Beausang, R. M. Clark, R. A. Cunningham, D. B. Fossan, A. Gizon, J. Gizon, K. Hauschild, I. M. Hibbert, A. N. James *et al.*, High-spin states in doubly odd ^{112}I , *J. Phys. G: Nucl. Part. Phys.* **21**, 1001 (1995).
- [10] M. J. Taylor, D. M. Cullen, A. J. Smith, A. McFarlane, V. Twist, G. A. Alharshan, M. G. Procter, T. Braunroth, A. Dewald, E. Ellinger *et al.*, A new differentially pumped plunger device to measure excited-state lifetimes in proton emitting nuclei, *Nucl. Instrum. Methods Phys. Res., Sect. A* **707**, 143 (2013).
- [11] M. Leino, J. Jyst, T. Enqvist, P. Heikkinen, A. Jokinen, M. Nurmi, A. Ostrowski, W. Trzaska, J. Uusitalo, K. Eskola, P. Armbruster, and V. Ninov, Gas-filled recoil separator for studies of heavy elements, *Nucl. Instrum. Methods Phys. Res., Sect. B* **99**, 653 (1995).
- [12] R. D. Page, A. N. Andreyev, D. E. Appelbe, P. A. Butler, S. J. Freeman, P. T. Greenlees, R.-D. Herzberg, D. G. Jenkins, G. D. Jones, P. Jones *et al.*, The {GREAT} spectrometer, *Nucl. Instrum. Methods Phys. Res., Sect. B* **204**, 634 (2003).
- [13] C. W. Beausang and J. Simpson, Large arrays of escape suppressed spectrometers for nuclear structure experiments, *J. Phys. G: Nucl. Part. Phys.* **22**, 527 (1996).
- [14] C. W. Beausang, S. A. Forbes, P. Fallon, P. J. Nolan, P. J. Twin, J. N. Mo, J. C. Lisle, M. A. Bentley, J. Simpson, F. A. Beck, D. Curien, G. de France, G. Duchêne, and D. Popescu, Measurements on prototype Ge and {BGO} detectors for the Eurogam array, *Nucl. Instrum. Methods Phys. Res., Sect. A* **313**, 37 (1992).
- [15] G. Duchêne, F. A. Beck, P. J. Twin, G. de France, D. Curien, L. Han, C. W. Beausang, M. A. Bentley, P. J. Nolan, and J. Simpson, The Clover: A new generation of composite Ge detectors, *Nucl. Instrum. Methods Phys. Res., Sect. A* **432**, 90 (1999).
- [16] I. H. Lazarus, D. E. Appelbe, P. A. Butler, P. J. Coleman-Smith, J. R. Cresswell, S. J. Freeman, R. D. Herzberg, I. Hibbert, D. T. Joss, S. C. Letts *et al.*, The great triggerless total data readout method, *IEEE Trans. Nucl. Sci.* **48**, 567 (2001).
- [17] P. Rahkila, Grain a Java data analysis system for total data readout, *Nucl. Instrum. Methods Phys. Res., Sect. A* **595**, 637 (2008).
- [18] A. Dewald, O. Müller, and P. Petkov, Developing the recoil distance Doppler-shift technique towards a versatile tool for lifetime measurements of excited nuclear states, *Prog. Part. Nucl. Phys.* **67**, 786 (2012).
- [19] A. Dewald, S. Harissopoulos, and P. von Brentano, The differential plunger and the differential decay curve method for the analysis of recoil distance Doppler-shift data, *Z. Phys. A* **334**, 163 (1989).
- [20] D. Radford, Background subtraction from in-beam HPGE coincidence data sets, *Nucl. Instrum. Methods Phys. Res., Sect. A* **361**, 306 (1995).
- [21] D. Radford, Esc8r and levit8r: Software for interactive graphical analysis of HPGE coincidence data sets, *Nucl. Instrum. Methods Phys. Res., Sect. A* **361**, 297 (1995).
- [22] W. Nazarewicz, G. Leander, and J. Dudek, Octupole shapes and shape changes at high spins in Ra and Th nuclei, *Nucl. Phys. A* **467**, 437 (1987).
- [23] W. Nazarewicz, R. Wyss, and A. Johnson, Structure of superdeformed bands in the $A \approx 150$ mass region, *Nucl. Phys. A* **503**, 285 (1989).
- [24] S. M. Harris, Higher order corrections to the cranking model, *Phys. Rev.* **138**, B509 (1965).
- [25] R. B. Firestone, C. M. Baglin, and S. Chu, *Table of Isotopes*, Vol. 4 (Wiley, New York, 1999).

The remainder of this page was intentionally left blank.

Appendix B

Lifetime measurements in ^{50}Mn

This appendix presents the lifetime measurements of the first excited 2^+ state in ^{50}Mn . The lifetimes were measured using the Cologne plunger at the University of Cologne, Germany. ^{50}Cr , ^{50}Mn , and ^{50}Fe form an isobaric analogue triplet ideal for studying isospin symmetry breaking. The results of the lifetime measurement were submitted to the journal *Physical Review C*.

Probing isospin symmetry in the (^{50}Fe , ^{50}Mn , ^{50}Cr) isobaric triplet via electromagnetic transition rates

M.M. Giles, B.S. Nara Singh,* L. Barber, D.M. Cullen, and M.J. Mallaburn
*School of Physics & Astronomy, Schuster Building,
 The University of Manchester, Manchester M13 9PL, United Kingdom*

M. Beckers, A. Blazhev, T. Braunroth, A. Dewald, C. Fransen, A. Goldkuhle,
 J. Jolie, F. Mammes, C. Müller-Gatermann, D. Wölk, and K.O. Zell
Institut für Kernphysik, Universität zu Köln, Köln D-50937, Germany

S.M. Lenzi
*Dipartimento di Fisica e Astronomia dell'Università and INFN,
 Sezione di Padova, Via F. Marzolo 8, Padova I-35131, Italy*

A. Poves
*Departamento de Física teórica and IFT, UAM-CSIC,
 Universidad Autónoma de Madrid, Madrid E-28049, Spain*
 (Dated: December 27, 2018)

Lifetimes of the isobaric analog $T = 1$, $I^\pi = 2^+$ states in ^{50}Mn and ^{50}Cr were simultaneously measured by employing the recoil distance Doppler-shift (RDDS) technique. The states were populated in a fusion-evaporation reaction with a ^{12}C beam on a ^{40}Ca target. An analysis of the data and the calculations from the present work, together with the available $B(E2 : 2^+ \rightarrow 0^+)$ data of the isobaric analog states in ^{50}Fe and ^{50}Cr , have been used to study isospin symmetry in the three $A = 50$ isobaric nuclei. Shell-model calculations reproduce the magnitudes as well as the increasing trend of the $B(E2)$ data with Z . In order to draw a conclusion on the level of isospin mixing in the triplet, a new precision measurement of the $2^+ \rightarrow 0^+$ transition rate in ^{50}Fe will be required.

I. INTRODUCTION

Self-conjugate nuclei occupy a special place in the Segré chart where isospin-symmetry breaking (ISB) at the sub-nucleon level can manifest itself in bulk nuclear properties. For example, the observed slight differences between isobaric nuclei in the analogue level energies can originate from ISB [1]. Near identical level energies for isobaric analog states and the associated Coulomb energy differences (CED) have been extensively studied for $N \sim Z$ nuclei in the $A \sim 50$ and 70 regions [2–9]. The observed trends in the CED have been used to study nuclear phenomena such as backbending, rotational alignments of nucleons, changes in deformation, correlations of pairs of particles, and the evolution of radii [2–4, 6, 7, 9]. In addition to the Coulomb interaction, an isospin non-conserving interaction between nucleons has been required to explain the CED, implying ISB [5, 7, 8, 10].

Electromagnetic (EM) transition rates in nuclei can rigorously probe the associated nuclear wave functions and are subjected to additional constraints due to the selection rules for the transitions [11]. Therefore, lifetime data or reduced transition probabilities can be used to validate any conclusions drawn on ISB using CED data and

to stringently test models. In the context of the present lifetime measurements of the 2^+ states decaying through $E2$ γ -ray transitions, the matrix element

$$\sqrt{B(E2 \uparrow)} = M_{\text{tot}} = M^0 + \frac{M^1 T_z}{\sqrt{T(T+1)(2T+1)}}$$

has to be a linear function of $T_z = \frac{N-Z}{2}$ for isobaric nuclei with isospin-pure wave functions [12]. Here, M^0 and M^1 are the isoscalar and isovector matrix elements, respectively. In a $T_z = 0$ $N = Z$ nucleus, the isospin $T = 0$ and $T = 1$ states may reside close in energy, providing favorable conditions for the wave functions to mix in isospin. For example, the first excited 2^+ state of $T = 1$ type in ^{50}Mn resides ~ 1 MeV below the second known excited 2^+ state as shown in Fig. 1 [6]. If the latter is of $T = 0$ type and isospin mixing occurs significantly between these two states, then it could cause a nonlinear relationship between M_{tot} and T_z for the $A=50$ triplet. A compilation of data from several works designed to search for such nonlinearities in the $A = 22, 26, 30, 34, 38$ and 42 isobaric triplet nuclei is given in Ref. [12]. A significant deviation from a linear trend could be observed only for the $A = 38$ case.

Along the $N = Z$ line, the level of isospin mixing is expected to increase quadratically with proton number [13, 14]. Consequently, higher Z nuclei should in general serve as better candidates to study ISB. However, sensitivity of nuclear structure properties to the level of isospin mixing may be masked by nuclear phe-

*Present address: School of Engineering and Computing, University of the West of Scotland, Paisley, PA1 2BE, United Kingdom

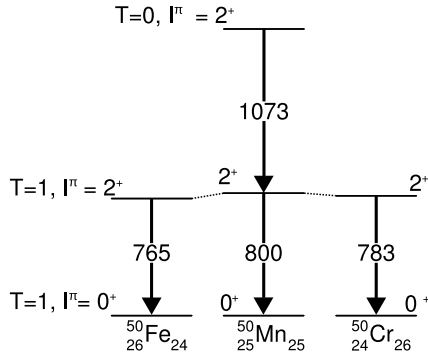


FIG. 1: A schematic representation of the $T = 1, 2^+ \rightarrow 0^+$ γ -ray transition energies (in keV) in the $A = 50$ triplet. In ^{50}Mn , the known second 2^+ state at an excitation energy of 1873 keV is also shown with a tentative assignment of $T = 0$ along with the observed 1073-keV γ decay to the first $T = 1, 2^+$ state [6].

nomena such as shape coexistence. Indeed, nuclei in the $A \sim 70, N \sim Z$ region prominently exhibit shape coexistence and therefore $A \sim 50, N \sim Z$ nuclei may well be relatively better candidates to isolate and study isospin mixing [15]. Despite such expectations and a strong motivation to study ISB of fundamental interest, measurements of transition rates in the $A \sim 50$ region have been extremely limited. This can be attributed to the low-production rates, hampering high-precision measurements [16–21].

In the present work, the lifetimes of the isobaric analog first 2^+ states in ^{50}Mn and ^{50}Cr nuclei have been simultaneously measured. The result for ^{50}Cr has been compared with the available precise data to estimate any systematic uncertainties that might be present in our measurements. The lifetime for $^{50}\text{Mn}(2^+)$ has been obtained for the first time. Although with a large uncertainty, the $B(E2 : 2^+ \rightarrow 0^+)$ value was previously measured for the analog 2^+ state in ^{50}Fe [22]. Combined with our shell-model calculations using well-developed effective nucleon-nucleon interactions, the data allowed us to carry out a comparative study of the EM transition rates in the $A = 50, N \sim Z$ isobaric triplet.

II. EXPERIMENTAL DETAILS

Excited states in $^{50}\text{Mn}/^{50}\text{Cr}$ were populated using the $^{40}\text{Ca}(^{12}\text{C}, \text{pn}/2\text{p})$ fusion-evaporation reaction in a chamber housing the Cologne plunger device [23] at the FN Tandem facility of the University of Cologne. A 30.5-MeV ^{12}C beam of ~ 5 -pnA current bombarded a 0.5 -mg/cm 2 ^{40}Ca target for ten days. The target foil had a ^{197}Au layer with a thickness of ~ 2 mg/cm 2 on one side (upstream) and of ~ 0.1 mg/cm 2 on the other side (down-

stream) to protect it from oxidation. To detect γ rays from the reaction products, the chamber was surrounded by 11 germanium detectors that were placed at a distance of ~ 12 cm from the center of the ^{40}Ca target. The arrangement resulted in two rings of detectors, namely, Ring(1) at $\theta = 142.3^\circ$ and Ring(2) at $\theta = 45.0^\circ$ with respect to the beam axis, consisting of 5 and 6 detectors, respectively. An additional detector, referred to as Ring(3), was placed at a similar distance from the target and at $\theta = 0^\circ$. Data from all of the detectors were recorded with time stamps using a 80-MHz clock. The ^{12}C beam energy was varied between 30 and 36 MeV [18, 24] and the observed intensity of the 343-keV $3^+ \rightarrow 2^+$ γ -ray transition in ^{50}Mn was used to conclude that a beam energy of 30.5 MeV would be optimal. The ^{50}Mn and ^{50}Cr recoils had velocities of $v \sim 1\% \times c$ after leaving the ^{40}Ca target (see Table I) and were stopped in a ^{181}Ta foil (stopper) with a thickness of ~ 3.5 mg/cm 2 . Here, c is the velocity of light. These two velocity regimes resulted in a Doppler-shifted (fully-shifted) peak and an unshifted peak with corresponding intensity components of I^s and I^{us} for a given γ -ray transition of interest in an energy spectrum. The ‘target-to-stopper’ (plunger) distances, x , were chosen so as to cover the expected ‘‘region of sensitivity’’ for a measurement of the lifetime of the 2^+ state in ^{50}Cr . In this region, there was a significant variation in $I^s(x)$ both for the 783- and 800-keV γ rays from the decays of the 2^+ states in ^{50}Cr and ^{50}Mn , respectively (cf. Fig. 1). Therefore, lifetime measurements for these states were carried out in the same experiment. Table I gives the ten plunger distances used in the present work. The procedure used to calculate the effective velocities, v_{eff} , as well as the effective distances, x_{eff} corresponding to the ^{50}Cr and ^{50}Mn recoils, which are required to perform the lifetime analysis, is discussed below (cf. Sec. III). Data were collected for ~ 12 hours at each of the distances and were analyzed using the differential decay curve method (DDCM) within the recoil distance Doppler-shift (RDDS) technique [23, 25, 26].

III. ANALYSIS AND RESULTS

Data were sorted offline using the SOCO2 software package [27]. Peaks with widths of $t_p \sim 500$ ns were observed in $\gamma\gamma$ time-difference (timing) spectra, corresponding to prompt γ rays at the target position. Therefore, time windows with widths of $t_{\text{bl}} \sim t_{\text{br}} \sim 250$ ns on the left and the right sides of this peak were used for background subtraction purposes. Ring(i) versus Ring(j) $\gamma\gamma$ energy matrices were thus constructed using the above values of t_p , t_{bl} and t_{br} . Here, i and j can take values of 1, 2 and 3, representing the three rings in the present setup. A $\gamma\gamma$ -coincidence analysis was then performed using the standard RADWARE package [28].

Figure 2(a) shows the Ring(1) γ -ray spectrum that was obtained by taking the total projection of the Ring(1) versus Ring(2) $\gamma\gamma$ energy matrix constructed us-

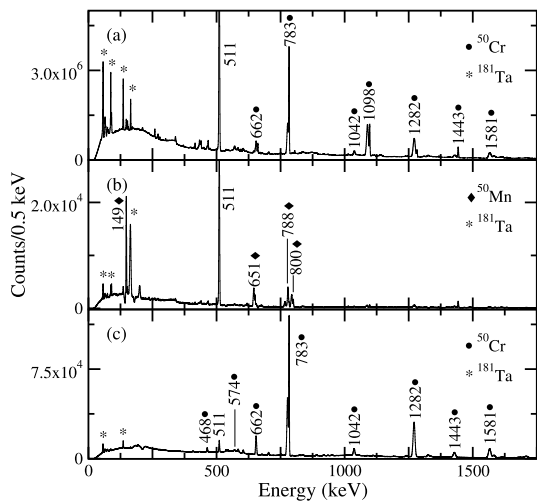


FIG. 2: γ -ray energy spectra of Ring(1), showing the total statistics collected for all of the distances given in Table I. The histograms were obtained by utilising the Ring(1) versus Ring(2) $\gamma\gamma$ energy matrix and (a) taking the total projection, (b) gating with the 343-keV line corresponding to the $3^+ \rightarrow 2^+$ γ decay in ^{50}Mn , and (c) gating with the 1098-keV line corresponding to the $4^+ \rightarrow 2^+$ γ decay in ^{50}Cr . The 610-keV transition is known to be much weaker compared to the 662-keV transition, therefore, was not prominent in the spectra [18].

ing all of the data collected at all of the plunger distances. The observed γ rays mainly belong to ^{50}Cr and ^{50}Mn . A few γ decays in ^{181}Ta , originating from the inelastic scattering of the beam, are also observed. Figure 2(b) shows a Ring(1) γ -ray spectrum gated by the $(3^+ \rightarrow 2^+)$ 343-keV line observed in Ring(2). As can be seen, the γ rays belonging to ^{50}Mn are enhanced. In Fig. 2(c), a similar spectrum gated by the $(4^+ \rightarrow 2^+)$ 1098-keV transition in ^{50}Cr shows γ rays mainly from ^{50}Cr . Figure 3 shows partial level schemes of ^{50}Mn and ^{50}Cr nuclei deduced from an analysis of the present data. Only low-lying levels were populated in ^{50}Mn . This can be attributed to the lower beam energy (or lower excitation energy of the compound nucleus) and to the more asymmetric reaction (or lower grazing angular momentum) used in the present work in comparison with that of the previous works [6]. Consequently, higher-lying states were expected to have a weak (or no) influence on the population of the first 2^+ state, allowing a reliable lifetime analysis.

Among all of the possible Ring(i) versus Ring(j) $\gamma\gamma$ energy matrices, the Ring(1) versus Ring(2) matrix was found to be the best choice for a clean lifetime analysis. Specifically in the Ring(1) γ -ray spectra, lines from contaminants appear away from the 800-keV line, corresponding to the 2^+ state decay in ^{50}Mn . For all of the other choices of matrices, contaminants overlapped

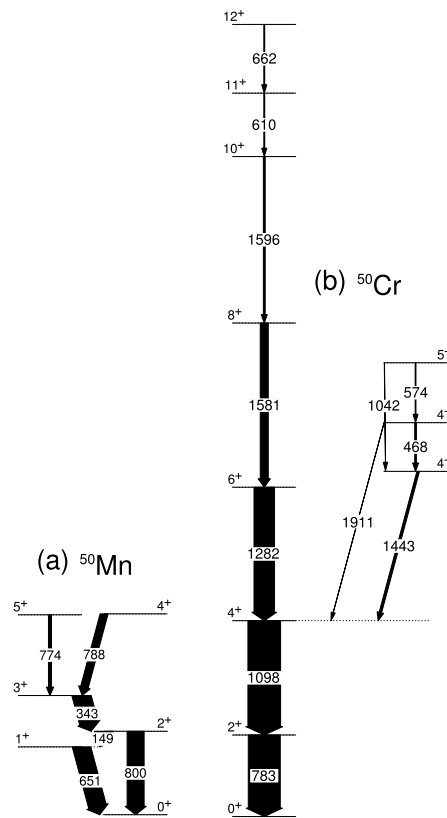


FIG. 3: Partial level schemes of (a) ^{50}Mn and (b) ^{50}Cr obtained from the present data. Only decays from low-lying states with spins ≤ 5 can be seen in ^{50}Mn due to much lower cross sections compared to ^{50}Cr .

with the γ -rays of interest. Therefore, they have not been used in the lifetime analysis. Figure 4 presents Ring(1) γ -ray spectra for all of the ten distances, x . The region relevant to the fully-shifted and unshifted components of the $2^+ \rightarrow 0^+$ 783-keV transition in ^{50}Cr is shown. These histograms are gated by the fully-shifted peak of the 1098-keV γ ray, corresponding to the $4^+ \rightarrow 2^+$ transition in ^{50}Cr (cf. Fig. 3(b)), in the Ring(2) γ -ray spectrum. High statistics and a clear separation between the fully-shifted and unshifted peaks allowed us to perform an accurate lifetime analysis. Table I gives the normalized intensities, $I^{us} \equiv \{I_{1098}^s, I_{783}^{us}\}(x)$ and $I^s \equiv \{I_{1098}^s, I_{783}^s\}(x)$. Here, $\{I_A^s, I_B^{us}\}$ is the intensity of the unshifted component of B in coincidence with the fully-shifted component of A . To extract, I^s , Gaussian fits were performed by leaving the width and centroid parameters free. In the case of the unshifted peaks, these parameters were fixed to those obtained with the data collected at $x = 20.8 \mu\text{m}$.

The lifetime of the 2^+ state in ^{50}Cr was determined in

TABLE I: A table of physical distances (x) between the target and the stopper, the normalized intensities of the fully-shifted ($I^s \equiv \{I_A^s, I_B^s\}(x)$) and the unshifted ($I^{us} \equiv \{I_A^{us}, I_B^{us}\}(x)$) components of B in coincidence with the fully-shifted component of A , the energy shift in the fully-shifted peak for Ring(1) (ΔE) and the effective velocity of the recoils at a given distance (v_{eff} relative to the velocity of light). x_{eff} is calculated using v_{eff} (see the text for details).

$x(\mu\text{m})$	$\{I_{343}^s, I_{800}^s\}$	$\{I_{343}^{us}, I_{800}^{us}\}$	$\Delta E_{800}^{\text{Mn}}(\text{keV})$	$\frac{v_{\text{eff}}^{\text{Mn}}}{c}(\%)$	$x_{\text{eff}}^{\text{Mn}}(\mu\text{m})$	$\{I_{1098}^s, I_{783}^s\}$	$\{I_{1098}^{us}, I_{783}^{us}\}$	$\Delta E_{783}^{\text{Cr}}(\text{keV})$	$\frac{v_{\text{eff}}^{\text{Cr}}}{c}(\%)$	$x_{\text{eff}}^{\text{Cr}}(\mu\text{m})$
20.8(2)	1793(59)	1177(44)	6.10(5)	0.963(6)	20.8(2)	24698(450)	69421(1290)	5.32(3)	0.864(3)	20.8(2)
26.8(2)	1895(62)	1085(33)	6.29(7)	0.995(10)	25.9(3)	30205(512)	73706(1220)	5.47(5)	0.888(7)	26.0(3)
29.7(2)	2257(78)	920(47)	6.30(11)	0.995(13)	28.8(3)	33712(821)	68149(1450)	5.55(7)	0.902(9)	28.5(3)
33.8(2)	2325(57)	845(34)	6.27(8)	0.990(11)	32.9(3)	37980(560)	67395(828)	5.64(5)	0.917(6)	31.8(3)
38.8(2)	2515(57)	655(26)	6.40(11)	1.010(13)	37.0(3)	45965(751)	61752(950)	5.82(5)	0.945(7)	35.4(3)
48.8(2)	2689(72)	386(28)	6.48(9)	1.024(11)	45.9(3)	59841(974)	49474(769)	5.94(5)	0.966(7)	43.6(3)
58.8(2)	2869(78)	325(27)	6.61(7)	1.044(9)	54.2(4)	69215(1167)	41369(719)	6.17(6)	1.003(7)	50.6(4)
68.8(2)	2949(89)	290(32)	6.64(6)	1.049(8)	63.1(4)	79940(1411)	32012(579)	6.19(3)	1.006(4)	59.0(4)
78.8(2)	2928(77)	121(20)	6.71(6)	1.060(8)	71.6(4)	86324(1594)	25621(553)	6.32(3)	1.028(4)	66.2(4)
166.8(2)	3261(147)	7(24)	6.76(6)	1.067(7)	150.5(8)	109442(2081)	5457(390)	6.51(2)	1.059(3)	136.0(8)

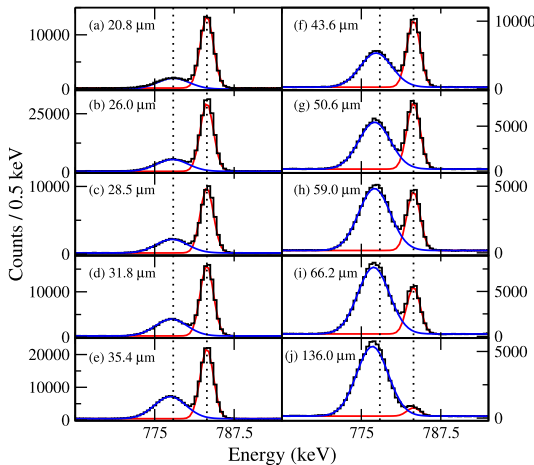


FIG. 4: γ -ray energy spectra of Ring(1), showing the fully-shifted and the unshifted peaks corresponding to the 783-keV γ -ray transition in ^{50}Cr . The histograms were obtained by utilising the Ring(1) versus Ring(2) $\gamma\gamma$ energy matrix and gating with the fully-shifted peak of the $4^+ \rightarrow 2^+$ 1098-keV transition on the Ring(2) axis. Each of the spectra (from (a) to (j)) is labelled with the effective plunger distance $x_{\text{eff}}^{\text{Cr}}$. The dotted lines corresponds to the centroids of fully-shifted and unshifted peaks of the 783-keV γ -ray at $x_{\text{eff}}^{\text{Cr}} = 20.8 \mu\text{m}$.

the standard DDCM [23] by using

$$\tau_{2+}(x) = -\frac{1}{v} \frac{d}{dx} \frac{\{I_{1098}^s, I_{783}^{us}\}(x)}{\{I_{1098}^s, I_{783}^s\}(x)}.$$

Firstly, $\tau_{2+}(x)$, was obtained from a piecewise fit to the fully-shifted peak intensities, i.e. $\{I_{1098}^s, I_{783}^s\}(x)$ [29]. Final values of τ_{2+} were then determined by using a χ^2 minimization procedure to fit $\{I_{1098}^s, I_{783}^{us}\}(x)$ to the derivative of this piecewise fitted function multiplied with

$v\tau_{2+}(x)$. The computer code NAPATAU [29] was used for this purpose. A weighted average of $\tau_{2+}(x)$ values within the ‘‘region of sensitivity’’ gives the measured lifetime, τ_{2+} , of the first 2^+ state in ^{50}Cr . The influence of the side-feeding on the lifetime result is avoided by gating directly above on the fully-shifted peak of the 1098-keV γ ray feeding the 2^+ state and analyzing I^s and I^{us} for the 783-keV γ ray [23]. The uncertainty in τ_{2+} has contributions from statistics, branching ratio, normalization procedure, distances and recoil velocities. The latter two are discussed below in more detail.

The intensities I^s and I^{us} were normalized in order to correct for differences in the total number of beam particles for the measurements carried out at different x . Three choices, namely, i) total counts in the Ring(1) γ -ray energy spectra that were obtained by taking total projections of the Ring(1) versus Ring(2) matrices, ii) intensities of the γ -ray transitions in ^{181}Ta and iii) intensities of the γ -ray transitions in ^{50}Cr , were tried [26]. In the latter method, statistics were sufficiently large and no systematic trend was present in $\tau(x)$ as a function of x . This indicates that the systematic error due to the presence of any contaminant nuclei was minimized and therefore proved to be the most reliable method. It also avoids any systematic errors that might be present in the choice (i). For example, uncertainties arising from the presence of activation γ -rays, which do not reflect the total number of beam particles used for a measurement at a given x , are avoided. In any case, the lifetime results obtained using the three different normalization methods were found to be consistent with each other within the uncertainties.

Figure 5 presents an analysis, using NAPATAU, of $I^s(x_{\text{eff}})$ and $I^{us}(x_{\text{eff}})$ for the 783-keV γ ray given in Table I. The measurement at $x_{\text{eff}}^{\text{Cr}} = 20.8 \mu\text{m}$ is not considered due to the unphysical gradients observed for $I^s(x)$ and $I^{us}(x)$, which might have originated from a relatively high systematic uncertainty for this smallest plunger distance. A lifetime value of 13.3(6) ps was thus obtained

for the 2^+ state in ^{50}Cr . This result is in a very good agreement with the published values of 12.8(7) ps [16, 17] and 13.2(4) ps [19], indicating an absence of any significant systematic errors in the present measurements. As shown in Fig. 6, a similar analysis for the 4^+ state in ^{50}Cr gives a lifetime of 4.9(7) ps that is consistent with the previously measured values of 3.2(4) ps [16, 17] and 3.2(7) ps [19]. The ratio

$$B_{4/2} = \frac{B(E2: 4^+ \rightarrow 2^+)}{B(E2: 2^+ \rightarrow 0^+)} = \frac{\tau_{2^+} E_\gamma^5(2^+ \rightarrow 0^+)}{\tau_{4^+} E_\gamma^5(4^+ \rightarrow 2^+)}$$

is calculated to be 0.50(8) using our results [30, 31]. Here, E_γ is the energy of the γ -ray transition. This result is in disagreement with the expected values of ~ 1.4 for a rotational nucleus and of ~ 2 for a vibrational nucleus. The calculated ratios using the available data for ^{50}Cr varied between 0.7 to 1.13 [16, 17, 19, 30, 32]. Clearly, the $B_{4/2}$ value in ^{50}Cr is found to be much less than 1 in the present work. Currently, this result is considered to be anomalous and cannot be explained by theoretical models [30, 31] and adds to such data in the $A \sim 50, 70, 110$ and 160 regions [33, 34].

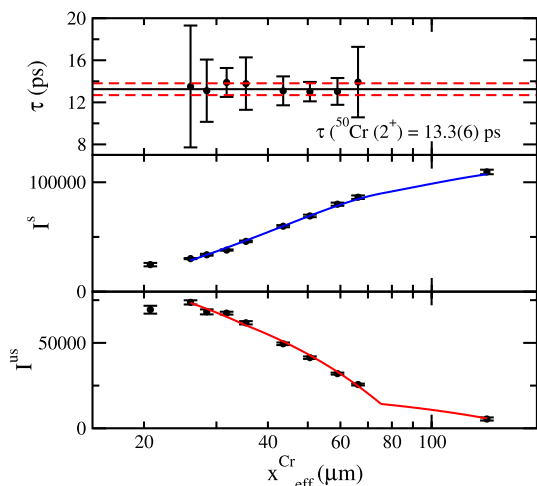


FIG. 5: An analysis of the intensities of the 783-keV γ -ray given in Table I to obtain the lifetime of the 2^+ state in ^{50}Cr . (a) The individual lifetimes obtained at eight distances in the “region of sensitivity” are shown. The final result from a weighted average is also given. The intensities, I^s and I^{us} at different distances are shown in (b) and (c), respectively, along with the best fits (solid lines) to those data obtained using NAPATAU [29].

Figure 7 shows the Ring(1) γ -ray spectra gated by the fully-shifted peak of the $3^+ \rightarrow 2^+$ 343-keV decay in ^{50}Mn (cf. Fig. 3(a)), observed in the Ring(2) γ -ray spectra. The region relevant to the $2^+ \rightarrow 0^+$ 800-keV transition in ^{50}Mn is shown for all x with the clearly separated fully-shifted and unshifted peaks. The I^s and I^{us} for

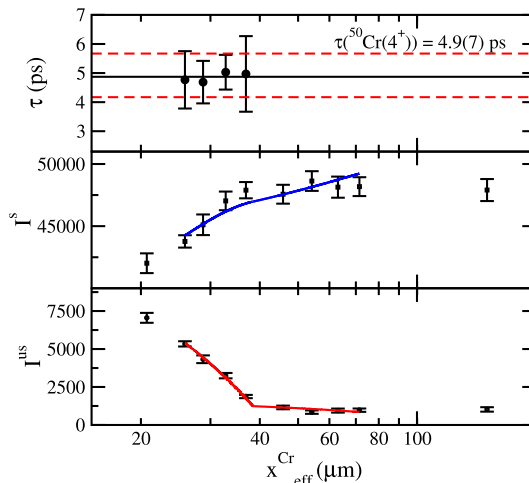


FIG. 6: Same as Fig. 5 for the 4^+ state in ^{50}Cr .

the 800-keV line, obtained from these spectra, are given in Table I. Figure 8 shows an analysis using NAPATAU, resulting in a lifetime value of $\tau(^{50}\text{Mn}(2^+)) = 6.4(2)$ ps.

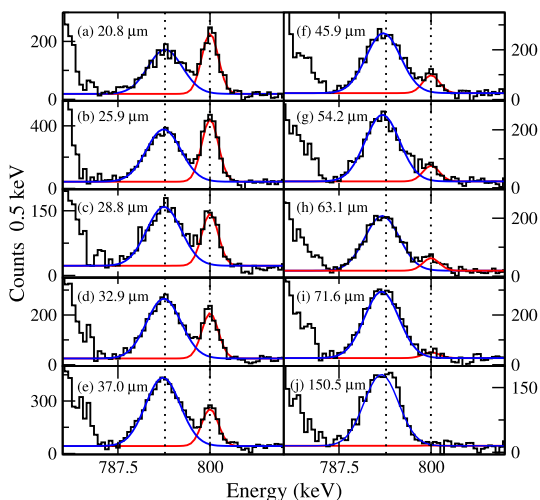


FIG. 7: Similar to Fig. 4, γ -ray energy spectra gated by the fully-shifted peak of the $3^+ \rightarrow 2^+$ 343-keV transition in ^{50}Mn , showing the fully-shifted and unshifted peaks of the 800-keV γ -ray.

It is evident from Figs. 4 and 7 that there is a systematic variation in the centroid of the fully-shifted peak as a function of x , similar to that discussed in Ref. [35]. This can be understood in terms of the recoil-velocity distribution corresponding to the fully-shifted peak. In par-

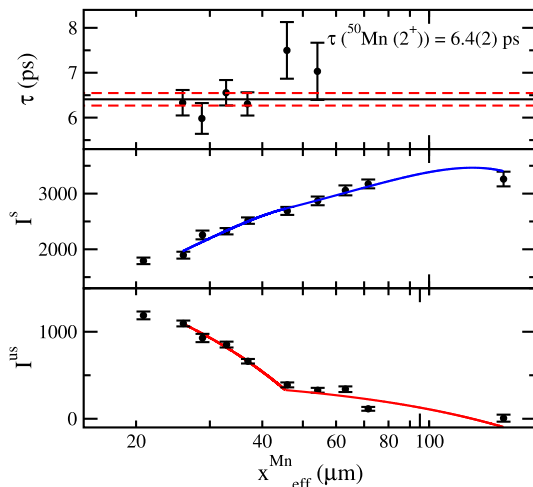


FIG. 8: Same as Fig. 5 for the 2^+ state in ^{50}Mn .

ticular, the effect arises because the relation of the recoil velocity with flight time (or x) between the foils is linear while it is exponential between I^s and x . In other words, the γ -ray intensities in the fully-shifted peaks have more contributions from slower recoils at smaller distances. In order to account for this, firstly, the Doppler shift observed for the 800-keV $2^+ \rightarrow 0^+$ γ -ray transition in ^{50}Mn was obtained at $x \sim 20.8 \mu\text{m}$. The corresponding effective velocity of the recoils (v^{rec}) was then deduced by using $|\Delta E_\gamma| = (v^{\text{rec}}/c) \times |\cos\theta|$. Here, θ is the angle of the ring of γ -ray detectors under consideration with respect to the beam direction. This effective recoil velocity ($v_{\text{eff}}^{\text{rec}}$) at $\sim 20.8 \mu\text{m}$ was fixed to be the ‘nominal recoil velocity’ ($v_{\text{nom}}^{\text{rec}}$). Differences between $v_{\text{nom}}^{\text{rec}}$ and $v_{\text{eff}}^{\text{rec}}(x)$ at all of the other x , $dv^{\text{rec}}(x) = v_{\text{nom}}^{\text{rec}} - v_{\text{eff}}^{\text{rec}}(x)$, were then obtained by using the correspondingly observed Doppler shifts for the 800-keV γ ray. As shown in Table I for the case of ^{50}Mn , a systematic change in the effective recoil velocity from $v_{\text{eff}}^{\text{rec}}/c \sim 0.96\%$ (around $20 \mu\text{m}$) to $\sim 1.07\%$ ($170 \mu\text{m}$) was observed as a function of x . The effective plunger distances ($x_{\text{eff}}^{\text{rec}}$), corresponding to $v_{\text{nom}}^{\text{rec}}$, were then obtained by correcting the original plunger distances with the flight path corresponding to $dv^{\text{rec}}(x)$. A similar analysis was also performed for the 783-keV $2^+ \rightarrow 0^+$ γ decay in ^{50}Cr . The x and $x_{\text{eff}}^{\text{rec}}$ corresponding to these recoil nuclei are reported in Table I. The latter was used for the lifetime analysis performed using NAPATAU. Slight differences between the effective velocities of ^{50}Mn and ^{50}Cr recoils can be noted from the table. This is not surprising because these nuclei were produced in two different (pn and $2p$) reaction channels with a broader velocity distribution for ^{50}Cr recoils. In addition, the corresponding 2^+ states have significantly different lifetimes, leading to a larger x range for $I^{\text{us}}/I^{\text{tot}}$ in the case of ^{50}Cr compared to that for ^{50}Mn . Monte-Carlo simulations [36]

were performed in order to understand the effective recoil velocity as a function of distance. The variations in centroids observed in Figs. 4 and 7 could be reproduced when the thickness of the ^{40}Ca target-foil was set to be 0.65 mg/cm^2 . This is different from the quoted value of 0.50 mg/cm^2 , which could have been underestimated. It is also possible that the recoils traveled through the ^{197}Au layer that was thicker than 0.1 mg/cm^2 , the effect of which could not be disentangled unambiguously from the effect of the difference in the target thickness. In summary, simulations using slightly higher overall foil thickness traversed by the recoils reproduce the observed systematic trends in the centroids of the fully-shifted peak.

IV. DISCUSSION

The $B(E2 \downarrow: 2^+ \rightarrow 0^+)$ value of $237(8) e^2\text{fm}^4$ for ^{50}Mn obtained from the present work is reported in Table II together with the known value for ^{50}Fe [22]. The measured relative intensities of 64.1(12) and 100 (2) were used for the 149 keV and 800 keV γ -decays, respectively, in order to calculate the $B(E2)$ value from the measured lifetime of the first 2^+ state in ^{50}Mn [37]. The $B(E2)$ value presented for ^{50}Cr is a weighted average of the data from the present and previous works [16, 17, 19]. The experimental values are compared with our theoretical predictions obtained using the shell model code ANTOINE [38] in the full pf space. Two sets of calculations are reported in Table II. The $B(E2)_{gxc}$ values have been predicted using the GXPF1A effective interaction [39] plus the Coulomb matrix elements obtained in the harmonic oscillator basis with single-particle energy corrections following Ref. [2] and the standard effective charges of $e_\pi = 1.5$ and $e_\nu = 0.5$. In the case of $B(E2)_{kbc}$, the KB3GR effective interaction has been used [40] together with $e_\pi = 1.31$ and $e_\nu = 0.46$ that were deduced in Ref. [41]. The Coulomb matrix elements have been obtained in the same way as for the other calculation, but with the single-particle energy corrections that reproduce the experimental energies in ^{41}Ca and ^{41}Sc . The $B(E2)_{gxc}$ values calculated using the GXPF1A effective interaction and without the Coulomb matrix elements are also reported for comparison. Figure 9 summarizes $M(E2) = \sqrt{B(E2 \uparrow: 0^+ \rightarrow 2^+)}$ values for the $A = 50$, $T = 1$ triplet, presenting the current status of the agreement between the data and the calculations. Both of the calculations reproduce the data for the triplet with good accuracy. The shell-model values follow a rather linear and slightly increasing behavior with Z for the $M(E2)$ matrix element, which is fully consistent with the data. However, the high uncertainty in the measurement of ^{50}Fe precludes a final conclusion. The calculations suggest a very small isospin mixing, as the non-diagonal Coulomb matrix elements are of the order of a few tens of keV. A more precise determination of the $B(E2)$ value in ^{50}Fe would allow for more definitive conclusions on the presence or absence of a nonlinear dependence of the

TABLE II: A comparison between data and shell model predictions of the $B(E2)$ values for the $A = 50$, $T = 1$ triplet. Here, gxc and kbc correspond to the calculations carried out using the GXPF1A and the KB3GR interactions, respectively, that include Coulomb matrix elements while gx corresponds to the prediction without Coulomb contribution and using the GXPF1A interaction (see text for details).

Nucleus	$E(2^+)_{ex}$ (keV)	$E(2^+)_{gxc}$ (keV)	$B(E2)_{ex}$ ($e^2\text{fm}^4$)	$B(E2)_{gxc}$ ($e^2\text{fm}^4$)	$B(E2)_{gx}$ ($e^2\text{fm}^4$)	$B(E2)_{kbc}$ ($e^2\text{fm}^4$)
^{50}Fe	765	779	281(61)	217	225	201
^{50}Mn	800	796	237(8)	214	221	200
^{50}Cr	783	784	211(4)	211	217	196

matrix element with T_z .

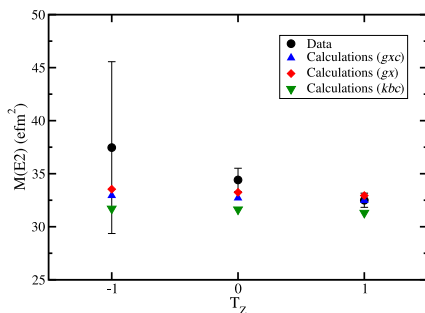


FIG. 9: The matrix element $M(E2)$ as a function of T_z for the three $T = 1$, $A = 50$ isobaric nuclei. Datum for ^{50}Mn was obtained for the first time in the present work. In the case of ^{50}Cr , the data point is a weighted average of our result and that from Refs. [16, 17, 19] while the result from Ref. [22] has been used for the case of ^{50}Fe with $T_z = -1$. The predictions from our calculations are also shown (see the text for details).

V. CONCLUSIONS

The lifetimes of the $T=1$ isobaric analog 2^+ states in ^{50}Cr and ^{50}Mn were measured in the same experiment us-

ing the plunger technique. The present datum for ^{50}Cr agrees with that from the previous works, granting reliability for the new result obtained for ^{50}Mn . Both the data and the predictions from the large-scale shell model calculations exhibit a rather linear and slightly increasing behavior of the $M(E2)$ matrix element with Z for the $A = 50$, $T = 1$ isobaric triplet. At present the data available for the proton-rich ^{50}Fe nucleus has a very large uncertainty and a high precision measurement is required in order to conclude on isospin-symmetry breaking in this triplet.

VI. ACKNOWLEDGMENTS

We gratefully acknowledge the support of accelerator staff and the students at the FN Tandem facility of the University of Cologne. M.M.G., B.S.N.S., L.B., D.M.C., and M.M. acknowledge support of the Science and Technology Facilities Council, Grant No. ST/L005794/1. M.B., A.B., T.B., A.D., A.G., C.F., J.J., F.M., C.M., D.W. and K.O.Z. were funded by the German Ministry of Science and Education (BMBF), Grant No. 05P15PKFNA. A.P. was partially supported by MINECO (Spain) grants FPA2014-57196, the Severo Ochoa Programme SEV-2016-0597.

- [1] P. Baczyk *et al.*, arXiv:1701.04628 [nucl-th] (2017).
- [2] M.A. Bentley and S.M. Lenzi, *Prog. Part. Nucl. Phys.* **59**, 497 (2007).
- [3] D.D. Warner *et al.*, *Nature Phys.* **2**, 311 (2006).
- [4] S.M. Lenzi *et al.*, *Phys. Rev. Lett.* **87**, 122501 (2001).
- [5] P. J. Davies *et al.*, *Phys. Rev. Lett.* **111**, 072501 (2013).
- [6] C.D. O'Leary *et al.*, *Phys. Lett. B* **525**, 49 (2002).
- [7] S.A. Milne *et al.*, *Phys. Rev. Lett.* **117**, 082502 (2016).
- [8] J. Henderson *et al.*, *Phys. Rev. C* **90**, 051303 (2014).
- [9] B.S. Nara Singh *et al.*, *Phys. Rev. C* **75**, 061301 (2007).
- [10] A.P. Zuker, S.M. Lenzi, G. Martínez-Pinedo and A. Poves, *Phys. Rev. Lett.* **89**, 142502 (2002).
- [11] L.A. Radicati, *Phys. Rev.* **87** 521 (1952) and the references therein.
- [12] F.M. Prados Estevez *et al.*, *Phys. Rev. C* **75**, 014309 (2007) and the references therein.
- [13] P. Van Isacker, *Rep. Prog. Phys.* **62**, 1661 (1999).
- [14] G. Colo *et al.*, *Phys. Rev. C* **52**, R1175 (1995).
- [15] A. Petrovici, *Phys. Rev. C* **91**, 014302 (2015).
- [16] L.K. Peker, *Nucl. Data Sheets* **68**, 271 (1993), T.W. Burrows, *ibid.* **68**, 1 (1993), **75**, 1 (1995), Huo Junde, *ibid.* **71**, 659 (1994).
- [17] F. Brandolini *et al.*, *Nucl. Phys. A* **642**, 387 (1998).
- [18] N. Pietralla *et al.*, *Phys. Rev. C* **65**, 024317 (2002).
- [19] R. Ernst *et al.*, *Phys. Rev. C* **62**, 024305 (2000), *Phys. Rev. Lett.* **84**, 416 (2000) and <http://www.nmdc.bnl.gov/ensdf/>.
- [20] M.A. Bentley, Priv. comm.

- [21] K. Jessen *et al.*, Phys. Rev. C **74**, 021304 (2006).
- [22] K. Yamada *et al.*, Eur. Phys. J A **25**, 409 (2005) and <http://www.nndc.bnl.gov/ensdf/>.
- [23] A. Dewald, O. Moller, and P. Petkov, Prog. Part. Nucl. Phys. **67**, 786 (2012).
- [24] C.W. Beausang *et al.*, Nucl. Instr. Meth. Phys. Res. A **452**, 431 (2000).
- [25] A. Dewald, S. Harissopulos, and P. von Brentano, Z. Phys. A At. Nucl. **334**, 163 (1989).
- [26] D. Hodge *et al.*, Phys. Rev. C **94**, 034321 (2016).
- [27] The SOCO software package developed by nuclear physics group of The University of Cologne, N. Saed-Samii, Diploma Thesis (2013).
- [28] D. C. Radford, Nucl. Instr. Meth. Phys. Res., Sect. A **361**, 297 (1995).
- [29] G. Böhm, A. Dewald, P. Petkov, and P. von Brentano, Nucl. Instr. Meth. Phys. Res. A **329**, 248 (1993).
- [30] D. Hertz-Kintish, L. Zamick, and S.J.Q. Robinson, Phys. Rev. C **90**, 034307 (2014).
- [31] B. Cederwall *et al.*, Phys. Rev. Lett. **121**, 022502 (2018).
- [32] F. Brandolini *et al.*, Phys. Rev. C **70**, 034302 (2004).
- [33] B. Saygi *et al.*, Phys. Rev. C, **96**, 021301(R) (2017).
- [34] R. B. Cakirli, R. F. Casten, J. Jolie, and N. Warr, Phys. Rev. C **70**, 047302 (2004).
- [35] K. Arnsward *et al.*, Phys. Lett. B **772**, 599 (2017).
- [36] T. Braunroth, PhD Thesis (2017), https://kups.ub.uni-koeln.de/7956/1/Braunroth_Dissertation_pub.pdf.
- [37] A. Schmidt *et al.*, Phys. Rev. C **62**, 044319 (2000).
- [38] E. Caurier and F. Nowacki, Act. Phys. Pol. B **30**, 705 (1999).
- [39] M. Honma, T. Otsuka, B. A. Brown and T. Mizusaki, Phys. Rev. C **65**, 061301 (2002).
- [40] E. Caurier and A. Poves, *unpublished*.
- [41] M. Dufour and A. P. Zuker, Phys. Rev. C **54**, 1641 (1996).

The remainder of this page was intentionally left blank.

Appendix C

Triple foil plunger for exotic nuclei (TPEN)

This appendix presents the paper submitted to Nuclear instruments and Methods A. The paper summarises the results of the commissioning experiment presented in this thesis.



Contents lists available at ScienceDirect

Nuclear Inst. and Methods in Physics Research, A

journal homepage: www.elsevier.com/locate/nima

TPEN: A Triple-foil differential Plunger for lifetime measurements of excited states in Exotic Nuclei

M.M. Giles^{a,*}, D.M. Cullen^a, L. Barber^a, B.S. Nara Singh^{a,1}, M.J. Taylor^{a,2}, A.J. Smith^a, A. McFarlane^a, C. Read^a, T. Grahn^b, H. Badran^b, P.T. Greenlees^b, R. Julin^b, J. Pakarinen^b, J. Partanen^b, P. Rahkila^b, P. Ruotsalainen^b, M. Sandzelius^b, J. Sarén^b, J. Sorri^b, S.V. Szwece^b, J. Uusitalo^b, J. Heery^c, E. Parr^c, P. Papadakis^c, R.D. Herzberg^c

^a School of Physics & Astronomy, Schuster Building, The University of Manchester, Manchester M13 9PL, United Kingdom

^b University of Jyväskylä, Department of Physics, P.O. Box 35, FI-40014, Finland

^c Department of Physics, Oliver Lodge Laboratory, University of Liverpool, Liverpool, L69 7ZE, United Kingdom



ARTICLE INFO

Keywords:

Plunger
Triple-foil plunger
Excited-state lifetimes
¹⁵⁶Dy
RDDS
DDCM

ABSTRACT

A Triple-foil differential Plunger for Exotic Nuclei (TPEN) has been developed to measure the lifetimes of excited states in nuclei with small production cross-sections. TPEN utilises one target foil and two degrader foils to make differential lifetime measurements: directly determining the decay function and its derivative at a single plunger distance setting. The direct measurement of the decay function and its derivative removes the requirement to measure γ -ray intensities at several target-to-degrader distances, thereby reducing the beam-time required relative to a conventional plunger with a single-degrader foil. This paper describes the commissioning of TPEN in the lifetime measurement of the first excited 4^+ state in ¹⁵⁶Dy using this differential lifetime technique. The 46(2) ps measured lifetime was found to be in good agreement with the 45.6(5) ps deduced from a previous high-statistics experiment using a conventional two-foil plunger. A comparison between the differential mode with TPEN, and that using TPEN as a conventional two-foil plunger reveals that it achieves the same statistical accuracy with a ~ 4 -fold reduction in beam-time in the differential mode, for the reaction and experimental setup used in this work. TPEN opens up new opportunities to study exotic nuclei with lower production cross-sections that were previously not accessible.

1. Introduction

Experimental studies of nuclei at the limits of existence will form a major part of international research programmes at radioactive ion beam facilities. Determining the lifetimes of excited states in these exotic nuclei can reveal subtle properties of the nuclear force which are masked in the more strongly bound nuclei near to the valley of stability. As the electromagnetic (EM) operator is extremely well understood, transition rates between excited nuclear states provide useful knowledge of the wave functions of the states involved. For example, the lifetimes of nuclear states are particularly sensitive to a variety of nuclear structure features including changes in conventional shell gaps, shape co-existence, isospin symmetry, proton–neutron coupling and the coupling between discrete levels and the continuum [1–5].

The main obstacle in performing experiments on exotic nuclei far from stability is their small production cross-sections. For example, conventional plunger devices such as the Differential Plunger for Unbound

Nuclear States, (DPUNS) [6] are limited to measuring lifetimes in nuclei with production cross-section greater than 10–20 μb [7–11]. In order to study nuclei with smaller production cross-sections, the Triple-foil differential Plunger for Exotic Nuclei (TPEN) was developed at The University of Manchester. TPEN is more efficient than traditional two-foil plungers as it utilises the differential mode of the differential-decay curve method (DDCM) to directly determine the decay function and its derivative at a single plunger distance setting [12].

TPEN was commissioned at the Accelerator Laboratory of the University of Jyväskylä (JYFL), Finland. This paper presents the results of this commissioning experiment in which the lifetime of the first excited 4^+ state in ¹⁵⁶Dy was measured. The lifetime measured with TPEN was found to be in agreement with that determined from a conventional plunger experiment [13]. A comparison between the differential mode of TPEN and TPEN acting as a conventional plunger reveals that it achieves the same statistical accuracy with approximately 4-fold reduction in beam-time with this ²⁴Mg(¹³⁶Xe, 4n) reaction. The improved

* Corresponding author.

E-mail address: Michaelgiles145@gmail.com (M.M. Giles).

¹ Present address: School of Engineering and Computing, The University of The West of Scotland, Paisley, PA1 2BE, United Kingdom.

² Present address: Division of Cancer Sciences, The University of Manchester, Manchester, M20 4BX, United Kingdom.

<https://doi.org/10.1016/j.nima.2019.01.089>

Received 3 December 2018; Received in revised form 26 January 2019; Accepted 28 January 2019

Available online 4 February 2019

0168-9002/© 2019 Published by Elsevier B.V.

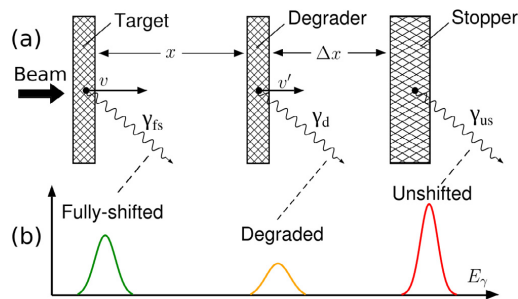


Fig. 1. (a) A schematic illustration of the TPEN target, degrader and stopper foils along with (b) the three Doppler shifted γ -rays and their energies. The Doppler shifts shown are for backward angled detectors such as those used in this experiment.

beam-time efficiency will allow lifetime measurements in more exotic nuclei. As an example, TPEN could be used to study: (a) proton-emitting nuclei in fusion-evaporation reactions with the Jurogam III setup at the University of Jyväskylä, (JYFL) Finland; (b) neutron-rich exotic nuclei with COULEX-plunger experiments or multi-nucleon transfer reactions at the MINIBALL setup at HIE-ISOLDE, CERN [14,15].

2. Method

2.1. Differential lifetime measurement

The Recoil Distance Doppler-Shift method (RDDS) provides a method of studying the lifetimes of excited states in nuclei [12,16]. In a typical RDDS experiment, a heavy ion beam impinges a target foil to produce recoiling nuclei in high-spin states. A stopper foil is placed close to the target foil to stop the recoils. The γ rays emitted from the recoiling nucleus will experience a different Doppler shift in energy depending on whether the recoiling nucleus decays before or after the degrader foil. The intensities of the fully-shifted and degraded components of the γ -ray transition are measured at several target-to-degrader distances and are used to extract the lifetime of the state of interest. The Differential Decay Curve Method (DDCM) is an analysis technique within the RDDS method. The DDCM and RDDS methods are described in depth in Refs. [12,16], respectively.

Reference [12] also presents the idea of a three-foil differential plunger which comprises of one target foil and two degrader foils. A three-foil plunger utilises the DDCM but directly measures the decay function and its derivative with a single set of plunger distances, eliminating the requirement to measure γ -ray intensities at multiple distance settings. Fig. 1(a) shows a schematic illustration of the target, degrader and stopper foils used in the new three-foil plunger TPEN.

As shown in Fig. 1(a), the incoming beam is directed onto a target foil, producing excited nuclei which subsequently decay via γ -ray emission. These nuclei recoil out of the target foil and travel towards the degrader foil with a velocity v , taking a time $t = x/v$ to reach the degrader foil, where x is the target-to-degrader foil distance. As the recoils pass through the degrader foil their velocity is reduced to v' and they continue towards the stopper foil where they are stopped. The time taken from leaving the degrader foil to reaching the stopper foil is $\Delta t = \Delta x/v'$, where Δx is the degrader-to-stopper foil distance. If the excited state is short lived compared with t , then the γ -ray decay is likely to occur between the target and degrader foil and the emitted γ rays will be observed fully-shifted (fs) and the observed γ -ray energy is γ_{fs} . Alternatively, if the excited states decay after the degrader foil but before the stopper foil, then the γ -rays are observed with a smaller Doppler shift in energy and are said to be degraded (d) with γ -ray energy γ_d . Finally, if the nuclei decay in the stopper foil, no Doppler shift in

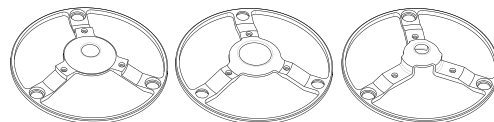


Fig. 2. Computer-aided-drawing of the target (left), degrader (centre) and stopper (right) stretching cones used to mount the foils in TPEN. The cones are all 88 mm in diameter and 3 mm thick and made from aluminium.

energy is experienced and the observed γ -energy is unshifted (us), γ_{us} . Therefore, by varying the target-to-degrader distance, x , and degrader-to-stopper distance, Δx , and measuring the intensities of γ_{fs} , γ_d and γ_{us} , the lifetimes of excited states in the recoiling nucleus can be accurately measured. It should be noted that a second degrader foil can replace the stopper foil allowing the recoiling nucleus to pass into a recoil separator for subsequent tagging as has been used with a conventional two-foil plunger [6–8,17–22].

The normalised probability for a decay to occur after the recoil has been implanted into the stopper foil as a function of flight time, is known as the decay curve, $R(t)$. Both the decay curve, and the derivative of the decay curve must be known in order to measure a lifetime [23]. The decay curve is directly measured by measuring the intensity, I^{us} , of γ_{us} . In a two-foil plunger, the derivative of the decay curve must be inferred from the shape of the decay curve, which requires measurements at several target-to-degrader distances (see Ref. [23] for more details). The third foil in TPEN allows for a direct measure of both the decay function and the derivative of the decay function. This direct measure of the derivative of the decay function eliminates the need for measuring $R(t)$ at several target-to-degrader distances. In order to accurately infer the derivative $\frac{d}{dt}R(t)$ from the measured quantity $R(t)$, the typical number of target-to-degrader distances required in a two-foil plunger experiment is 6–10. Hence using TPEN there is a potential reduction in the total number of γ -ray events required for a lifetime measurement of a factor of ~ 6 –10 [12,23]. However, this advantage is somewhat reduced because the additional foil creates additional scattering and the observed γ -ray decays are now distributed over three component peaks with TPEN instead of two component peaks from a conventional plunger. This is further discussed in Section 6. This reduction in beam-time requirement is one of the main advantages of TPEN as the precision of lifetime measurements in RDDS is mostly limited by the number of γ -ray events observed [23].

When measuring nuclear lifetimes, it is often favourable to use coincidence gates in order to remove the effects of side-feeding. In the situation where a γ -ray coincidence gate is placed on the Doppler-shifted components of a γ -ray energy directly feeding a state of interest, the lifetime of that state can be measured directly from the three intensity components using a single distance measurement [12]. The lifetime of the state is given by Eqn. (1) [12],

$$\tau = \frac{I^{us} \Delta x}{I^d v'} \quad (1)$$

where I^d is the intensity component of the degraded peak.

Alternatively, if a coincidence gate on the Doppler-shifted components of a γ -ray not directly feeding a state of interest is used, then the lifetime of the state of interest is given by [12]:

$$\tau_i = \frac{I^{us} - b_{ij} \sum_h \frac{a_{hi} I^{us}}{a_{ij} I^d} \Delta x}{I^d v'}. \quad (2)$$

Here, b_{ij} is the normalised branching ratio of the state of interest, L_i , to the state L_j , a_{hi} and a_{ij} reflect any difference in the intensity between feeding and depopulating transitions and is defined in Ref [23], and I_{hi}^{us} is the intensity of the unshifted peaks of the transition L_h to L_i . Derivations of Eqs. (1) and (2) are given in Ref. [12] and show that the equations only hold under the condition that Δt is small compared with



Fig. 3. Photograph of a degrader foil stretched over a degrader cone.

τ . A correction factor $C(\tau, \Delta t)$, discussed in Ref. [24], is used to account for any difference between the measured quantity I^d and $\frac{d}{dt}R(t)$ and is given by:

$$C(\tau, \Delta t) = \frac{\exp(\Delta t/\tau) - 1}{\Delta t/\tau}. \quad (3)$$

For measurements where the decay curve can be approximated as a simple exponential decay, the correction factor should be applied iteratively to the lifetime calculated from Eqs. (1) and (2).

3. Design

TPEN consists of three foils mounted onto stretching cones. Computer-aided-drawings of the stretching cones are shown in Fig. 2.

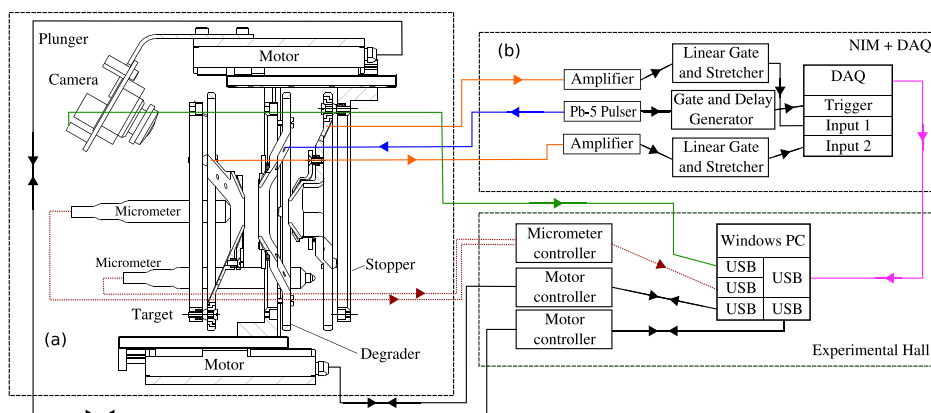


Fig. 4. (a) A diagram showing TPEN and (b) the electronic modules used to control the constant feedback system. If required the target cone can be replaced with a stopper cone the degrader foil can be rotated through 180° to allow for very small degrader-to-stopper distances.

Fig. 3 shows a photograph of a degrader foil stretched over one of these cones. The foil stretching cones are connected to foil mounts using three hard springs placed 120° apart which are compressed using screws. The cones are arranged inside TPEN, typically with the flat faces (the face that can be seen in Fig. 3) of the target foil and the flat face of the degrader foil facing each other, and the stopper foil nested in the degrader cone. TPEN can also be arranged with the flat faces of the degrader foil and stopper foil facing each other, with the target nested inside the degrader cone. This paper uses the first arrangement, which is seen in Fig. 4. The compression of the springs between the stretching cones and the foil mount allows for the alignment of the foils. The screws that vary the compression of the springs sit inside Boron Nitride (BN) insulating blocks. These BN blocks were used to electrically isolate the cones from the foil-mounts and allow heat to dissipate into the mounts, preventing heat build up when TPEN is used under vacuum conditions.

Fig. 4(a) shows a schematic diagram of the TPEN central chamber and Fig. 4(b) details the online feedback system used to control and monitor the distances between the three foils. The stopper, degrader and target stretching cones are shown in Fig. 4(a). The target foil is at a fixed position, whereas the degrader and stopper foils are mounted on Physik Instrumente (PI) [25] Linear Piezo Positioning Stage-45 (LPS-45) piezoelectric motors (Fig. 4), which can change the target-to-degrader and degrader-to-stopper distances independently. The LPS-45s each have a total travel range of 26 mm and have a position resolution of 1 nm. These motors utilise a constant negative-feedback system which keeps the target-to-degrader and degrader-to-stopper distances at the set value throughout the experiment. A BNC model PB-5 pulser is used to apply a voltage pulse to the degrader foil. The induced voltage on the target and stopper foils is used for feedback, see Fig. 4(b). A 16-Bit National Instruments [26] USB-6251 data acquisition (DAQ) card was used to sample the induced voltage at a rate of 1.25×10^6 samples per second. If the induced voltage moves outside an accepted range, then the feedback system acts to move the motors accordingly. Two TESA [27] GT43 axial miniature probes and a TESA TT20 electronic micrometre were used to calibrate the induced voltage against target-to-degrader and degrader-to-stopper distance. A modified version of the Köln plunger control software, adapted for Windows 10, was used to run the constant feedback system independently from the data acquisition system. The software was originally developed for the Köln plunger [23].

4. Commissioning

TPEN was commissioned at the Accelerator Laboratory of the University of Jyväskylä, Finland, by measuring the known 45.6(5) ps lifetime

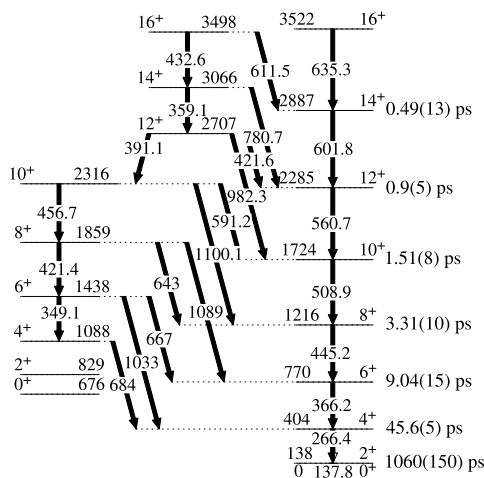


Fig. 5. Partial level scheme of ^{156}Dy according to Ref. [28]. The lifetimes of the known states from Ref. [13] are given for the rotational band built upon the ground state.

of the first 4^+ excited state in ^{156}Dy [13]. The $^{24}\text{Mg}(^{136}\text{Xe}, 4n)^{156}\text{Dy}$ fusion-evaporation reaction was used at a beam energy of 590 MeV with a cross-section of ~ 100 mb. The 4^+ lifetime in ^{156}Dy was originally measured with a conventional two-foil plunger using the $^{124}\text{Sn}(^{36}\text{S}, 4n)$ reaction at 155 MeV [13]. Fig. 5 shows the partial level scheme of ^{156}Dy , taken from Ref [28].

Our commissioning experiment tested the differential mode of TPEN and compared the lifetime obtained with that of the previous measurement [13]. In the present experiment, a ~ 1 pA $^{136}\text{Xe}^{25+}$ beam from the K130 cyclotron was used for 6 days to bombard a 1 mg/cm 2 natural magnesium target foil placed inside TPEN. The reaction produced ^{156}Dy nuclei with a measured average recoil velocity of 6.99(10)% c . Two 6.6 mg/cm 2 ^{56}Ni foils were placed downstream from the target position to degrade and stop the produced recoils, respectively. The degraded recoil velocity was measured to be $v' = 2.86(6)\%c$.

Four Compton-suppressed Jurogam Phase-1 [29,30] germanium detectors were placed at an angle of 157.5° with respect to the beam axis around TPEN in order to measure the γ -ray intensities. The detectors were placed at a distance of 12.5 cm from the target position on a specially constructed table, where their combined absolute efficiency was measured to be $\sim 0.2\%$ at 1.3 MeV. Fig. 6 shows TPEN installed inside the target vacuum chamber and the four germanium detectors used in the measurement. The central vacuum housing of TPEN is an aluminium ball, 176 mm in diameter with a wall thickness of 2 mm. The foils are arranged inside TPEN such that γ -rays detected in the germanium detectors pass through only the 2 mm aluminium wall.

The total data readout (TDR) [31] data acquisition system was employed to record the events from all four germanium detectors. The GRAIN software package was used to perform offline analysis and construct 2D γ - γ matrices [32] where the two γ rays were detected within 100 ns of each other. A total of five sets of distances, $(x, \Delta x) = (700 \mu\text{m}, 31 \mu\text{m}), (700 \mu\text{m}, 51 \mu\text{m}), (400 \mu\text{m}, 31 \mu\text{m}), (400 \mu\text{m}, 51 \mu\text{m}), (400 \mu\text{m}, 71 \mu\text{m})$, were used for differential lifetime analysis. The three intensity components of the 266-keV γ -ray were measured at each of these plunger distances and Eq. (1) was used to extract the lifetime of the 4^+ state in ^{156}Dy . The components were measured at several distances to ensure the differential technique was valid across a range of distances but the lifetime of the state was measured independently at each of these distances.

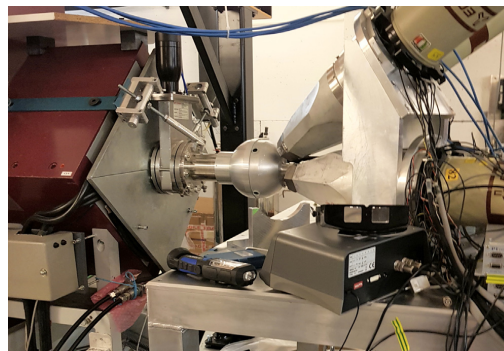


Fig. 6. A photograph of the TPEN vacuum housing surrounded by the 4 backward facing germanium detectors, two of which can be seen. RITU [33] can also be seen downstream from the central chamber, although this was not used in the present experiment.

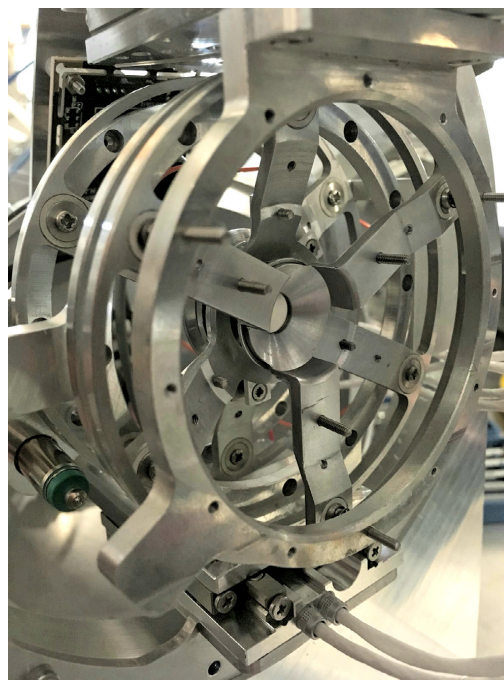


Fig. 7. A photograph of the TPEN. The stopper foil can be seen mounted on a LPS-45 motor on the right of the image. The foil mounts for the degrader and target foils can also be seen.

5. Results

5.1. Differential mode

Fig. 7 shows the three-foil system inside the central TPEN chamber.

The three foils were aligned in order to achieve small foil separations. The alignment of the foils was performed in two steps. Firstly, the degrader foil-mount was rotated through 180° , relative to that shown in Fig. 4, so that the flat faces of the stopper and degrader foils were

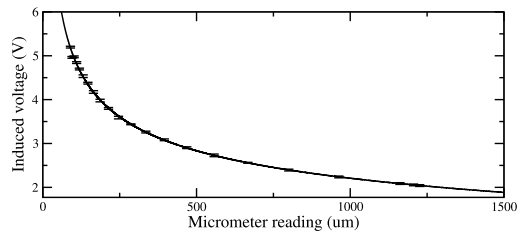


Fig. 8. The target to degrader calibration curve showing induced voltage versus distance.

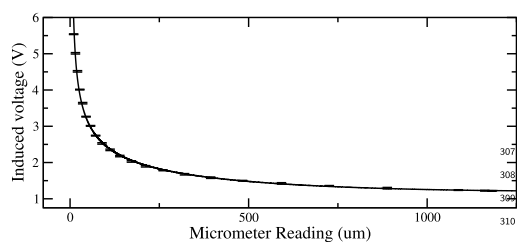


Fig. 9. The degrader to stopper calibration curve showing induced voltage versus distance.

facing each other. The stopper foil was optically aligned with the degrader foil by varying the compression on the springs with the screws. The degrader foil was then rotated back through 180° to its original position so that the flat faces of the target and degrader foils were facing each other and the stopper foil was nested inside the degrader, as shown in Fig. 4. Using the optical alignment as a starting position, the degrader and stopper foils were aligned using the capacitance measurement, again by varying the compression on the springs. Once the degrader and stopper foils were aligned, the target foil was aligned with the degrader foil by adjusting the springs on the target mount only. The alignment was performed optically and then fine tuned with the capacitance measurement. After the alignment was completed, a distance calibration was performed in order to determine the offset between electrical contact between the foils and the zero separation distance. The calibration curve for the target-to-degrader distance is shown in Fig. 8 and the calibration curve for the degrader-to-stopper distance is shown in Fig. 9. The calibration curves were compared to parallel-plate capacitors to determine the offsets. The offset between the target and degrader was found to be $90(20) \mu\text{m}$ and the offset between the degrader and stopper foils was found to be $8(1) \mu\text{m}$. For lifetimes measurements using a single set of distances with TPEN, this offset is required for the lifetime analysis and contributes to the overall systematic error in the lifetime measurement. For high-statistics plunger experiments, this systematic error in the absolute distance can be large compared to the statistical uncertainty. Therefore, for high-statistics experiments several plunger distances in differential mode should be used to remove this systematic uncertainty.

Fig. 10(a) shows the total projection of the 2D γ - γ coincidence matrix for any of the four germanium detectors versus any other detector. This spectrum contains the data from all distances combined in order to illustrate the quality of our data. As a natural magnesium target was used, several contaminants were produced with a significant cross-section of $\sim 30 \text{ mb}$, estimated from gated projections of the γ - γ coincidence matrix. These are highlighted with symbols in Fig. 10(a). To select the γ rays originating from ^{156}Dy , and to remove the effects of side-feeding, a γ -ray coincidence gate was placed on the fully-shifted

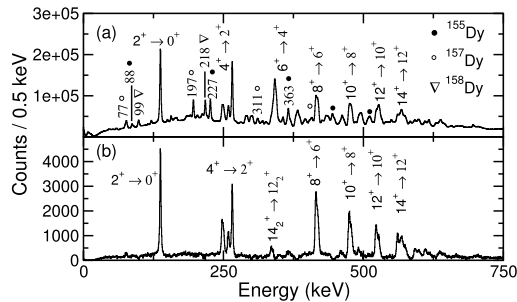


Fig. 10. (a) Spectrum showing the total projection of a 2D γ - γ coincidence matrix for any detector versus any detector, for all distances combined. The γ -rays from transitions in ^{156}Dy are labelled with their initial and final states and the main contaminants are labelled with symbols. (b) Spectrum showing γ -rays in coincidence with the fully-shifted and degraded components of the $6^+ \rightarrow 4^+$ transition in ^{156}Dy , for all distances combined.

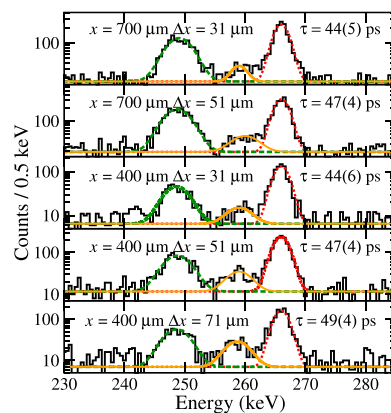


Fig. 11. Spectra gated on the fully-shifted and degraded components of the $6^+ \rightarrow 4^+$ transition in ^{156}Dy for different target-to-degrader and degrader-to-stopper distances, showing the fully-shifted (green-dashed), degraded (orange-solid) and stopped (red-dotted) intensity components of the 266-keV γ ray.

and degraded components of the 366-keV γ ray, which directly feeds the 4^+ state in ^{156}Dy . Fig. 10(b) shows a background subtracted spectrum of γ rays in coincidence with the fully shifted and degraded components of the 366-keV γ -rays.

Two dimensional γ - γ matrices were produced for each of the plunger distance settings collected in the experiment. In order to analyse the lifetime of the 4^+ state in ^{156}Dy , a gate was placed on fully shifted and degraded components of the 366 keV, $6^+ \rightarrow 4^+$, transition in each of these γ - γ matrices. Fig. 11 shows the resultant gated spectra on a logarithmic scale, zoomed in on the $4^+ \rightarrow 2^+$ transition for each distance setting. Gaussian fits to the fully-shifted (green), degraded (orange) and stopped (red) intensity components of the 266-keV γ ray transition were made in order to extract the component intensities. Table 1 shows these intensities at the five plunger distances.

The lifetime of the 4^+ state was then calculated from Eq. (1) at each of the plunger distances, and these are also given in Table 1. The correction factor, from Eq. (3), was applied iteratively to the lifetime calculated from Eq. (1) and accounted for a $\sim 3\%$ change in the measured lifetime. The average and standard deviation for these lifetime values is $46(1) \text{ ps}$. As our lifetime measurements at each

Table 1

The target-to-degrader, x , and degrader-to-stopper distances, Δx used during the commissioning experiment. The distances given are relative to the electrical contact point between the foils. The intensities of the unshifted (I^u), degraded (I^d) and fully-shifted (I^s) components of the 266-keV transition are given for different x and Δx combinations, along with the lifetimes, τ , calculated with Eq. (1).

x (μm)	Δx (μm)	I^u	I^d	I^s	τ (ps)
700	31	1337(40)	140(20)	1149(40)	44(5)
700	51	1824(47)	275(27)	1827(49)	47(4)
400	31	786(30)	82(13)	395(23)	44(6)
400	51	1460(41)	222(22)	781(33)	47(4)
400	71	1048(34)	209(18)	520(26)	49(4)

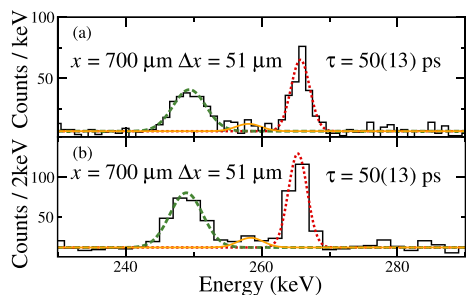


Fig. 12. Spectra gated on the 4^+ state in ^{156}Dy using multiplicity three events at $x = 700 \mu\text{m}$, $\Delta x = 51 \mu\text{m}$. The fully-shifted (green), degraded (orange) and stopped (red) intensity components of the 266-keV γ ray are shown. The data is shown using histogram channel widths of 1 (a) and 2 keV (b). (For interpretation of the references to colour in this figure legend, the reader is referred to the web version of this article.)

distance setting were independent, no normalisation of the measured γ -ray intensities was required. This removes one source of error associated with conventional two-foil plungers which require normalisation of γ -ray intensities across ~ 6 – 10 distance settings. Therefore, a weighted average of $\tau = 46(2)$ ps was calculated from the five distances used in our differential analysis. This $46(2)$ ps lifetime is in good agreement with the $45.6(5)$ ps measured in Ref. [13] from a high-statistics, two-foil plunger experiment, demonstrating that TPEN works with differential lifetime measurements.

In order to understand the performance of TPEN in the limit of low statistics, a subset of higher-fold, multiplicity 3 events were used to perform a similar lifetime analysis. At a plunger distance of $x = 700 \mu\text{m}$, $\Delta x = 51 \mu\text{m}$, a $2\text{D } \gamma\text{-}\gamma$ matrix was produced which only included events with multiplicity 3 or above. A coincidence gate was set on the fully shifted and degraded components of the 366 keV, 6^+ to 4^+ , transition in ^{156}Dy . Fig. 12 shows a zoomed in spectrum of the 4^+ to 2^+ transition with two histogram channel widths (a) 1 keV per channel and (b) 2 keV per channel. Gaussian fits to the fully-shifted (green), degraded (orange) and stopped (red) intensity components of the 266-keV γ ray transition are shown. The number of counts recorded in the fully shifted, degraded and stopped components of the 266-keV γ ray, were 210(20), 28(9) and 200(16), respectively. Using Eq. (1) and the component intensities, the lifetime of the 4^+ state in ^{156}Dy was found to be $50(13)$ ps, which is in good agreement with the literature value [13]. This low-statistics analysis demonstrates that TPEN can be used in differential mode for lifetime measurements in nuclei with small production cross sections.

5.2. Using TPEN as a standard two-foil plunger

The lifetime of the 4^+ state in ^{156}Dy was also measured using TPEN as a standard plunger to allow a direct comparison of the precision of results using the two different techniques. The intensities of γ -ray decays

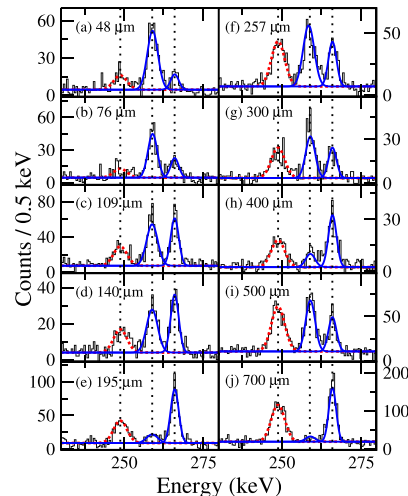


Fig. 13. The background subtracted spectra showing the three intensity components of the 266-keV transition in ^{156}Dy , in coincidence with the fully-shifted component of the 366-keV transition at 10 plunger distances. Gaussian fits to the decays occurring before the first degrader foil are shown in red-dashed and Gaussian fits to the decays occurring after the first-degrader foil are shown in blue-solid.

before and after the first degrader foil were measured in coincidence with the fully-shifted component of the 366-keV transition at target-to-degrader distances of $48 \mu\text{m}$, $76 \mu\text{m}$, $109 \mu\text{m}$, $140 \mu\text{m}$, $195 \mu\text{m}$, $257 \mu\text{m}$, $300 \mu\text{m}$, $400 \mu\text{m}$, $500 \mu\text{m}$ and $700 \mu\text{m}$. These data are shown in Fig. 13. Gaussian fits to the data were made in order to extract the component intensities. The measured intensities were normalised to the total number of counts in the gated projection, to correct for different number of beam particles between runs.

The degraded and stopped components of the 266-keV were combined to form the decay curve, i.e. the intensity of decays after the first degrader foil. Combining the stopped and degraded components effectively allows TPEN to be used as a standard two-foil plunger. In this way the decay curve is measured at various distances and the differential of the decay curve is inferred from the shape of the decay curve, as in the standard DDCM [12].

Fig. 14 shows the lifetime of the 4^+ state in ^{156}Dy calculated using the standard DDCM analysis using the NAPATAU computer programme. The normalised intensities of the fully-shifted components the 266-keV transition in coincidence with the fully-shifted component of the 366-keV transition is shown as a function of distance in Fig. 14(b). The combined normalised intensities of the degraded and stopped components the 266-keV transition in coincidence with the fully-shifted component of the 366-keV transition, as a function of distance are also shown in Fig. 14(c). A piece-wise second order polynomial is fitted to the fully-shifted component (red-dashed), the uncertainty on this fit is shown in red-shaded. The red-shaded area shows the change to the fit given by increasing the total χ^2 by 1, i.e. increasing the average variance by 1. The derivative of this second-order polynomial, multiplied by the lifetime of the state, is fitted to the intensity of decays after the degrader foil (blue-solid), with the uncertainty in blue-shaded. The normalised intensities of the decays before and after the degrader foil are given in Table 2. The lifetime of the state is calculated at each of the 10 target-to-degrader distances and is shown in Fig. 14(a) along with the uncertainty on the average lifetime, taking into account the uncertainty on the fit to the data.

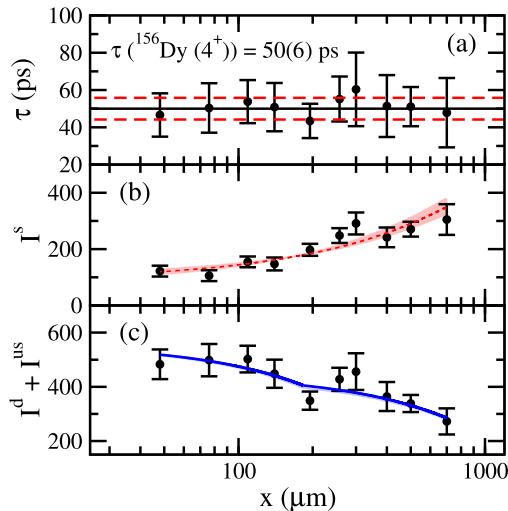


Fig. 14. The intensity of the 266-keV transition in ^{156}Dy before and after a degrader foil, in coincidence with the fully-shifted component of the 366-keV transition at 10 plunger distances. (a) the calculated lifetime at each of the plunger distances and the average lifetime, (b) the fully-shifted component of the 266-keV transition and a piece-wise polynomial fit to the data (red-dashed) along with the uncertainty on the fit (red-shaded), (c) the derivative of the fit to (b) multiplied by τ (blue-solid) and the uncertainty on this (blue-shaded). The uncertainty on the derivative is of the same order as the line thickness. (For interpretation of the references to colour in this figure legend, the reader is referred to the web version of this article.)

Table 2

The target-to-degrader, x , and the normalised measured intensities of the 266-keV γ -ray transition before and after the degrader. The distances given are relative to the electrical contact point between the foils.

$x(\mu\text{m})$	I^s	$I^d + I^s$
48	122(20)	480(55)
76	106(20)	500(60)
109	155(20)	500(50)
140	150(25)	450(50)
195	200(21)	350(35)
257	250(25)	430(45)
300	290(40)	450(70)
400	240(20)	360(50)
500	270(25)	340(30)
700	305(25)	270(40)

6. Discussion

6.1. Beam-time improvement with TPEN

This commissioning experiment has demonstrated that the newly constructed TPEN is capable of performing differential lifetime measurements in the limit of low statistics. The main advantage of a triple-foil differential plunger is the reduced beam-time required for a lifetime measurement compared to that of a conventional two-foil plunger. In the present work, a total of 7×10^7 γ - γ events were collected using TPEN for the differential lifetime measurements performed at five sets of target-to-degrader and degrader-to-stopper distances. This resulted in a 13 000(200) events in the three components of the 266-keV γ -ray transition for the differential lifetime analysis, yielding a lifetime value with a 4% uncertainty, seen in Fig. 11.

When using the standard DDCM analysis by using TPEN as a standard plunger, 10 000(100) counts were used across all distances to yield a lifetime value with a 12% uncertainty, seen in Fig. 14. From this, it is

estimated that $\sim 50\,000(1\,000)$ counts would provide a measurement with a 4% uncertainty using TPEN as a two-foil plunger. Directly taking the ratio of the statistics required in the two modes of TPEN, with identical detector set-ups, it can be concluded that TPEN in differential mode requires a factor of 3.8(1) less in statistics or in beam time compared to a standard plunger with the reaction used in this work.

6.2. Future use of TPEN

For lifetime measurements in nuclei produced with small production cross-sections, it is often essential to use tagging techniques in order to select the nuclei of interest from the overwhelming background from the less exotic reaction products [17–21]. These tagging techniques are often performed using recoil separators such as RITU [33] at JYFL. The overall transmission efficiency of separators is reduced by any material in the beam's path. Hence, the extra foil in TPEN will reduce the tagging efficiency compared with a conventional two-foil plunger and therefore reduce the beam-time improvement estimated above. In this case with the $^{24}\text{Mg}(^{136}\text{Xe}, 4n)$ reaction, simulations show that with the RITU separator [33] the addition of a 1 mg/cm^2 Mg degrader foil reduces the overall transmission efficiency by $\sim 33\%$. Simulations specific to the reaction should be performed for reliable values. Therefore, if recoil tagging techniques were employed for the reaction described in this work, then the overall beam-time improvement using TPEN would be a factor of $\sim 3.5 \times 0.66 = 2.3$ relative to using a two-foil conventional plunger. As two-foil plungers have performed tagged lifetime measurements in nuclei with production cross-sections of 10–20 μb [7,22], TPEN would therefore be capable of performing tagged lifetime measurements in nuclei with production cross-sections down to ~ 4 –8 μb .

7. Conclusions

A new triple foil plunger, TPEN, has been developed in order to study nuclei with production cross-section of the order of a few microbarn. A commissioning experiment at the accelerator laboratory of the University of Jyväskylä, Finland, has been performed. The first 4^+ excited state in ^{156}Dy was measured at five distances independently. All of the measurements were in good agreement with the current literature value of 45.6(5) ps [13], with an average lifetime from all distances being 46(2) ps. This measurement demonstrated the capability of TPEN to measure lifetimes using a single set of distances and showed a reduction in beam-time requirements of a factor of ~ 4 for measurements with no tagging, and a factor of ~ 2 for experiments when tagging is employed.

Acknowledgements

The authors acknowledge GAMMAPOOL support for the JUROGAM detectors and M.M.G., L.B., D.M.C., B.S.N.S., M.J.T., M.M., A.J.S., A.M., and C.R. acknowledge support of the Science and Technology Facilities Council, UK, Grant No. ST/L005794/1. This work was supported by the EU 7th Framework Programme, Integrating Activities Transnational Access, Project No. 262010 ENSAR, and by the Academy of Finland under the Finnish Centre of Excellence Programme (Nuclear and Accelerator Based Physics Programme at JYFL).

References

- [1] D. Steppenbeck, et al., Evidence for a new nuclear 'magic number' from the level structure of ^{54}Ca , *Nature* 502 (2013) 207 EP –.
- [2] M. Stanoiu, et al., $N = 14$ And 16 shell gaps in neutron-rich oxygen isotopes, *Phys. Rev. C* 69 (2004) 034312.
- [3] Kris Heyde, John L. Wood, Shape coexistence in atomic nuclei, *Rev. Modern Phys.* 83 (2011) 1467–1521.
- [4] J. Engel, K. Langanke, P. Vogel, Pairing and isospin symmetry in proton-rich nuclei, *Phys. Lett. B* 389 (2) (1996) 211–216.
- [5] D.S. Delion, et al., Investigations of proton-neutron correlations close to the drip line, *Phys. Rev. C* 82 (2010) 024307.

- [6] M.J. Taylor, et al., A new differentially pumped plunger device to measure excited-state lifetimes in proton emitting nuclei, *Nucl. Instrum. Methods A* 707 (2013) 143–148.
- [7] D. Hodge, et al., Deformation of the proton emitter ^{113}Cs from electromagnetic transition and proton-emission rates, *Phys. Rev. C* 94 (2016) 034321.
- [8] M.J. Taylor, et al., Oblately deformed isomeric proton-emitting state in ^{151}Lu , *Phys. Rev. C* 91 (2015) 044322.
- [9] M.J. others Taylor, Competing single-particle and collective states in the low-energy structure of ^{113}I , *Phys. Rev. C* 88 (5) (2013).
- [10] M. others Doncel, Lifetime measurement of the first excited 2^+ state in ^{112}Te , *Phys. Rev. C* 91 (6) (2015).
- [11] M.G. others Procter, Isomer-tagged differential-plunger measurements in ^{113}Xe , *Phys. Rev. C* 87 (2013) 014308.
- [12] A. Dewald, S. Harissopulos, P. von Brentano, The differential plunger and the differential decay curve method for the analysis of recoil distance Doppler-shift data, *Z. Phys. A* 334 (2) (1989) 163–175.
- [13] O. Möller, et al., Electromagnetic transition strengths in ^{156}Dy , *Phys. Rev. C* 74 (2006) 024313.
- [14] P. Reiter, et al., The MINIBALL array, in: 5th International Conference on Radioactive Nuclear Beams, *Nuclear Phys. A* 701 (1) (2002) 209–212.
- [15] N. Warr, et al., The Miniball spectrometer, *Eur. Phys. J. A* 49 (3) (2013) 40.
- [16] T.K. Alexander, J.S. Forster, Lifetime measurements of excited nuclear levels by Doppler-shift methods, in: *Advances in Nuclear Physics*, vol. 10, Springer US, Boston, MA, 1978, pp. 197–331.
- [17] A.N. Steer, et al., Recoil-beta tagging: A novel technique for studying proton-drip-line nuclei, *Nucl. Instrum. Methods Phys. Res. A* 565 (2) (2006) 630–636.
- [18] W. Korten, In-beam spectroscopy of exotic nuclei using recoil-decay tagging, *Nuclear Phys. A* 654 (1, Supplement 1) (1999) 677c – 682c.
- [19] T. Grahn, et al., Collectivity of ^{196}Po at low spin, *Phys. Rev. C* 80 (2009) 014323.
- [20] H. Watkins, et al., Lifetime measurements probing triple shape coexistence in ^{175}Au , *Phys. Rev. C* 84 (2011) 051302.
- [21] B. Cederwall, et al., Lifetime measurements of excited states in ^{172}Pt and the variation of quadrupole transition strength with angular momentum, *Phys. Rev. Lett.* 121 (2018) 022502.
- [22] M.G. Procter, et al., Lifetime measurement in the protonunbound nucleus ^{109}I , *AIP Conf. Proc.* 1409 (1) (2011) 105–110.
- [23] A. Dewald, O. Müller, P. Petkov, Developing the Recoil Distance Doppler-Shift technique towards a versatile tool for lifetime measurements of excited nuclear states, *Prog. Part. Nucl. Phys.* 67 (3) (2012) 786–839.
- [24] H. Iwasaki, et al., The TRIPLE PLunger for EXotic beams TRIPLEX for excited-state lifetime measurement studies on rare isotopes, *Nucl. Instrum. Methods Phys. Res. A* 806 (2016) 123–131.
- [25] Physik instrumente (pi) gmbh & co., 2018, <https://www.physikinstrumente.co.uk/en/>.
- [26] National instruments corporation, 2018, <http://www.ni.com/en-gb.html>.
- [27] Tesa technology uk ltd, 2018, <http://www.tesatechnology.com/en-gb/home/>.
- [28] C. Reich, Nuclear data sheets for $a = 156$, *Nucl. Data Sheets* 99 (4) (2003) 753–1030.
- [29] C.W. Beausang, et al., Measurements on prototype Ge and BGO detectors for the Eurogam array, *Nucl. Instrum. Methods A* 313 (1 2) (1992) 37–49.
- [30] P.T. Greenlees, et al., Heavy element spectroscopy at JYFL, *AIP Conf. Proc.* 764 (1) (2005) 237–242.
- [31] I.H. Lazarus, et al., The great triggerless total data readout method, *IEEE Trans. Nucl. Sci.* 48 (3) (2001) 567–569.
- [32] P. Rahkila, GRAIN A java data analysis system for total data readout, *Nucl. Instrum. Methods A* 595 (3) (2008) 637–642.
- [33] M. Leino, et al., Gas-filled recoil separator for studies of heavy elements, *Nucl. Instrum. Methods B* 99 (1 4) (1995) 653–656.

The remainder of this page was intentionally left blank.

Bibliography

- [1] D. Steppenbeck *et al.*, “Evidence for a new nuclear ‘magic number’ from the level structure of ^{54}Ca ,” *Nature*, vol. 502, pp. 207 EP –, Oct 2013.
- [2] M. Stanoiu *et al.*, “N= 14 and 16 shell gaps in neutron-rich oxygen isotopes,” *Phys. Rev. C*, vol. 69, p. 034312, Mar 2004.
- [3] K. Heyde and J. L. Wood, “Shape coexistence in atomic nuclei,” *Rev. Mod. Phys.*, vol. 83, pp. 1467–1521, Nov 2011.
- [4] J. Engel *et al.*, “Pairing and isospin symmetry in proton-rich nuclei,” *Physics Letters B*, vol. 389, no. 2, pp. 211 – 216, 1996.
- [5] D. S. Delion *et al.*, “Investigations of proton-neutron correlations close to the drip line,” *Phys. Rev. C*, vol. 82, p. 024307, Aug 2010.
- [6] A. Dewald *et al.*, “Developing the Recoil Distance Doppler-Shift technique towards a versatile tool for lifetime measurements of excited nuclear states ,” *Progress in Particle and Nuclear Physics*, vol. 67, pp. 786–839, 2012.
- [7] P. J. Nolan and J. F. Sharpey-Schafer, “The measurement of the lifetimes of excited nuclear states ,” *Reports on progress in physics*, 1979.
- [8] T. K. Alexander and J. S. Forster, *Lifetime Measurements of Excited Nuclear Levels by Doppler-Shift Methods*, pp. 197–331. Boston, MA: Springer US, 1978.
- [9] A. Dewald *et al.*, “The differential plunger and the differential decay curve method for the analysis of recoil distance doppler-shift data,” *Zeitschrift für Physik A Atomic Nuclei*, vol. 334, pp. 163–175, Jun 1989.

- [10] T. K. Alexander and K. W. Allen, “Lifetimes of the ^{16}O 6.13-MeV level and the ^{17}O 0.871-MeV level,” *Canadian Journal of Physics*, vol. 43, no. 9, pp. 1563–1573, 1965.
- [11] M. J. Taylor *et al.*, “A new differentially pumped plunger device to measure excited-state lifetimes in proton emitting nuclei,” *Nuclear Instruments and Methods in Physics Research Section A: Accelerators, Spectrometers, Detectors and Associated Equipment*, vol. 707, pp. 143 – 148, 2013.
- [12] D. Hodge *et al.*, “Deformation of the proton emitter ^{113}Cs from electromagnetic transition and proton-emission rates,” *Phys. Rev. C*, vol. 94, p. 034321, Sep 2016.
- [13] M. J. Taylor *et al.*, “Oblately deformed isomeric proton-emitting state in ^{151}Lu ,” *Phys. Rev. C*, vol. 91, p. 044322, Apr 2015.
- [14] M. J. Taylor *et al.*, “Competing single-particle and collective states in the low-energy structure of ^{113}I ,” *Physical Review C - Nuclear Physics*, vol. 88, no. 5, 2013.
- [15] M. Doncel *et al.*, “Lifetime measurement of the first excited 2+ state in ^{112}Te ,” *Physical Review C - Nuclear Physics*, vol. 91, no. 6, 2015.
- [16] M. G. Procter *et al.*, “Isomer-tagged differential-plunger measurements in $^{113}_{54}\text{Xe}$,” *Phys. Rev. C*, vol. 87, p. 014308, Jan 2013.
- [17] M. M. Giles *et al.*, “TPEN: a triple-foil differential plunger for lifetime measurements of excited states in exotic nuclei,” *Nuclear Instruments and Methods in Physics Research Section A: Accelerators, Spectrometers, Detectors and Associated Equipment*, vol. 923, pp. 139 – 146, 2019.
- [18] P. T. Greenlees *et al.*, “Heavy element spectroscopy at JYFL,” *AIP Conference Proceedings*, vol. 764, no. 1, pp. 237–242, 2005.
- [19] C. W. Beausang *et al.*, “Measurements on prototype Ge and {BGO} detectors for the Eurogam array,” *Nucl. Instrum. Methods A*, vol. 313, no. 1 2, pp. 37 – 49, 1992.
- [20] O. Möller *et al.*, “Electromagnetic transition strengths in ^{156}Dy ,” *Phys. Rev. C*, vol. 74, p. 024313, Aug 2006.

- [21] M. G. Procter *et al.*, “Anomalous transition strength in the proton-unbound nucleus ^{109}I ,” *Physics Letters B*, vol. 704, no. 3, pp. 118 – 122, 2011.
- [22] M. G. Procter *et al.*, “Proton emission from an oblate nucleus ^{151}Lu ,” *Physics Letters B*, vol. 725, no. 1, pp. 79 – 84, 2013.
- [23] P. Reiter *et al.*, “The MINIBALL array,” *Nuclear physics A*, vol. 701, pp. 209–212, 2002.
- [24] N. Warr *et al.*, “The MINIBALL spectrometer,” *The European Physical Journal A*, vol. 49, p. 40, Mar 2013.
- [25] “National instruments corporation.” <http://www.ni.com/en-gb/shop/labview.html>, 2018.
- [26] B. Cederwall *et al.*, “Lifetime measurements of excited states in ^{172}Pt and the variation of quadrupole transition strength with angular momentum,” *Phys. Rev. Lett.*, vol. 121, p. 022502, Jul 2018.
- [27] H. Bateman, “The solution of a system of differential equations occurring in the theory of radioactive transformations ,” *Mathematical Proceedings of the Cambridge Philosophical Society*, vol. 15, pp. 423–427, 1910.
- [28] R. Thibes and S. Oliveira, “General solution to Bateman’s differential equations with direct index notation ,” *International Journal of Pure and Applied Mathematics*, vol. 93, pp. 879–883, 2014.
- [29] D. Ward *et al.*, “Lifetimes for levels above the ”rotational phase change” in ^{158}Er ,” *Phys. Rev. Lett.*, vol. 30, pp. 493–496, Mar 1973.
- [30] G. F. Knoll, *Radiation detection and measurement*. Wiley, 1979.
- [31] A. Steane, *Relativity Made Relatively Easy*. OUP Oxford, 2012.
- [32] R. F. Casten, *Nuclear Structure from a Simple Perspective*. Oxford science publications, Oxford University Press, 2000.
- [33] E. der Mateosian and A. Sunyar, “Tables of angular-distribution coefficients for gamma rays of mixed multiplicities emitted by aligned nuclei,” *Atomic Data and Nuclear Data Tables*, vol. 13, no. 5, pp. 407 – 462, 1974.

- [34] K. S. Krane, *Introductory Nuclear Physics*. Wiley, 1987.
- [35] P. Petkov *et al.*, “The nuclear deorientation effect in ^{122}Xe and ^{128}Ba ,” *Nuclear Physics A*, vol. 589, no. 2, pp. 341 – 362, 1995.
- [36] M. M. Giles *et al.*, “Study of isospin symmetry in the $A=50$ isobaric triplet via the γ -ray transition rates,” *Unpublished manuscript*, 2018.
- [37] J. F. Ziegler *et al.*, “Srim the stopping and range of ions in matter (2010),” *Nuclear Instruments and Methods in Physics Research Section B: Beam Interactions with Materials and Atoms*, vol. 268, no. 11, pp. 1818 – 1823, 2010. 19th International Conference on Ion Beam Analysis.
- [38] G. Gamow, “Mass defect curve and nuclear constitution,” *Proceedings of the Royal Society of London A: Mathematical, Physical and Engineering Sciences*, vol. 126, no. 803, pp. 632–644, 1930.
- [39] N. Bohr and J. A. Wheeler, “The mechanism of nuclear fission,” *Phys. Rev.*, vol. 56, pp. 426–450, Sep 1939.
- [40] M. G. Mayer, “Nuclear configurations in the spin-orbit coupling model. I. empirical evidence,” *Phys. Rev.*, vol. 78, pp. 16–21, Apr 1950.
- [41] M. G. Mayer, “Nuclear configurations in the spin-orbit coupling model. II. theoretical considerations,” *Phys. Rev.*, vol. 78, pp. 22–23, Apr 1950.
- [42] C. Cockrell *et al.*, “Lithium isotopes within the ab initio no-core full configuration approach,” *Phys. Rev. C*, vol. 86, p. 034325, Sep 2012.
- [43] T. Yoshida *et al.*, “Intrinsic structure of light nuclei in,”
- [44] T. Abe *et al.*, “Benchmarks of the full configuration interaction, monte carlo shell model, and no-core full configuration methods,” *Phys. Rev. C*, vol. 86, p. 054301, Nov 2012.
- [45] S. C. Pieper *et al.*, “Quantum Monte Carlo calculations of excited states in $A = 6 - 8$ nuclei,” *Phys. Rev. C*, vol. 70, p. 054325, Nov 2004.
- [46] O. Haxel *et al.*, “On the “Magic Numbers” in nuclear structure,” *Phys. Rev.*, vol. 75, pp. 1766–1766, Jun 1949.

- [47] O. Haxel *et al.*, “Modellmäßige deutung der ausgezeichneten nukleonenzahlen im kernbau,” *Zeitschrift für Physik*, vol. 128, pp. 295–311, Apr 1950.
- [48] D. Sharp, *Trends in single-particle energies in $N=51$ nuclei*. PhD thesis, 2012.
- [49] K. Heyde, *Basic Ideas and Concepts in Nuclear Physics: An Introductory Approach, Second Edition*. Taylor & Francis, 1998.
- [50] J. Lilley, *Nuclear Physics: Principles and Applications*. Wiley, 2013.
- [51] S. F. Ashley, *Recoil Distance Doppler Shift Lifetime Measurements of Excited States in ^{103}Pd and $^{106,107}\text{Cd}$* . PhD thesis, May 2007.
- [52] D. Hodge, *Deformation of ^{113}Cs from Proton-emission and Electromagnetic Transition Rates*. PhD thesis, Sept. 2016.
- [53] S. Drissi *et al.*, “The ^{112}Cd laboratory: An extension. e_0 strengths, multiphonon states and coupled vibrations,” *Nuclear Physics A*, vol. 614, no. 2, pp. 137 – 182, 1997.
- [54] E. Teller and J. A. Wheeler, “On the Rotation of the Atomic Nucleus ,” *Physical review letters*, vol. 53, p. 778, May 1938.
- [55] A. Bohr and B. Mottelson, *Nuclear Structure: Volume II: Nuclear Deformations*. World Scientific Pub Co Inc, 1997.
- [56] A. C. Li and A. Schwarzschild, “Lifetimes of 4^+ and 2^+ states in the rotational nuclei ^{160}Dy , ^{162}Dy , ^{166}Er , ^{168}Er , and ^{180}Hf ,” *Phys. Rev.*, vol. 129, pp. 2664–2678, Mar 1963.
- [57] E. Noether, “Invariante variationsprobleme,” *Nachrichten von der Gesellschaft der Wissenschaften zu Gttingen, Mathematisch-Physikalische Klasse*, vol. 1918, pp. 235–257, 1918.
- [58] R. B. Firestone *et al.*, *Table of isotopes*. No. v. 4, Wiley, 1999.
- [59] V. F. Weisskopf, “Radiative transition probabilities in nuclei,” *Phys. Rev.*, vol. 83, pp. 1073–1073, Sep 1951.
- [60] R. Bass, “Fusion of heavy nuclei in a classical model,” *Nuclear Physics A*, vol. 231, no. 1, pp. 45 – 63, 1974.

- [61] O. A. Capurro and D. Di Gregorio, “Average angular momentum in fusion reactions deduced from evaporation-residue cross sections,” vol. 57, 01 1998.
- [62] O. A. Capurro *et al.*, “Average angular momentum in compound nucleus reactions deduced from isomer ratio measurements,” *Phys. Rev. C*, vol. 55, pp. 766–774, Feb 1997.
- [63] R. P. Feynman, “Space-time approach to quantum electrodynamics,” *Phys. Rev.*, vol. 76, pp. 769–789, Sep 1949.
- [64] D. Cline, “Nuclear shapes studied by Coulomb excitation ,” *Annual Review of Nuclear and Particle Science*, vol. 36, pp. 683–713, 1986.
- [65] J. de Boer and J. Eichler, *The Reorientation Effect*, pp. 1–65. Boston, MA: Springer US, 1968.
- [66] K. Heyde and J. L. Wood, “Shape coexistence in atomic nuclei,” *Rev. Mod. Phys.*, vol. 83, pp. 1467–1521, Nov 2011.
- [67] A. Petrovici *et al.*, “Microscopic aspects of shape coexistence in ^{72}Kr and ^{74}Kr ,” *Nuclear Physics A*, vol. 665, no. 3, pp. 333 – 350, 2000.
- [68] R. B. Piercey *et al.*, “Evidence for deformed ground states in light Kr isotopes,” *Phys. Rev. Lett.*, vol. 47, pp. 1514–1517, Nov 1981.
- [69] A. Frank *et al.*, “Evolving shape coexistence in the lead isotopes: The geometry of configuration mixing in nuclei,” *Phys. Rev. C*, vol. 69, p. 034323, Mar 2004.
- [70] A. Gorgen, “Shapes and collectivity of exotic nuclei via low-energy coulomb excitation,” *Journal of Physics G: Nuclear and Particle Physics*, vol. 37, no. 10, p. 103101, 2010.
- [71] K. Szymańska *et al.*, “Resolution, efficiency and stability of HPGe detector operating in a magnetic field at various gamma-ray energies,” *Nuclear Instruments and Methods in Physics Research A*, vol. 592, pp. 486–492, 2008.
- [72] M. Berger and S. Seltzer, “Response functions for sodium iodide scintillation detectors,” *Nuclear Instruments and Methods*, vol. 104, no. 2, pp. 317 – 332, 1972.

- [73] J. G. Campbell and A. J. F. Boyle, “Energy resolution of γ -radiation up to 18 MeV by sodium iodide scintillation counters,” *Australian Journal of Physics*, vol. 6, pp. 171–189, Jun 1953.
- [74] H. O. Anger and D. H. Davis, “ γ -ray detection efficiency and image resolution in sodium iodide,” *Review of Scientific Instruments*, vol. 35, no. 6, pp. 693–697, 1964.
- [75] M. Moszynski *et al.*, “Energy Resolution of Scintillation Detectors - New Observations,” *IEEE Transactions on Nuclear Science*, vol. 55, pp. 1062–1068, June 2008.
- [76] J. Eberth *et al.*, “MINIBALL: A Ge detector array for radioactive ion beam facilities,” *Progress in Particle and Nuclear Physics*, 2001.
- [77] CERN, “Isolde miniball webpage,” 2016.
- [78] H. Iwasaki *et al.*, “The triple plunger for exotic beams TRIPLEX for excited-state lifetime measurement studies on rare isotopes,” *Nuclear Instruments and Methods in Physics Research Section A: Accelerators, Spectrometers, Detectors and Associated Equipment*, vol. 806, pp. 123 – 131, 2016.
- [79] “Physik instrumente (pi) gmbh & co..” <https://www.physikinstrumente.co.uk/en/>, 2018.
- [80] “Tesa technology uk ltd.” <http://www.tesatechnology.com/en-gb/home/>, 2018.
- [81] “National instruments corporation.” <http://www.ni.com/en-gb.html>, 2018.
- [82] R. Jaeger, *Introduction to Microelectronic Fabrication*. Modular series on solid state devices, Prentice Hall, 2002.
- [83] M. Leino *et al.*, “Gas-filled recoil separator for studies of heavy elements,” *Nucl. Instrum. Methods B*, vol. 99, no. 1 4, pp. 653 – 656, 1995.
- [84] G. Duchêne *et al.*, “The clover: a new generation of composite Ge detectors,” *Nucl. Instrum. Methods in Physics Research A*, vol. 432, no. 1, pp. 90 – 110, 1999.
- [85] A. J. Smith. “Engineering drawings produced for TPEN”.

- [86] W. Cady, *Piezoelectricity: An introduction to the theory and applications of electromechanical phenomena in crystals*. Dover Publications, 1978.
- [87] I. H. Lazarus *et al.*, “The GREAT triggerless total data readout method,” *Nuclear Science, IEEE Transactions on*, vol. 48, pp. 567–569, Jun 2001.
- [88] P. Rahkila, “GRAIN a java data analysis system for total data readout,” *Nucl. Instrum. Methods A*, vol. 595, no. 3, pp. 637 – 642, 2008.
- [89] “Physik instrumente (pi) gmbh & co.” <https://www.physikinstrumente.co.uk/en/products/controllers-and-drivers/motion-controllers-for-piezomotors/e-870-pishift-drive-electronics-900640/>, 2018.
- [90] M. M. Giles, “TPEN user manual.” PDF Document from the University of Manchester, Jan. 2018.
- [91] C. Reich, “Nuclear data sheets for $A = 156$,” *Nuclear Data Sheets*, vol. 99, no. 4, pp. 753 – 1030, 2003.
- [92] E. Liukkonen, “New K130 cyclotron at Jyväskylä,” *Proceedings of the 13th International Conference on Cyclotrons and their Applications, Vancouver*, 1993.
- [93] R. Geller, “ECRIS: The Electron Cyclotron Resonance Ion Sources,” *Annual Review of Nuclear and Particle Science*, vol. 40, no. 1, pp. 15–44, 1990.
- [94] M. G. Procter, *High- K states and critical-point symmetries in ^{138}Gd* . PhD thesis, 2012.
- [95] Y. Khazov *et al.*, “Nuclear data sheets for $A = 133$,” *Nuclear Data Sheets*, vol. 112, no. 4, pp. 855 – 1113, 2011.
- [96] Wang, M and others
- [97] D. C. Radford, “2000 Radware software package.”
- [98] R. D. Page *et al.*, “The GREAT spectrometer ,” *Nucl. Instrum. Methods B*, vol. 204, no. 0, pp. 634 – 637, 2003.
- [99] M. Sandzelius, *In beam spectroscopy of extremely neutron deficient nuclei ^{110}Xe , ^{163}Ta , ^{169}Ir and ^{172}Hg* . PhD thesis, Sept. 2009.

- [100] P. Campbell. “Private Communications”.
- [101] W. Haynes, *CRC Handbook of Chemistry and Physics, 97th Edition*. CRC Press, 2016.
- [102] O. Tarasov and D. Bazin, “LISE++: Exotic beam production with fragment separators and their design,” *Nuclear Instruments and Methods in Physics Research Section B: Beam Interactions with Materials and Atoms*, vol. 376, pp. 185 – 187, 2016.
- [103] A. Gavron, “Statistical model calculations in heavy ion reactions,” *Phys. Rev. C*, vol. 21, pp. 230–236, Jan 1980.
- [104] “TK-Analysis NAPATAU manual.” PDF Document from the University of Köln, 2018.
- [105] A. N. Steer *et al.*, “Recoil-beta tagging: A novel technique for studying proton-drip-line nuclei,” *Nuclear Instruments and Methods in Physics Research Section A: Accelerators, Spectrometers, Detectors and Associated Equipment*, vol. 565, no. 2, pp. 630 – 636, 2006.
- [106] W. Korten, “In-beam spectroscopy of exotic nuclei using recoil-decay tagging,” *Nuclear Physics A*, vol. 654, no. 1, Supplement 1, pp. 677c – 682c, 1999.
- [107] T. Grahn *et al.*, “Collectivity of ^{196}Po at low spin,” *Phys. Rev. C*, vol. 80, p. 014323, Jul 2009.
- [108] H. Watkins *et al.*, “Lifetime measurements probing triple shape coexistence in ^{175}Au ,” *Phys. Rev. C*, vol. 84, p. 051302, Nov 2011.
- [109] P. Ruotsalainen *et al.*, “Recoil- β tagging study of the N=Z nucleus ^{66}As ,” *Phys. Rev. C*, vol. 88, p. 024320, Aug 2013.
- [110] D. M. Cullen *et al.*, “Identification of excited states in doubly odd ^{140}Eu by recoil-isomer tagging,” *Phys. Rev. C*, vol. 66, p. 034308, Sep 2002.
- [111] U. Jakobsson *et al.*, “Recoil-decay tagging study of ^{205}Fr ,” *Phys. Rev. C*, vol. 85, p. 014309, Jan 2012.
- [112] P. J. R. Mason *et al.*, “Isomer-tagged differential-plunger measurements in proton-unbound ^{144}Ho ,” *Physics Letters B*, vol. 683, no. 1, pp. 17 – 20, 2010.

- [113] D. M. Cullen *et al.*, “Identification of the $K^\pi = 8^-$ rotational band in ^{138}Gd ,” *Phys. Rev. C*, vol. 58, pp. 846–850, Aug 1998.
- [114] C. Scholey *et al.*, “Recoil isomer tagging in the proton-rich odd-odd $N = 77$ isotones, $^{142}_{65}\text{Tb}$ and $^{144}_{67}\text{Ho}$,” *Phys. Rev. C*, vol. 63, p. 034321, Feb 2001.
- [115] P. J. R. Mason *et al.*, “Prompt and delayed spectroscopy of ^{142}Tb using recoil-isomer tagging,” *Phys. Rev. C*, vol. 79, p. 024318, Feb 2009.
- [116] D. M. Cullen *et al.*, “ $20\mu\text{s}$ isomeric state in doubly odd $^{134}_{61}\text{Pm}$,” *Phys. Rev. C*, vol. 80, p. 024303, Aug 2009.
- [117] T. Grahn. “Private Communications”.
- [118] P. T. Greenlees. “Private Communications”.
- [119] J. Sar en, *The ion-optical design of the MARA recoil separator and absolute transmission measurements of the RITU gas-filled recoil separator. PhD Thesis, University of Jyv skyl *. PhD thesis, Jan. 2011.
- [120] J. Sar en. “Private Communications”.
- [121] L. Barber *et al.*, “Simultaneous lifetime measurements with the TPEN plunger,” *Unpublished Manuscript*, Nov. 2018.
- [122] S.  berg, P. B. Semmes, and W. Nazarewicz, “Spherical proton emitters,” *Phys. Rev. C*, vol. 56, pp. 1762–1773, Oct 1997.
- [123] S.  berg, P. B. Semmes, and W. Nazarewicz, “Erratum: Spherical proton emitters [phys. rev. c 56, 1762 (1997)],” *Phys. Rev. C*, vol. 58, pp. 3011–3011, Nov 1998.
- [124] R. J. Irvine *et al.*, “Proton emission from drip-line nuclei ^{157}Ta and ^{161}Re ,” *Phys. Rev. C*, vol. 55, pp. R1621–R1624, Apr 1997.
- [125] K. Lagergren *et al.*, “High-spin states in the proton-unbound nucleus ^{161}Re ,” *Phys. Rev. C*, vol. 74, p. 024316, Aug 2006.
- [126] P. Moller *et al.*, “Nuclear ground-state masses and deformations,” *Atomic Data and Nuclear Data Tables*, vol. 59, no. 2, pp. 185 – 381, 1995.

-
- [127] T. Klug *et al.*, “The $B(E2:4_2^+ \rightarrow 2_2^+)$ value in ^{152}Sm and β -softness in phase coexisting structures,” *Physics Letters B*, vol. 495, no. 1, pp. 55 – 62, 2000.